ABSTRACT

Title of Document: FLOW AND ATOMIZATION
                                CHARACTERISTICS OF CRYOGENIC
                                FLUID FROM A COAXIAL ROCKET
                                INJECTOR

                                Vivek Gautam, Ph.D., 2007

Directed By: Professor, Ashwani K. Gupta, Department of
                                Mechanical Engineering

High thrust-to-weight ratio and consistent performance over a range of operating conditions make cryogenic rocket engines one of the best options for space propulsion. However, future space explorations and missions to moon, mars and beyond require improvements in our present knowledge of the rocket engine combustion technology. In order to help improve the performance and reliability of current rocket engine combustors, several key issues need to be considered. Injector performance is one such issue related to the development of a new generation of rocket engine combustors.

Previous research has suggested that coaxial injectors are most preferable for injection of cryogenic propellants inside the combustion chamber because of their simple design, low losses and high combustion stability. An experimental facility was designed and fabricated to simulate a single element shear coaxial injector. Gases of different densities were injected through the annulus between the two injector tubes

over a large range of velocities, while liquid nitrogen flows through the inner tube. In this research, liquid nitrogen was used to simulate liquid oxygen because it is very similar to liquid oxygen, chemically inert, easy and safe to install in laboratory testing. High speed cinematography and Schlieren imaging have been used to examine the evolutionary flow behavior and global features of the liquid nitrogen jet, while PIV imaging was used to characterize the gaseous flow.

This research has analyzed the transient behavior and unfolds the detailed evolutionary characteristics of both the cryogenic liquid and gaseous phase evolving from the shear coaxial injector for the first time. The effect of density ratio, velocity ratio and momentum ratio on the behavior of steady-state liquid nitrogen jet from a coaxial injector at atmospheric pressure has also been examined in detail. The impact of these parameters on primary instability of liquid core, the shear/spreading angle and its potential core length have been examined. Furthermore, the impact of some of the important non-dimensional numbers such as, Reynolds number, Weber number and Prandtl number, have been examined to develop scaling laws for the prediction of cryogenic potential core lengths. New correlations have been provided that describes the cryogenic jet behavior under simulated rocket injector operating conditions.

FLOW AND ATOMIZATION CHARACTERISTICS OF CRYOGENIC FLUID
FROM A COAXIAL ROCKET INJECTOR

By

Vivek Gautam

Dissertation submitted to the Faculty of the Graduate School of the
University of Maryland, College Park, in partial fulfillment
of the requirements for the degree of
Doctor of Philosophy
2007

Advisory Committee:
Professor Ashwani K. Gupta, Chair
Professor Michael R. Zachariah
Professor Kenneth Kiger
Professor Peter Sunderland
Professor Kenneth Yu, Dean's Representative

Dedication

I would like to dedicate this thesis to my parents, Late Mr. Tribhuwan Nath Singh, and Mrs. Pushpa Singh. Without their continuing support and blessings I could not have ever made it this far in life. Because of their understanding and unconditional belief in my hopes and aspirations I have been able to drive myself to excel in my studies. Their contributions have been tremendous and wide-ranging in nature, and for that I will forever be indebted to them. It is for these reasons and countless more that this work is presented and dedicated in their honor.

.

Acknowledgements

I would first like to acknowledge my family and friends who have done their level best to keep me motivated during the grinds of grad school. I'd like to thank my brother, Rohit Gautam, for his example and inspiration, my sister, Gargi Gautam, for the love she has always shown towards me, and my brother in law, Karn Singh for the confidence he has always had in me.

My advisor, Dr. Ashwani K. Gupta, whose constant help, guidance and encouragement has been paramount in my success as a graduate student, and in my successful completion of this dissertation. I would also like to thank my committee members Dr. Ken Yu, Dr. Ken Kiger, Dr. Michael Zachariah and Dr. Peter Sunderland for giving me guidance throughout my graduate studies and providing valuable insights on my research. Dr. Mark Lewis and Dr. Greg Jackson taught me insights into fundamental physical principles and their importance in real life problems.

My roommates Nikhil Vichare, Sandeep Nayak and Yuki Fukuda made sure that I never feel alone staying away from home. Martin Linck and Jakub Gmurczyk taught me what determination really means and Howard Grossenbacher showed me how to be extremely good at everything you do. Special thanks go to Ms Chrisy Button for always being there as a friend and as an awesome exercise partner. Thanks also to Ahmed Abdelhafez, Magnus Mörtberg, Adam Klimanek, Sean Archer, Pierre Rousseau, Kyle Sullivan, James Diorio, Amit Kale and to my compatriots in the Combustion Lab.

.

Table of Contents

List of Tables

.

List of Figures

.

Nomenclature

A $\quad = \quad$ Inlet area of the flow

$B_T \quad = \quad$ Heat transfer number, $Cp_\infty(T_\infty - T_l)/L$

C $\quad = \quad$ Experimental constant

$C_p \quad = \quad$ Specific heat

D $\quad = \quad$ Inlet diameter of the flow

I $\quad = \quad$ Pixel intensity

k $\quad = \quad$ Thermal conductivity

L $\quad = \quad$ Latent heat of vaporization of the cryogenic fluid

$L_b \quad = \quad$ Potential core length

M $\quad = \quad$ Momentum ratio between the gaseous and liquid jets, $\rho_g V_g^2 / \rho_l V_l^2$

Oh $\quad = \quad$ Ohnesorge number, $\mu_l / \sqrt{\rho_l \sigma_l D_l}$

Pr $\quad = \quad$ Prandtl number, $\mu Cp/k$

Re $\quad = \quad$ Reynolds number, $\rho V D_l / \mu$

T $\quad = \quad$ Temperature

V $\quad = \quad$ Velocity

We $\quad = \quad$ Weber number, $\rho V^2 D_l / \sigma$

$\sigma \quad = \quad$ Surface tension of the fluid

$\rho \quad = \quad$ Density

$\mu \quad = \quad$ Viscosity

$\theta \quad = \quad$ Shear or Spreading angle

$\delta \quad = \quad$ Vorticity thickness

λ =   Wavelength

ν =   Frequency

Subscripts:

∞ =   Ambient medium

g   =   Gaseous

l   =   Liquid

n   =   Normalized

rel   =   Relative

.

1. Motivation and Objectives

High thrust-to-weight ratio and consistent performance over a range of operating conditions have made cryogenic rocket engines one of the best options for space propulsion. However, future space explorations and missions to moon, mars and beyond require improvements in our present knowledge of the rocket engine combustion technology. Efficient fuel-oxidizer mixing under all operational conditions still remains one of the major challenges for all types of engines. It is critical to obtain good mixing inside the combustion chamber for rapid ignition and efficient and stable combustion. In case of cryogenic rocket engines mixing between fuel and oxidizer and ignition delay depend on the injector design, operating conditions and propellant's physical and chemical properties. If the length required for efficient mixing is reduced, this will greatly reduce the overall weight to thrust ratio of the vehicle and result in improved performance and high specific impulse of the engine.

Injector performance is one of the most important issues related to the development of new generation of rocket engines. Development of an optimum injector for a rocket engine requires multiple considerations, including geometrical configuration, thermal compatibility, combustion stability, weight, losses, ease of manufacture. However, it is challenging to study the effects of all the above parameters on injector performance analytically because of large uncertainties associated with each parameter.

In general rocket injectors can be placed into two different categories based on their configuration. The first type is an impinging element where mixing takes place

by direct impingement of the fuel and oxidizer streams at an acute angle to each other. The second type of injector configuration is of non-impinging type configured in the form of a coaxial element where the fuel and oxidizer streams flow in parallel. Here the mixing takes place through development of a shear layer. Coaxial injectors are often preferred because of their simple design, low pressure losses and better combustion stability as compared to other injector designs. In case of cryogenic propellants the oxidizer is generally liquid oxygen (LOX) while the fuel is gaseous hydrogen (GH_2). This injector configuration has been used successfully in many cryogenic rocket engines such as, SSME, J-2, RL-10 and Ariane 5 Vulcain. Figure 1.1 shows a schematic of SSME engine assembly with a multi-element shear coaxial injector. Table 1.1 shows some relevant operating conditions for a coaxial liquid rocket injector. Figure 2.1 shows a schematic diagram of a typical single element shear coaxial injector.
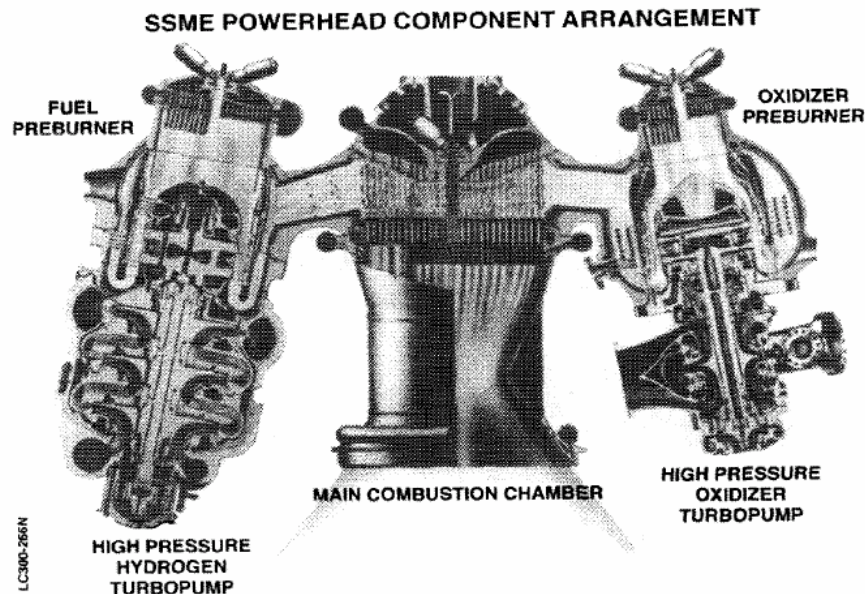
Figure 1.1. Drawing of a typical SSME engine with multi-element injector (Paster and Stohler, 1989)

Propellant	Velocities (m/s)	Velocity Ratio	Momentum Ratio	Mixture Ratio
LOX/GH$_2$	20-40/200-400	10-20	5-10	5-10

Table 1.1. Some relevant operating conditions for characteristic coaxial rocket injectors
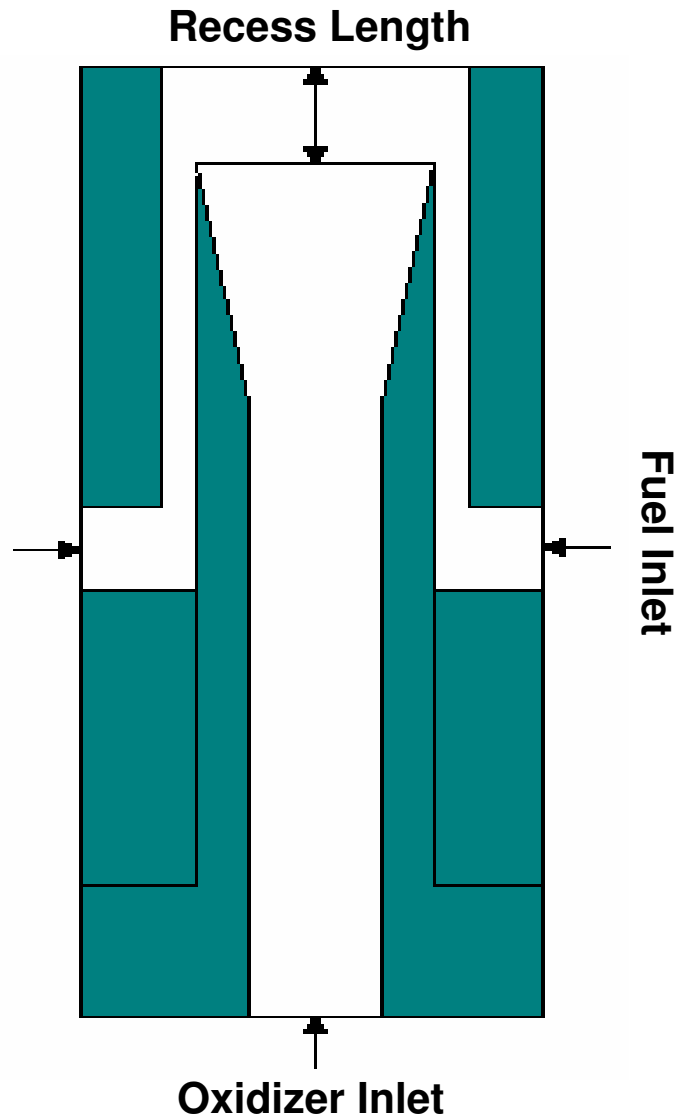
Figure 1.2. Schematic of a typical single element shear coaxial injector

Although the cryogenic propellants are injected into the rocket engine under steady state conditions, the initial introduction of propellants into the combustor are far from steady state. For example, in some of the rocket engines, during the initial 40 seconds (preceding ignition), the oxygen flow rate through the injector is substantial enough to chill the injector surfaces sufficiently so that the oxygen present in the injector at ignition is probably two-phase. Therefore, under realistic engine operating conditions, propellants such as liquid oxygen and gaseous hydrogen initially mix under unsteady conditions to trigger the onset of flow instabilities. The oxygen flow rate is reduced immediately prior to ignition, due to the closure of the control valve to the start position, but the oxygen flow remains two-phase during this initial period. Hydrogen fuel is in gaseous form under conditions occurring in the injector immediately prior to ignition. Thus, close examination of the initial transient flow behavior as well as mixing between two-phase oxygen and gaseous hydrogen flows is necessary to develop a better understanding of the fate of propellants during the pre-ignition conditions.

Figure 1.3 shows schematic of a typical flowfield from a coaxial injector. Generally flowfield from a typical coaxial injector can be divided into three different zones. The first zone is close to the exit of the injector and known as initial merged zone. In this zone both inner liquid core and outer gaseous core are present with very little or no interaction between each other. The expansion of the jets is also very little in this zone. The second zone is known as intermediate merged zone where inner liquid core start vaporizing and expanding rapidly. In this zone shear layer development and primary mixing between inner and outer flows take place. This zone

is considered very important for the ignition point of view. The third and final zone is known as fully merged zone where inner liquid core is completely vaporized and the fluid starts expanding rapidly. In this zone the flow is fully developed and secondary mixing between two fluids takes place. This zone is considered very important to achieve high combustion efficiency and smaller combustor size. Detailed knowledge of the two phase jet coming out of the injector, specially the flow evolution and various length scales present in the flow (Figure 1.4), is essential for the performance prediction and model validation.
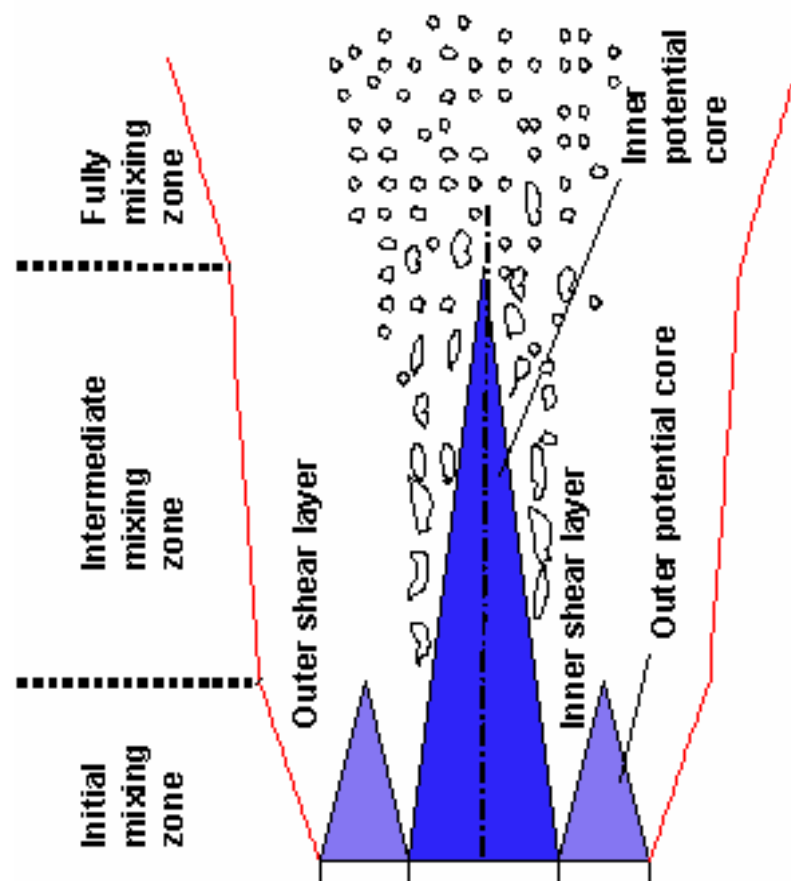
Figure 1.3. Schematic of a typical flowfield from a coaxial injector
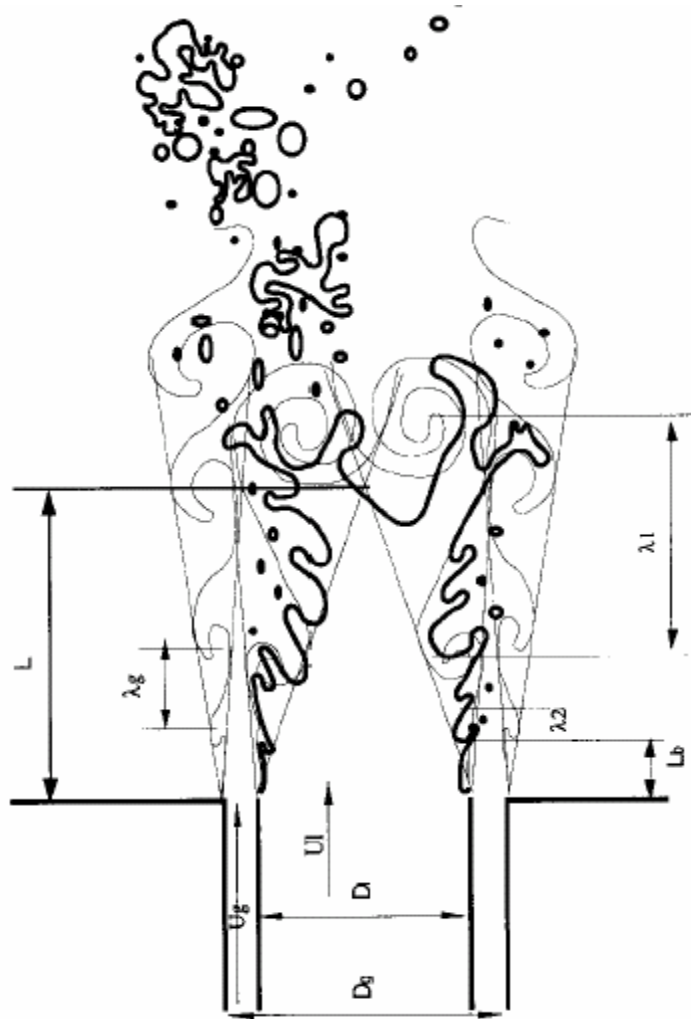
Figure 1.4. Schematic of various length scales present in the flow (Lasheras and Hopfinger, 2000)

Potential core length or breakup length of a liquid jet is defined as the location where the initially intact liquid jet is completely broken into ligaments and droplets. Beyond this point only separate ligament blobs and droplets exist in the flow that further break down into smaller ligaments and droplets along with excessively enhanced evaporation due to increase in surface area. However it is not easy to accurately measure the core length of a cryogenic jet due to two phase nature and optically opaque behavior.

In case of cryogenic fluids, analyzing the flow behavior of the jet, its destabilization, disintegration, and evaporation becomes complicated because of large variations in the physical properties and non-isothermal flow conditions. The destabilization of a liquid jet in a two-phase coaxial flow takes place due to several complex physical processes, such as, the development of a shear layer due to velocity gradients, the turbulent interactions and vorticity produced by the boundary layer, and the interaction between inertial, surface tension and viscous forces. A combination of all these destabilization processes along with the complex thermo-physical processes related to phase change makes it very challenging to understand and analyze the flow and atomization behaviors of two-phase cryogenic flows.

Significant research has been conducted in order to analyze the various physical process associated with the disintegration of cryogenic/non-cryogenic liquid jet from a coaxial injector. Some important parameters have also been identified that affect these physical processes, such as, velocity ratio, density ratio and momentum ratio between the jets, inlet temperature of the fluids, shape and geometry of the injector exit, recess length of the injector and temperature and pressure of the mixing chamber. However, in spite of all these research efforts, attaining comprehensive understanding of the liquid breakup, dispersion, evaporation and mixing of cryogenic fluids under all relevant and realistic operating conditions is still a major challenge involving highly complicated phenomena.

Thus, the objective of this research is to analyze the effects of some of the important parameters such as density ratio, velocity ratio and momentum ratio on the flow and atomization behavior of liquid nitrogen (LN_2) jet (simulating liquid oxygen

(LOX)) in a coaxial gaseous jet under steady-state and transient operating conditions. The effects of these parameters on primary instability of liquid core, its length and spray angle have been examined at atmospheric pressures. Furthermore, the impact of some of the important non-dimensional numbers such as, Reynolds number, Prandtl number and Weber number on the flow have been examined to analyze the effect of some of the major physical processes such as shear layer destabilization and heat transfer on the core length of cryogenic jet in coaxial gaseous stream.

2. Literature Review

An extensive review was conducted on the experimental and theoretical work performed on two phase coaxial flow, atomization, mixing and combustion behavior. The experimental and computational data, available in the literature, on such type of flows is either incomplete or ambiguous. Most of the previous theoretical models present in the literature are only valid for a limited range of operating conditions and are often incapable of accurately predicting the flow behavior under all realistic conditions.

2.1. Non-Cryogenic Coaxial Jets (Non-reacting)

The first part of literature review is focused on the research performed on non-reacting two phase coaxial jets with non-cryogenic liquids such as water, ethanol and glycol. Chandrashekhar (1961) performed a classic linear stability analysis of coaxial jets examining the effect of shear, gravity, surface tension, heat, centrifugal force and turbulence. He summarized various instability mechanisms present in single phase or two phase flow and showed the conditions that lead to a certain type of instability in the flow. Figure 2.1 shows development of a typical Kelvin-Helmholtz instability at the interface of two fluid jets of different densities. Similarly Spalding (1963) gave detailed overview of several non-dimensional parameters that can be utilized to examine the importance of physical processes that affect the flow instability, atomization, evaporation and mixing of liquid jet in quiescent or flowing gaseous medium.
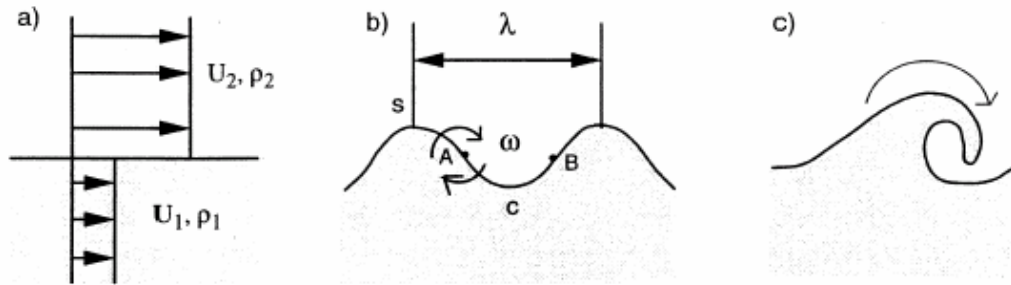
Figure 2.1. Kelvin-Helmholtz instability mechanism (Raynal, 1997)

Reitz and Bracco (1982) performed extensive experiments to analyze the various physical processes associated with liquid jet destabilization and atomization as proposed in linear stability analysis. Their work involved the atomization behavior of an atomizing liquid jet for a range of Reynolds number, Ohnesorge number and different surrounding gas properties along with the effect of nozzle geometry at ambient pressure. They showed that the growth rate or spray angle of an isothermal jet depends strongly on the densities of liquid jet and surrounding gas i.e. $\theta \approx 0.27(\rho_g/\rho_l)^{0.5}$. However they concluded that turbulence and aerodynamic surface wave growth mechanisms are not the only processes that affect liquid jet instability and atomization behavior. Many other parameters affect the liquid jet instability and atomization process and significant research is still needed to study and analyze these processes.

Arai et al. (1985, 1991) used an electrical resistance method to calculate the potential core length of a liquid jet (water) in quiescent air. They examined the effect of jet velocity and analyzed the various regimes of the flow from laminar to turbulent and examined their impacts on the potential core length of the liquid jet. The results

showed that the potential core length increased with increase in Reynolds number in the laminar regime whereas it decreased in the transition regime. The potential core length started increasing again in turbulent regime until the fully developed condition is achieved; beyond that point the potential core length of liquid jet started smoothly decreasing with Reynolds number (Figure 2.2). They also looked at the influence of ambient pressure on the potential core length of the liquid jet and concluded that the ambient pressure changes the density of the surrounding medium which eventually affects the destabilization of liquid jet due to shearing action. This effect was found to be not so significant in laminar regime but very significant in other regimes. Chehroudi et al. (1985) used a similar electrical resistance technique to extend the previous work by Arai et al. on the potential core length of liquid jet. However they found certain errors within the technique to predict the accurate potential core length of liquid jet, which in turn brought the previous work into question.
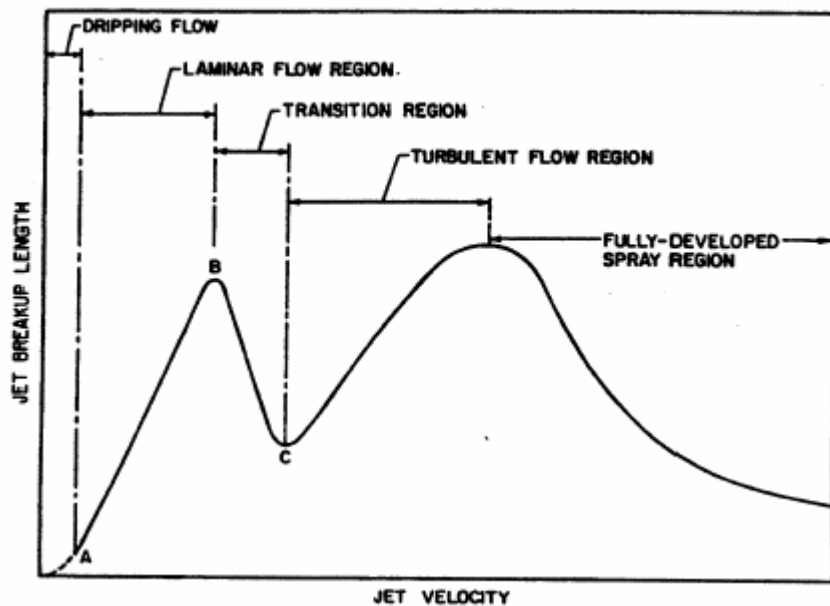
Figure 2.2. Variation of liquid jet breakup length with velocity (Lefebvre, 1988)

11

Arai and Hashimoto (1985) used a photographic technique to measure the potential core length of a thin liquid sheet in coflowing air. They also looked at some of the destabilization frequencies, droplet sizes and velocities present in the flow. Although the Reynolds numbers they examined were low (<1000), they showed the importance of aerodynamic Weber number on liquid jet destabilization and disintegration.

Eroglu et al. (1991) used a similar photographic technique to measure the potential core lengths of two phase coaxial jets under more relevant flow operating conditions. However they also used water and air as simulants for LOX and gaseous hydrogen. Their results showed that the potential core length first decreases and then increases with increase in liquid Reynolds number but it was found to decrease with Weber number. An empirical equation (Equation 2.1) was derived for the prediction of liquid core lengths generated by airblast coaxial atomizers. The results also showed that the round jet produced shorter intact lengths than flat liquid sheets due to the destabilizing effect of radius of curvature.

$$L_b/D_l \approx 0.5 We_g^{-0.4} Re_l^{0.6} \qquad\qquad [2.1]$$

Farago and Chigier (1992) investigated high speed spark photographs of water jet in coflowing air to analyze the effect of coaxial gas on liquid jet instability and atomization. They investigated a large range of liquid Reynolds number (200-20000) and Aerodynamic Weber numbers (0.001-600) to compare the results of linear stability analysis and prior experiments performed by Reitz and Bracco (1982) on turbulent liquid jets. The comparison showed strong disagreements at certain conditions. They finally presented a detailed classification of various jet

disintegration modes based on aerodynamic Weber number, which suggested when $We_g < 15$, the dominant disruption mode is axisymmetric Rayleigh breakup while it is non-axisymmetric Rayleigh breakup for $15 < We_g < 25$. Membrane type mechanism destabilized by Kelvin-Helmholtz waves was the dominant mode for $25 < We_g < 70$ whereas Fiber type ligament mode was the dominant mechanism for $We_g > 70$. However, for most of the technical applications for $We_g > 70$, hence the fiber type breakup mechanism is responsible for liquid jet atomization. The results also showed high pulsation rates for this mode of atomization, especially for $Re_l/We_g^{0.5} < 100$. Figure 2.3 shows various regimes of liquid atomization in the parameter space Re_l-We_g.
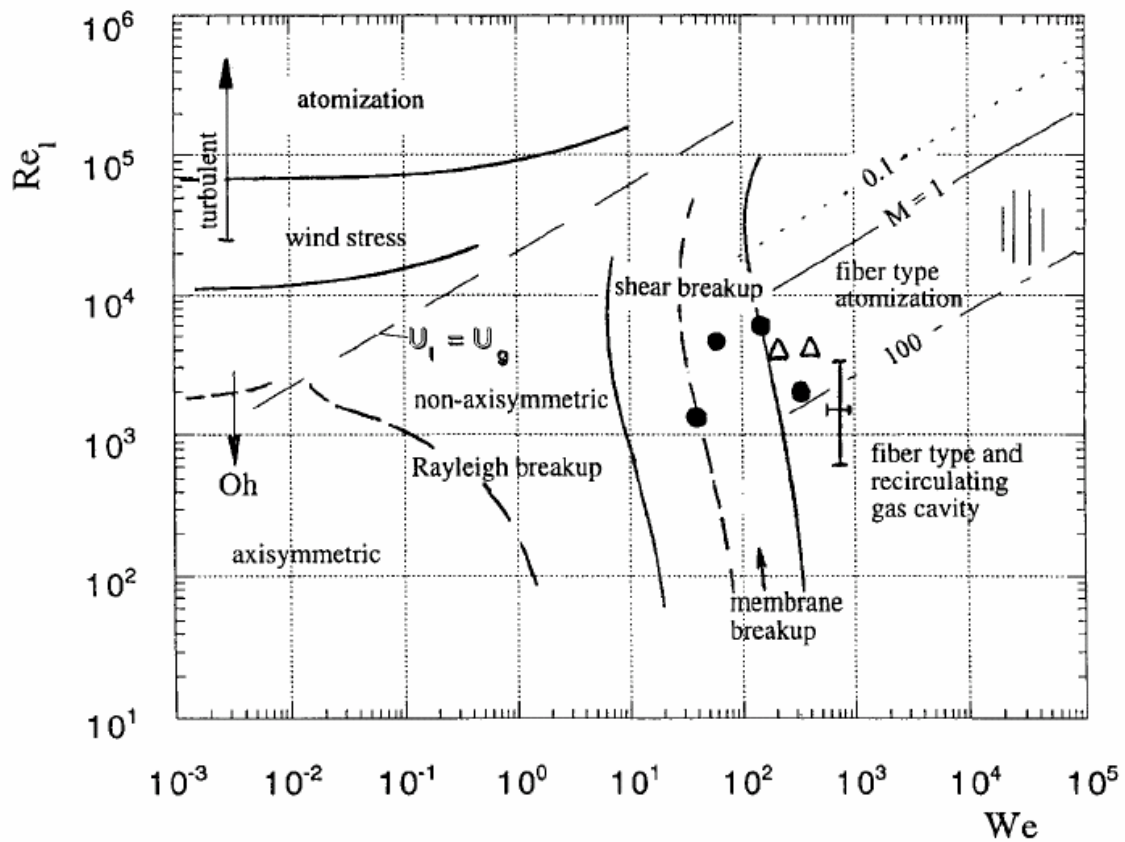
Figure 2.3. Various regimes of liquid jet breakup (Lasheras and Hopfinger, 2000)

13

Wu et al. (1992) performed an experimental study of primary breakup of turbulent liquid jets at various velocities into still air and helium at atmospheric pressure. They examined water, glycerol (42% glycerin by mass), and *n*-heptane using pulsed shadowgraph photography and holography to measure the breakup length as well as drop sizes and velocities after breakup. They also showed the importance of aerodynamic Weber number on atomization as well as droplet characteristics.

Mayer (1994) provided a brief summary of similar work performed on non-cryogenic two phase coaxial jets at DLR Germany. They used spark photography and high speed cinematography to observe the flow and atomization behavior for a broad range of conditions. The velocity range of their study varied from $0.4 < V_l < 30$ m/s and $0 < V_g < 300$ m/s for the liquid and gas, respectively. They also varied the chamber pressure from 1 atm – 20 atm to look at the effect of pressure or gas density on the liquid flow and atomization characteristics. Their results showed the importance of liquid surface waves on its eventual atomization. The wavelengths of liquid surface waves were shown to be strongly dependent on the structure of turbulence inside the liquid and the waves further grew or damped out depending on fluid properties and the strength of aerodynamic interaction. The aerodynamic forces amplified, deformed and stripped the waves off the liquid surface without affecting its wavelength. The amplified waves grew to critical amplitude which is comparable to its wavelength until parts of the wave detach in the form of ligaments or droplets.

Engelbert et al. (1995) then took another approach to examine the same problem. Instead of only looking at liquid Reynolds number (Re_l) and aerodynamic Weber number (We_g), they used momentum ratio, velocity ratio, liquid Reynolds number

(Re_l) and Weber number (We_l) as important parameters for two phase coaxial jet instability and atmozation behavior. Their diagnostics include high speed photography and phase doppler velocitmetry technique to study the turbulent water/air jet for a large range of momentum ratios ($M \approx 3\text{-}175$). Their results suggested that the liquid breakup length, the wave frequencies and flow oscillations were strongly dependent on the gas/liquid momentum and energy ratios apart from liquid Weber number and slip velocity of the two streams. The liquid jet breakup length decreased with the increase in momentum ratio or slip velocity between the jets (Equation 2.2). Similar trends were shown for the amplitude of surface waves structure of the liquid jet at breakup.

$$L_b/D_l \approx C/M^{0.3} \tag{2.2}$$

Chigier and Reitz (1996) performed an extensive review of all the above works along with some other relevant works performed on similar flows. Similarly Lin and Reitz (1998) reviewed drop and spray formation of a liquid jet based on linear stability theories aimed at the delineation of the different regimes and elucidation of the associated physical mechanisms. Their study discussed various regimes of breakup of liquid jets injected into both stagnant and coflowing gases and pointed out the unresolved scientific issues. The physical mechanisms at work in the different breakup regimes were described and available criteria for the transition between the regimes were reviewed. The influence of nozzle internal flow effects was shown to be important, but these effects were only included empirically in current wave-stability theories. They suggested that a useful area for future research would be the development of fundamentally based models that account for the effect of nozzle

15

internal flows on the liquid breakup process. In addition, current breakup models need to be extended to account for the nonlinear effects of liquid distortion, membrane formation, and stretching on the atomization process. These phenomena are especially important in liquid injections in a high-momentum coflowing gas.

Rehab et al. (1997) used laser induced fluorescence technique combined with fast response velocity and pressure measurements to investigate the near-field flow structure of coaxial jets with large gas/liquid velocity ratios. They came up with a critical gas/liquid velocity ratio to determine the instability and breakup mechanism of the liquid jet. When gas/liquid velocity ratio is smaller than the critical value, the primary instability mechanism was shown to be the jet-preferred mode with high frequency oscillations and the length of the inner potential cone is strongly dependent on gas/liquid velocity ratio. Whereas when gas/liquid velocity ratio is larger than critical the instability mechanism was shown to be wake-type instability with low frequency and large amplitudes compared to the Kelvin-Helmholtz mode.

Raynal (1997) performed extensive experiments using a laser beam and photo diode based setup combined with optical visualization technique to examine the primary breakup of water jets and evaluated the primary instability mechanism of the coaxial jets. He measured the velocity of the gas/liquid interface (convection velocity) in the near field region of the flow and showed that it is continuous and can be expressed as a function of momentum ratio between the jets therefore thin shear interface assumption taken by previous researchers is not accurate. He also calculated the wavelength and frequency of vortical structures on the liquid surface and found them to be similar to the wavelength and frequencies of Kevin-Helmholtz type

instabilities. He proved that gas vorticity thickness is responsible for these types of instabilities and the effect of surface tension is almost negligible. In the later part of his doctoral dissertation work, Raynal examined the various modes of liquid jet breakup and the effect of Reynolds and Weber numbers. He derived a simple correlation (Equation 2.3) based on momentum ratio to predict the breakup length of water jet in high speed coaxial air stream.

$$L_b/D_l \approx 0.5 + 307\ M^{-0.33} Re_{\delta l}^{-0.66} \hspace{4cm} [2.3]$$

Lasheras et al. (1998) analyzed the near and far field break-up and atomization of a water jet by a high-speed annular air jet by means of high-speed flow visualizations and phase doppler particle sizing techniques. Visualization of the jet's near field and measurements of the frequencies associated with the gas-liquid interfacial instabilities were used to study the underlying physical mechanisms involved in the primary breakup of the water jet. This process is shown to consist of the stripping of water sheets, or ligaments, which subsequently break into smaller lumps or drops. They also proposed a simple correlation (Equation 2.4) for liquid jet breakup length and an entrainment model for the near-field stripping of the liquid to describe the measured liquid shedding frequencies. The model qualitatively explained the dependence of shedding frequencies on the air-water momentum ratio in both initially laminar and turbulent water jets. They also investigated the role of the secondary liquid break-up in the far-field atomization of the water and the total flux of kinetic energy supplied by the gas per unit total mass of the spray jet was found to be the primary parameter determining the secondary break-up and coalescence of the droplets in the far field.

$$L_b/D_l \approx C\ M^{-0.5} \hspace{4.5cm} [2.4]$$

17

Villermaux (1998) demonstrated by doing a simple analysis that the global entrainment rate, potential core length and the primary drop formation in gas/liquid coaxial jets can be explained on the basis of the primary shear instability between the phases. It was shown that the shape of the velocity profile at the outer injector lip, and its vorticity thickness is of primary importance to set the growth rate of the instability and its preferred wavelength $\lambda \sim \delta(\rho_l/\rho_g)^{0.5}$, whereas inner potential core length (liquid intact length) is $L_b/D_l \approx 6/M^{0.5}$. He also showed that L_b is independent of liquid viscosity and surface tension and for M (momentum ratio) > 35, a transition to a recirculation flow occurs, whose efficient mixing properties were quantified.

Lasheras (2000) performed a review of various theoretical and experimental work performed on core length measurements, droplet formation and spray characteristics. He also reviewed various correlations available for liquid core length prediction and suggested several improvements for improved accuracy. A comparison of his suggested correlation (Equation 2.5) with experimental results of Raynal was also presented.

$$L_b/D_l \approx 6M^{-0.5}(1-0.001\sigma/\mu_g V_g)^{-0.5} \tag{2.5}$$

Varga et al. (2003) used high speed flow visualization and particle-sizing techniques (phase doppler anemometry) to examine the initial jet breakup processes and primary liquid atomization behavior. They investigated a small diameter liquid jet exposed to a large diameter high-speed gas jet (gas/liquid flow inlet area ratio of order 100 to 1000). They showed that the bulk of liquid atomization is completed within a few diameters of the injector exit for large aerodynamic Weber numbers; therefore jet breakup is completed within the initial zone of constant ambient gas

18

velocity. They argued that the mechanism of initial jet breakup is similar to that of a liquid drop suddenly exposed to a high-speed gas stream. They proposed a phenomenological breakup model for the liquid jet instability and breakup based on Kelvin–Helmholtz and Rayleigh–Taylor instability of the liquid jet surface, which were the primary and secondary destabilization mechanisms respectively.

Marmottant and Villermaux (2004) also performed similar experiments and proposed a two-stage mechanism for jet deformation. They suggested that shear instability first forms waves on the liquid surface which is further destabilized by Rayleigh–Taylor type of instability triggered at the wave crests, producing liquid ligaments, which further stretch in the air stream and break into droplets. They also confirmed Raynal's (1997) suggestions that the primary wavelength of the surface instabilities is strongly dependent on the vorticity thickness and density ratio between the two jets.

Villermaux et al. (2004) investigated the fiber type mode or ligament mediated spray formation of liquid jets in details. They suggested that the spray formed when a fast gas stream blows over a liquid volume presents a wide distribution of fragment sizes. The process involves a succession of changes of the liquid topology, the last being the elongation and capillary breakup of ligaments torn off from the liquid surface. The coalescence of the liquid volumes constitutive of a ligament at the very moment it detaches from the liquid bulk produces larger drops (Figure 2.4). This aggregation process has its counterpart on the size distribution associated with the ligament breakup. The size distribution is found to be very well represented by gamma distribution. The exponential shape of the overall distribution in the spray

coincides with the large excursion wing of these elementary distributions, underlying the crucial role played by the ligament dynamics in building up the broad statistics of sprays.
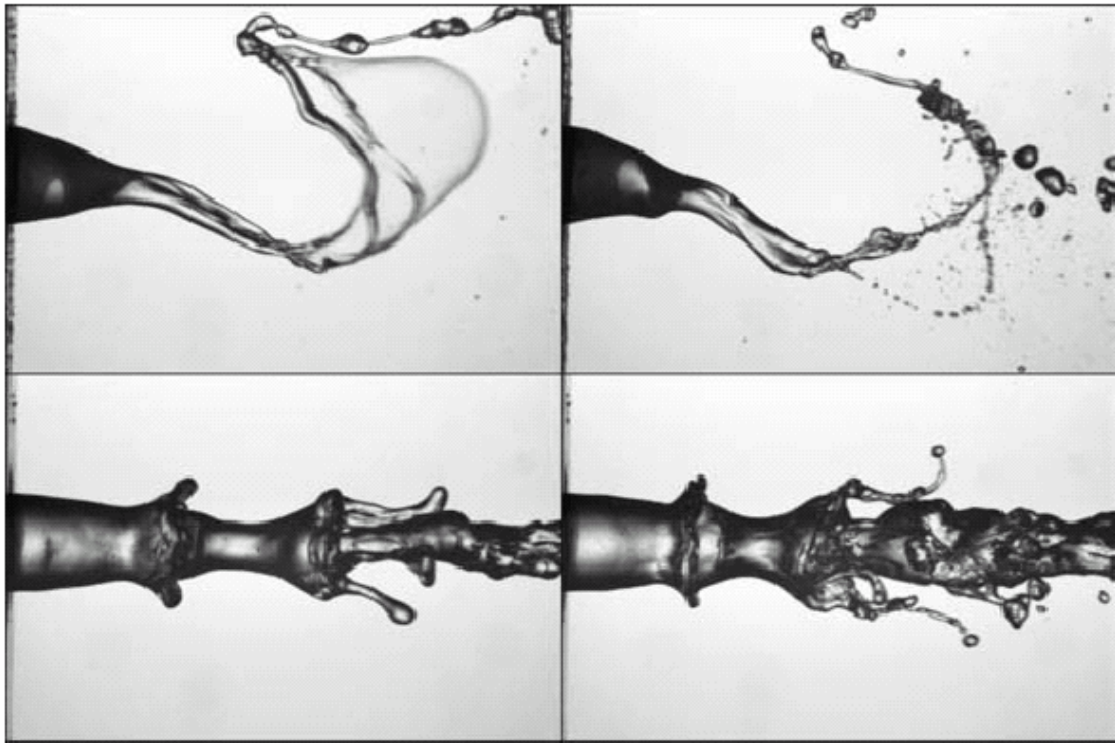
Figure 2.4. Breakup regimes of a liquid jet; Top: Low gas velocity, liquid jet meanders in the gas stream, Bottom: Higher gas velocities, ligament mediated breakup (Villermaux et al., 2004)

Kim and Heister (2004) performed detailed two-phase modeling of hydrodynamic instabilities in coaxial injectors. They developed a homogeneous flow model to assess hydrodynamic instabilities of coaxial atomizers in which a liquid jet/sheet is submerged in an annular gaseous stream. They found strong evidence of Kelvin–Helmholtz type instabilities under conditions where the gas velocity is substantially

greater than that of the liquid. Their parametric studies indicate the amplitude of the instability increases with gas velocity, gas density, and sheet recess/submergence length inside the channel, whereas increasing sheet thickness tended to decrease the amplitude of the oscillation. The frequencies observed were shown to be consistent with the channel transit time of the liquid. They further investigated a series of liquid post thicknesses to assess the effects of this parameter and observed recirculating flows at the post tip. Thin posts show greater amplitude instabilities than the zero-thickness case, whereas a thicker post proved to damp the amplitude of the oscillation. In addition, the thinner posts created much higher oscillation frequencies than the case of a zero-thickness post.

Branam and Mayer (2004) used high speed shadowgraph technique to examine the effect of jet velocity, Weber number and chamber pressure (gas density) on primary atomization behavior of ethanol jet flowing in coaxial nitrogen stream. They measured the amplitude and frequency of surface waves for a large range of conditions to analyze the physical processes associated with liquid jet atomization. Their results reinforced the previous works which found that aerodynamic forces are the dominating factor in jet breakup and they strongly affect the surface of the jet. For the cases where injection velocities of both the flows are equal (relative velocity is zero), turbulence is the primary source for surface disturbances and eventually leads to jet breakup which has been predicted by prior researchers. The effect of changing chamber pressure is incorporated in changing aerodynamic behavior of the gaseous jet due to change in its density. They also showed that at constant pressure, the location of droplet initiation is directly dependent on injection velocity and relative

21

velocity between the jets, the location at which a droplet separates decreases with increasing relative velocity as predicted by previous researchers. However they emphasized that the direction of the relative velocity significantly affects the injector performance and cannot simply be described by scalar geometrical and operational injection parameters (e.g., *We, Re* or *Oh*). In order to analyze this behavior, one has to include the injection 'vector' or direction of the atomizing fluids in relation to each other and in relation to the ambience (combustion chamber, etc.), thereby underlining the importance of injector–injector and injector–chamber interaction.

2.2. Cryogenic Coaxial Jets (Non-reacting)

The second part of this literature review is focused on the research performed on non-reacting two phase coaxial jets with cryogenic fluids such as liquid oxygen (LOX) and liquid nitrogen (LN_2). These experiments were performed to analyze the flow, atomization and mixing characteristics of shear coaxial injectors typically used in cryogenic rocket engines. Bellan (2000) performed an extensive review on subcritical and supercritical fluid atomization behavior and modeling issues. She showed that fluid jet disintegration under supercritical conditions is fundamentally different from the much studied subcritical liquid atomization. Instead of the subcritical wave formation at the surface of the liquid resulting from the relative velocity between the liquid and gas, ensuing in the subsequent instability and the further breaking of the liquid sheet, under supercritical conditions the fluid disintegrates in a remarkably different fashion. The optical data shows wispy threads of fluid emanating from the jet boundary and dissolving into the surrounding fluid. The existing information on two phase flows and atomization behavior is of

qualitative nature for supercritical fluids and considerable experimental work is necessary to provide data appropriate for model validation. She also discussed and evaluated the accuracy of existing models based on specific aspects supercritical fluids, such as intrinsic transient behavior, lack of a material surface, real gas equations of state, mixture non-ideality, increased solubility, Soret and Dufour effects and high pressure transport properties.

Woodward (1994) used X-ray radiography and instantaneous imaging technique to measure the potential core length of LOX simulant (KI in aqueous solution) for a large range of Reynolds number, Weber number and density ratios. His measurements included two different approaches to measure the intact core length of LOX simulant. The first technique was thresh-holding of jet images to reveal the core images corresponding a specific liquid integrated thickness while the second technique was deconvolution of time averaged images to obtain mean liquid volume fraction distributions. Although both the techniques had inherent unknown errors, they provided some very important measurements of cryogenic flow simulants for the first time. The results suggested that the potential core length of the cryogenic jet also depends on cavitation induced turbulence apart from the aerodynamic shear. In the aerodynamic shear regime, his results showed strong dependency of gas density on the potential core length, thus suggesting the importance of momentum ratio between the jets. He also came up with a non-dimensional correlation (Equation 2.6) based on liquid Reynolds number (Re_l), aerodynamic Weber number (We_g) and density ratio between the jets to predict the potential core length.

$$L_b/D_l \approx C(\rho_g/\rho_l)^{-0.36/Z} We_g^{0.22/Z} Re_l^{0.68} \qquad\qquad [2.6]$$

Glowgosky et al. (1994) performed an experimental investigation of the spray produced by a single shear coaxial injector. They used two different fluid combinations for spray characterization using stroboscopic photography and planar laser imaging to visualize the global spray characteristics and phase doppler interferometry to measure droplet size and velocity. The initial tests were performed with water/air at atmospheric pressure and the results were subsequently compared with the results from experiments using LN_2/GN_2. Their work also included the effect of recess and tapered LOX post and showed that the tapered LOX post recessed into the fuel annulus has strong impact on atomization behavior and spray structure. Spray visualization tests with LN_2/GN_2 at elevated pressures illustrated the strong influence of liquid to gas mixture ratio and chamber pressure on the overall morphology of the spray. Higher mixture ratios yielded large, poorly atomized and vaporized sprays while increasing chamber pressures below the critical point resulted in a contraction of the spray whereas the spray ceased to contract and extended deeper for a mixture ratio near unity and pressures above the critical point.

Vingert et al. (1996) performed a review on theoretical aspects of two-phase coaxial jet flow and atomization behavior along with experimental work conducted at ONERA, France. The experiments performed at ONERA characterized droplet sizes from a coaxial injector for non-cryogenic (water) and cryogenic (LOX) fluid both. The effect of chamber pressure was also investigated. The results showed significant differences between cryogenic and non-cryogenic fluid behavior, which according to the author's was an effect of vaporization of LOX. The non-cryogenic test also didn't match well with theoretical work performed by prior researchers so the authors

24

emphasized on the need of development of new and improved models for prediction of flow and atomization behavior of cryogenic jet from a coaxial injector.

Carreau et al. (1997) used a liquid presence probability (LPP) technique with an optical probe to calculate the core length of LOX jet in a coaxial gaseous stream (He and N_2). They performed experiments for a large range of liquid Reynolds number ($Re_l \sim$ 54700-80500) and aerodynamic Weber number ($We_g \sim$ 9210-31600) and showed that density ratio between the jets had an important effect on the liquid core atomization behavior apart from momentum ratio between the jets. They also proposed a correlation to predict the potential core length of the LOX jet based on the liquid Reynolds number (Re_l), aerodynamic Weber number (We_g) and density ratio between the jets which was very similar to the Woodward's correlation (Equation 2.7).

$$L_b/D_l \approx 6.10^{-4}(\rho_g/\rho_l)^{-0.32} We_g^{0.03} Re_l^{0.55} \qquad\qquad [2.7]$$

Mayer et al. (1998) performed studies of LOX droplet breakup using flashlight photography and high-speed cinematography under high-pressure subcritical conditions near the critical pressure. They showed that breakup initiation times decreased but that the total breakup time increased as the droplet Weber number increased. They also compared the LOX droplets and ethanol droplets under similar conditions and showed that transition to higher breakup regimes occur at larger droplet Reynolds numbers for the ethanol droplets. They conjectured those results to be an effect of lower surface tension of LOX droplets than the ethanol droplets, which was confirmed by the fact that as pressures increased into a transcritical regime, no indication of surface tension was found and the droplets were incapable of resisting

deformation. Their results revealed a remarkable difference between subcritical and supercritical spray formation, evaporation and mixing behavior (Figure 2.5). This was because, as chamber pressure approaches the critical pressure, injection can no longer be regarded as simple ''spray'' formation, but rather as a fluid/fluid mixing process that can be extremely sensitive to small perturbations in pressure, temperature, local mixture concentrations, and initial injection conditions.
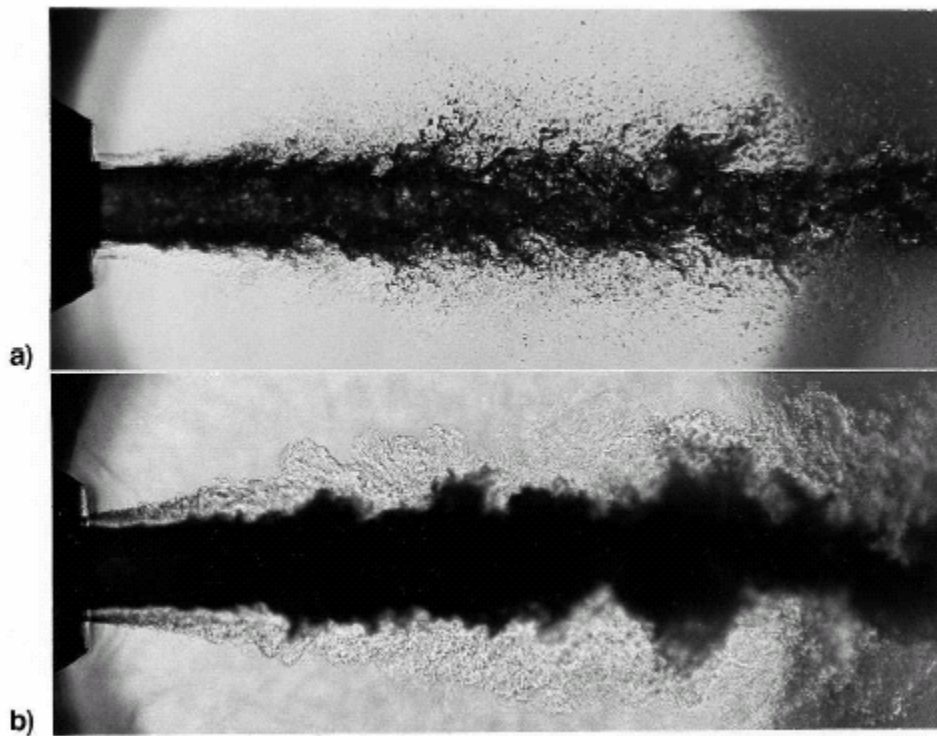
Figure 2.5. Coaxial LN$_2$/He injection at a) 1.0 and b) 6.0 MPa (Mayer at al., 1998)

Branam and Mayer (2002) examined the length scales present in supercritical liquid nitrogen jet from a single coaxial injector using shadowgraph imaging. They analyzed chamber pressures from 4 to 6 MPa at two flow velocities (2 and 5 m/s) and two injection temperatures (120 and 130 K). The geometrically averaged length

scales determined using two-point correlation method from the shadowgraph images showed a strong correlation with the Taylor microscale which characterizes the average energy dissipation length scale. Their results suggested little influence due to variations in temperature, velocity, and pressure on the average length scales, but components in the axial and radial direction showed some influence primarily caused by temperature gradient.

Porcheron et al. (2002) used a liquid presence probability (LPP) technique as proposed by Carreau et al. (1997) to further investigate the core length of LOX jet in a coaxial gaseous stream (He, N_2 and Ar). They performed experiments for a large range of momentum ratios ($M \sim 2$- 21.6) by varying the velocities and densities of the jets. Their results again revealed the important effect of density ratio between the jets on the liquid core atomization behavior apart for constant momentum ratios between the jets. The authors explained this phenomenon by taking into account the differential reduction in gaseous velocity for different density gaseous jets injected in the same surrounding medium at same velocity thus changing the local Weber number (We_g) and momentum ratio (M). They also improved the correlation proposed by Carreau et al. (1997) to predict the potential core length of the LOX jet based of momentum ratio, Ohnesorge number (Oh) and density ratio between the jets (Equation 2.8).

$$L_b/D_l \approx 2.85(\rho_g/\rho_l)^{-0.38}Oh^{0.34}M^{-0.13}$$
[2.8]

Chehroudi et al. (2002) investigated cryogenic jets (LOX and LN_2) initially at a subcritical temperature injected into supercritical temperature environment and at various pressures ranging from subcritical to supercritical values. They

experimentally examined the flow near the exit region using a Charged Coupled Device (CCD) camera illuminated by a short duration backlit strobe light. Figure 2.6 shows the effect of pressure on cryogenic jet spreading and atomization behavior of LOX jet. At low subcritical chamber pressures, the jets behaved like non-cryogenic jets, showing wavy surface irregularities that amplified downstream and eventually broke up into ligaments and droplets. At subcritical chamber pressures close to critical pressure, the transition to a full atomization regime was inhibited. The jet structure at this point changed and began to resemble a turbulent gas jet with no detectable droplets due to reduction in surface tension and vaporization enthalpy as shown by Branam and Mayer (2002). They also measured the initial divergence angle of the jet at the exit and compared it with the divergence angle of a large number of other mixing layer flows, including atomized liquid sprays, turbulent incompressible gaseous jets, supersonic jets, and incompressible but variable density jets. The results showed that the jet growth rate measurements agreed quantitatively with the theory for incompressible but variable density gaseous mixing layers at and above the critical pressure of cryogenic fluid whereas it matched the results for non-cryogenic sprays at low subcritical pressures. They finally improved the Reitz and Bracco's model to predict the growth rate of shear layer by using his experiments (Equations 2.9, 2.10 and 2.11, where, $x=1.0$ for LN_2/GN_2, and $x=0.2$ for LN_2/GHe)

$$\theta = 0.27[F(x(\rho_g/\rho_l)) + (\rho_g/\rho_l)^{0.5}] \qquad [2.9]$$

$$F(\rho_g/\rho_l) = 5.325(\rho_g/\rho_l) + 0.0288 \text{ for } \rho_g/\rho_l < 0.0885 \qquad [2.10]$$

$$F(\rho_g/\rho_l) = 0.5 \text{ for } \rho_g/\rho_l \geq 0.0885 \qquad [2.11]$$
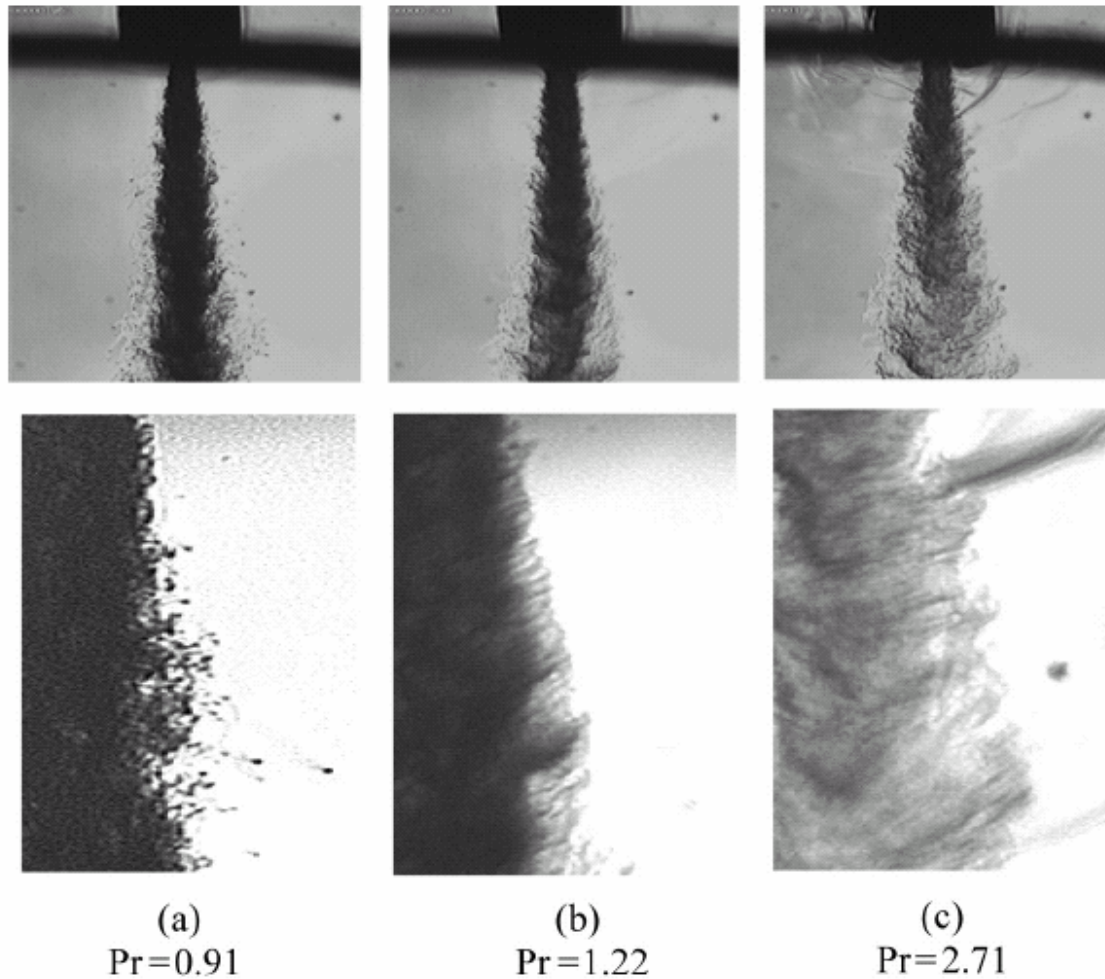
Figure 2.6. LN$_2$ injected into room temperature nitrogen at different reduced pressures (Pr = P/Pc) (Chehroudi et al., 2002)

Oschwald and Micci (2002) conducted spontaneous Raman measurements on cryogenic LN$_2$ jet from a shear coaxial injector to examine jet spreading angles and the variation of centerline densities downstream of the injector. The spreading angle data matched well with compressible shear-layer models and some of Chehroudi's (2002) experiments. However, the centerline density profiles showed some interesting results where a dependence of density ratio on centerline density variation of trans and supercritical LN$_2$ jet was observed. The results suggested that supercritical LN$_2$

cannot be treated as a variable density ideal gas therefore a different formulation is required for predicting the flow behavior of supercritical jets.

Ferraro et al. (2002) investigated a subscale rocket combustion chamber operated with a single full-size SSME pre-burner element at a liquid oxygen flow rate of 0.113 kg/s. The effect of gas/liquid velocity and momentum ratios on LOX droplet size and velocity distribution was examined using PDPA for global fuel/oxidizer mixture ratios between 3.2 and 5.6. Droplet sizes were found to decrease with increasing gas/liquid velocity or momentum ratio while the droplet velocities increased. The c^* efficiency was found to increase with increasing velocity and momentum ratios. They also presented a correlation to predict the droplet arithmetic mean diameter as a function of gas/liquid momentum ratio for chamber pressures between 2.0 and 4.5 MPa.

Branam and Mayer (2003) further extended their previous work (2002) on length scales measurements in supercritical liquid nitrogen jet from a single coaxial injector using shadowgraph and Raman imaging techniques. They also came up with a validated numerical model to predict the flowfield of supercritical jets. Their model showed good agreement with density, length scales, and jet spreading angles obtained from Raman and shadowgraph images.

Vingert et al. (2004) performed another more detailed review on theoretical aspects of two-phase coaxial jet flow and atomization behavior along with experimental work conducted at ONERA and some other laboratories. They concluded that no unified theory is currently available for cryogenic flow and

atomization behavior and experimental investigations remain the best way to characterize cryogenic flow from a coaxial injector.

Oschwald et al. (2006) performed an extensive review of work performed at DLR and AFRL on cryogenic injection at subcritical and supercritical pressures, with application to liquid rocket engines. Their review confirmed that the visual appearance of the cryogenic jet undergoes a drastic change as the pressure is increased from a subcritical to a supercritical value. The subcritical jet had the appearance of a conventional spray, but the supercritical jet has a more gas-like appearance as suggested by previous research. They also confirmed that the spreading rate of supercritical jets based on shadowgraph measurements is quantitatively the same as that predicted by theory for variable density gas mixing layers. The comparison of shadowgraph measurements with density profiles obtained from spontaneous Raman scattering showed that Raman measurements were most useful in supercritical jets, due to issues with stimulated and plasma emission in subcritical jets. The density profiles of supercritical jets approached self-similar shapes at about 10 diameters downstream. The spreading angles of supercritical jets measured using shadowgraphy correspond to the spreading angles measured using Raman scattering when the jet width using the latter is defined to be twice the full width half maximum (FWHM) distance of the measured density profiles. The comparison of potential core length measurements performed by both the laboratories showed that AFRL measurements (shadowgraphy) were larger by a factor of 1.5 to 2 than the DLR measurements (Raman scattering). DLR also demonstrated a significant effect of the initial jet temperature, depending on whether this temperature is above or below the

pseudo-boiling temperature, defined to be the temperature at a supercritical pressure where the specific heat reaches a maximum. AFRL studied the effect of transverse acoustic waves on the jets, and found that the waves have a significant effect on subcritical jets, but significantly less effect on supercritical jets. Raman studies were performed on LN_2/H_2 jets, where N_2 and H_2 densities could be measured separately by detecting different wavelengths. It was found that the H_2 co-flow produced more efficient mixing than without co-flow. Initial temperatures above the pseudo-boiling temperature also produced more efficient mixing than initial temperatures below it. It was also found that the H_2 density can increase with downstream distance, due to cooling by the cold central jet.

Gautam and Gupta (2006) qualitatively showed the effect of confinement, momentum ratio, and recess length on the vaporization and mixing of LN_2 jet from a coaxial rocket engine injector using high speed cinematography, Schlieren and IR thermal imaging. They measured some of the experimental jet destabilization frequencies as well as the characteristic primary instability frequencies present in the coaxial jets using cryogenic fluid and surrounding gas of different densities. Their results showed that LN_2 jets dispersed into ligaments and droplets prior to vaporization. The confinement reduced the vaporization of the LN_2 jet by increasing the axial distance over which the jet persists before full vaporization and also significantly reduced the entrainment of surrounding gases and heat transfer from the surroundings to the injected fluids. Decrease in momentum ratio results in early expansion of the outer gas flow and higher entrainment of the surrounding gases but the LN_2 jet persisted over longer distances for lower momentum ratios, leading to its

reduced mixing with the surrounding gases. The recess length has little effect on the evaporation of the LN$_2$ jet but affected the expansion of the flow and entrainment of the surrounding gases significantly at downstream locations. The results also revealed an increase in liquid jet instability with increase in momentum ratio between the inner and outer flows of the injector.

Davis and Chehroudi (2007) measured the radial mean temperature for cryogenic flows from a coaxial injector at a fixed axial location near the injector exit plane for a range of gas/liquid velocity ratios. The experiments were performed at two different temperature levels (low (135–140 K) and high (185–200 K)) of the gaseous jet to investigate the impact of the velocity ratios and acoustic field on the cryogenic jet. Under subcritical pressures, temperature profiles exhibit a top-hat behavior at two distinct levels with an abrupt transition from a high (liquid like for the inner jet) to a low value representative of compressed gases. Large changes in velocity ratio had no impact on these profiles at the low outer-jet temperature, whereas the location of the transition point was affected under the higher outer-jet temperature. At near- and supercritical chamber pressures, the inner jet loses its top-hat shape and the temperature profiles exhibit a more gradual transition from the inner to outer jet. Backlit images were taken at both low (10 Hz) and high speeds (18 kHz) with and without the acoustic driver turned on at 3 kHz. Using images taken at high framing rates, velocity fluctuations in the chamber background fluid and within the jets were observed when the acoustic driver was on. They also developed an automated method for measurement of the dark core lengths (potential core lengths) from a large number of flow images and showed that the dark-core length decreases at higher chamber

pressures, due to the combined effects of inner tube heat transfer and better inter-jet mixing. The length of the dark core shortened with increase in velocity ratio at constant chamber pressure, and asymptotically approaches a constant value. This constant value appeared to be different for subcritical pressures. Their results also showed the dependence of the gas/liquid momentum ratio to an exponent, with the exponent having a different value for subcritical pressures as opposed to near- and supercritical pressures.

2.3. Cryogenic Coaxial Jets (Reacting)

The last part of literature review is focused on research performed on reacting two phase coaxial jets with liquid oxygen (LOX) and gaseous hydrogen. Although this research has not performed any reacting flow experiments for the present work, this literature review was conducted to provide the readers some insightful information about practical relevance of the present work and to generate more ideas for future research on reacting/non-reacting flows with cryogenic fluids.

Woodward (1994, 1996) performed hot fire tests with LOX and GH_2 and showed that injected LOX jet looked structurally similar for both cases. He also showed that similar helical wave mode is responsible for disintegration of LOX jets in hot fire tests too however the intact core length of the LOX jet appeared to be longer for hot-fire tests than cold flow conditions. Although his experiments were preliminary, he showed that the experiments under cold-flow conditions can also be used to predict the flow and flame behavior under reacting conditions.

Pal et al. (1996) performed drop size and velocity measurements of LOX/GH_2 flow using Phase Doppler Particle Analyzer (PDPA) from a single element shear

coaxial injector under combustion conditions. They also compared the results with a water-air measurement from the same injector under the same velocity and flowrate conditions. Their results showed that measured droplets for combusting cases were larger than that of cold flow cases. However they suggested more experiments for a large range of conditions in order to really understand the physics of the problem.

Mayer and Tamura (1996) performed combustion experiments with liquid oxygen and gaseous hydrogen at chamber pressures between 1.5-10.0 MPa. They investigated the injection, ignition and steady-state combustion using spark light photographs and high speed cinematography. For the cold-flow cases, their results showed the spray atomization behavior at subcritical pressures while gas-gas type of mixing behavior resulted at supercritical pressure. For the burning cases, flames always attached instantaneously after ignition to the LOX post. The recirculation zone behind the LOX post controlled the LOX/GH_2 mixing process and the interface between the LOX and hydrogen propellants was separated by a layer of reacting combustion gases (Figure 2.7). The influence of the hydrogen injection temperature, i.e., hydrogen injection density to the mixing process, was shown to be less effective than the effect of chamber pressure itself. The results of their combustion investigation also emphasized an important point; the recessed LOX posts do not the improve atomization performance as shown from cold flow tests the recess had important effects on the stability of the combustion process.
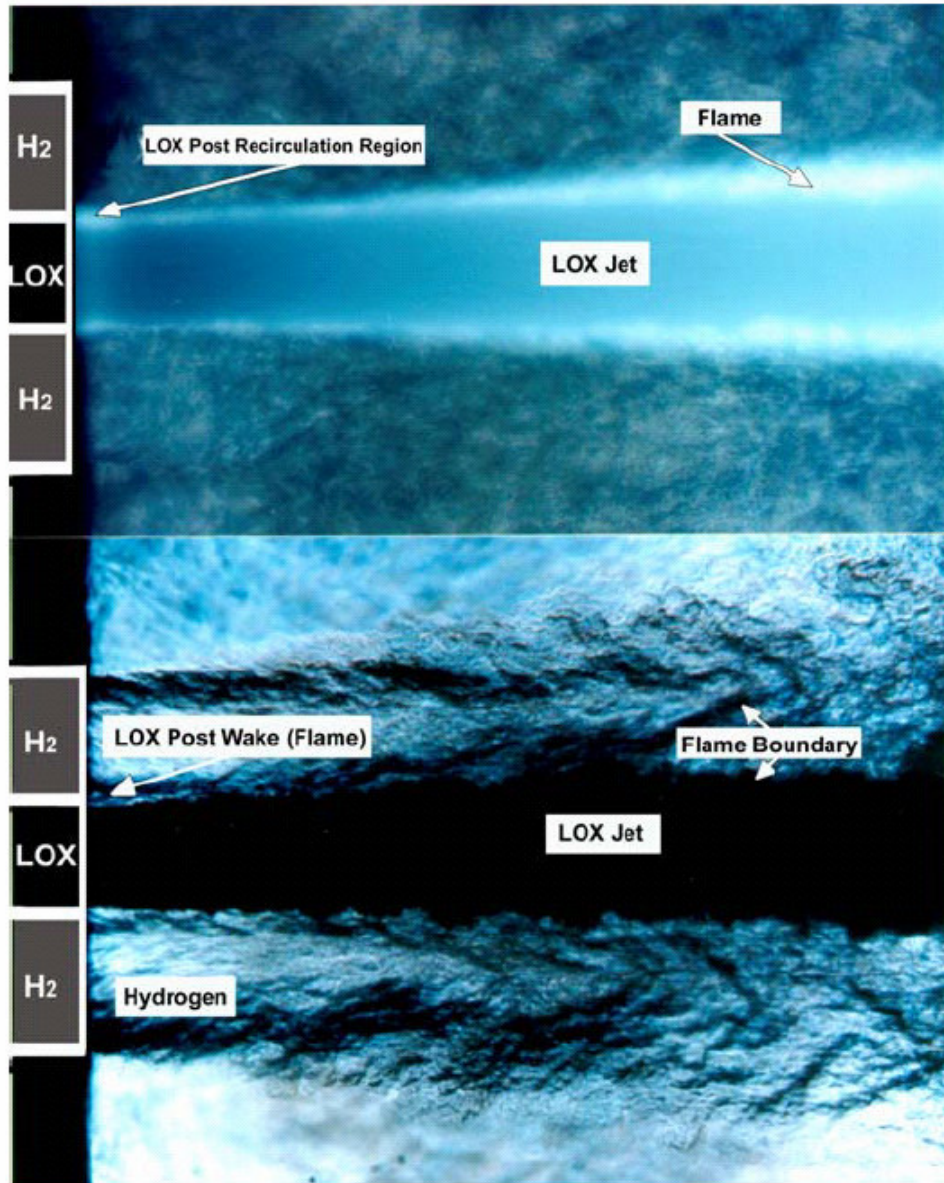
Figure 2.7. Various zones of a typical LOX/GH₂ flame from a coaxial injector Top: Long exposure flame radiation image, Bottom: Flow visualization (Mayer and Tamura, 1996)

Oefelien and Yang (1998) demonstrated the performance and accuracy requirements for a Computational Fluid Dynamics (CFD) model and highlighted various intricacies associated with transcritical and supercritical phenomena. The effect of pressure on near-critical mixing and combustion processes was highlighted.

Their results also examined the dominating effect of density gradient and diminished mass diffusion rates that accompany the liquid-like behavior of near-critical fluids. The overall model showed improvements required in terms of generality for application in performance prediction of cryogenic rocket engines.

Candel et al. (1998) examined the structure of cryogenic LOX/GH$_2$ flames from a single element shear coaxial injector. They also showed that the flame is stabilized in the vicinity of the LOX tube and takes the shape of a shell with thin and highly corrugated instantaneous reactive layer (Figure 2.8). The temperature was shown to be initially stratified in the radial direction and becomes more homogeneous further downstream after intense mixing, which supported the assumption that the LOX/GH$_2$ combustion rate is higher than turbulent mixing rate in cryogenic flames. This phenomenon was also corroborated by the fact that the flame was always attached (or nearly attached) to the lips of the coaxial injector.
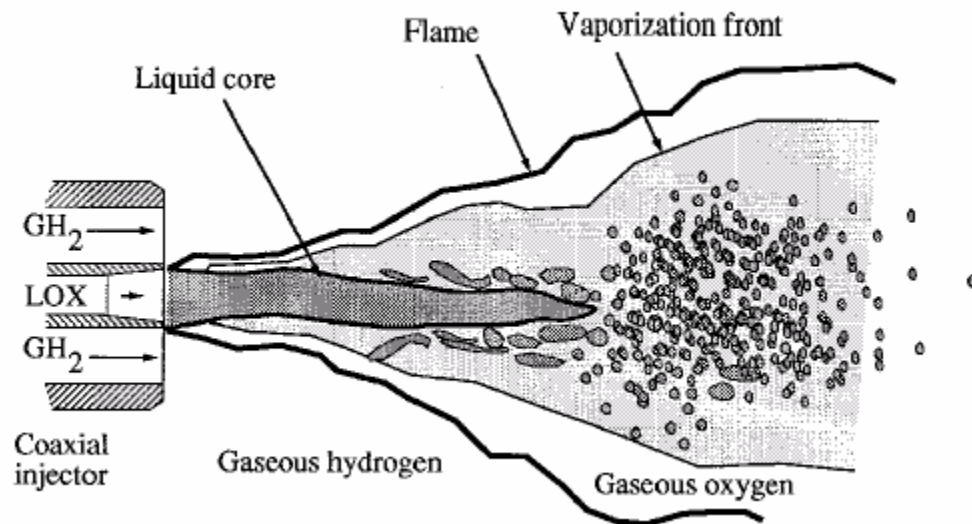
Figure 2.8. Schematic of a typical LOX/GH$_2$ flame from a coaxial injector (Candel et al., 1998)

Mayer et al. (2000) investigated LOX/GH$_2$ flame from a coaxial injector and showed that the interface between the propellants is always separated and affected by a layer of hot reacting gas during ignition and combustion as shown by Candel et al. (1998). Their results supported their previous work and gave more evidence that a diffusion flame resides within the annular post wake and is anchored by the small intensive recirculation zones behind these posts. The Optical Emission Spectroscopy (OES) of the flames showed that radiation intensity of the flame strongly depends on chamber pressure and increased downstream whereas the spectrum of the flame ranged continuously from Ultraviolet (UV) to Infrared (IR). The line intensities also showed very small dependence on mixture ratio indicating that the combustion gases were undergoing various degrees of reaction with a wide distribution in gas temperature and composition.

Mayer et al. (2001) performed experimental and theoretical studies to show the effect of heat flux and surrounding temperature on mixing behavior near and above the critical pressure. The decrease in density due to high temperature was shown to decrease the aerodynamic effect on atomization as compared to the cold-flow cases. They also measured the absolute flame propagation speed and found that to be on the order of 10–102 m/s.

Yeralan et al. (2001) performed line wise Raman imaging of LOX/GH$_2$ combustion at high pressures and at oxidizer-to-fuel mass ratio of unity. Specifically they measured single-shot temperature and major species profiles during combustion. The temperature profiles indicated relatively high temperatures at the wall regions of the rocket chamber and close to adiabatic flame temperatures at the center region of

the chamber. They also performed an error analysis of the data and revealed that the calibration of data acquisition procedure was important in order to improve the accuracy, which was 19%.

Ivancic and Mayer (2002) measured the length and time scales of the turbulent reacting flow from a coaxial injector experimentally and numerically. The length scales represented the structures present within the reactive shear layer and are responsible for the turbulent mixing process. The time scales of turbulent mixing and combustion processes were measured to analyze the interaction mechanism between turbulence and chemistry in the reactive shear layer by comparing the speed of the mixing process with the speed of the chemistry. The comparison showed that the studied flow and chemical timescales were strongly related to each other thus showing the importance of turbulence chemistry interaction for rocket engine combustion.

Smith and Mayer (2004) performed extensive review of work performed at DLR on mixing and combustion processes in liquid rocket engines at high pressures (3 - 20 MPa). Their review reemphasized the impact of subcritical and supercritical pressures on atomization and mixing of cryogenic propellants as shown in a lot of previous researches. Similarly for the combustion case, the impact of LOX post recess and the recirculation zone was emphasized.

Grisch et al. (2004) presented a detailed overview of efforts made by the German (DLR) and French (ONERA) aerospace research labs on the development of new diagnostics in order to study the spray and combustion behavior of LOX/GH2 rocket injectors. Specifically they focused on Coherent Antistoke Raman Scattering (CARS)

diagnostics for temperature and species measurements under realistic rocket engine conditions. The results suggested that CARS measurements were reasonably accurate in detection of H_2 and H_2O in the flowfield along with the thermal field of the combustor.

Habiballah et al. (2006) gave a brief overview of work performed at ONERA's Mascotte test bench on cryogenic propellant (LOX/GH$_2$) combustion. Their work examined the main physical and chemical processes involved in LOX/GH$_2$ combustion progressively from V01 bench (low pressure and ambient hydrogen temperature) to V03 bench (high pressure and cold hydrogen) with shear-coaxial injector and optical access. The diagnostics included both qualitative (high-speed photography, shadowgraphy, backlighting) and quantitative techniques (spray characterization with PDA, temperature measurements with CARS). The results summarized the effect of subcritical and supercritical pressures on LOX jet atomization behavior, which was very similar to the other works performed on the same topic. The reacting experiments showed that the flame front remained confined over about 2 mm around the LOX jet at supercritical pressures (6 MPa) but extended radially over a wider region at subcritical pressure (3.0MPa) showing the importance of LOX atomization behavior at various pressures.

Candel et al. (2006) preformed cryogenic combustion experiments at high pressures (0.1 to 7 MPa) on the Mascotte facility for gas to liquid momentum flux ratio ranges from 4 to 15. They used Optical Emission Spectroscopic (OES) technique using two synchronized Intensified Charged Coupled Device (ICCD) cameras to examine the LOX jet and the flame where the mean flame structure is

extracted by taking the Abel transformation of average emission images. The results showed that the flame burns in an external group combustion mode and takes the shape of a shell surrounding the LOX jet and LOX droplet cloud below the critical pressure of oxygen as shown by prior researchers. Their results also indicated that the rate of combustion is vaporization-limited when the pressure is below the critical pressure and is mixing-limited when the pressure is above the critical pressure, showing the importance of mixing for rocket combustion chambers designed to operate above the critical pressure of the liquid reactant. The results also confirmed that the flame remains attached to the lip of the oxygen injector over the complete range of pressure, inlet velocity and hydrogen temperatures studied.

3. Experimental Setup and Conditions

3.1. Coaxial Injector Facility for Atmospheric Pressure Experiments

The experimental facility consisted of a supply system for cryogenic liquid nitrogen, gaseous helium and argon, a single element coaxial injector, and an exhaust system. In this study, LN_2 was used to simulate LOX because LN_2 is chemically inert, safe to install for laboratory testing, and environmentally benign. Table 3.1 shows some of the physical properties of LN_2 and LOX. The values of the boiling temperature, viscosity, latent heat of vaporization and surface tension are close; thus the liquid atomization and evaporation behavior was expected to be similar for both fluids. Similarly Table 3.2 shows a comparison of physical properties of various gases used for our experiments.

Fluid	Density	Boiling Point	Surface Tension	Latent Heat	Viscosity
LOX	1141 kg/m^3	91 K	0.0132 N/m	198.4 kJ/kg	2.0E-4 Pa-s
LN_2	808 kg/m^3	77 K	0.0089 N/m	212.9 kJ/kg	1.6E-4 Pa-s

Table 3.1. Some physical properties of cryogenic liquids at atmospheric pressure

Fluid	Density	Viscosity	Heat Capacity	Thermal Conductivity
H_2	0.089 kg/m^3	8.8E-6 Pa-s	14.5 J/g.K	168.35 mW/m-K
He	0.164 kg/m^3	2.0E-5 Pa-s	5.25 J/g.K	142.64 mW/m-K
Ar	1.64 kg/m^3	2.2E-5 Pa-s	0.525 J/g.K	17.7 mW/m-K

Table 3.2. Some physical properties of gases at atmospheric conditions (1 atm and 298 K)

A schematic diagram of the injector tubes along with the injector face plate with dimensions through which the flows emerge is shown in Figures 3.1 and 3.2. The inner injector tube has inner diameter of $D_1 = 0.33$ inches with a wall thickness of 0.02 inches. Figures 3.3, 3.4 and 3.5 show a schematic of the experimental facility along with the pictures assembled for atmospheric pressure experiments. The flows of the gaseous and cryogenic fluids into the experimental facility were controlled using fast response (< 50 ms) solenoid valves in order to obtain temporal resolution on the evolutionary behavior of the flow upon exit from the injector.
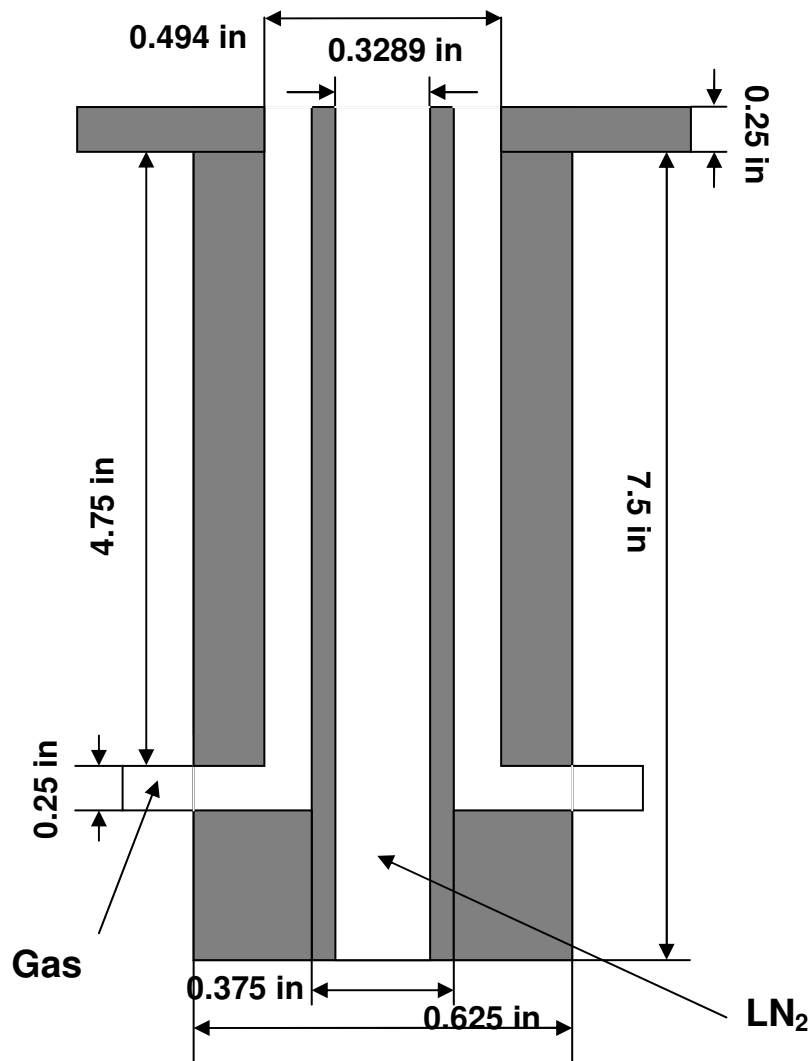
Figure 3.1. A schematic diagram of the coaxial injector setup along with the dimensions
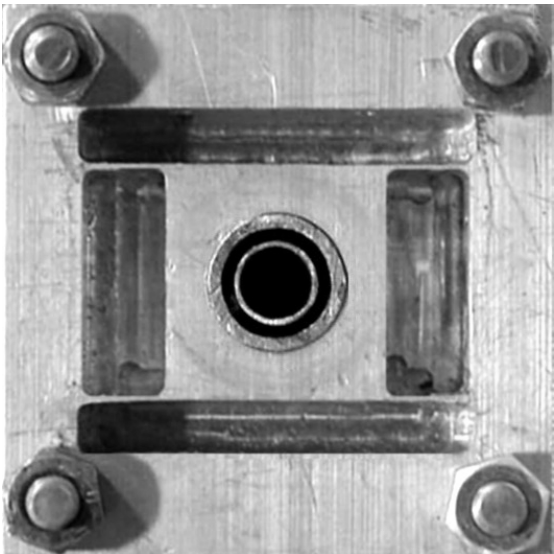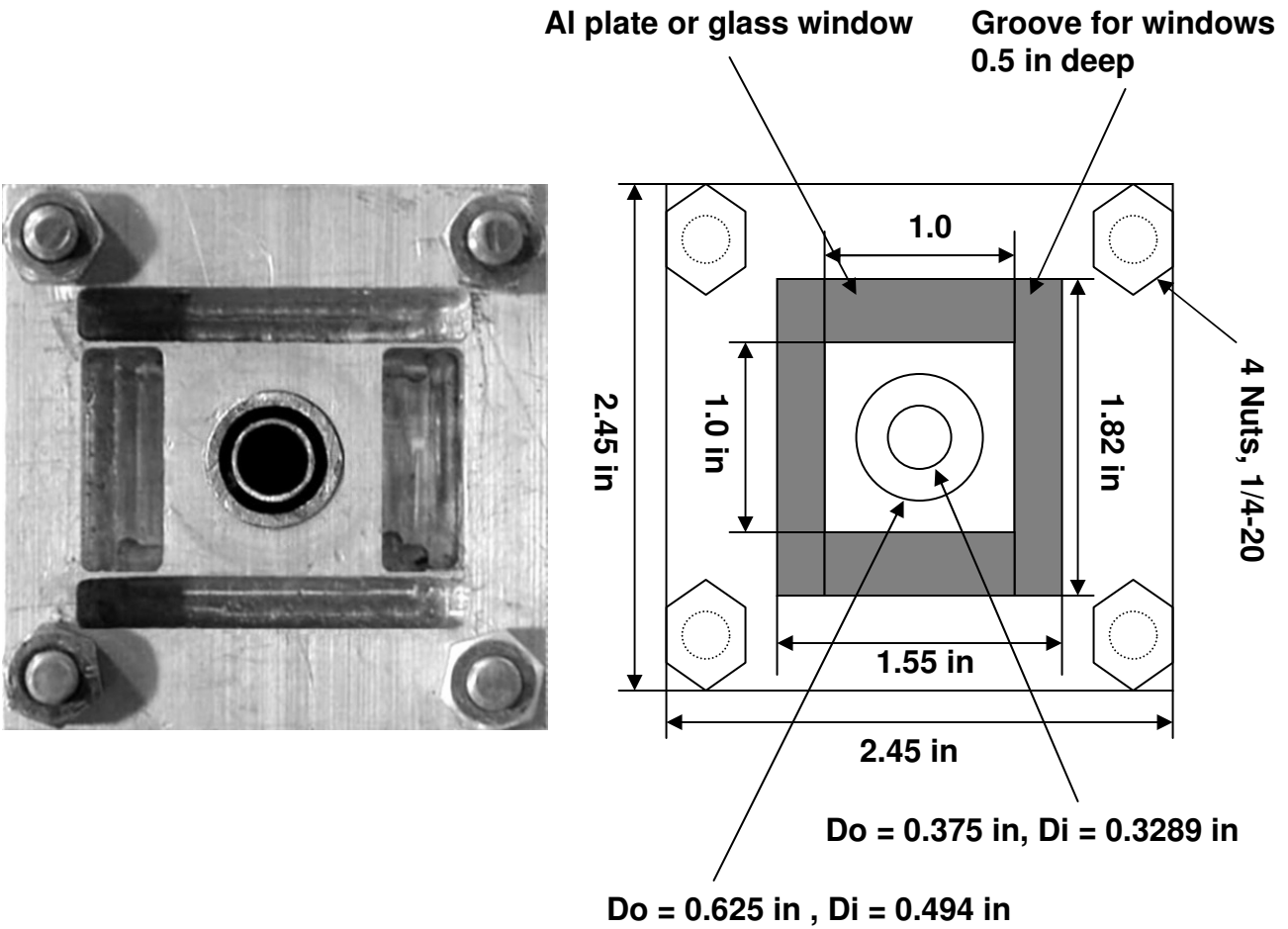
Fig. 3.2. Picture of faceplate along with dimensions
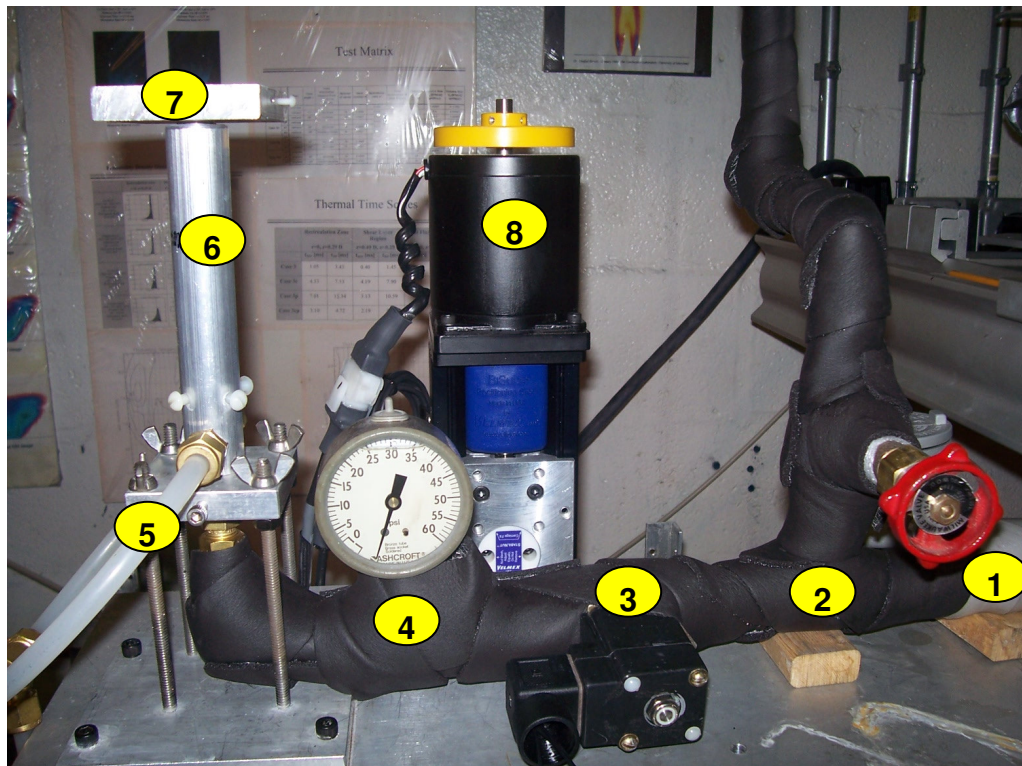
Al plate or glass window

Groove for windows 0.5 in deep

4 Nuts, 1/4-20

1.0

2.45 in

1.0 in

1.82 in

1.55 in

2.45 in

Do = 0.375 in, Di = 0.3289 in

Do = 0.625 in , Di = 0.494 in

44

Fig. 3.3. Schematic of the experimental facility

1) Turbine flowmeter, 2) Bleed connection, 3) LN_2 solenoid valve, 4)
Pressure gauge, 5) Gas supply, 6) Injector, 7) Face plate,
8) Elevation mechanism

Fig. 3.4. Picture of the experimental facility
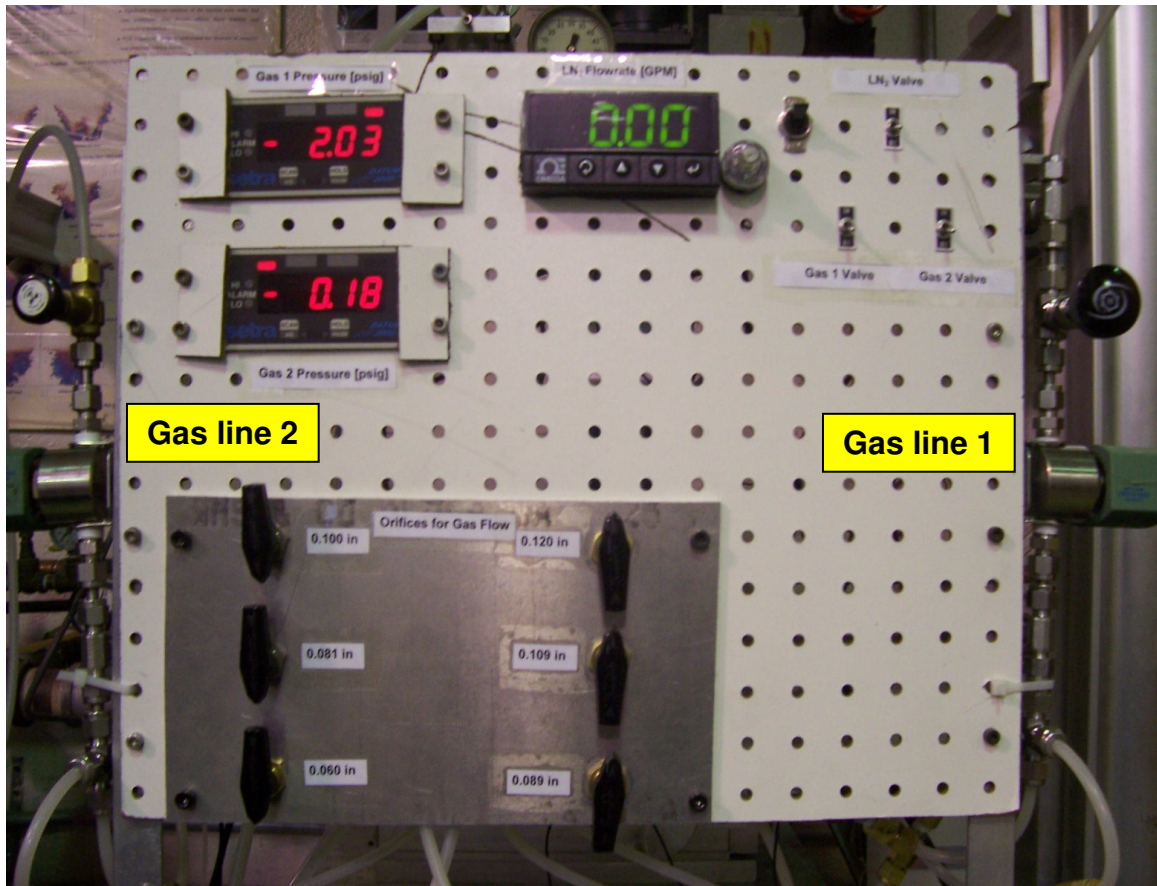
Fig. 3.5. Picture of facility control board along with gaseous flow lines

3.2. Cryogenic Flow Characterization

The precise measurement of cryogenic flowrate is a challenge and is not reported much in the literature. For the present experiments the flowrate of liquid nitrogen was measured using a high-precision turbine flowmeter, designed to handle cryogenic liquids. The challenge here was to ensure that the fluid entering and exiting the turbine flow meter remain in liquid phase since any transformation to vapor phase would result in erroneous readings on the metered cryogenic flow rate. Therefore, to assure that the measurements were accurate, the flowmeter was cooled down to LN_2 temperatures before getting steady-state readings to confirm liquid flow through the

flowmeter with no vapor or two phase flow formation. The procedure of acquiring LN_2 flowrate measurements started by bleeding LN_2 through the turbine flowmeter at very low flowrates, until the temperature of flowmeter reached the LN_2 cryogenic temperature. Once this was achieved, the bleed valve was closed and the fast response control valve to the injector was opened completely before starting the measurements. This approach assured that the variations in flowrate reduce to less than 5%. The flowrate through the injector was also calculated using Bernoulli's equation by measuring pressures upstream and downstream of the coaxial injector. The difference in measured and calculated flow velocities was less than ±5% for several different test runs, which is actually reasonable for a cryogenic fluid that posseses complex flow and heat transfer characteristics. This procedure allowed one to alleviate the onset of artificial very high cryogenic flow rate at the start of the experiment (due to artifact), and determine the true flow rates using two different approaches. The volumetric flowrate of LN_2 was fixed at 4.5 GPM (5.0 m/s) for all experiments with average temperature and density of the LN_2 jet at the injector exit taken as 77 K and 808 kg/m^3, respectively. The Reynolds and Weber numbers of the LN_2 jet calculated at 77K and 1 atm were found to be 2.21E+5 and 1.93E+4 respectively.

3.3. Gaseous Flow Characterization

The flowrate of the gaseous jet was measured using precision orifices preceded by a digital pressure sensor. The average temperature of the gaseous flow at the injector exit was measured using a thermocouple and found to be 263 K, and the velocity was calculated under the assumption of ideal gas behavior. However in order to check the characteristics of the annular jet, a 2-D PIV system was used to examine the flow

behavior of the gaseous flow field. The test section was illuminated by means of a solo PIV Nd:YAG laser. Submicron propylene droplets (4-5 microns) were introduced into the annular flow using an atomizer. The characteristic relaxation time of the droplets, τ_d, was found to be approximately 60 μs and Stokes number was approximately 0.08 for maximum velocity of 70 m/s. It can therefore be concluded that properties of the flows examined here, such as mean velocities, can be effectively examined through use of the Submicron propylene droplets.

A Charged Coupled Device (CCD) camera with an active pixel array of 1280 × 1024 was used to record the images. The camera, placed at an acute angle to the laser sheet, was operated by a control module for image acquisition. The frequencies of the laser and the camera were synchronized at 5 Hz. The measured area in the test section was 20 × 20 mm in the radial and axial directions, respectively. Five-hundred image pairs were acquired for each case to determine the mean and turbulence properties associated with the flow field. Figures 2a and b show axial and radial flow velocity distributions respectively of a gaseous helium jet injected at 70.8 m/s. One can see that both the axial and radial velocity profiles are symmetric around the longitudinal centerline axis of the injector and a recirculation zone is present at the center near the injector exit. The velocity magnitude was found to be close to the calculated injection velocity which confirms that our tubes are concentric and the losses inside the tube are negligible.

Flow	Measured Velocity	Calculated Velocity
LN$_2$	5.0	4.7
Helium	70.8	70.0

Table 3.3. Comparison of measured and calculated velocities of the two flows

48
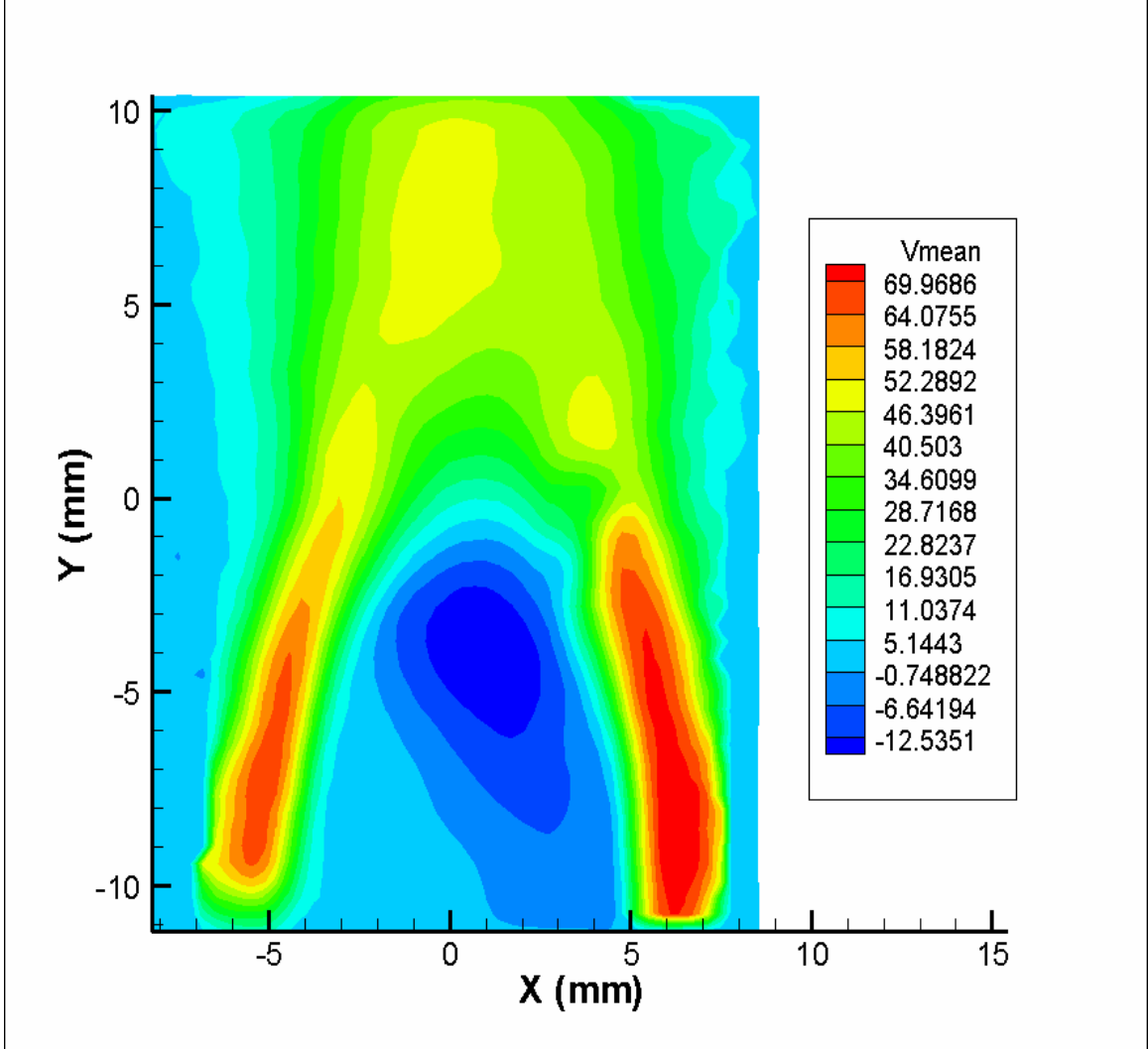
Figure 3.6. Axial velocity distribution of helium jet injected axially at 70.8 m/s
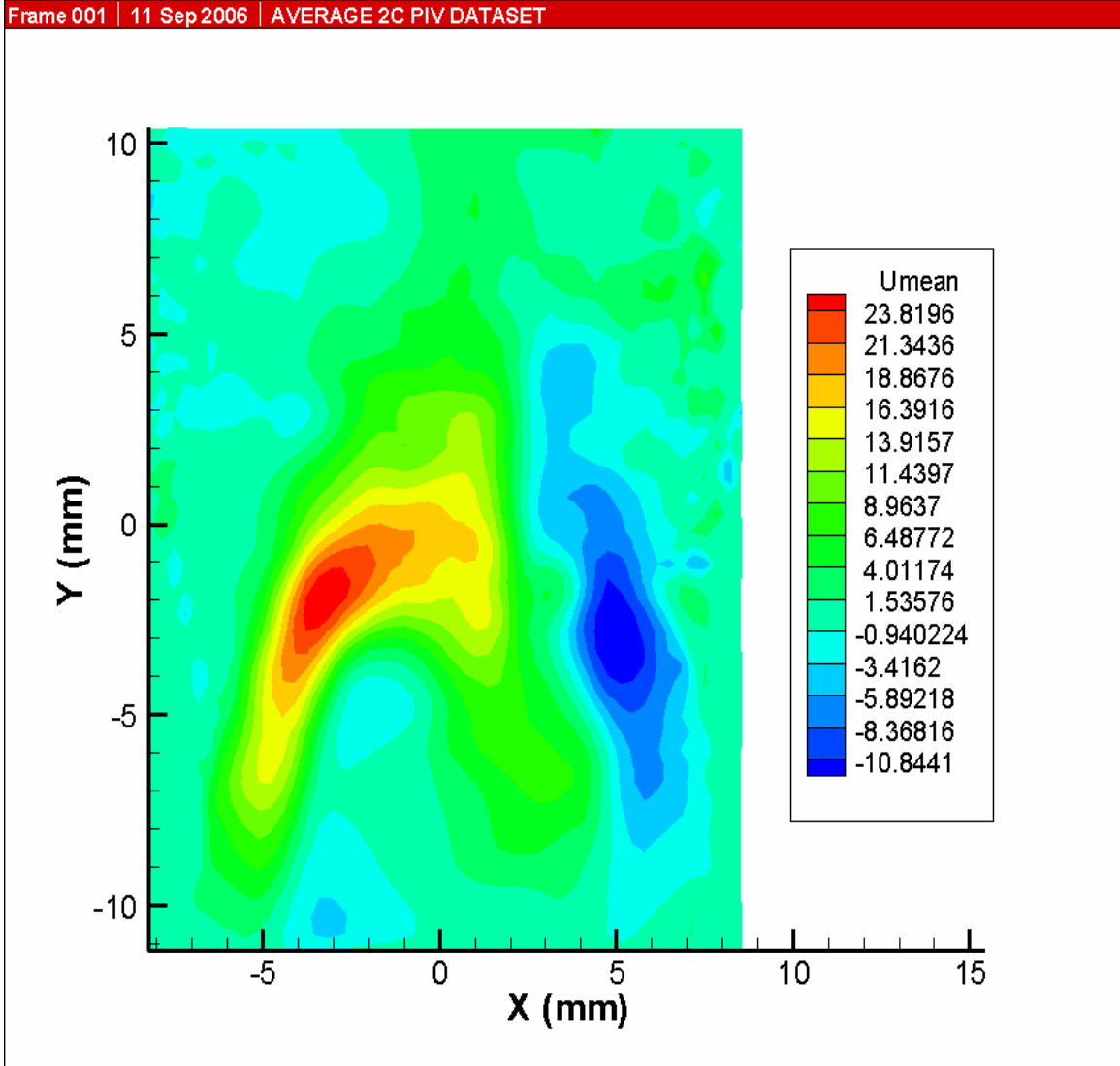
Figure 3.7. Radial velocity distribution of helium jet at 70.8 m/s

3.4. Schlieren Setup

The diagnostics used for the present research are high speed cinematography and Schlieren imaging. A high-speed camera (Photron Fastcam Ultima 1024), capable of recording up to 16,000 monochrome images per second, was used to record images of the flow. The maximum resolution of the camera was 1024×1024 pixels.

Figure 3.8 shows a schematic of the Schlieren setup, using two mirrors and a high speed camera connected to the computer. Schlieren imaging provides the first derivative of the refractive index of the test region, thus providing an estimate of the density gradients in the test region. The intensity of captured light can be further processed using image processing techniques (explained later) to obtain more quantitative information of the flow. The liquid and gaseous streams, as well as the two phase regions in the coaxial flow from the injector, could be examined directly using this technique.
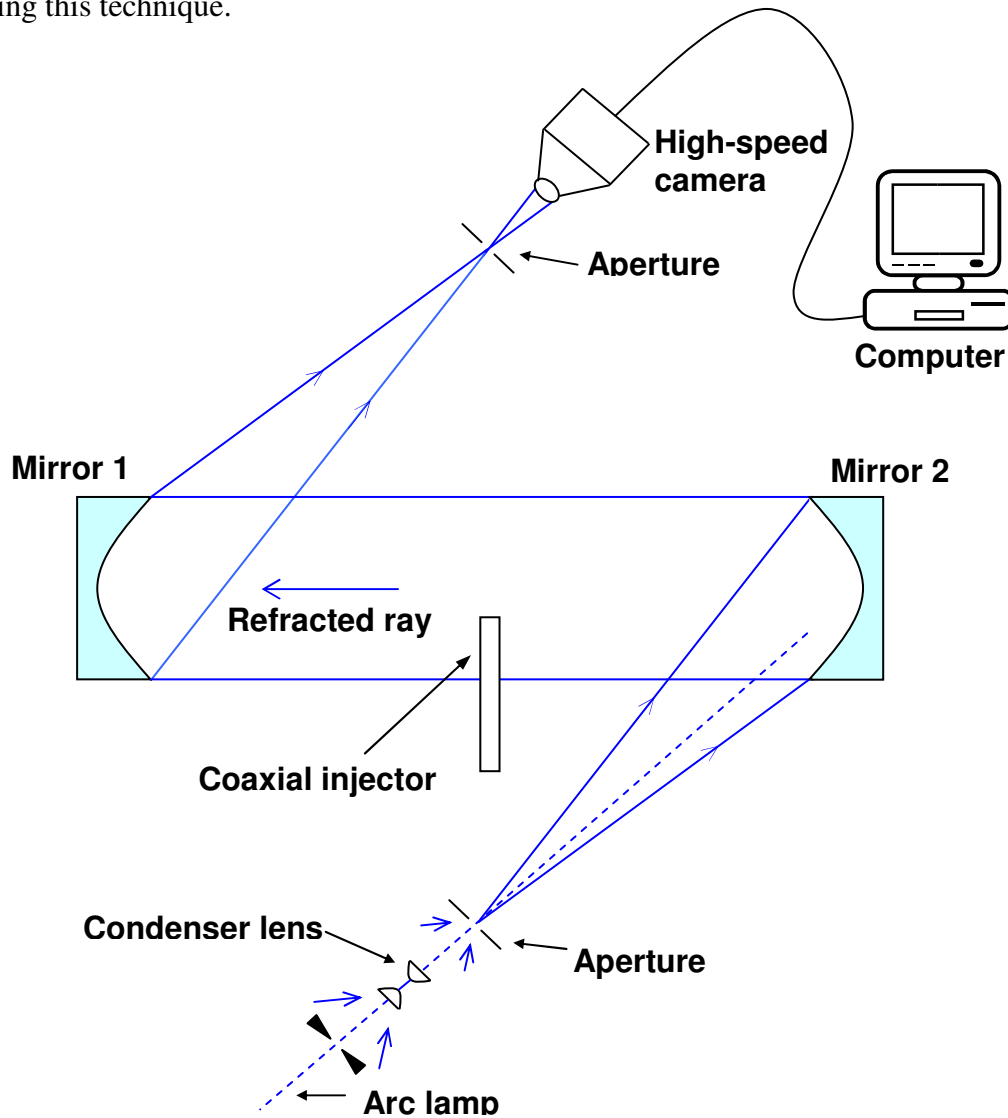
Fig. 3.8. Schamatic of the Schlieren setup

3.5. Low Pressure Setup

The experimental facility was modified to perform near vacuum experiments to simulate the flow and mixing behavior under in-space conditions. For these experiments a sealed pressure tight enclosure (2.5×2.5 in) was installed surrounding the injector and exhaust of the facility was replaced by a large blowup tank (2500 gallons) at 0.1 atm pressure (Figures 3.9 and 3.10).
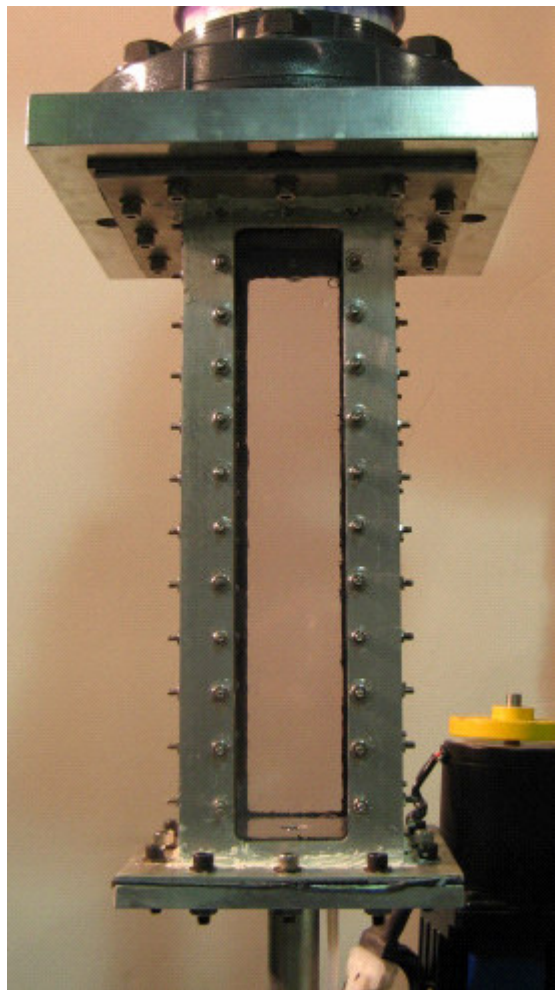
Fig. 3.9. Picture of modified experimental facility for low pressure experiments

Fig. 3.10. Picture of pressure sensor showing pressure less than 27.0 in of Hg in vacuum (0.1 atm)

4. Experimental Data Analysis

4.1. Quantitative Measurements

Data analysis for the present set of experiments included obtaining time resolved images from the high speed videos and applying image processing techniques on those images in order to calculate the averaged length scales, potential core lengths and shear angles for the various test cases. Matlab image processing toolbox is used for all the data analysis. Table 4.1 shows the test matrix for the flow inlet conditions examined during the present research. Three different set of experiments were performed to examine the detailed effects of velocity ratio, density ratio and momentum ratio between the jets on the cryogenic flow and atomization behavior. For the first set of experiments, the density of gaseous jet (helium) was kept constant while its velocity was varied from no flow to 630 m/s. Similarly for the second and third cases the velocity of gaseous jet were kept constant at 100 m/s and 200 m/s respectively, while the density was varied by mixing helium and argon jets in different ratios.

Case No.	Inner Fluid	Outer Fluid	Velocity [m/s] (liquid/gas)	Density Ratio (gas/liquid)	Momentum Ratio (gas/liquid)	Mass Ratio (gas/liquid)
1	LN_2	He	5 / 0	—	0	—
2	LN_2	He	5 / 5	2.3E-04	2.3E-04	2.4E-04
3	LN_2	He	5 / 10	2.3E-04	9.2E-04	4.8E-04
4	LN_2	He	5 / 20	2.3E-04	3.7E-03	9.7E.04
5	LN_2	He	5 / 30	2.3E-04	8.3E-03	1.5E-03

6	LN$_2$	He	5 / 40	2.3E-04	14.7E-03	1.9E-03
7	LN$_2$	He	5 / 50	2.3E-04	23.0E-03	2.4E-03
8	LN$_2$	He	5 / 100	2.3E-04	91.9E-03	4.9E-03
9	LN$_2$	He	5 / 150	2.3E-04	0.21	7.2E-03
10	LN$_2$	He	5 / 200	2.3E-04	0.37	9.7E-03
11	LN$_2$	He	5 / 250	2.3E-04	0.57	1.2E-02
12	LN$_2$	He	5 / 300	2.3E-04	0.83	1.4E-02
13	LN$_2$	He	5 / 325	2.3E-04	0.98	1.6E-02
14	LN$_2$	He	5 / 350	2.3E-04	1.13	1.7E-02
15	LN$_2$	He	5 / 390	2.3E-04	1.4	1.9E-02
16	LN$_2$	He	5 / 460	2.3E-04	1.95	2.2E-02
17	LN$_2$	He	5 / 500	2.3E-04	2.3	2.4E-02
18	LN$_2$	He	5 / 565	2.3E-04	2.92	2.7E-02
19	LN$_2$	He	5 / 630	2.3E-04	3.68	3.0E-02

20	LN$_2$	He	5 / 100	2.3E-04	0.092	4.9E-03
21	LN$_2$	He + Ar	5 / 100	5.2E-04	0.21	1.1E-02
22	LN$_2$	He + Ar	5 / 100	9.2E-04	0.37	1.9E-02
23	LN$_2$	He + Ar	5 / 100	1.4E-03	0.57	3.0E-02

24	LN$_2$	He	5 / 200	2.3E-04	0.37	9.7E-03
25	LN$_2$	He + Ar	5 / 200	3.6E-04	0.57	1.5E-02
26	LN$_2$	He + Ar	5 / 200	5.2E-04	0.83	2.2E-02
27	LN$_2$	He + Ar	5 / 200	7.0E-04	1.13	3.0E-02
28	LN$_2$	He + Ar	5 / 200	9.1E-04	1.47	3.9E-02
29	LN$_2$	He + Ar	5 / 200	1.2E-03	1.87	4.9E-02
30	LN$_2$	He + Ar	5 / 200	1.4E-03	2.30	6.1E-02

Table 4.1. Test matrix for the flow inlet conditions examined

Fig. 4.1a shows an instantaneous high-speed Schlieren image of steady-state LN$_2$

jet in a coaxial He flow. This image shows the development of the shear layer

between the two flows. Initially a high density liquid jet (dark region) can be seen emerging from the injector exit along with the coaxial low density helium stream (light region) until around 2 diameters downstream. This is an indication of initial mixing zone where the two jets have little or no interaction with each other. As the flow progresses farther downstream, the formation of vortical structures, as a result of shear layer development, destabilized the inner liquid core to break-up and mix with the surrounding gases. The cryogenic jet expansion, potential core length (L_b), and the characteristic length scales (λ) associated with the unstable LN_2 jet can also be observed from Fig. 1a. The length scales of the vortical structures were estimated using the edge detection capabilities of Matlab and averaged over 150 images, whereas the average frequencies were calculated using averaged length scales and liquid jet velocity ($v = V_l/\lambda$). Fig. 4.1b shows an average of 150 high-speed Schlieren images for the same case. This image was obtained to enable the calculation of the average potential core length and shear angle. It can be seen that the vortical structures are not visible for the averaged case anymore, because of the cancellation and smoothening of the flow structures during the averaging process. In both parts of Fig. 1, however, the LN_2 jet is opaque to the light and thus appears dark (light intensity close to zero in this region), whereas the surroundings gases are brighter and have a higher light intensity (close to 240).
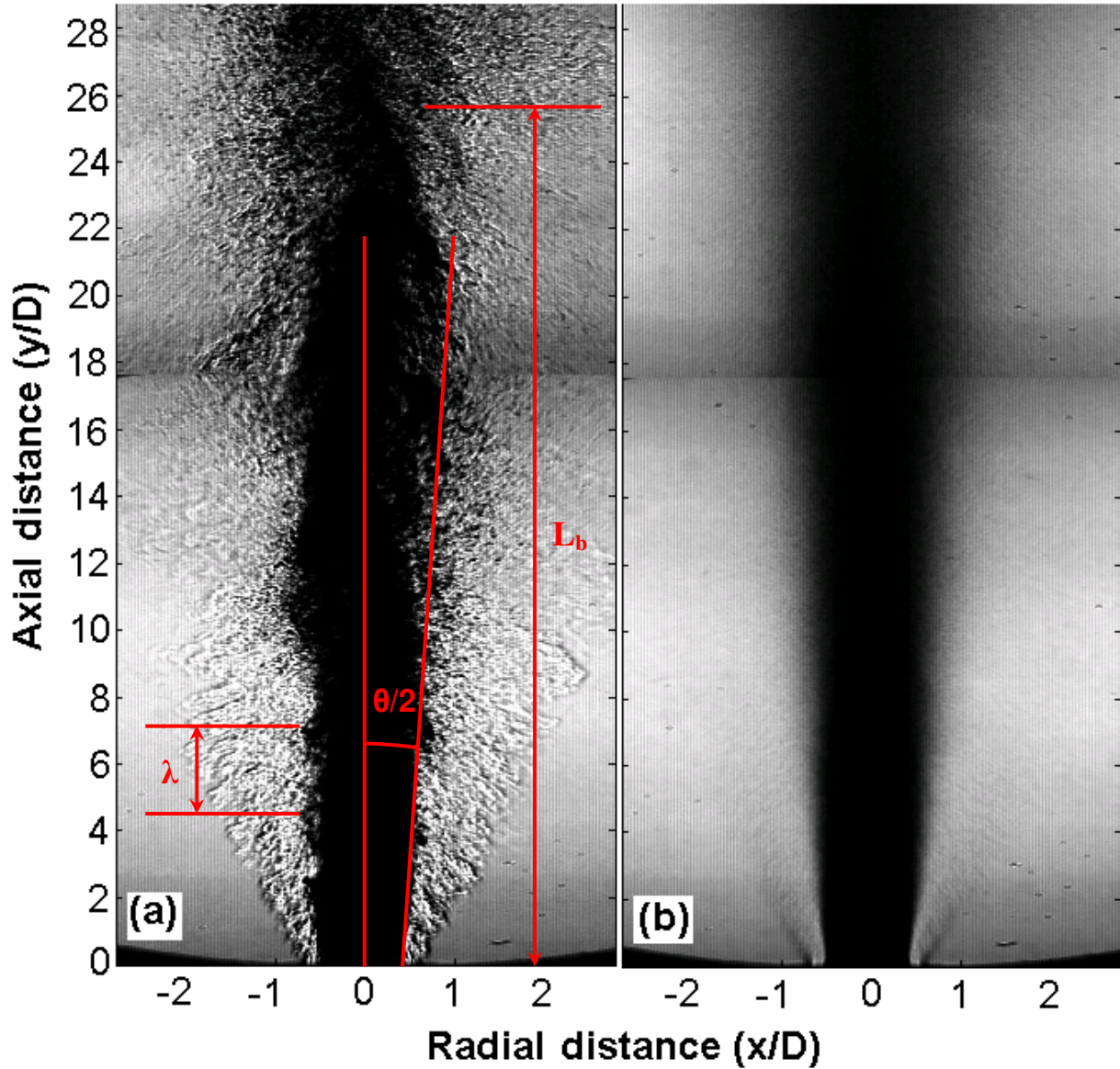
Figure 4.1. Sample high-speed Schlieren image of LN$_2$/He flow, D = D$_l$
a) Instantaneous image, b) Average of 150 images

Figure 4.2 shows the variation of light intensity with radial distance at various axial locations, obtained from the averaged Schlieren image. This plot was obtained to show the liquid jet expansion and calculation of shear angle between the jets. One can see the presence of a symmetric, highly dense, dark liquid core (intensity close to zero) along with its expansion over the axial distance, as it progresses further

downstream from the injector exit. The jet width (*w*) of the flow is defined as the distance between the two points where the radial intensity reached half of the maximum intensity (FWHM) i.e. 120. These two points, and consequently the width of the flow, were determined after processing the images using image processing techniques. The shear angle (Figure 4.3) of the flow was calculated at different axial distances (*y*) based on the jet width according to equations 4.1 and 4.2.

tan (θ/2) = 0.5 jet width / equivalent axial distance [4.1]

∴ tan (θ/2) = 0.5(jet width-D$_l$) / y [4.2]
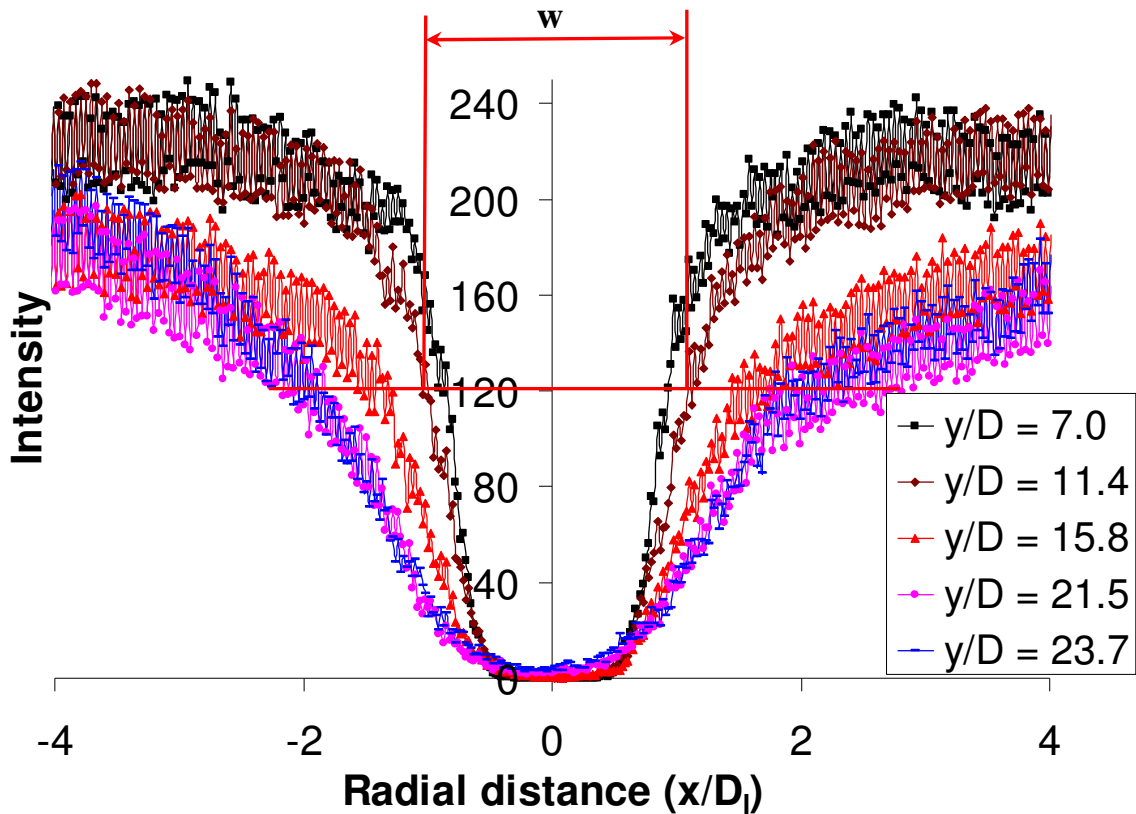
Figure 4.2. Radial intensity distribution of LN$_2$/He flow at various axial locations
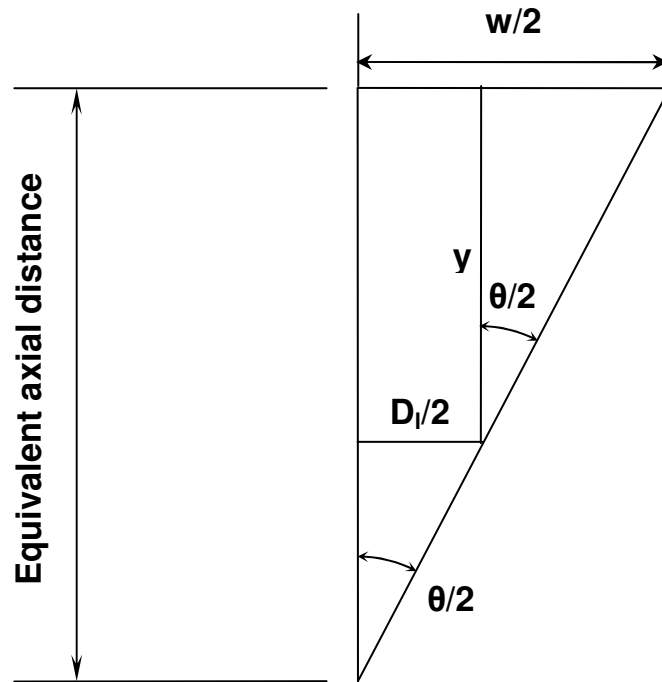
Figure 4.3. Description of the parameters used in the calculation of the shear angle of the flow

Figure 4.4 shows axial distribution of the averaged centerline intensity obtained from the averaged image. The centerline intensity was plotted to show the behavior of the LN_2 jet quantitatively, as it progresses downstream of the injector exit. The increase in centerline intensity indicates the decrease in density of the fluid at the centerline to reveal the process of LN_2 jet breakup and mixing with the surrounding gases. The increase in centerline intensity (decrease in fluid density) remains low and insignificant, until the breakup length of the liquid potential core is reached. Beyond this point, the liquid jet breaks into droplets and ligaments and starts vaporizing rapidly. This rapid evaporation of liquid droplets and ligaments and its mixing with the surrounding gases further reduces the density of centerline fluid to cause a rapid

increase in the centerline intensity. For the present experiments, the potential core length is defined as the point where the centerline intensity has the largest axial gradient. The axial gradients were analyzed using the image processing capabilities of Matlab. This point was found to be close to an intensity of 1.0-2.0 for all the cases and was found independent of the intensity of the light source used for Schlieren imaging. A comparison of the centerline intensities for some of the selected cases are shown in Figure 4.5. This figure suggests that gas velocity significantly affects the centerline intensity distribution and subsequently the potential core length of the cryogenic fluid jet. However, this figure does not show a visible trend of the effect of gas velocity on the centerline intensity.
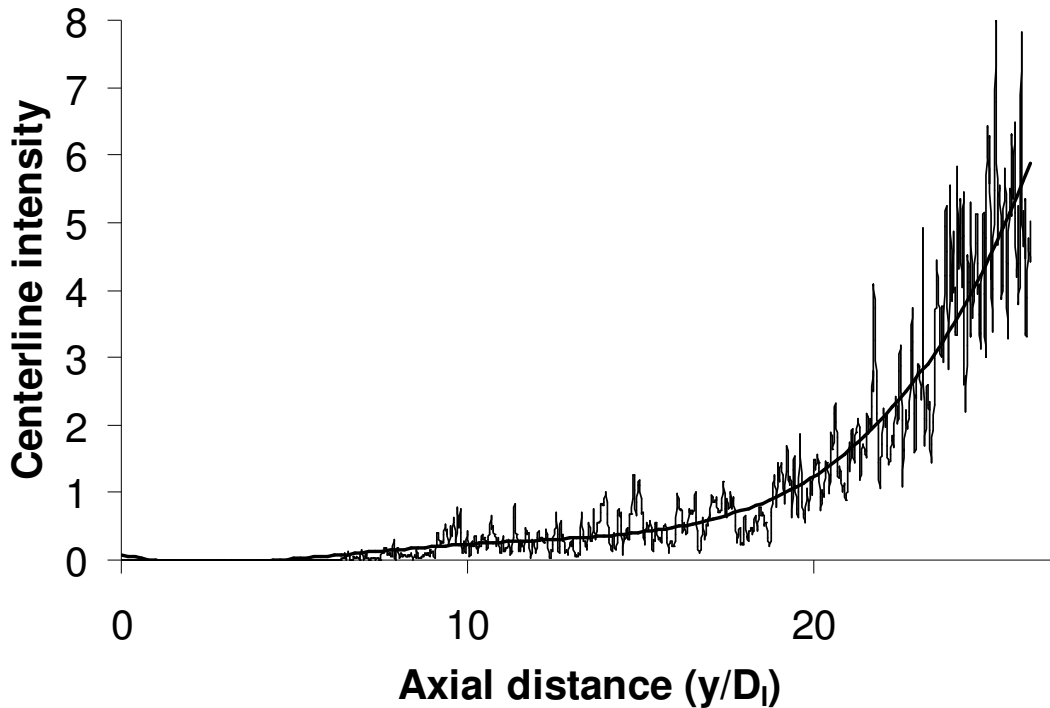
Figure 4.4. Averaged centerline intensity distribution of LN$_2$/He flow
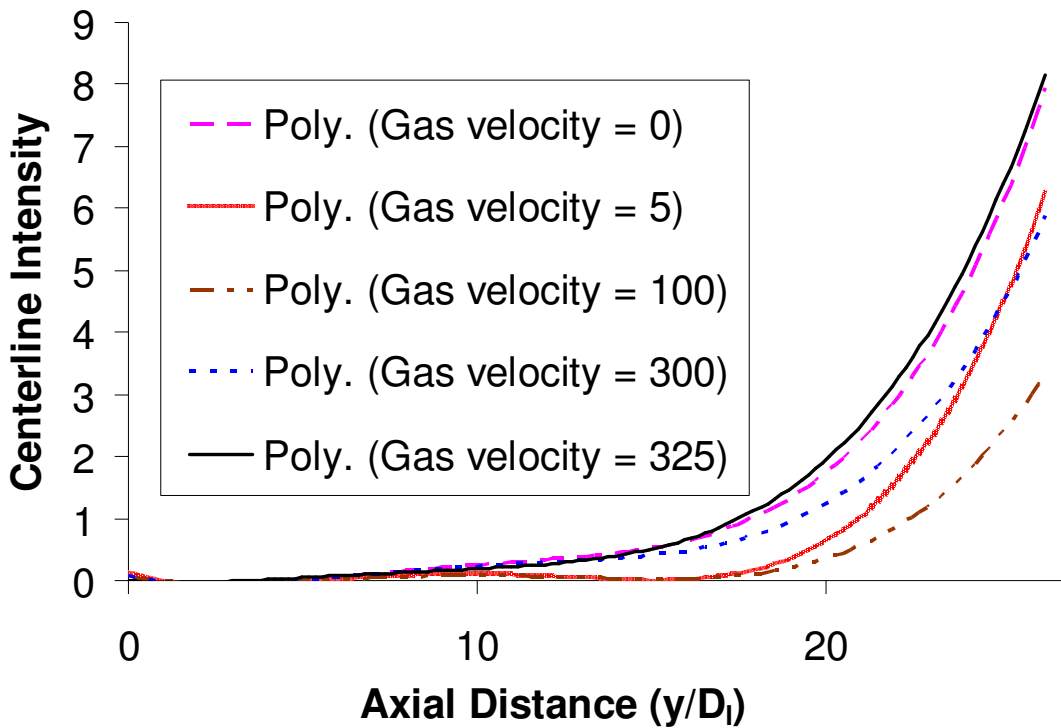
Figure 4.5. Averaged centerline intensity distribution of LN$_2$/He flow for different velocities of the coaxial gaseous jet

The biggest challenge associated with quantitative measurements performed with cryogenic flow are uncertainties. Cryogenic flows are generally unsteady due to turbulence and strong heat transfer from the surroundings. These unsteady behaviors are further aggravated by feed pressure fluctuations along with chugging instabilities. Therefore error analysis is very crucial for performing quantitative measurements with cryogenic fluids. Most of the prior works lack error analysis of their measurements. As part of this research, simple error analyses of the potential core length and shear angle measurements were performed, which are presented in the next section.

4.2. Shear Angle Measurements and Error Analysis

Figure 4.6 shows the variation of light intensity with radial distance for LN_2/He flow at 5 m/s and 300 m/s respectively at an axial location of 7D, repeated over 5 different times. One can see that all of the five plots overlapped each other suggesting very little variation in shear angles. However, the shear angle measurements (Table 4.2) show significant variation. The mean for the five cases came out be approximately 5.44 whereas the percentage variation in shear angle was approximately ± 5.0% for all the cases. This is due to the fact that shear angles are extremely small so even a very minute change in flow width can cause significant variation in the shear angle.
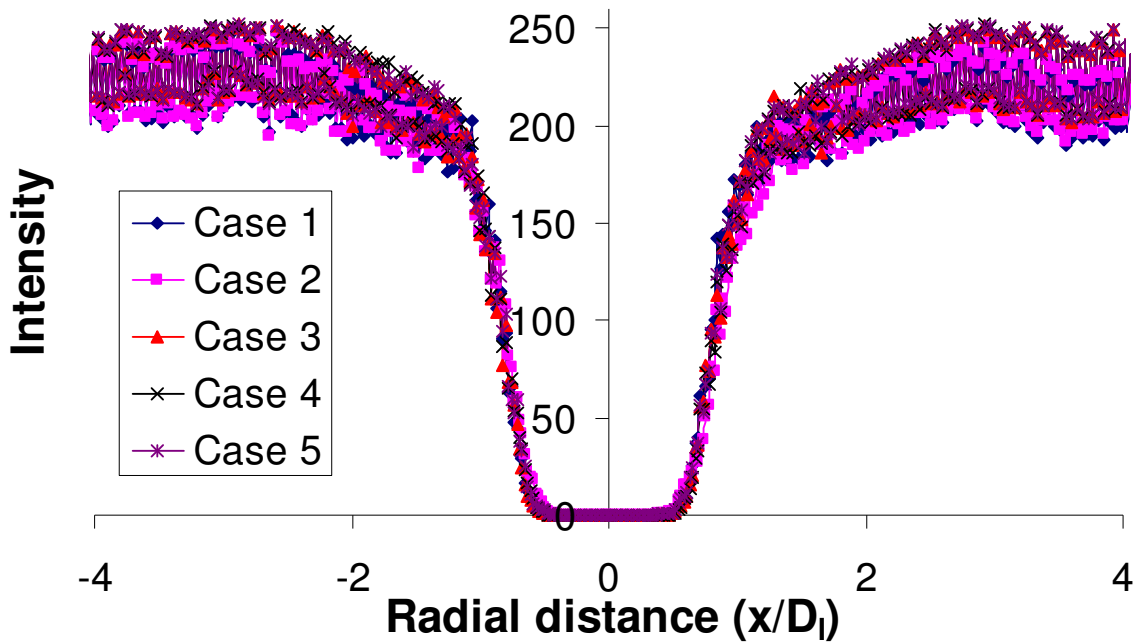
Figure 4.6. Averaged radial intensity variation of LN_2/He flow for the same experimental conditions

Case 1	Case 2	Case 3	Case 4	Case 5
5.12	5.66	5.48	5.3	5.66

Table 4.2. Shear angle variation of LN_2 jet for the same experimental conditions

4.3. Potential Core Length Measurements and Error Analysis

Figure 4.7 shows averaged centerline intensity distribution of LN_2/He flow at 5 m/s and 300 m/s respectively, repeated over 5 different times. As one can see, the centerline intensity distributions look completely different for all the cases even though the experimental conditions had been kept constant. Table 4.2 shows the variation in potential core length measurements for the 5 cases. The percentage variation (0.5*[max-min]/mean) in the potential core length measurement came out to be approximately ± 4.6%. This process was repeated for all experimental cases and the maximum variation was found to be approximately ± 5.0%. The actual potential core length was assumed to be the largest value among the five different cases in order to get the most conservative estimate and the values were plotted with error bars showing ± 5.0% errors.

Case 1	Case 2	Case 3	Case 4	Case 5
19.0	17.7	19.5	17.5	18.7

Table 4.2. Potential core length variation of LN_2 jet for the same experimental conditions
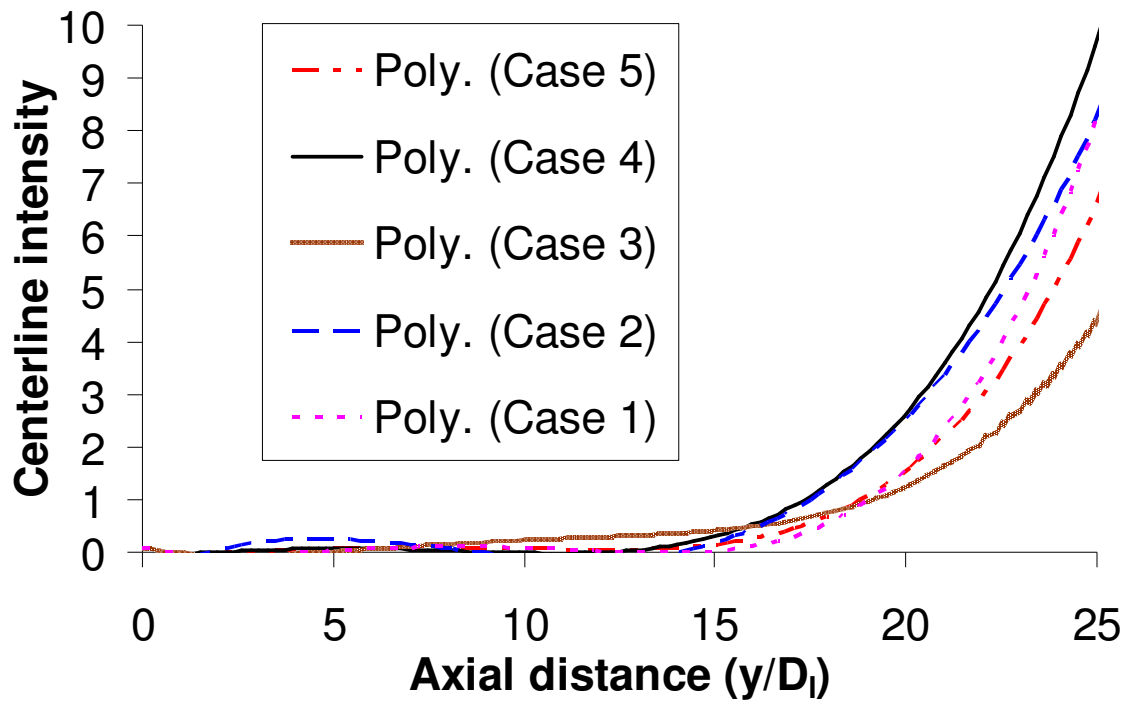
Figure 4.7. Averaged centerline intensity variation of LN$_2$/He flow for the same experimental conditions

5. Results and Discussions

5.1. Transient Atmospheric Pressure Results

In the first set of results, the transient behavior of liquid nitrogen and gaseous helium injected in quiescent air from a shear coaxial injector has been examined, starting from the initial exit of the cryogenic fluid from the injector. The initial, dynamic interaction of the cryogenic liquid with the surrounding gas has been imaged for the first time to reveal the three dimensional two-phase flow behavior of the LN_2 jet. These observations are significant, because instabilities observed at the two-phase boundary during startup clearly reveal the onset of flow instabilities, which then may affect ignition as well as the onset of unstable combustion in many cryogenic rocket engines.

Two specific experimental conditions examined here are evolutionary behavior of the flow (transient experiments) at atmospheric pressure as shown in Table 5.1. In the first case, the flow of liquid nitrogen through the inner tube of the injector was controlled in order to produce an average, steady-state cryogenic fluid velocity of 5 m/s. No gas was fed through the outer tube of the injector. The flow was initiated when a solenoid-operated control valve was opened. Schlieren images, showing the evolutionary behavior of the LN_2 jet after its exit from the injector during the initial 500 ms of the experiment, are shown in Figures 5.1-5.4. Time zero in this image corresponds to the very first trace of the cryogenic jet exiting the injector. Note that D_l in the figure represents the inner diameter of inner tube in the injector.

Liquid	Gas	Velocity (liquid/gas)	Density Ratio (gas/liquid)	Momentum Ratio (gas/liquid)	Mass Ratio (gas/liquid)
LN$_2$	—	5 / 0	—	0	—
LN$_2$	He	5 / 300	2.3E-04	0.83	1.4E-02

Table 5.1. Flow inlet conditions examined for the transient experiments

The Schileren images reveal that initially, the nitrogen emerged as vapor, and is visible in the image due to the gradient in density between the cold nitrogen gas and the surrounding ambient air. This is attributed to the rapid evaporation of the liquid nitrogen jet after it comes into contact with the initially warmer injector tubes downstream of the cryogenic valve. During the first few ms, the jet formed a mushroom-shaped structure, indicating that the interface between the flow and the quiescent surroundings was shaped by a starting vortex. After 7 ms, liquid nitrogen began to emerge, and a dynamically-evolving two-phase flow was established. The interface between the cryogenic liquid and the surrounding gas was highly unstable, with the observation of numerous ligaments and smaller droplets and this is attributed to Kelvin-Helmholtz instability mechanisms. An order of magnitude estimate of the frequencies of vortical structures at the interface showed them to be in the range of 300-3000 Hz. The higher frequencies were very close to the Kelvin-Helmholtz frequencies of the interface as predicted by the previous researchers[40,58,67]. The lower frequencies were of the larger vortical structure that were formed due to the coalescence of smaller vortical structures generated by Kelvin-Helmholtz instability.

The time period over which this initial vapor flow extends is not constant and depends on the complex heat transfer phenomena. This phenomenon can be explained by examining the temperature difference between the warm injector tubes and the

cryogenic liquid nitrogen jet (77 K), when the valve is opened. In the results presented here, this period is approximately 50 ms long. During these 50 ms, the injector walls get cold enough only to allow a "puff" of non-evaporated liquid to be injected, yet still not cold enough to sustain a continuous jet of liquid flow. This puff is recognizable by the sudden increase in darker regions during first 50 ms of the cryogenic flow. Because the injector walls are still significantly warm at this moment, local vapor formation continues to exist in their vicinity with less vapor formation at the centerline away form the walls, which explains the global Schlieren images presented here characterizing the flow in the 50 – 300 ms time frame. The darker regions associated with the initial liquid puff at 50 ms disappear at 100 ms, and lighter regions dominate especially close to the injector walls turning slightly darker at the centerline where the local vapor formation is less. Once the walls gradually approach the cryogenic temperature of liquid nitrogen (between 300-400 ms), the local vapor formation near the walls diminishes. At this time the flow is dominated by the dark regions of central liquid flow and no significant changes are observed anymore (i.e., the steady state conditions are almost achieved) at about 500 ms. The development of the flow from the moment the fluid leaves the injector exit to the achievement of steady state involves the same qualitative analysis described above but is not limited to the same instants presented here. In other words, the appearance of the initial liquid puff and the achievement of steady state can be roughly at about 30 and 350 ms, respectively, if the experiment is restarted with colder injector walls.
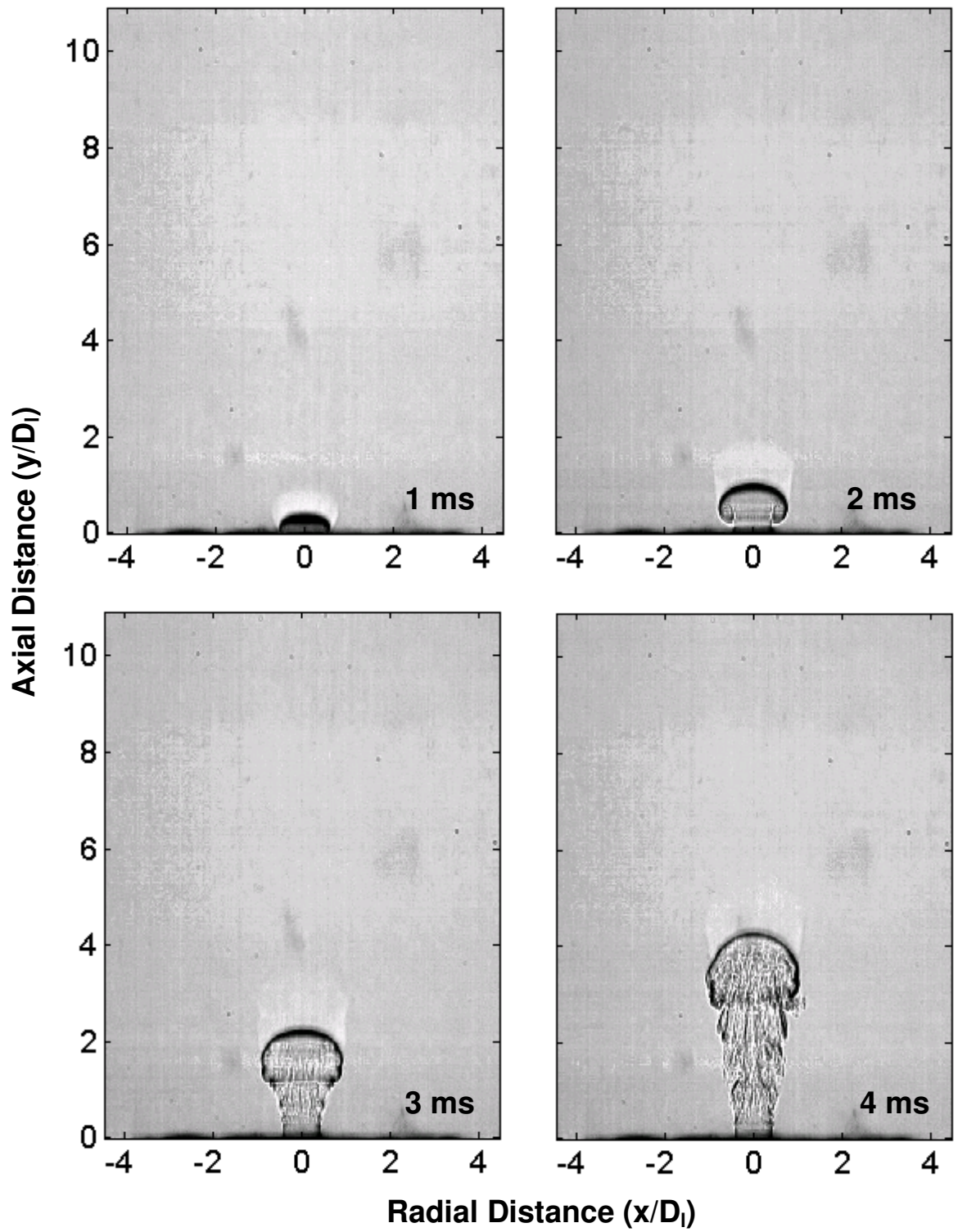
Fig. 5.1. Initial emergence of liquid nitrogen jet into quiescent air during the first 4 ms
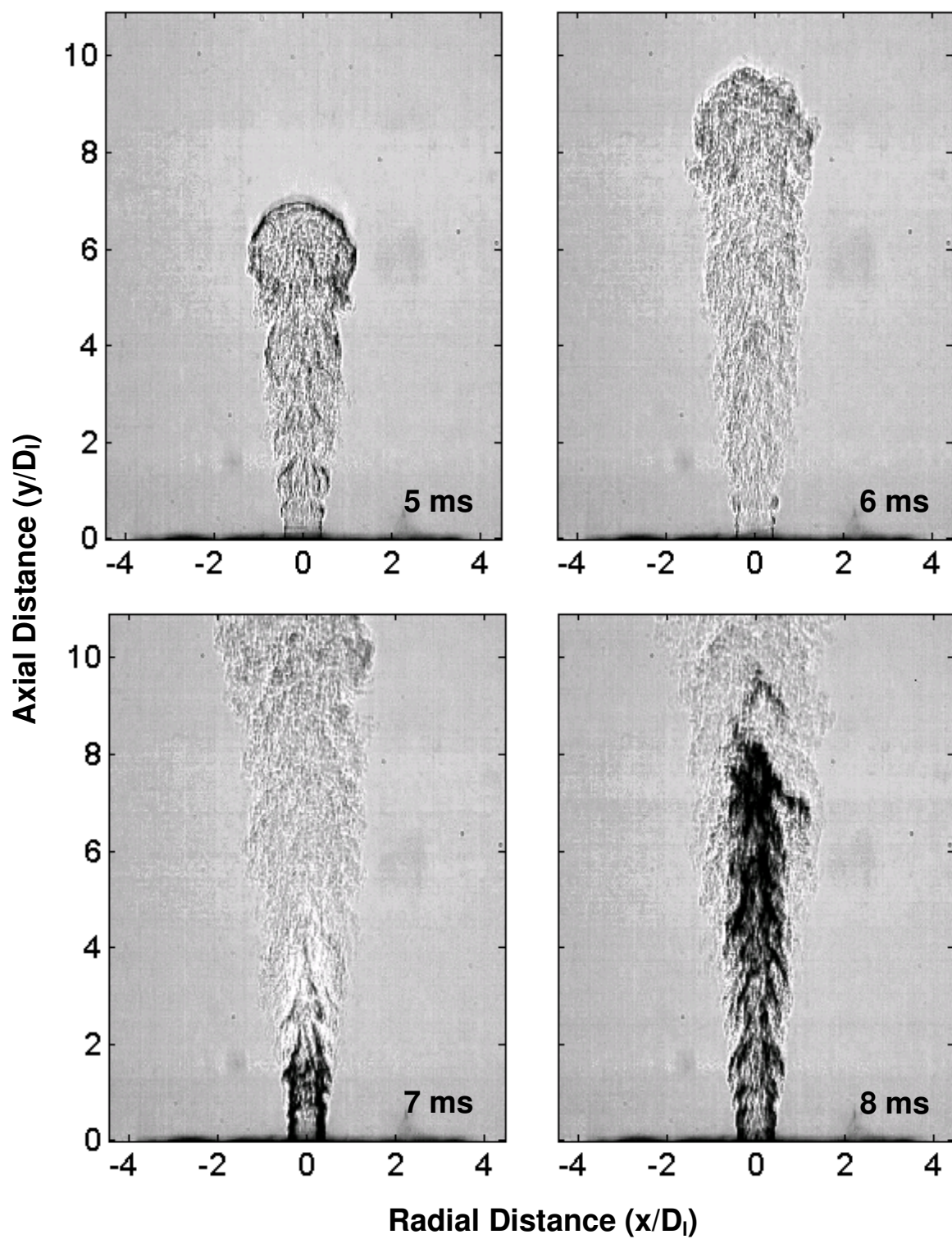
Fig. 5.2. Fate of liquid nitrogen jet from 5 to 8 ms after initial exit emerging into quiescent air
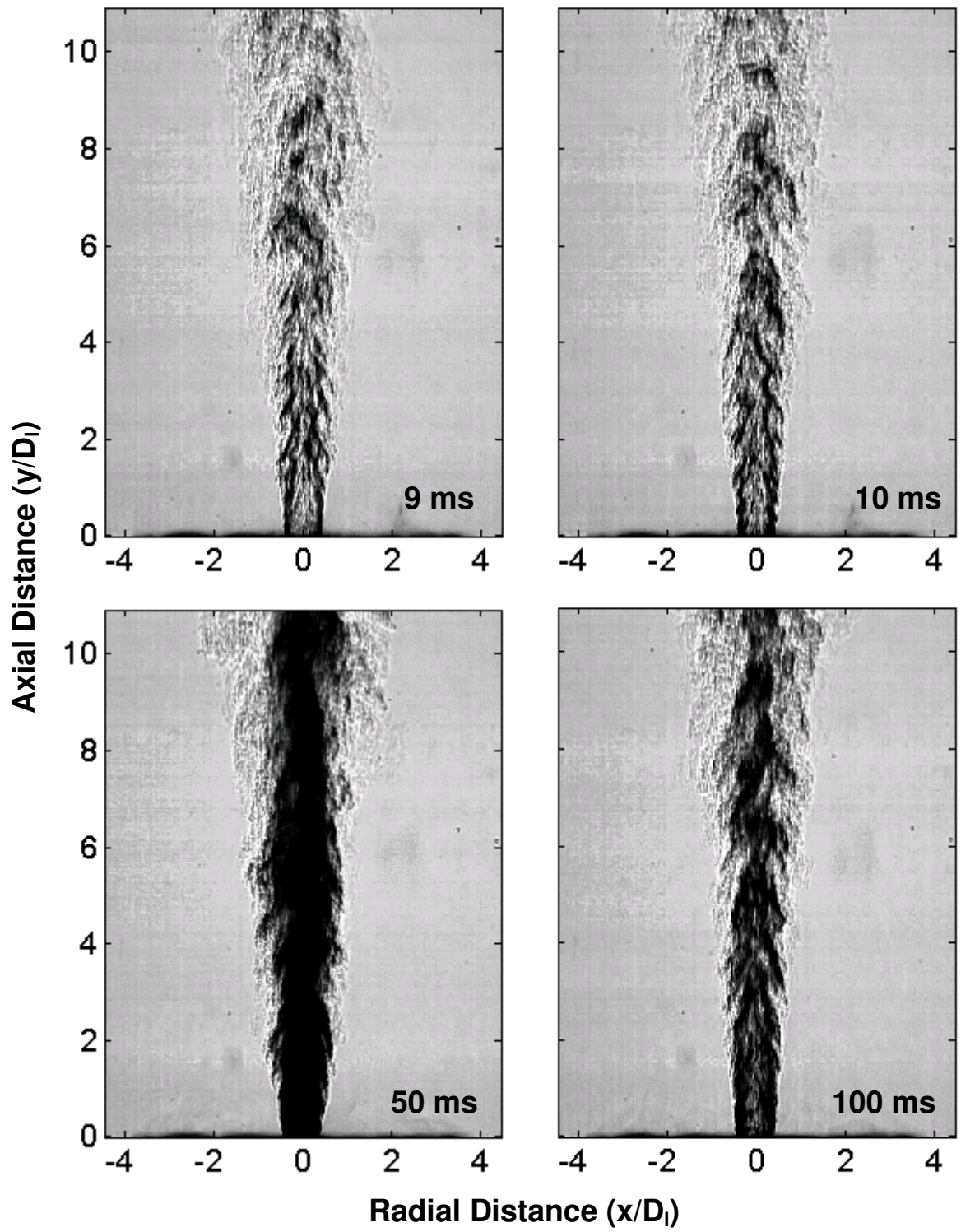
Fig. 5.3. Fate of liquid nitrogen jet from 9 to 100 ms after initial exit emerging into quiescent air
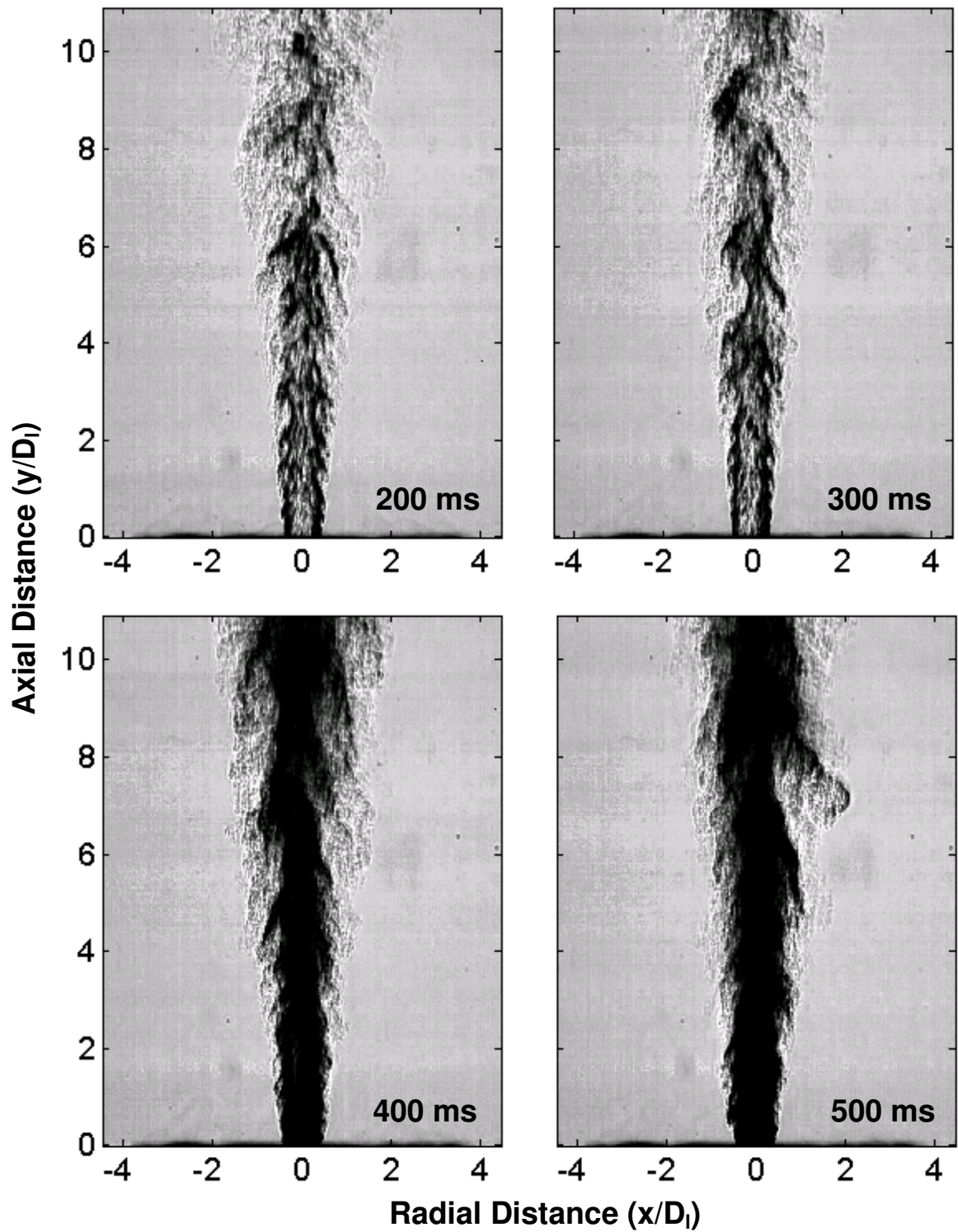
Fig. 5.4. Fate of liquid nitrogen jet from 10 to 500 ms after initial exit emerging into quiescent air

In the second experiment, a steady stream of liquid nitrogen was allowed to emerge from the central tube of the injector. The injector system was allowed to cool down to 77 K at which point the steady mean velocity of liquid nitrogen was 5 m/s. A solenoid valve on the helium line was then opened to allow a flow of helium with a mean axial velocity of 300 m/s to emerge from the outer annulus of the injector. This condition produced a gas/liquid momentum ratio of 0.83. The Schlieren images obtained for the first 100 milliseconds under these experimental conditions are shown in Figures 5.5-5.8.

The sheath of helium emerging from the outer annulus was found to form a toroidal vortex during the initial few milliseconds of its emergence. This is due to a starting vortex and the effect of Rayleigh-Taylor instability mechanism which occurs when a lighter fluid is injected into a denser medium. Another important observation from these images is that the time taken by the gaseous jet to reach the top of the image is much longer than the liquid nitrogen jet, even though the gaseous jet is injected at a much higher speed (300 m/s) than the liquid nitrogen jet (5 m/s). This is due to the higher momentum of liquid nitrogen jet than gaseous helium jet and the dispersion of gaseous helium due to its very high diffusivity. A more complex interaction between the helium and nitrogen streams was observed after first few milliseconds. Momentum was exchanged between the helium and nitrogen streams, in ways that produced distortions of the interface at a variety of length scales. The frequencies of these length scales were found to be in the range of 300-3000 Hz as predicted by previous researchers[40,58,67]. These scales affect liquid jet atomization and its eventual mixing with the surrounding gases, and are significant in understanding

mechanisms driving unstable phenomena in reacting systems. The evolutionary behavior of the flow reveals that the flow upon exit from the injector is unsteady at the initial injection of the cryogenic fluid in to the rocket engine. Once this instability is formed this sustains or grows itself in the engine to affect the mixture ratio, ignition and combustion behavior. These instabilities once formed persisted for the entire duration of the experiments, much beyond the initial few milliseconds of the data presented here. This data exemplifies the presence of flow instabilities in rocket engines right from the beginning of engine start-up.
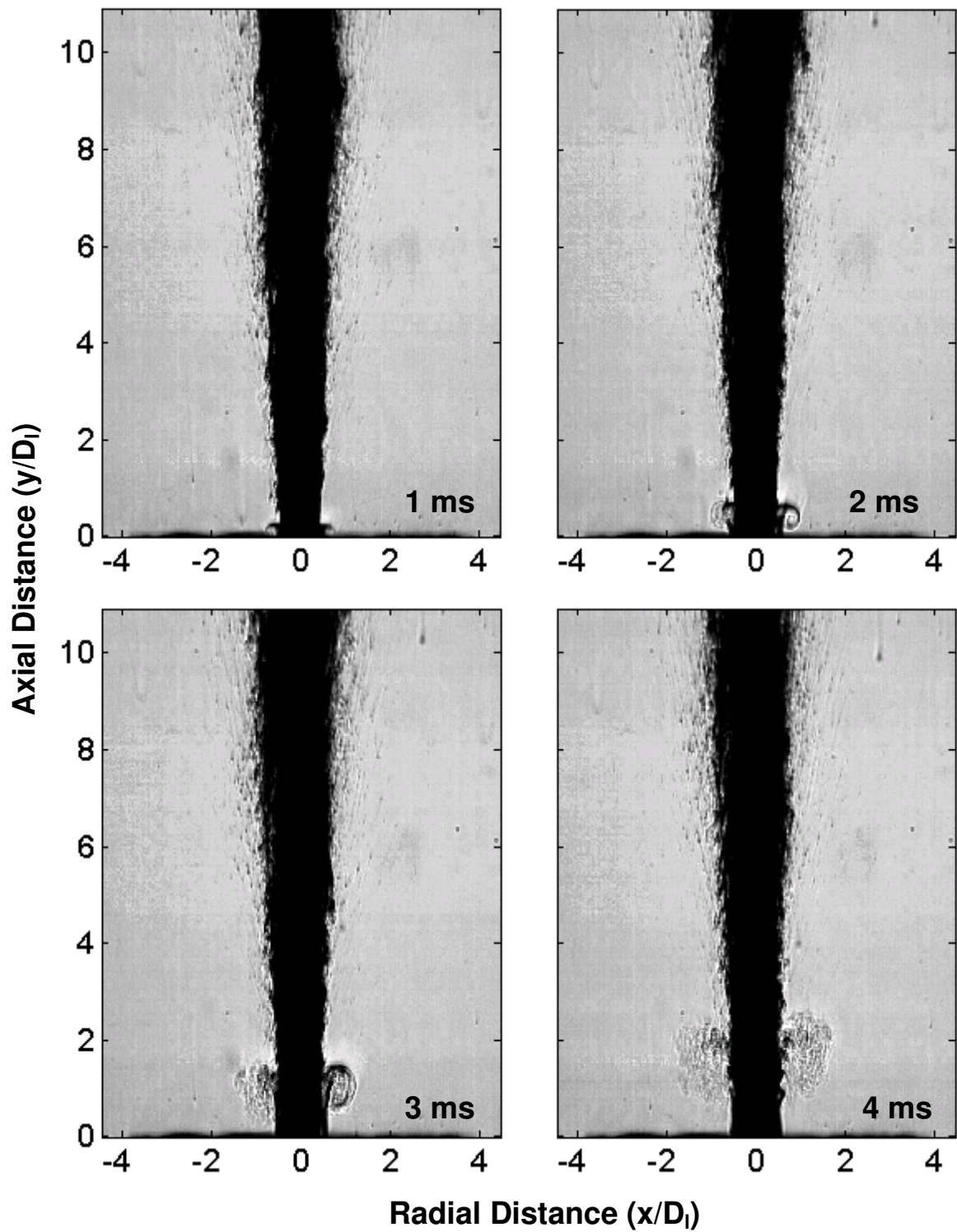
Fig. 5.5. Initial emergence of coaxial gaseous helium jet into steady LN₂ jet during the first 4 ms
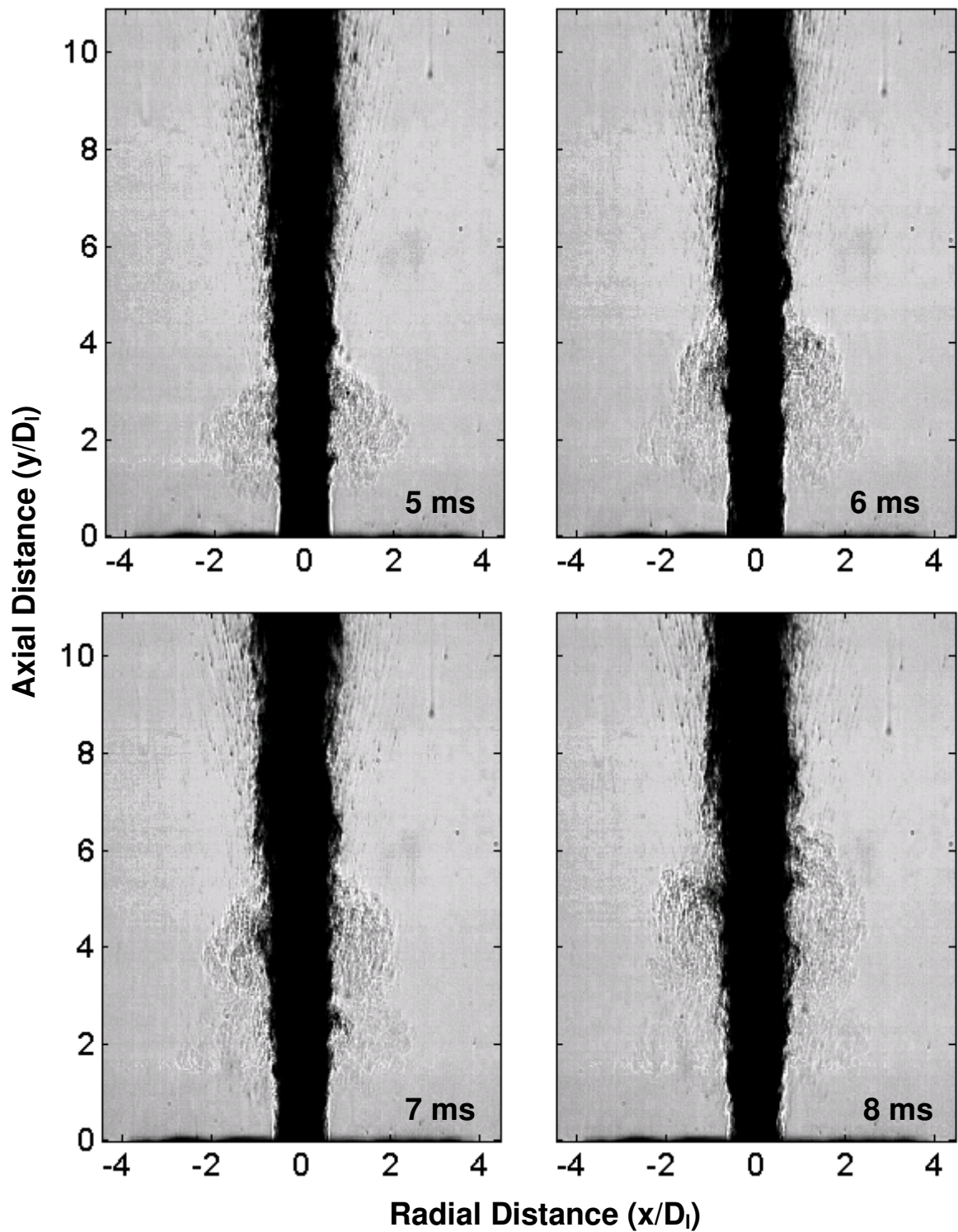
Fig. 5.6. The fate of gaseous helium during the first 5 to 8 ms from the injector exit with steady stream of LN₂ jet
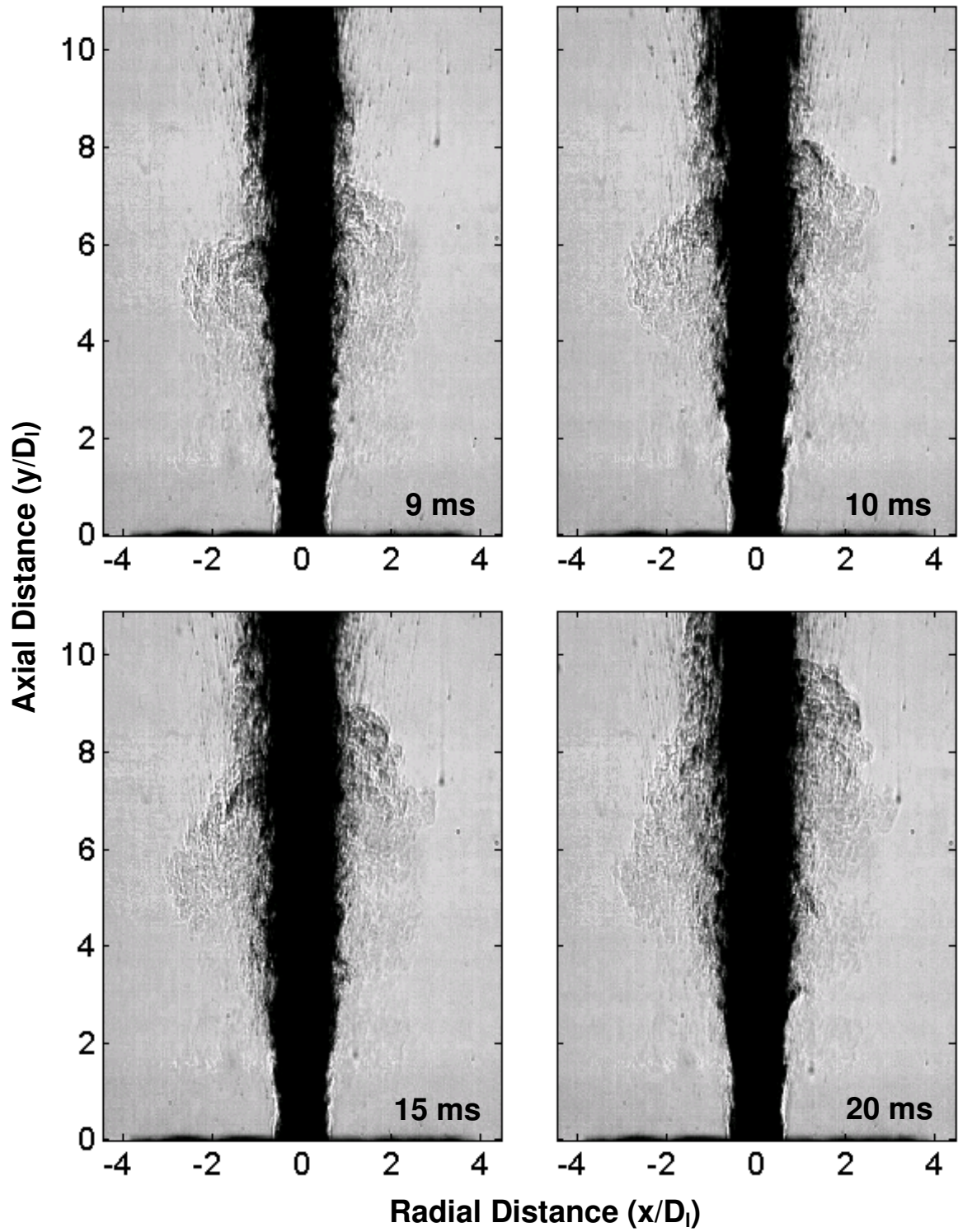
Fig. 5.7. The fate of gaseous helium during the first 9 to 20 ms from the injector exit with steady stream of LN₂ jet
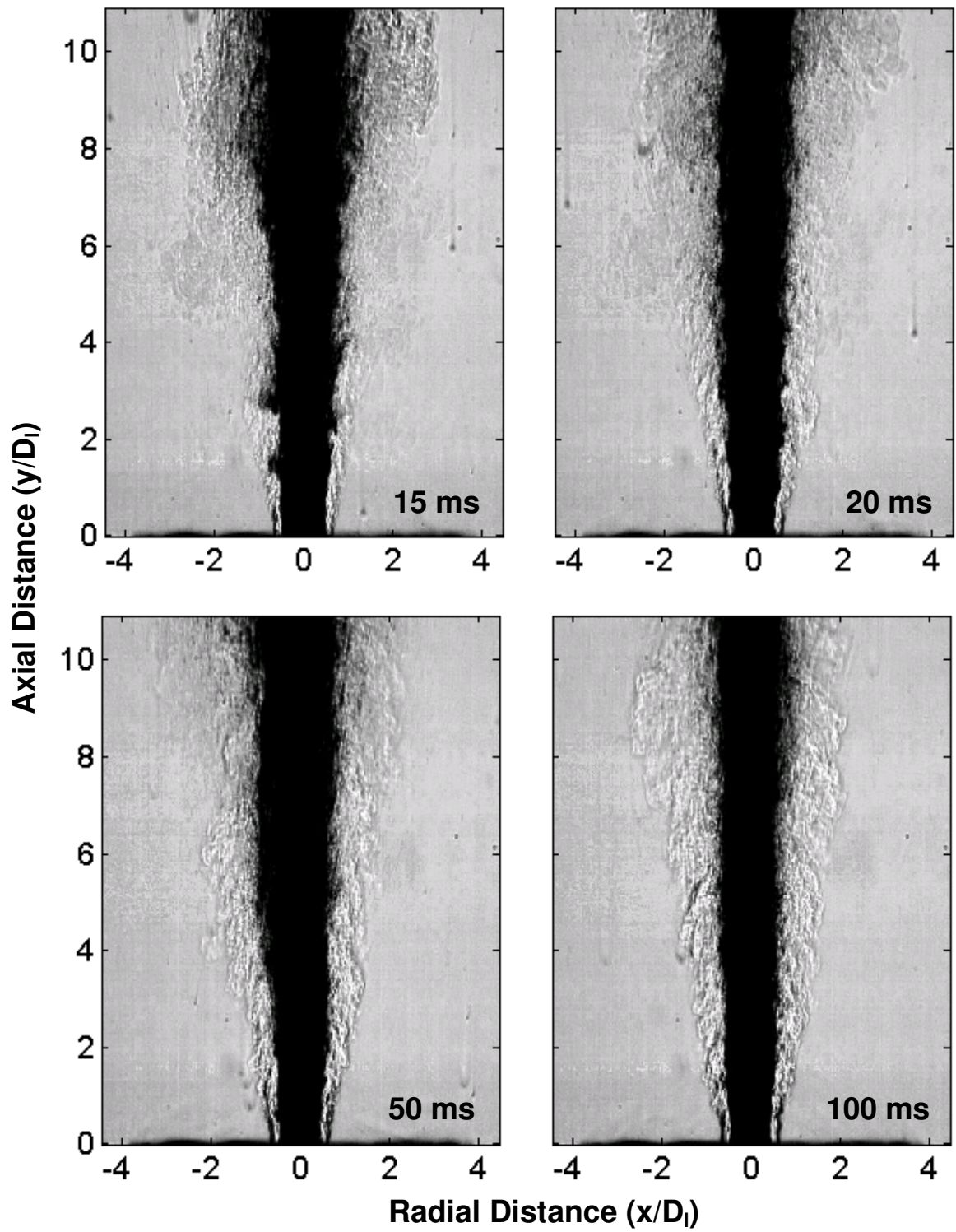
Fig. 5.8. The fate of gaseous helium during the first 30 to 100 ms from the injector exit with steady stream of LN$_2$ jet

5.2. Steady Atmospheric Pressure Results

In the second set of results, the steady-state behavior of liquid nitrogen jet injected into quiescent air and coaxial gaseous jets from a shear coaxial injector have been examined to study the growth of shear layer and primary atomization behavior.

Figure 5.9 shows an image of a LN_2 jet in quiescent air. This image has been extracted from a high speed clip taken at 500 frames/s. The close-up view of the flow, shown in Figure 5.9b, is an image from a clip taken at 1000 frames/s. The evolutionary behavior of the LN_2 jet in a coaxial gaseous stream can be seen. The expansion of the jets and its effect on the surrounding entrained air can also be visualized. The dense white fog, visible downstream of the injector exit, is due to the rapid condensation and freezing of the moisture present in the surrounding air that gets entrained into the gaseous jet. Although the presence of this white fog around the LN_2 stream deteriorates the visibility of the jet, one can still observe that it disperses into ligaments and droplets prior to its vaporization further downstream, where it eventually mixes with the surrounding gas.
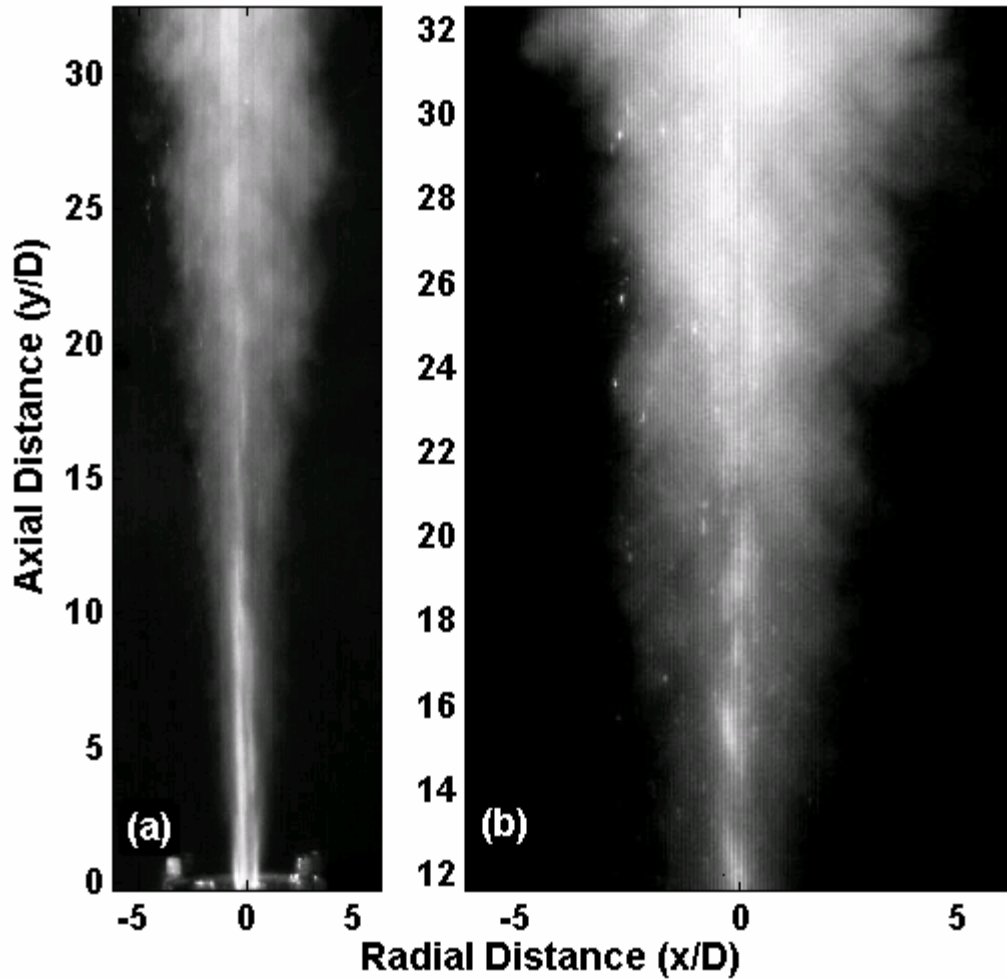
Figure 5.9. High speed images of LN_2 flow; $D = D_l$

a) 500 frames/sec, b) 1000 frames/sec

One important parameter that is used to describe the macro structure of a jet is shear or spreading angle. The shear or spreading angle is a direct quantification of the growth rate of shear layer between the fluids, which is directly responsible for the destabilization of the jets. Shear angles for the present set of experiments were measured as discussed in the data analysis section. Figure 5.10 shows the shear angle of the steady LN_2 jet in quiescent air at different axial locations. The plotted values are mean for five different experiments at the same location with same inlet

conditions with a maximum variation of ± 5.0%. The definition of the flow width for the present set of experiments was assumed at light intensity of 120 (I = 120) as discussed previously, however the results for some other values of intensities (I = 60 and 30) are also presented for comparison purposes. The shear angle of the flow reduced with decrease in intensity values because the assumed value of jet width was reduced. Also the shear angles remained relatively constant over the axial distance, thus confirming that the jet is steady and fully developed. The mean shear angle averaged over axial distance was found to be 6.4° ± 5.0%, 4.2° ± 5.0% and 2.7° ± 5.0% for $I = 120, 60$ and 30 respectively. The predicted spreading angle for water jet in quiescent air was approximately 0.6° using Reitz and Bracco's correlation ($\theta \approx 0.27(\rho_g/\rho_l)^{0.5}$) whereas it was approximately 1.2° and 8.4° for subcritical and supercritical LN$_2$ jets respectively using Chehroudi's correlation ($\theta \approx 0.27[F(x(\rho_g/\rho_l))+(\rho_g/\rho_l)^{0.5}]$). The measured value for our experiment was in between the predicted values for subcritical and supercritical cases. This was due to the fact that LN$_2$ jet in our case is injected into atmosphere at subcritical pressure (1 atm) and supercritical temperature (295 K). Also the cooling effect of LN$_2$ jet on surrounding air increased the density of surrounding air thus increased the shear or spreading angle. One can also notice that the shear angle values for $I = 120$ was closer to the supercritical case while it was closer to the subcritical value for $I = 30$ case. This is because the light intensity value of 30 was closer to the light intensity of the intact LN$_2$ jet ($I = 0$) than the light intensity of 120 case.
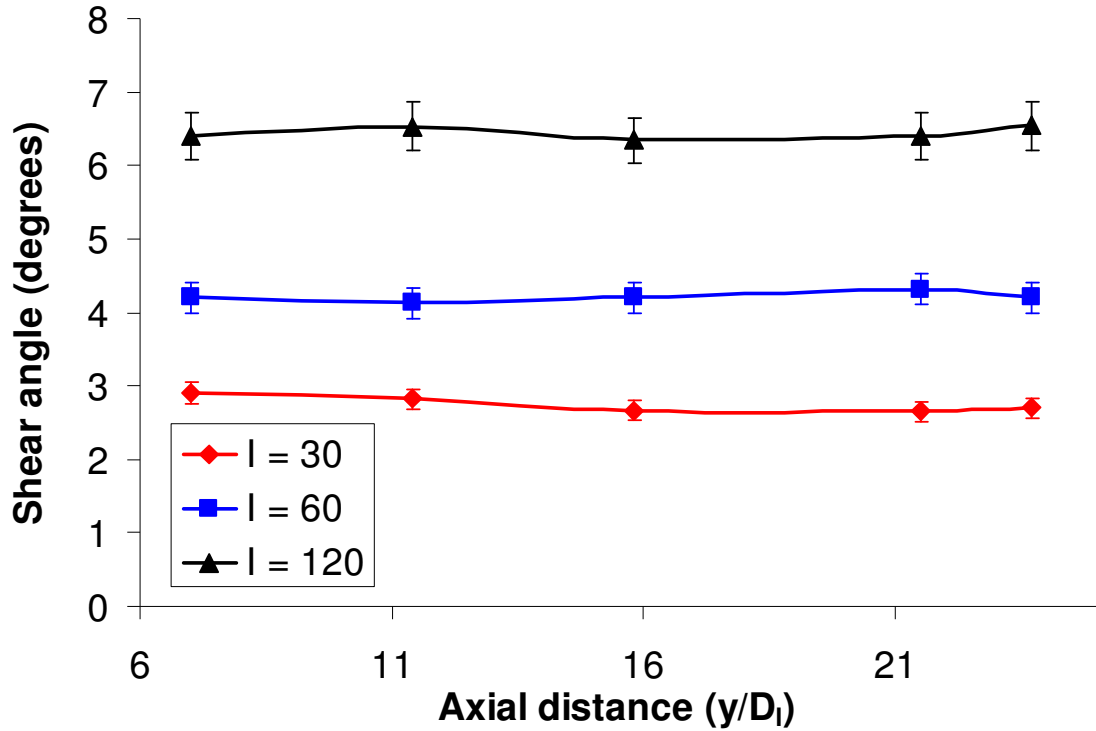
Figure 5.10. Shear angle of LN_2 jet in quiescent air at various axial locations

In order to further investigate these effects, shear angles were measured for LN_2 jet in coaxial helium stream at 300 m/s (Figure 5.11). As one can see the shear angles for both the flows is constant over axial distance, however the shear angle of LN_2/He flow is smaller than the shear angles of LN_2 jet in quiescent air. This further confirmed the effect of surrounding gas density on liquid jet spreading. The flow of helium reduced the effective density of the surrounding air, thus reducing the jet spread. However even for helium case the shear angle was higher than the predicted value for subcritical LN_2 jet in quiescent air (1.2°) which shows the effect of heat transfer and transcritical behavior along with the entrainment of surrounding air into the coaxial gaseous flow.
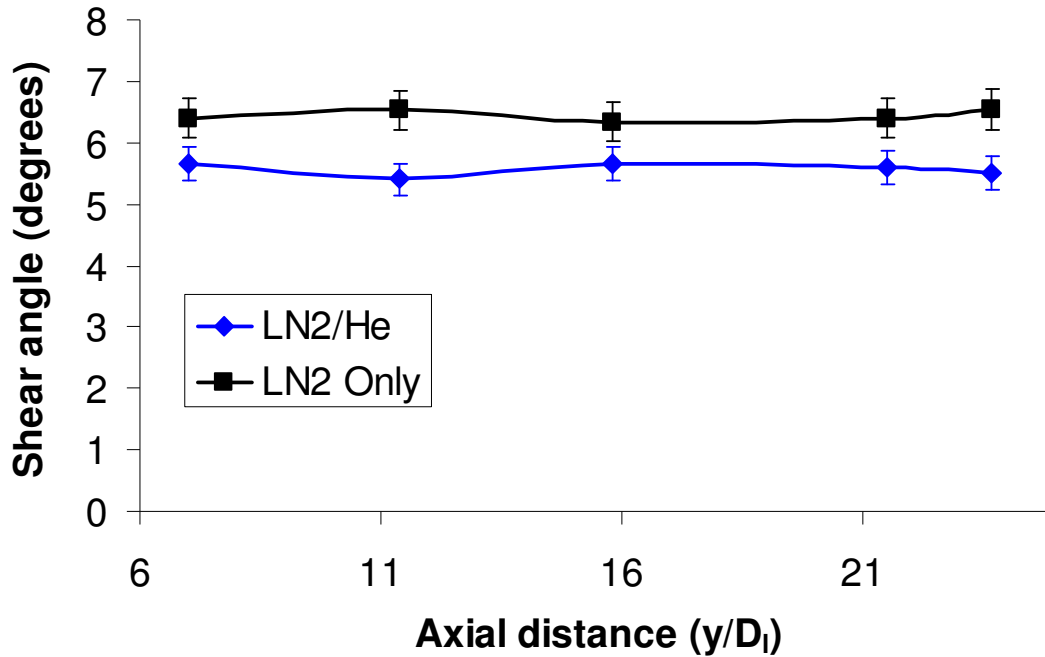
Figure 5.11. Shear angles of LN$_2$ jet in quiescent air and with coaxial helium stream at various axial locations

Figure 5.12 shows the shear angles of all the cases averaged over axial distance and plotted against the coaxial helium velocity. The predicted spreading angles for LN$_2$ jet in quiescent helium were approximately 0.7º and 8.0º for subcritical and supercritical pressures using Chehroudi's correlation. It can be seen that the shear angle decreased uniformly with increase in coaxial helium velocity and moved towards the predicted value. This further proved our assertion that injection of helium reduced the density of surrounding medium thus reducing the jet spread. As the velocity of helium jet increased, the mass flow rate of helium gas injected into the surrounding air increased, thus reducing the effective density of the surrounding medium.
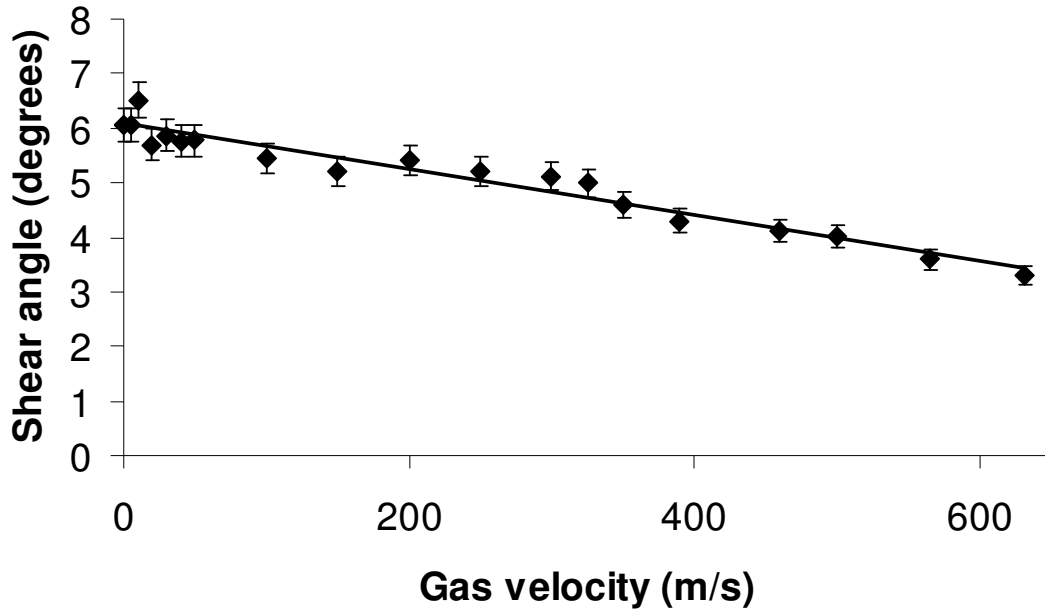
Figure 5.12. Shear angle of LN$_2$/He flow for different velocities of the coaxial helium jet

Another important parameter used to describe the macro structure of a jet is the potential core length. The potential core lengths (L_b/D_l) for the various cases calculated as discussed in the data analysis section are shown in Table 5.2 (note that LN$_2$ Reynolds and Weber numbers were kept constant at 2.21E+05 and 1.93E+04 respectively).

Case No.	Inner Fluid	Outer Fluid	Velocity [m/s] (liquid/gas)	Gas Reynolds number	Momentum Ratio (gas/liquid)	Potential core length L_b/D_l± 5.0%
1	LN$_2$	He	5 / 0	0.00E+00	0	18
2	LN$_2$	He	5 / 5	1.64E+02	2.3E-04	21
3	LN$_2$	He	5 / 10	3.29E+02	9.2E-04	21.2
4	LN$_2$	He	5 / 20	6.58E+02	3.7E-03	21.4
5	LN$_2$	He	5 / 30	9.87E+02	8.3E-03	21.5

6	LN$_2$	He	5 / 40	1.32E+03	14.7E-03	21.7
7	LN$_2$	He	5 / 50	1.64E+03	23.0E-03	22
8	LN$_2$	He	5 / 100	3.29E+03	91.9E-03	22.5
9	LN$_2$	He	5 / 150	4.93E+03	0.21	22
10	LN$_2$	He	5 / 200	6.58E+03	0.37	22
11	LN$_2$	He	5 / 250	8.22E+03	0.57	21.4
12	LN$_2$	He	5 / 300	9.87E+03	0.83	19.5
13	LN$_2$	He	5 / 325	1.07E+04	0.98	17.7
14	LN$_2$	He	5 / 350	1.15E+04	1.13	16
15	LN$_2$	He	5 / 390	1.28E+04	1.4	13
16	LN$_2$	He	5 / 460	1.51E+04	1.95	9
17	LN$_2$	He	5 / 500	1.64E+04	2.3	8.2
18	LN$_2$	He	5 / 565	1.86E+04	2.92	7.8
19	LN$_2$	He	5 / 630	2.07E+04	3.68	7.6

20	LN$_2$	He	5 / 100	3.29E+03	0.092	22.5
21	LN$_2$	He + Ar	5 / 100	6.61E+03	0.21	22.4
22	LN$_2$	He + Ar	5 / 100	1.13E+04	0.37	22.3
23	LN$_2$	He + Ar	5 / 100	1.80E+04	0.57	21.5

24	LN$_2$	He	5 / 200	5.98E+03	0.37	22
25	LN$_2$	He + Ar	5 / 200	9.37E+03	0.57	21.2
26	LN$_2$	He + Ar	5 / 200	1.36E+04	0.83	19.3
27	LN$_2$	He + Ar	5 / 200	1.84E+04	1.13	16.1
28	LN$_2$	He + Ar	5 / 200	2.39E+04	1.47	13.1
29	LN$_2$	He + Ar	5 / 200	3.04E+04	1.87	9.4
30	LN$_2$	He + Ar	5 / 200	3.75E+04	2.30	8.5

Table 5.2. Potential core lengths for the various flow inlet conditions examined

Figure 5.13 shows the potential core length of LN$_2$ with coaxial helium velocity. The predicted potential core lengths, proposed by previous researchers, have also

been plotted for the purposes of comparison. It can be seen that the present results do not match with the predicted potential core length of non-cryogenic jet (water); however it matches well with the predicted core length of cryogenic jet at higher gas velocities or momentum ratio between the jets.
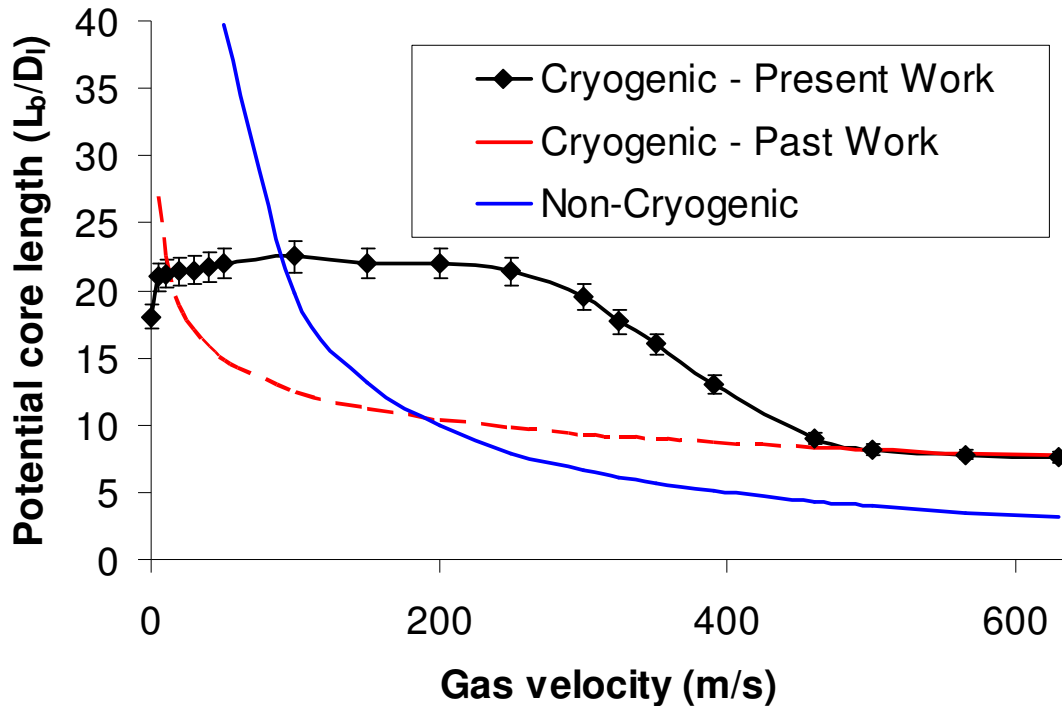
Figure 5.13. Potential core length of LN_2 jet for different velocities of the coaxial gaseous jet (solid line – experimentally validated, dotted line – predicted)

This plot reveals some interesting features. The potential core length of the LN_2 jet increases with the increase in velocity of the gaseous jet, until this velocity reaches a value of about 100 m/s, beyond which the potential core length of the liquid jet drops. In contrast to these results, previous research had suggested that the potential core length of the liquid jet should decrease absolutely with the increase in velocity of the gaseous jet, because this increases the momentum ratio between the jets. These suggestions are undoubtedly accurate, if the liquid jet is a subcritical isothermal fluid

(water for example). The unique behavior of LN_2 jet is, however, due to the heat transfer effects of the surroundings on the supercritical LN_2 jet. All of the previous research, conducted on the characterization of the potential core length of a liquid jet inside a coaxial gaseous stream has been either on non-cryogenic fluids where the heat transfer effects were negligible or with cryogenic fluids but at very high gas velocities compared to the liquid velocity. However, the case is substantially different for a cryogenic LN_2 jet that is being injected in warm surroundings.

The vaporization of LN_2 due to the heat transfer from the surroundings has an effect as significant as that of the shearing of the surrounding gaseous jet on the breakup of the LN_2 jet. In light of this vitally important fact, the discrepancy observed in Figure 5.13 between the results of this work and those of previous research can be explained as follows. Initially, when LN_2 is injected solely with no coaxial gaseous jet, the LN_2 jet is in direct contact with the atmosphere that acts as a heat source for the cold jet (77 K). The heat transfer from the surrounding atmosphere makes the central core to vaporize fast and break sooner, resulting in a shorter potential core length than non-cryogenic jet. Another important feature of Figure 5.13 is longer potential core length of cryogenic LN_2 jet than non-cryogenic ones at higher gas velocities. This is due to another effect of heat transfer from coaxial gaseous jet to cold LN_2 jet. The moment coaxial gaseous jet comes in contact with cold LN_2 jet, an infinitesimally small layer of gaseous nitrogen forms at the interface of the two fluids. This gaseous nitrogen layer expands radially outwards and pushes the coaxial gas away from the LN_2 jet, which in turns reduces the shearing effect of coaxial gaseous

jet on central cryogenic jet. This reduction in shearing effect causes the larger liquid core lengths at higher helium jet velocities.

The introduction of coaxial gas has two major effects on the cryogenic jet, i.e., shear layer destabilization and heat transfer. The effect of heat transfer is controlled by gaseous jet Reynolds number (Re_g) and Prandtl number (Pr_g). For a constant Prandtl number (Pr_g), when the gaseous jet is at lower velocity it acts like a heat shield for the cold cryogenic jet whereas this effect doesn't remain prominent at higher velocities of the coaxial gas. This phenomenon can be explained by examining the effect of gas Reynolds number on potential core length of the cryogenic jet (Figure 5.14). At lower velocities, the gaseous jet is laminar so convective heat transfer is minimal but heat conduction from the surrounding is reduced because gaseous jet creates a thermal insulation around the cold LN_2 jet due to its really low thermal conductivity. Convective heat transfer increases with increase in Reynolds number but conduction decreases as a thicker layer of gas now surrounds the liquid jet and shields it from warm atmospheric, which acts as a heat source so those effects start balancing each other out. As the Reynolds number further increases the flow reaches a fully developed turbulent condition so heat transfer is completely controlled by convection and the effect of heat shielding becomes negligible.
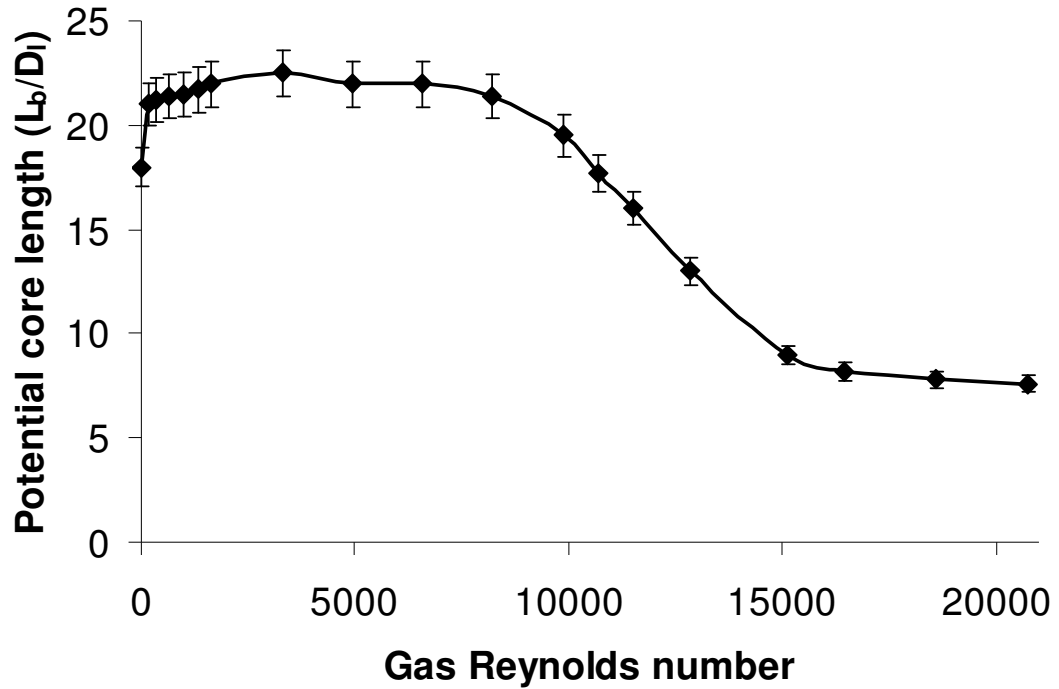
Figure 5.14. Variation of potential core length of LN$_2$ jet Reynolds number of the gaseous jet

The effect of shear layer destabilization however which has been explained in previous works[27,40,55] is controlled by momentum ratio (Figure 5.15) between the jets and is generally negligible for momentum ratios less than one (M << 1). Shear layer destabilization starts increasing at momentum ratios close to one (M ~ 1) and become significant for momentum ratios greater than one (M > 1).
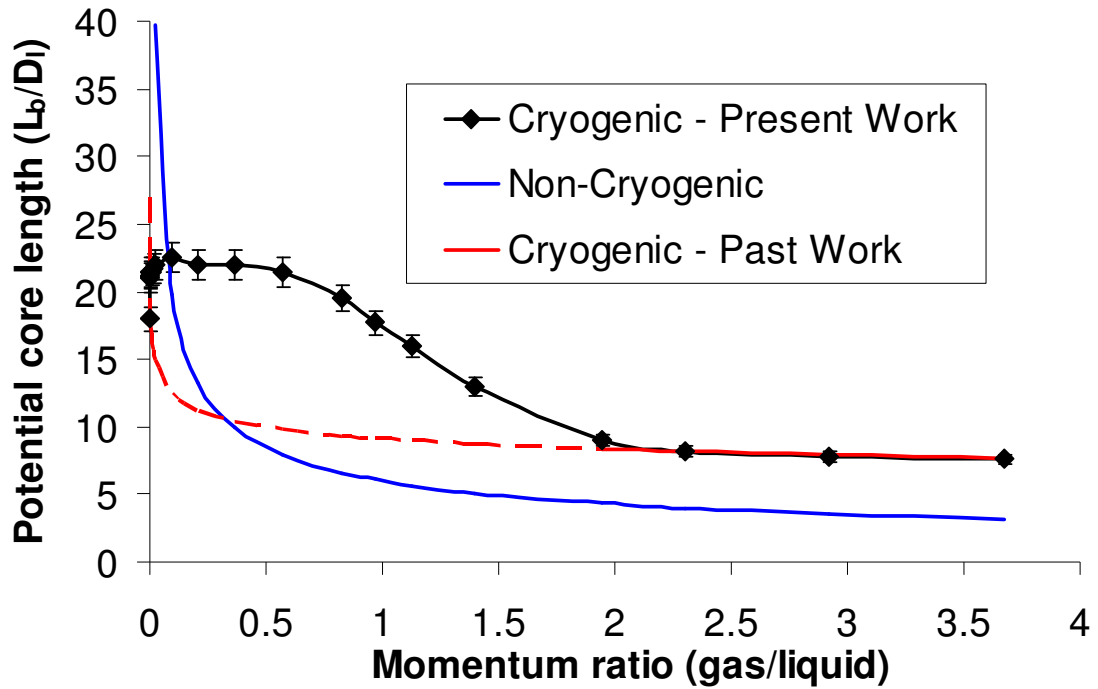
Figure 5.15. Variation of potential core length of LN_2 jet with momentum ratio between the jets (solid line – experimentally validated, dotted line – predicted)

At low helium velocities (up to about 100 m/s), the destabilization of LN_2 due to the shearing effects of helium is still minor and not quite effective. However, the destabilization due to heat transfer, which is the dominant mode of destabilization at these conditions, gets affected by the introduction of helium, which results in longer potential cores, as the helium velocity is slightly increased. Close to a helium velocity of 100 m/s, the heat-shielding effect of the helium jet reaches its maximum while shear-layer effect is still negligible, which makes the potential core length to achieve a local maximum. When the helium velocity reaches approximately 300 m/s, the heat shielding effect of the helium jet start diminishing due to increase in convective heat transfer whereas the shear-layer destabilization effect start increasing exponentially causing a steep reduction in potential core length. At a helium velocity of about 325

m/s (MR ≈ 1), the potential core length of the LN_2 jet becomes even shorter than the corresponding one in the absence of the helium jet, which suggests that at 325 m/s, and beyond, the effect of shear-layer destabilization of helium on the LN_2 jet has finally prevailed over the helium heat-shielding effect completely.

The second and third set of experiments conducted in this study on the characterization of the LN_2 potential core length investigate the effect of density of the gaseous jet, keeping its injection velocity constant (cases 20 – 23 in Table 4.1). In order to further strengthen the observations made from Figure 5.13, Figure 5.16 shows the variation of potential core length with surrounding gas density at a constant gas velocity of 100 m/s. This plot also suggests the effect of heat transfer on the potential core length and negligible effect of shear layer destabilization for momentum ratios less than one. Another fact to be extracted from Figures 5.13 and 5.16 is that the potential core lengthens considerably, once a surrounding gaseous jet is introduced, in comparison to its length in the absence of a coaxial gaseous jet. This again confirms the heat shielding effect of the coaxial gaseous jet.

Figure 5.16. Potential core length of LN$_2$ jet for different densities of the coaxial gaseous jet at constant velocity of 100 m/s

It can be seen from Figures 5.17 and 5.18 that the potential core length remains unaffected with the change in density of the surrounding gas jet, although increasing the gas density increased the momentum ratio and Reynolds number of the jet, thus increasing shear layer destabilization and convective heat transfer. The effect of shear layer destabilization as explained earlier should be negligible as the momentum ratios are less than one ($M << 1$). To further the heat transfer effect we looked at some of the heat transfer characteristics of the gases used to create these gas mixture jets of different densities. For the present experiments, helium and argon have been used in different proportions to create a gas mixture of the desired target density. Since helium and argon are both monatomic gases, their heat capacities are the same, but their individual thermal conductivities possess a striking difference. While the thermal conductivity of helium is approximately 0.151 W/m.K, that of argon is only

91

0.018 W/m.K. This suggests that as the density of the gas mixture is increased by mixing more argon and less helium, the Reynolds number of the gas mixture jet increases but at the expense of decreased thermal conductivity at the same time which reduces the conductive heat transfer. Figure 5.19 shows the variation of thermal conductivity (mW/m.K) of the mixture gaseous jet with gas density, wherein thermal conductivities for the mixtures are calculated by the correlation given in reference 44.
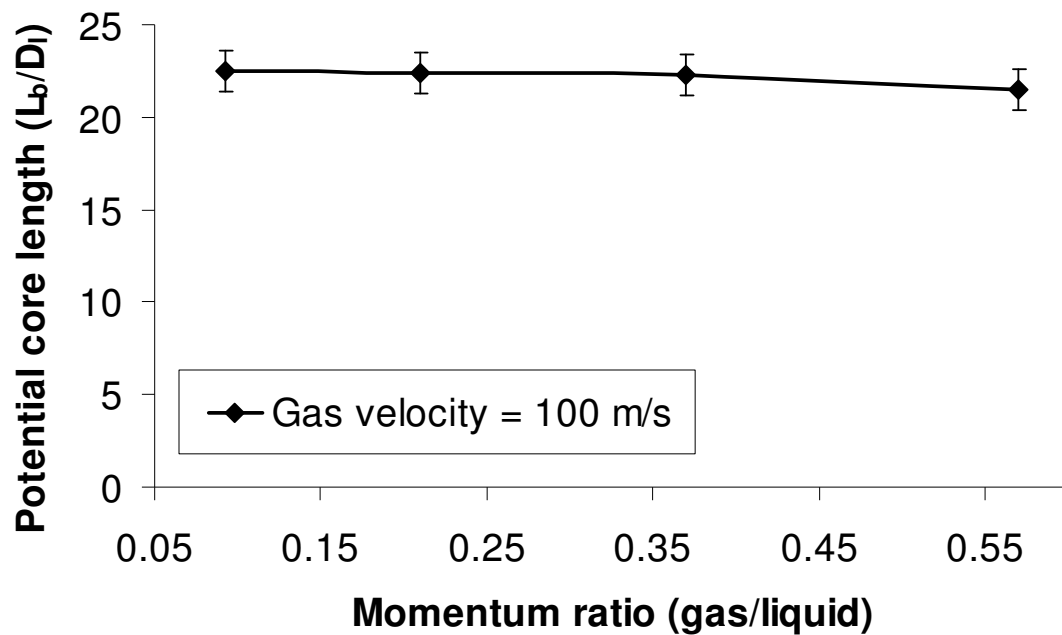
Figure 5.17. Variation of potential core length of LN$_2$ jet with momentum ratio between the jets at constant gas velocity of 100 m/s
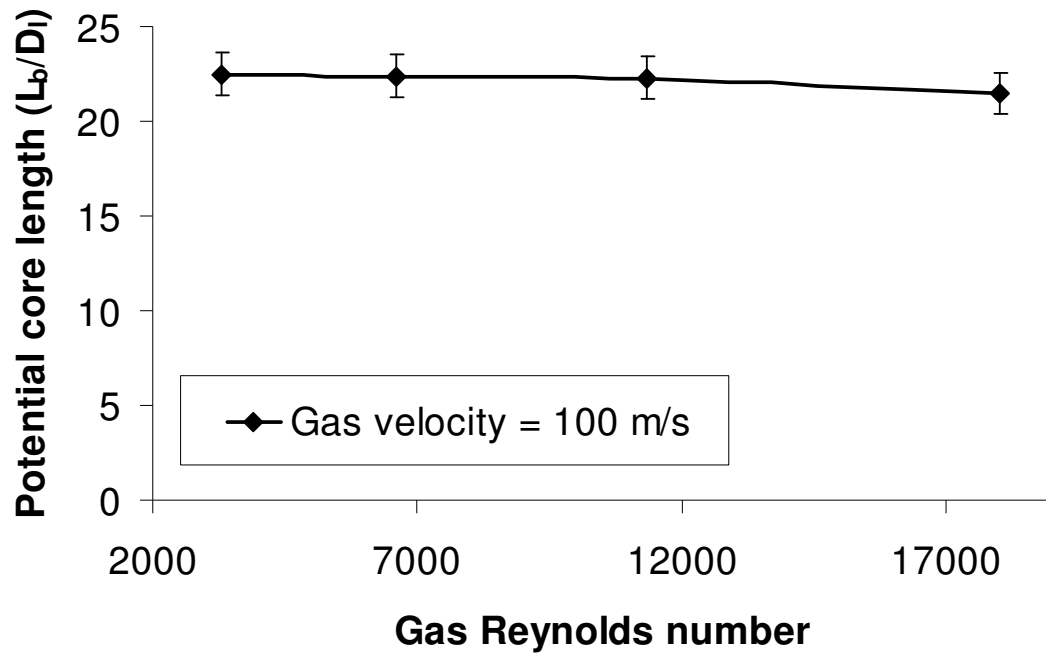
Figure 5.18. Potential core length of LN$_2$ jet with Reynolds number of the gaseous jet at constant gas velocity of 100 m/s
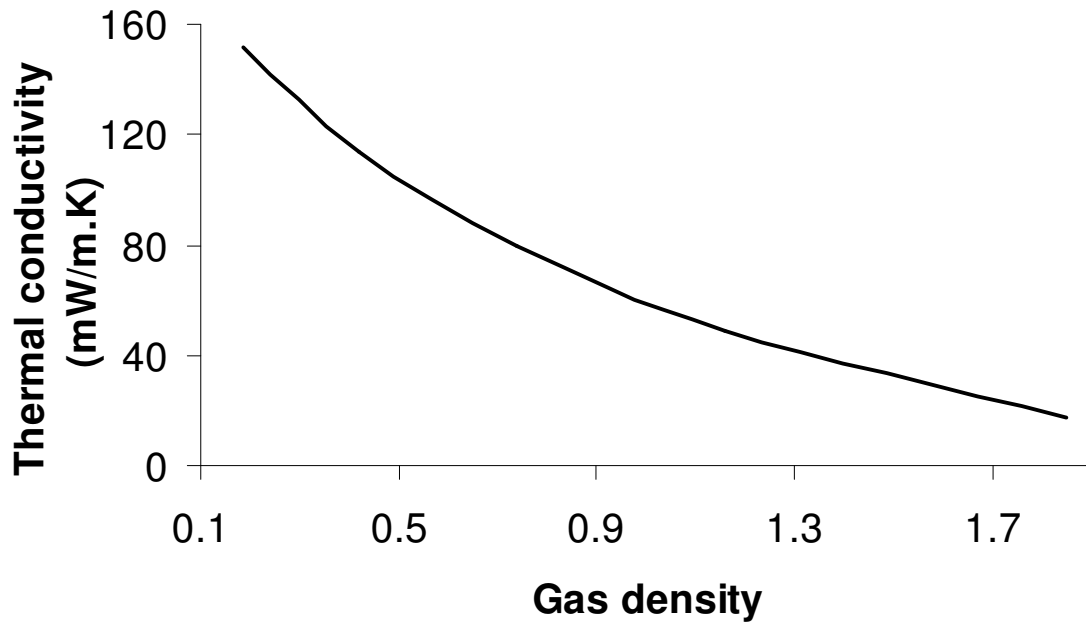
Figure 5.19. Variation of thermal conductivity with the density of the gaseous jet using mixtures of helium and argon

Therefore, increasing the density of the coaxial gas at 100 m/s affects neither the heat transfer nor the shear layer destabilization. Hence, no change occurs in the potential core length of the LN_2 jet as the density of the surrounding gas mixture is changed. In order to further support those findings we conducted another set of experiment to examine the variation of potential core length of LN_2 with coaxial gas density at a higher gas velocity of 200 m/s (cases 24 – 30 in Table 4.1).. This experiment was performed to look at a larger range of momentum ratio (0.37-2.3) for constant gas velocity. The results (Figures 5.20 and 5.21) also supported strongly the finding that core of length of LN_2 jet is not affected much at momentum ratios of less than one. However, as the momentum ratio reaches one the potential core length starts decreasing exponentially until the momentum ratio of approximately two which is very similar behavior to that observed in Figure 5.15. Figure 5.22 shows a comparison of potential core lengths obtained for the three experimental sets, all the three plots overlapped, which confirms the similar effects of momentum ratio and heat transfer for all the three experimental sets. All these results strengthen our belief further on the important role of the effect of heat transfer on cryogenic fluid flow. This has not been emphasized or examined in the available previous research.

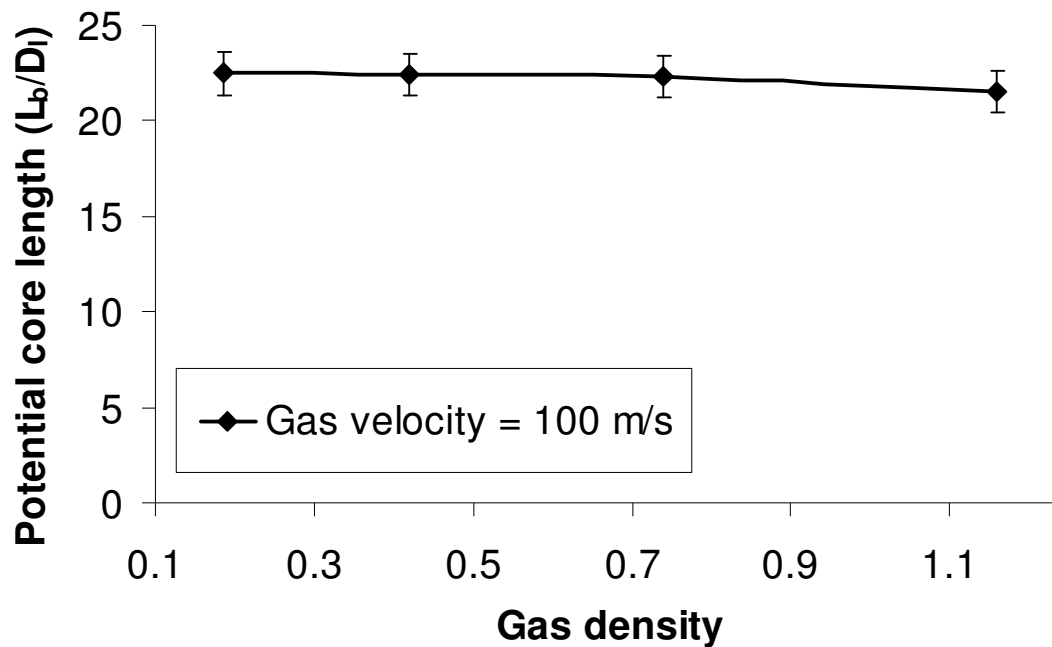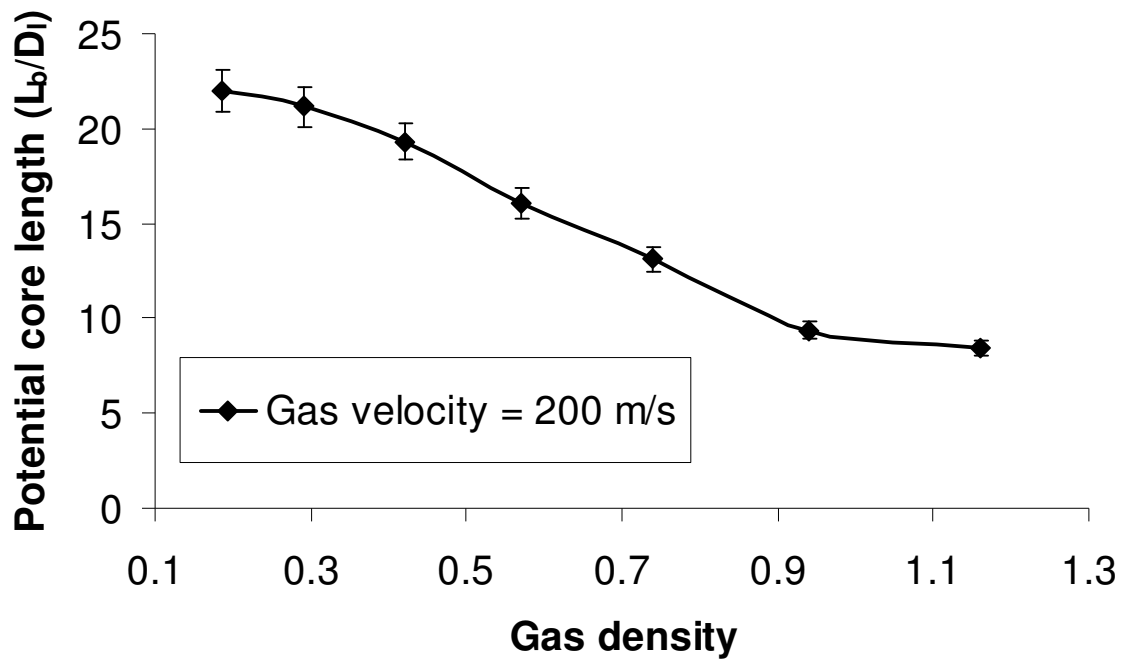**Figure 5.20. Potential core length of LN$_2$ jet for different densities of the coaxial gaseous jet at constant velocity of 200 m/s**
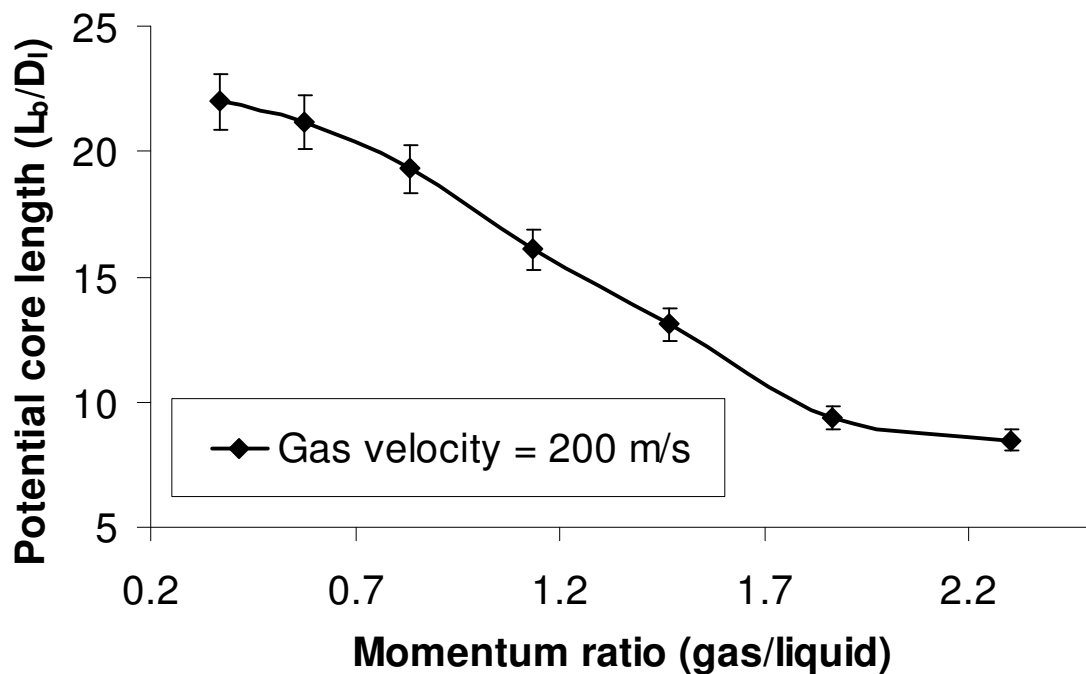
Figure 5.21. Variation of potential core length of LN$_2$ jet with momentum ration between the jets at constant gas velocity of 200 m/s
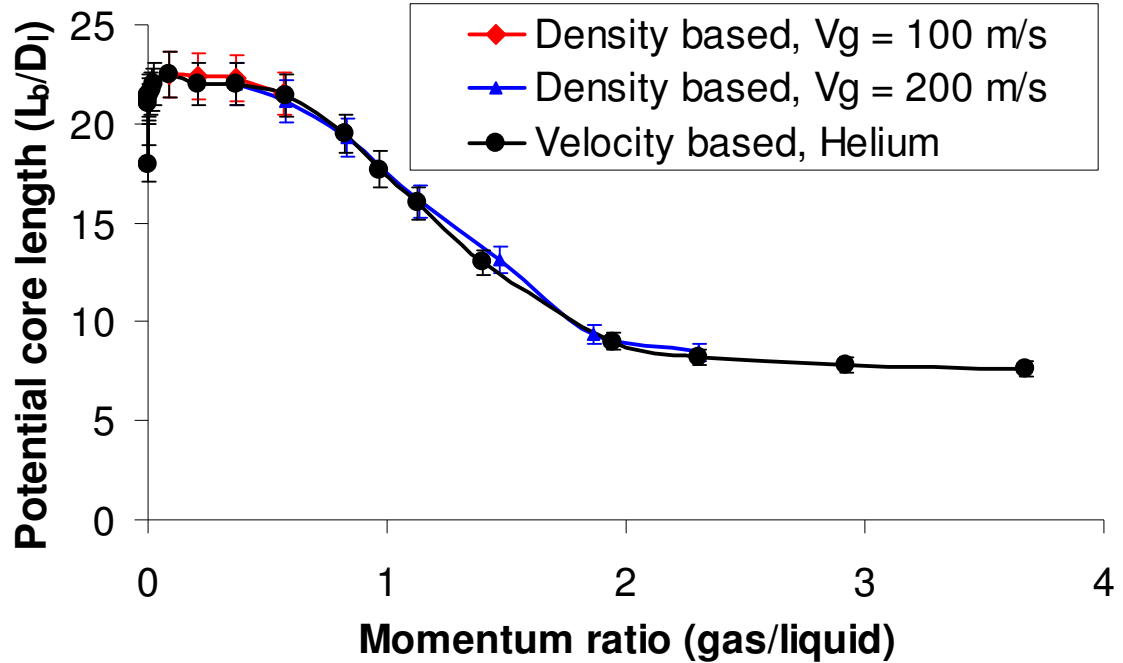
Figure 5.22. Variation of potential core length of LN$_2$ jet with momentum ratio between the jets (constant gas velocities)

5.3. Theoretical Analysis

Prior research has proved using dimensional analysis that normalized potential core length of two phase coaxial jets depends on several important parameters such as, velocity, density and area ratios between the jets along with aerodynamic Weber number and Reynolds number of the liquid jet (Equation 5.1).

$$L_b/D_l = f(V_{rel}/V_l,\ A_g/A_l,\ \rho_l/\rho_g,\ We_g,\ Re_l) \tag{5.1}$$

Other researchers further improved that analysis and showed that it is better to use the momentum ratio between jet and Ohnesorge number ($Oh = \mu_l/\sqrt{\rho_l \sigma_l D_l}$) instead of aerodynamic Weber number and Reynolds number of the liquid jet (Equation 5.2).

$$L_b/D_l = f(V_{rel}/V_l,\ \rho_l/\rho_g,\ A_g/A_l,\ M,\ Oh) \tag{5.2}$$

In order to develop a correlation for cryogenic jet in a coaxial gas stream, we first have to look at other correlations available in literature. Equation 5.3 shows Baron's correlation for water jet in quiescent air, which works extremely well for turbulent non-cryogenic jets in quiescent medium where $We_l = \rho_l V_l^2 D_l/\sigma$. However this correlation over predicts the potential core length of cryogenic fluid in quiescent medium.

$$L_b/D_l = 538 We_l^{0.5} Re_l^{-0.625} \qquad [5.3]$$

This is due to the fact that there is strong temperature gradient between the fluid and surroundings for cryogenic jets in a quiescent medium, so heat transfer and evaporation of the cryogenic jet is also important. Therefore it can be suggested that heat transfer number defined by $B_T = Cp_\infty(T_\infty - T_l)/L$, should also be considered while predicting the potential core length of cryogenic fluid in quiescent medium as shown in Equation 5.4. It has been proved in prior literature that steady-state evaporation of spherical droplets is proportional to $ln(1+B_T)$.

$$L_b/D_l = f(We_l, Re_l, B_T) \qquad [5.4]$$

So a simple modified correlation can be used for cryogenic fluid by including the effect of heat transfer coefficient, which is shown in Equation 5.5, where C_1 is the proportionality constant which can be calculated using experimental results. However the above proposed expression can be further refined by performing more detailed analysis and experiments.

$$L_b/D_l = C_1 We_l^{0.5} Re_l^{-0.625} ln(1+B_T) \qquad [5.5]$$

Due to their strong relevance in real life problems, a lot of correlations are available for two phase coaxial jets (both cryogenic and non-cryogenic). Woodward

(1994) (Equation 5.6) showed that for cryogenic simulants (Potassium Iodide in aqueous solution) potential core length is a function of liquid Reynolds number (Re_l), aerodynamic Weber number (We_g) and density ratio between the jets.

$$L_b/D_l \approx C(\rho_g/\rho_l)^{-0.36/Z} We_g^{0.22/Z} Re_l^{0.68} \qquad [5.6]$$

Rehab (1997) and Raynal (1997) showed that L_b/D_l for non- cryogenic coaxial jets is inversely proportional to V_{rel}/V_l and $M^{0.5}$, whereas Porcheron et al. (2002) (Equation 5.7) predicted that potential core of a cryogenic jet in a coaxial gas stream depends on density ratio, Ohnesorge number and momentum ratio between the jets. Although all these correlations work well for their respective set of conditions, they do not remain accurate for all range of conditions as shown in the figure. This is due to the fact that no one has yet looked at the effect of heat transfer at the potential core length of cryogenic fluid.

$$L_b/D_l \approx C(\rho_g/\rho_l)^{-0.38} Oh^{0.34} M^{-0.13} \qquad [5.7]$$

Based on the experimental results and prior correlations, it can be argued that the potential core length of cryogenic jet in a coaxial gaseous stream should be equal to the potential core length of the cryogenic jet in quiescent medium including the effect of co-flowing gas. Therefore one can say that, potential core length of a cryogenic jet in coaxial gas stream will be equal to the potential core length of cryogenic jet in quiescent medium including the effect of heat transfer and shear destabilization as shown in Equation 5.8.

$$L_b(coaxial\ jet)/D_l \approx (L_b(quiescent\ medium)/D_l)(1 + Heat\ Transfer + Shear\ destabilization) \qquad [5.8]$$

Prior research has shown that convective heat transfer is a function of Re_g and Pr_g whereas shear destabilization is a function of M and V_{rel}/V_l. Therefore we assumed that the final correlation for the prediction of potential core length of a cryogenic jet in coaxial gaseous stream should look like Equation 5.9 where C_1, C_2 and C_3 are experimental constants.

$$L_b/D_l \approx C_1 We_l^{0.5} Re_l^{-0.625} ln(1+B_T)\{1 + C_2(f_1(Re_g, Pr_g)) + C_3(f_2(M,V_{rel}/V_l)\} \qquad [5.9]$$

$$f_1(Re_g, Pr_g) \approx 0.01 Re_g^{0.8} Pr_g^{0.4} \qquad [5.10]$$

$$f_2(M,V_{rel}/V_l) \approx (1-exp(-0.42M^{2.5}))(1+0.0001 \left| V_{rel}/V_l \right|) \qquad [5.11]$$

$$L_b/D_l \approx 365 We_l^{0.5} Re_l^{-0.625} ln(1+B_T)\{1 + 0.25(f_1(Re_g, Pr_g)) - 0.82(f_2(M,V_{rel}/V_l)\} \qquad [5.12]$$

Equations 10, 11 and 12 are obtained after performing a curve fit to equation 9 with our experimental results. Figure 5.23 shows the normalized potential core length of LN_2 jet in coaxial gas stream w.r.t. to core length of LN_2 jet in quiescent air (Equation 5.13). One can see the individual effects of shear layer destabilization and heat transfer along with their combined effect.

$$(L_b/D_l)_n \approx 1 + 0.25(f_1(Re_g, Pr_g)) - 0.82(f_2(M,V_{rel}/V_l) \qquad [5.13]$$
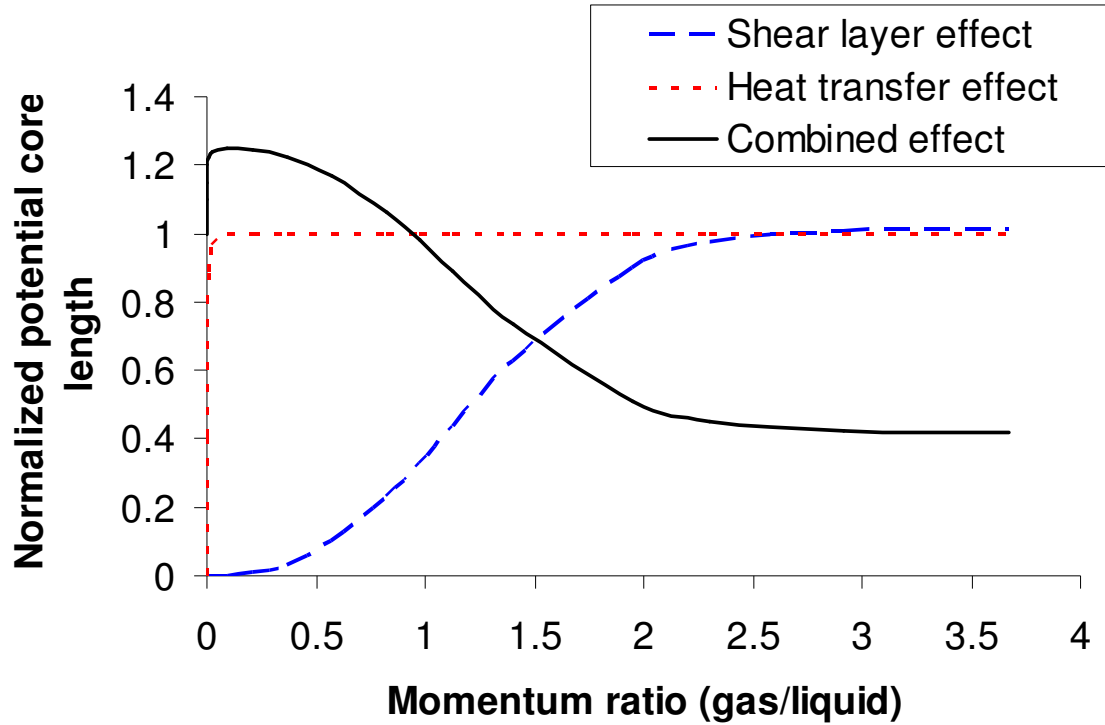
Figure 5.23. Normalized potential core length of LN$_2$ jet for different velocities of the coaxial gaseous jet

Figure 5.24 shows a comparison of experimental result with our correlation for experiments where density of the coaxial gas was kept constant while varying its velocity. The correlation shows a very good fit with the experimental data with root mean square error was less than 3%. Similarly Figure 5.25 shows the comparison between present correlation and experimental results for density cases where the gas density was varied while keeping its velocity constant. Even these experiments show very good agreement with our correlation and root mean square errors were less than 2% and 5% respectively.
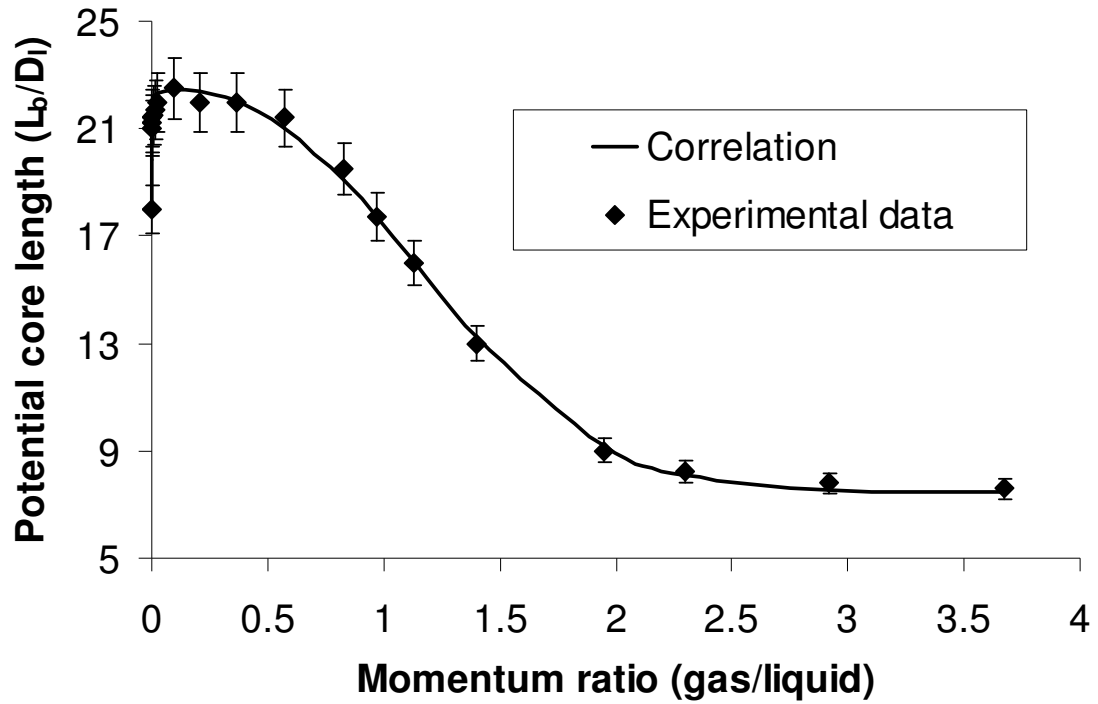
Figure 5.24. Comparison of experimental results with empirical correlation (constant gas density)
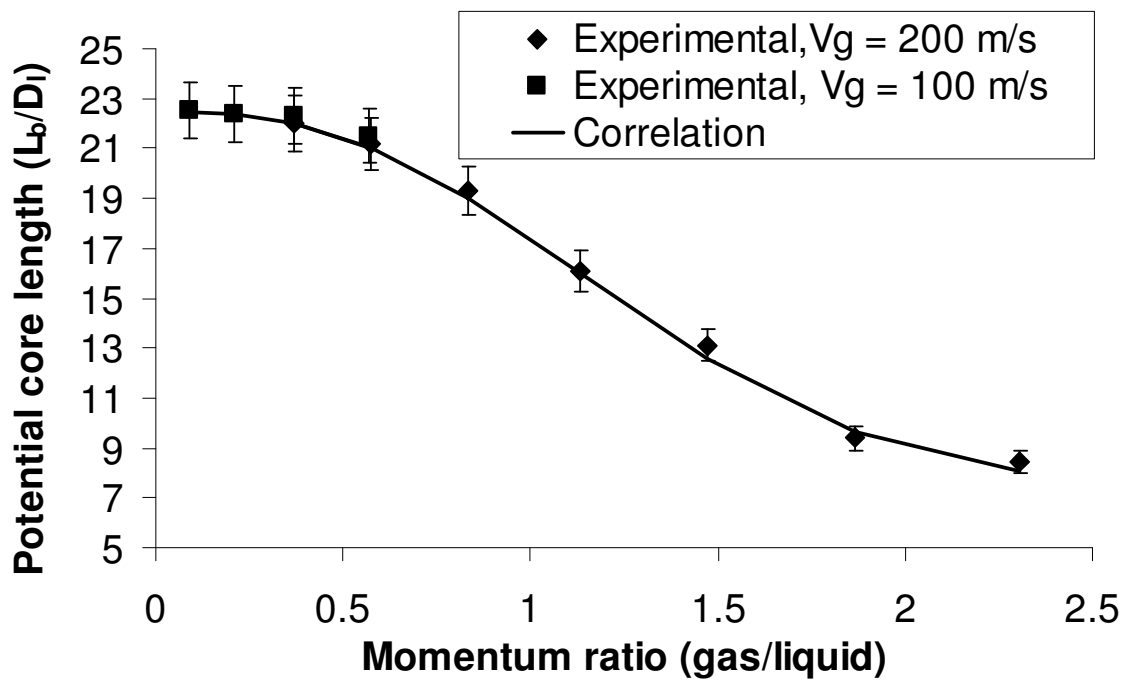
Figure 5.25. Comparison of experimental results with empirical correlation (constant gas velocities)

After performing all of the previous experiments at atmospheric pressure, the experimental setup was modified as explained in the experimental setup section to analyze the cryogenic flow and mixing behavior at below atmospheric pressures. These preliminary results were obtain to study the fuel-oxidizer mixing before startup under different environmental conditions such as those found at the moon-mars or during reentry of the vehicle into earth's atmosphere. Two specific experimental conditions are examined for these experiments as shown in Table 5.3. In the first case, the evolution of liquid nitrogen at an average, steady-state cryogenic fluid velocity of 5 m/s was examined. No gas was fed through the outer tube of the injector for the first case whereas for the second case, the evolution of liquid nitrogen jet was examined with steady coaxial helium jet at 300 m/s.

Liquid	Gas	Velocity (liquid/gas)	Density Ratio (gas/liquid)	Momentum Ratio (gas/liquid)	Mass Ratio (gas/liquid)
LN_2	—	5 / 0	—	0	—
LN_2	He	5 / 300	2.3E-04	0.83	1.4E-02

Table 5.3. Flow inlet conditions examined for the near vacuum experiments

Figure 5.26 shows the evolution of liquid nitrogen jet from the coaxial injector obtained using high-speed cinematography (Mie-scattering) imaging at 0.1 atm pressure. Time zero in these experiments corresponds to the very first trace of the cryogenic jet exiting the injector and the results are presented after the initial puff (0-100 ms) of liquid nitrogen as discussed in the transient atmospheric pressure results was over and injector walls were cold enough to sustain a continuous jet of LN_2 flow.

These images show the effect of lower pressure along with the heat transfer effect from the warm injector tubes. Initially (100 ms) the injector tubes are relatively warm so most of the liquid nitrogen jet emerges in gaseous form showing thin jet emerging from the injector exit. As the flow progresses, the injector walls gradually approach the cryogenic temperature of liquid nitrogen, the local vapor formation near the walls diminishes and the flow is dominated by the central liquid flow by approximately 500 ms. One can also notice the extraordinary expansion of liquid jet due to very low pressures inside the chamber. However the most crucial observation that can be obtained from these images is solidification of liquid nitrogen jet at this pressure as shown by emergence of solid particles in Figure 5.26d. The sudden expansion of liquid jet at 0.1 atm pressure causes some of the droplets and ligaments to freeze since the triple point of liquid nitrogen is 63.18 K and 0.125 atm. Figure 5.27 shows an approximate phase diagram of nitrogen showing the important features of nitrogen's three phase behavior.

(a) **(b)**

(c) **(d)**
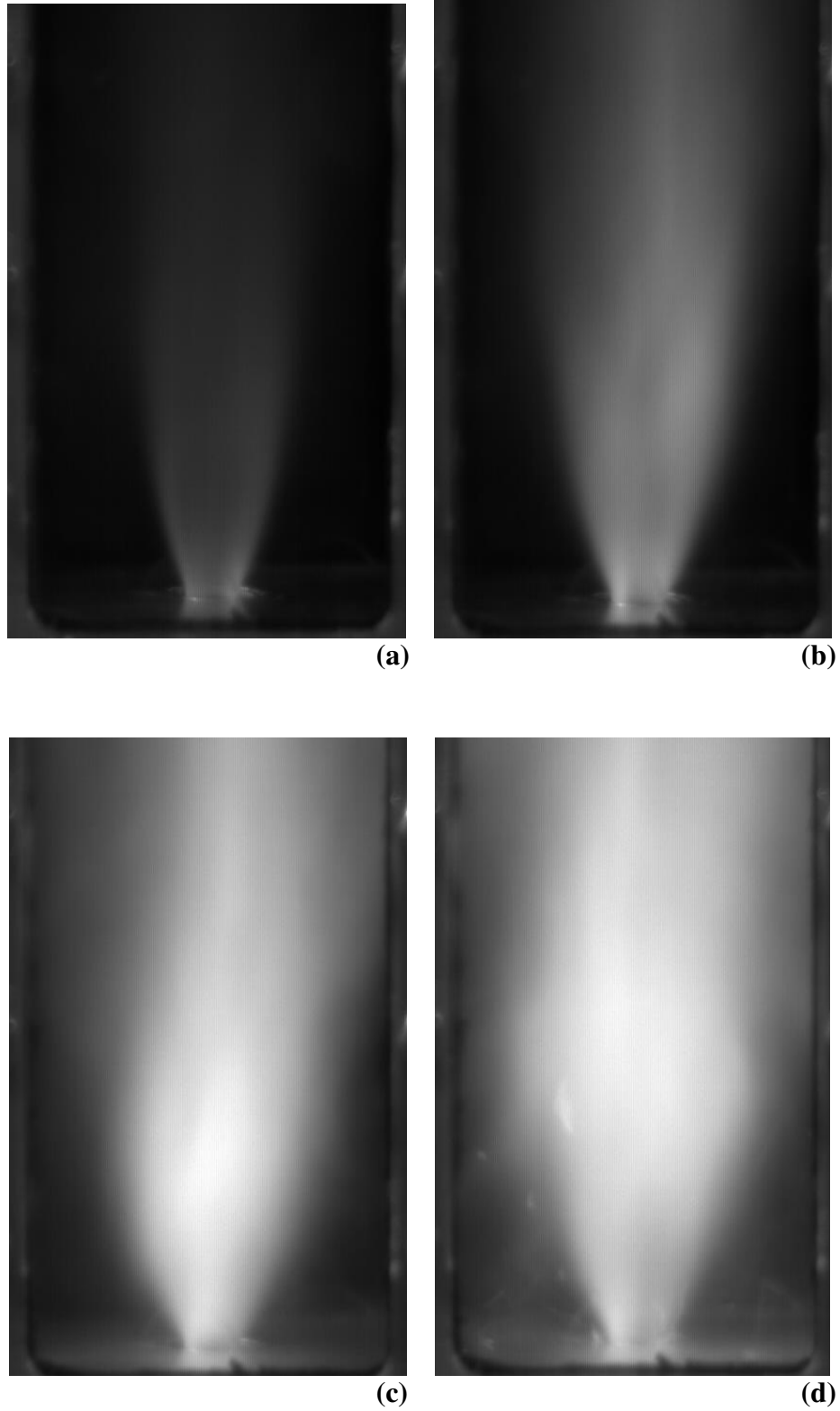
Figure 5.26. High-speed Mie Scattering image of LN$_2$ flow at 0.1 atm
a) t = 100 ms; b) t = 200 ms ; c) t = 300 ms; d) t = 500 ms
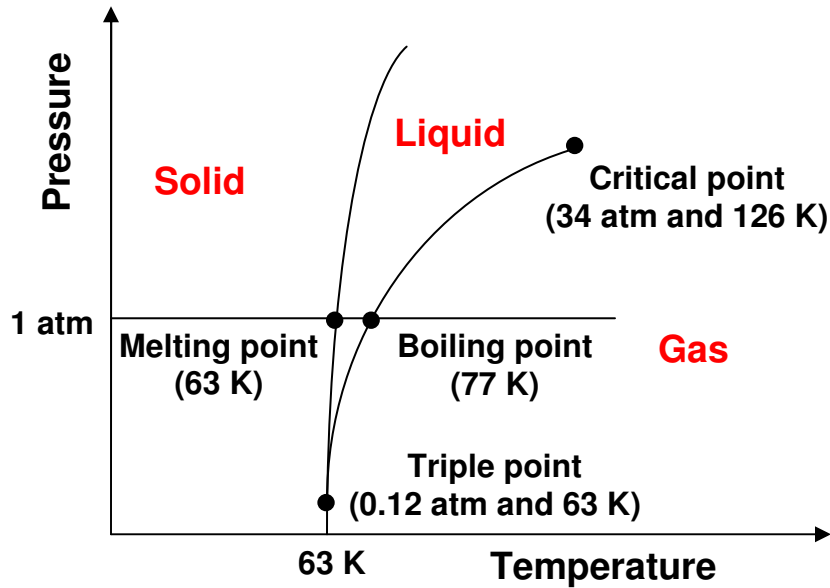
Figure 5.27. Approximate phase diagram of Nitrogen

In order to further confirm the Mie-scattering results we performed high speed Schlieren imaging on the same flow. Figure 5.28 shows the evolution of liquid nitrogen jet from a coaxial injector obtained using high-speed Schlieren imaging at 0.1 atm pressure. Since Schlieren shows density gradients inside the flow, the darker regions in these images correspond to high density or liquid phase where the lighter regions correspond to low density or gaseous phase. As one can see these images confirm the findings of Mie-scattering results. Initially when the injector tubes are warm, most of the liquid nitrogen jet emerges in gaseous form showing smaller darker regions near the injector exit. Once again as the flow progresses, the injector walls cool down to cryogenic temperature of liquid nitrogen and the flow is dominated by the central liquid flow or the dark regions. The extraordinary expansion of liquid jet due to very low pressures inside the chamber can also be seen. These results also confirmed the solidification of liquid nitrogen droplets and ligaments at this pressure as shown by emergence of solid particles in Figures 5.28c and 5.28d.

(a)

(b)

(c)

(d)
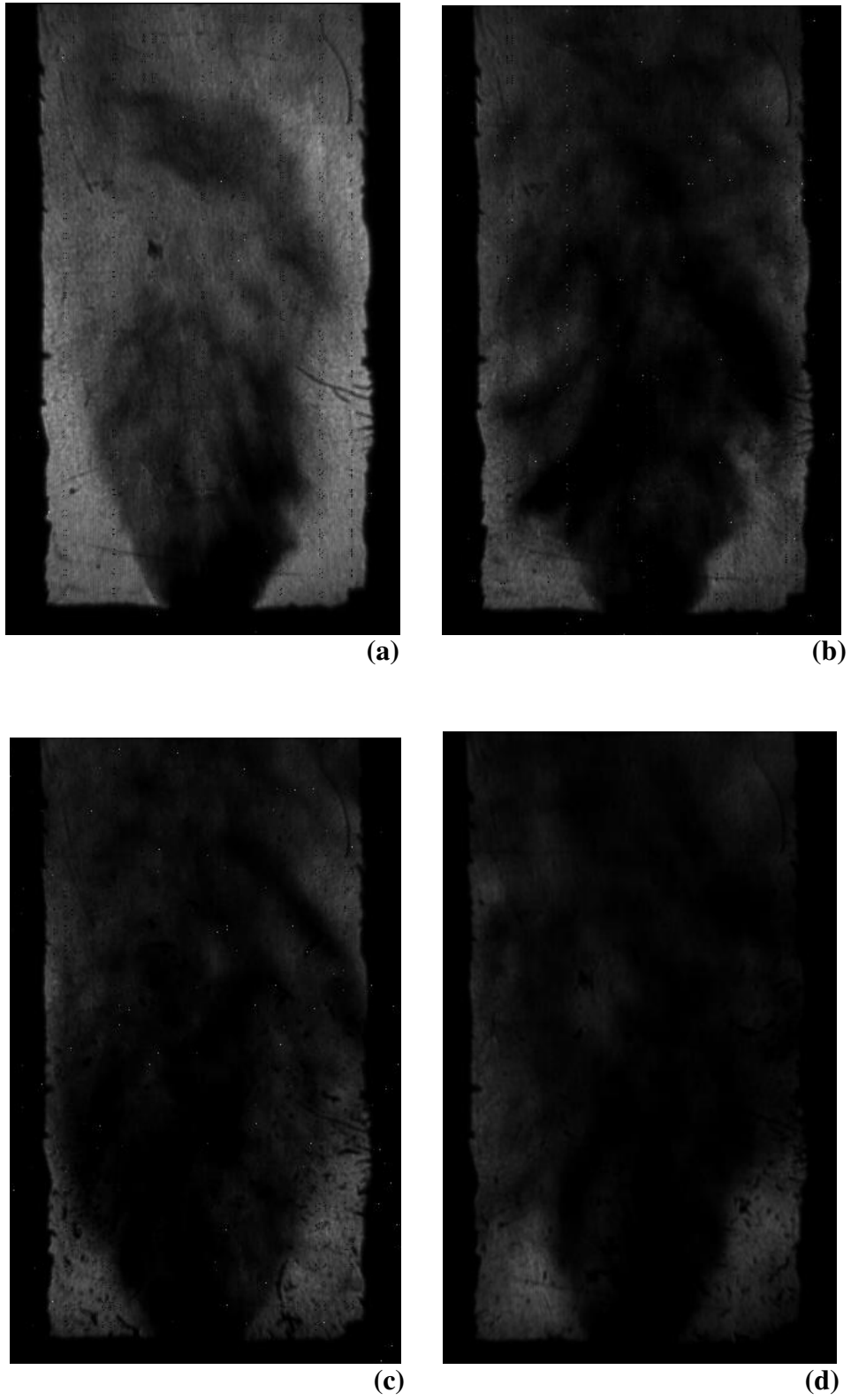
**Figure 5.28. High-speed Schlieren image of LN$_2$ flow at 0.1 atm
a) t = 100 ms; b) t = 200 ms ; c) t = 300 ms; d) t = 500 ms**

The effect of coaxial gaseous jet on the cryogenic flow evolution was also studied at 0.1 atm pressure. Figure 5.29 shows the evolution of liquid nitrogen jet in a steady coaxial helium jet at 300 m/s obtained using high-speed cinematography (Mie-scattering) imaging at 0.1 atm pressure. Even for this case time zero corresponds to the very first trace of the cryogenic jet exiting the injector and the results are presented after the initial puff (0-100 ms) of liquid nitrogen was over. These images again signify the important confining effect of coaxial gaseous jet on the central liquid nitrogen jet. As one can see the central core of the flow looks much brighter in the presence of coaxial jet. This is due to the heat shielding effect and flow confining effect of the coaxial gaseous jet. The coaxial jet prevented the expansion and evaporation of the liquid nitrogen jet in regions close to injector exit. However even for this case the flow looks much wider than the atmospheric pressure case which shows higher expansion of liquid jet due at very low pressures inside the chamber. The solidification of liquid nitrogen jet can also be seen by emergence of solid particles in Figure 5.29d.
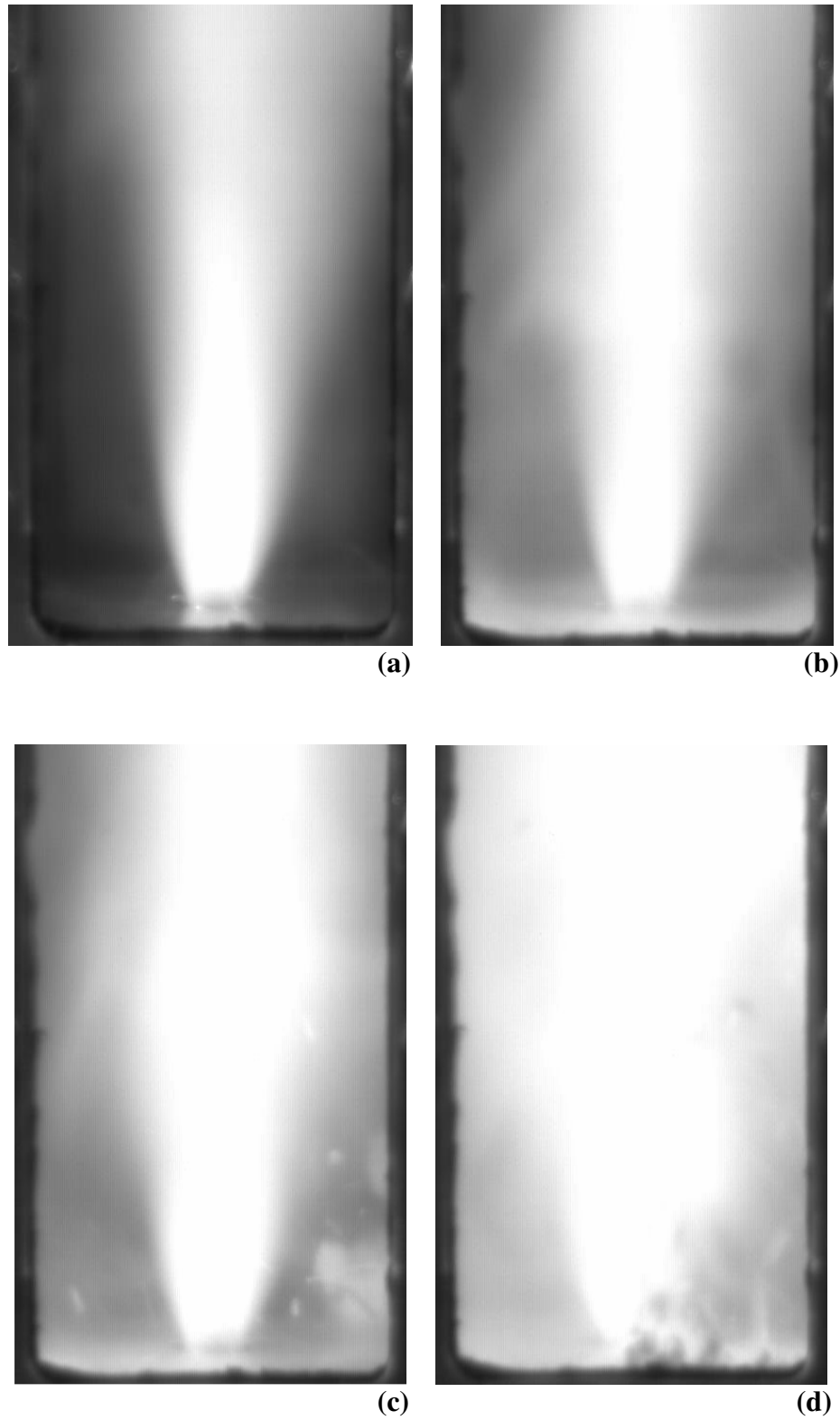
**Figure 5.29. High-speed Mie Scattering image of LN₂/He flow at 0.1 atm
a) t = 100 ms; b) t = 200 ms ; c) t = 300 ms; d) t = 500 ms**

Figure 5.30 shows the evolution of liquid nitrogen jet in a steady coaxial helium jet at 300 m/s obtained using high-speed Schlieren imaging at 0.1 atm pressure. Once again the results confirmed the findings of Mie-scattering results. The darker regions of the flow appeared to be less wide than the previous case confirming the confining and shielding effect of coaxial gaseous jet. For this case, one can also see the formation of vortical structures due to shearing action of the gaseous jet and the solidification of liquid nitrogen droplets and ligaments at this pressure is also clearly visible. Therefore, the preliminary experiments performed at near vacuum conditions showed the dramatic change in flow behavior of the cryogenic jet thus underlining the importance of pressure variation for in-space operations. Further experiments and detailed analysis is required to study the physics of this problem in details and to examine the startup characteristics of cryogenic rocket engines under in-space conditions.

(a)   **(b)**

(c)   **(d)**
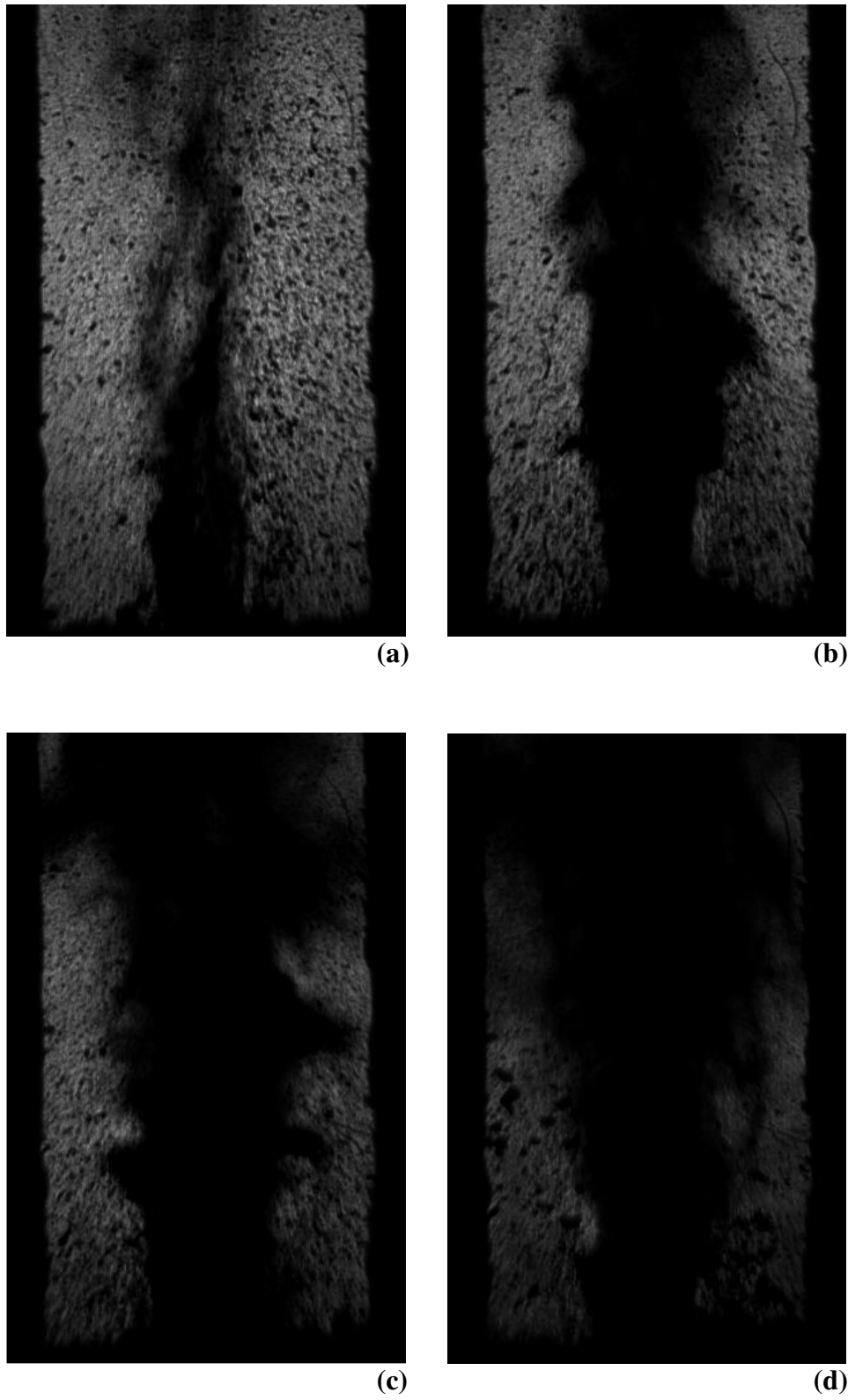
**Figure 5.30. High-speed Schlieren image of LN$_2$/He flow at 0.1 atm
a) t = 100 ms; b) t = 200 ms ; c) t = 300 ms; d) t = 500 ms**

110

6. Conclusions and Recommendations for Future Work

6.1. Conclusions

A simple method has been presented to determine the actual flow rate of cryogenic fluids using a turbine flow meter with good accuracy. The difference in measured and calculated average flow velocities (and hence flow rates) at steady-state was less than 10% for several different test runs. This reduced the measurement errors due to cryogenic fluid property variations, chugging instabilities and non-ideal nature. This method allowed us to alleviate the large errors associated with measurement of cryogenic fluids, thus improving our confidence in experimental work with cryogenic fluids.

The transient behavior showing the detailed features on the evolutionary characteristics of both the cryogenic liquid and gaseous phases evolving from the shear coaxial injector has been examined for the first time. Upon initial emergence, the flows were found to form distinct vortical structures depending on the inlet and surrounding conditions. Kelvin-Helmholtz instabilities appear to play a significant role in destabilizing interfaces between phases in the flows and ultimately developing the vortical structures observed. The complex 3-dimensional flow structures observed clearly revealed the onset of unsteady behavior from the injector exit during initial startup, which may contribute to instabilities in rocket engines.

The effects of some of the most important flow parameters, such as, velocity, density, and momentum ratios on the primary atomization of a steady-state cryogenic jet emerging from a single-element coaxial rocket injector have been analyzed at atmospheric pressure conditions. Furthermore, the impact of non-dimensional

numbers such as, Reynolds number, Prandtl number and aerodynamic Weber number on the flow have been examined to analyze the effect of the major physical processes, such as, shear layer destabilization and heat transfer on the potential core length of cryogenic jet surrounded with a coaxial gaseous stream. The flow conditions examined are characteristic of the rocket engine operating conditions at lift-off prior to ignition to provide a simple analogy and simulation of the flow and mixing behaviors from single-element injectors under relevant rocket engine conditions.

The shear angle measurements of the steady-state flow showed the trans-critical nature of the cryogenic fluid along with its cooling effect on surrounding gases. The measured shear angles matched very closely with the prior results and confirmed the effects of surrounding gas density on cryogenic jet expansion as predicted by previous researchers. Furthermore, detailed analysis of the results showed that the flow of coaxial helium reduced the shear angle as well as the entrainment of surrounding air into the coaxial gaseous flow.

The potential core length of the cryogenic fluid in quiescent medium was shorter than that of non-cryogenic fluid (water) and increased initially with the introduction of coaxial gas flow. It showed a local peak at approximately 100 m/s when plotted as a function of velocity of the gaseous jet. In contrast to the present results, previous research has suggested that the potential core length of the liquid jet should decrease absolutely with the increase in velocity of the gaseous jet, because this increases the momentum ratio between the jets. These suggestions are undoubtedly accurate, if the liquid jet is a subcritical isothermal fluid (e.g., water). The unique behavior of LN_2 jet is, however, due to the heat transfer effects of the surroundings on the cryogenic LN_2

jet. The results therefore provided a strong evidence of the heat transfer effect of the coaxial gaseous jet. The heat transfer from the surroundings to the cold LN_2 jet varies significantly with the Reynolds number of the gaseous jet, which strongly affects the potential core length of the LN_2 jet. The laminar jet of gaseous helium acts as a thermal insulation for the cold LN_2 jet, whereas this effect diminishes as the gaseous jet becomes turbulent and eventually dies out at very high Reynolds number. The effect of shear layer destabilization was found to be negligible for momentum ratios less than one ($M << 1$). Shear layer destabilization starts increasing at momentum ratios close to one ($M \sim 1$) and become significant for momentum ratios greater than one ($M > 1$).

The potential core length showed similar trends when measurements were performed at variable coaxial gas density but at constant gas velocity of 100 m/s. The potential core lengths were again longer than the potential core length of LN_2 jet in quiescent air and did not change much with the change in coaxial gas density for momentum ratios less than one ($M < 1$). This again confirmed the heat shielding effect of the coaxial gaseous jet for lower gas Reynolds number and negligible effect of shear layer destabilization for lower gas/liquid momentum ratios. However, the potential core lengths decreased exponentially with increase in momentum ratio for values close to 1 ($M \sim 1$) and above as shown by measurements performed at variable coaxial gas density but at constant velocity of 200 m/s. Therefore, the results clearly revealed a key effect of heat transfer from the surroundings on the potential core length of the cryogenic LN_2 jet from a shear coaxial injector. To the author's knowledge, this has not been reported in previous works. The effect of momentum

ratio was found to be pronounced as well but only close to a value of $M = 1$ and above.

Some of the prior correlations used for prediction of potential core length of cryogenic jet in a coaxial gaseous stream have been analyzed and compared with the present results. It was showed that the present results do not match with the predicted potential core length of non-cryogenic jet (water). In contrast they showed good agreement with the predicted core length of cryogenic jet at higher gas velocities (and also momentum ratio) between the jets. Also the prior correlations were only valid for a limited range of conditions since the experimental data were only available for a limited range of conditions. An improved semi-empirical correlation based on non-dimensional parameters has been proposed to predict the potential core length of cryogenic jet in a coaxial gaseous stream. The proposed correlation works well under all ranges of conditions investigated and the authors assume that this correlation would act as a guideline for all the further theoretical and experimental work on shear coaxial injectors for cryogenic rocket injectors.

Preliminary experiments performed at near vacuum conditions (0.1 atmospheres) showed a dramatic change in flow behavior of the cryogenic jet under these conditions thus underlining the importance of pressure variation for in-space operations (such as mixing, ignition, stability). The cryogenic jet undergoes extraordinary expansion due to very low pressures inside the chamber with directly observed initial freezing of liquid nitrogen droplets and ligaments. The introduction of coaxial jet showed its shielding effect even at low pressures.

A combination of experimental work and dimensional analysis has allowed us to examine the detailed primary atomization behavior of a cryogenic jet under simulated rocket engine operating conditions. The results from this research provide insightful information on the flow and mixing behavior of cryogenic jet flowing concentrically in a surrounding coaxial gaseous stream. These results will help in the development and validation of advanced computational models under non-reacting flow conditions.

6.2. Recommendations for Future Work

Even though the current research has provided new insights into the flow and atomization behavior of cryogenic fluid from a shear coaxial injector, there are still several issues that need to be addressed in order to fully understand the physical processes associated with coaxial injection of cryogenic fluids and predict the performance rocket injectors under all relevant conditions. Some of the important future research issues identified are given below:

1) One of the reasons why it is hard to analyze the flow behavior of cryogenic fluids is their property variations due to phase change. Present research only used LN_2 at a fixed flowrate to analyze the flow and atomization behavior in the presence of coaxial gaseous jet. However, in order to understand the complete injector physics associated with the problem, it is recommended to vary the type of cryogenic fluid and examine at different flowrates to determine the effect of variable fluid properties in details. This would also help in understanding the evaporation behavior of cryogenic jet and eventually it will be useful to examine the realistic and normally used LOX and hydrogen in the injector.

2) The effect of pressures requires examination since real rocket injectors mostly operates at pressures that are much higher than atmospheric, extending from sub-critical to supercritical range of the cryogenic fluids. During start-up the chamber pressure is initially low but it transitions to very high pressures as the flow stabilizes and combustion starts. Although some of the prior research given in the literature review have looked at the effect of chamber pressure in details, our knowledge of real injector physics associated with the problem still requires further examination.

3) In real rocket injectors, generally the temperature of cryogenic fluid does not vary much during the injection process but the gas temperature varies a lot due to the unsteady heat transfer from the combustion chamber to the incoming fuel flow. During startup or ignition the gaseous fuel temperature is very low (~ 30 K), but as the combustion starts the heat transfer from the combustion chamber enhances to cause increase in the fuel (gaseous hydrogen) temperature before it gets injected into the combustion chamber. This variation in fuel flow temperature impacts the density and other physical properties of the jet to change both the thermodynamic and hydrodynamic behavior of the injected propellants and has not been examined in previous works. Hence, the performance prediction of cryogenic rocket injectors requires detailed understanding of the temperature change of the gaseous flow and surroundings.

4) Present research and most of the prior works have used single element injector to examine the flow and atomization behavior of propellants in order to

116

predict the injector performance. However, the actual rocket injectors are not single element but multi-element, as shown in Figure 1.1. Therefore it is very important to examine the injector-injector and injector-wall interactions in order to fully understand the realistic rocket injector performance.

5) The main emphasis of this research and all of the prior researches has always been to eventually predict the ignition and combustion behavior of realistic cryogenic rocket engines. There have been some prior works in this area but reliable ignition and stable combustion of cryogenic rocket engine is still one of the biggest challenges. Therefore, the research on cryogenic rocket injectors would never be complete without reacting flow experiments under realistic conditions. So it is recommended to perform similar kind of detailed analysis for reacting LOX/H_2 flow for understanding the real physics of the problem and improving the reliability of rocket injectors by avoiding failures due to improper ignition or unstable combustion.

Appendix A: Matlab Codes used for Data Analysis

A.1. Edge Detection

```
function [eout,thresh] = edge(varargin)
%EDGE Find edges in intensity image.
%   EDGE takes an intensity or a binary image I as its input, and returns a
%   binary image BW of the same size as I, with 1's where the function
%   finds edges in I and 0's elsewhere.
%
%   EDGE supports six different edge-finding methods:
%
%       The Sobel method finds edges using the Sobel approximation to the
%       derivative. It returns edges at those points where the gradient of
%       I is maximum.
%
%       The Prewitt method finds edges using the Prewitt approximation to
%       the derivative. It returns edges at those points where the gradient
%       of I is maximum.
%
%       The Roberts method finds edges using the Roberts approximation to
%       the derivative. It returns edges at those points where the gradient
%       of I is maximum.
%
%       The Laplacian of Gaussian method finds edges by looking for zero
%       crossings after filtering I with a Laplacian of Gaussian filter.
%
%       The zero-cross method finds edges by looking for zero crossings
%       after filtering I with a filter you specify.
%
%       The Canny method finds edges by looking for local maxima of the
%       gradient of I. The gradient is calculated using the derivative of a
%       Gaussian filter. The method uses two thresholds, to detect strong
%       and weak edges, and includes the weak edges in the output only if
%       they are connected to strong edges. This method is therefore less
%       likely than the others to be "fooled" by noise, and more likely to
%       detect true weak edges.
%
%   The parameters you can supply differ depending on the method you
%   specify. If you do not specify a method, EDGE uses the Sobel method.
%
%   Sobel Method
%   ------------
%   BW = EDGE(I,'sobel') specifies the Sobel method.
%
%   BW = EDGE(I,'sobel',THRESH) specifies the sensitivity threshold for
```

```
%   the Sobel method. EDGE ignores all edges that are not stronger than
%   THRESH.  If you do not specify THRESH, or if THRESH is empty ([]),
%   EDGE chooses the value automatically.
%
%   BW = EDGE(I,'sobel',THRESH,DIRECTION) specifies directionality for the
%   Sobel method. DIRECTION is a string specifying whether to look for
%   'horizontal' or 'vertical' edges, or 'both' (the default).
%
%   [BW,thresh] = EDGE(I,'sobel',...) returns the threshold value.
%
%   Prewitt Method
%   --------------
%   BW = EDGE(I,'prewitt') specifies the Prewitt method.
%
%   BW = EDGE(I,'prewitt',THRESH) specifies the sensitivity threshold for
%   the Prewitt method. EDGE ignores all edges that are not stronger than
%   THRESH. If you do not specify THRESH, or if THRESH is empty ([]),
%   EDGE chooses the value automatically.
%
%   BW = EDGE(I,'prewitt',THRESH,DIRECTION) specifies directionality for
%   the Prewitt method. DIRECTION is a string specifying whether to look
%   for 'horizontal' or 'vertical' edges, or 'both' (the default).
%
%   [BW,thresh] = EDGE(I,'prewitt',...) returns the threshold value.
%
%   Roberts Method
%   --------------
%   BW = EDGE(I,'roberts') specifies the Roberts method.
%
%   BW = EDGE(I,'roberts',THRESH) specifies the sensitivity threshold for
%   the Roberts method. EDGE ignores all edges that are not stronger than
%   THRESH. If you do not specify THRESH, or if THRESH is empty ([]),
%   EDGE chooses the value automatically.
%
%   [BW,thresh] = EDGE(I,'roberts',...) returns the threshold value.
%
%   Laplacian of Gaussian Method
%   ----------------------------
%   BW = EDGE(I,'log') specifies the Laplacian of Gaussian method.
%
%   BW = EDGE(I,'log',THRESH) specifies the sensitivity threshold for the
%   Laplacian of Gaussian method. EDGE ignores all edges that are not
%   stronger than THRESH. If you do not specify THRESH, or if THRESH is
%   empty ([]), EDGE chooses the value automatically.
%
%   BW = EDGE(I,'log',THRESH,SIGMA) specifies the Laplacian of Gaussian
```

%   method, using SIGMA as the standard deviation of the LoG filter. The
%   default SIGMA is 2; the size of the filter is N-by-N, where
%   N=CEIL(SIGMA*3)*2+1.
%
%   [BW,thresh] = EDGE(I,'log',...) returns the threshold value.
%
%   Zero-cross Method
%   -----------------
%   BW = EDGE(I,'zerocross',THRESH,H) specifies the zero-cross method,
%   using the specified filter H. If THRESH is empty ([]), EDGE chooses
%   the sensitivity threshold automatically.
%
%   [BW,THRESH] = EDGE(I,'zerocross',...) returns the threshold value.
%
%   Canny Method
%   ---------------------------
%   BW = EDGE(I,'canny') specifies the Canny method.
%
%   BW = EDGE(I,'canny',THRESH) specifies sensitivity thresholds for the
%   Canny method. THRESH is a two-element vector in which the first element
%   is the low threshold, and the second element is the high threshold. If
%   you specify a scalar for THRESH, this value is used for the high
%   threshold and 0.4*THRESH is used for the low threshold. If you do not
%   specify THRESH, or if THRESH is empty ([]), EDGE chooses low and high
%   values automatically.
%
%   BW = EDGE(I,'canny',THRESH,SIGMA) specifies the Canny method, using
%   SIGMA as the standard deviation of the Gaussian filter. The default
%   SIGMA is 1; the size of the filter is chosen automatically, based
%   on SIGMA.
%
%   [BW,thresh] = EDGE(I,'canny',...) returns the threshold values as a
%   two-element vector.
%
%   Class Support
%   -------------
%   I can be of class uint8, uint16, or double. BW is of class uint8.
%
%   Remarks
%   -------
%   For the 'log' and 'zerocross' methods, if you specify a
%   threshold of 0, the output image has closed contours, because
%   it includes all of the zero crossings in the input image.
%
%   Example
%   -------

```
%   Find the edges of the rice.tif image using the Prewitt and Canny
%   methods:
%
%       I = imread('rice.tif');
%       BW1 = edge(I,'prewitt');
%       BW2 = edge(I,'canny');
%       imshow(BW1)
%       figure, imshow(BW2)
%
%   See also FSPECIAL.

%   OBSOLETE syntax
%   --------------------
%   BW = EDGE(... ,K) allows the specification of a directionality
%   factor, K.  This only works for the 'sobel', 'prewitt', and
%   'roberts' methods.   K must be a 1-by-2 vector, K = [kx ky].
%   For Sobel and Prewitt, K=[1 0] looks for vertical edges,
%   K=[0 1] looks for horizontal edges, and K=[1 1], the default,
%   looks for non-directional edges.   For the Roberts edge detector,
%   K=[1 0] looks for 135 degree diagonal edges, K=[0 1] looks
%   for 45 degree diagonal edges, and K=[1 1], the default, looks
%   for non-directional edges.
%
%   Copyright 1993-2002 The MathWorks, Inc.
%   $Revision: 5.26 $  $Date: 2002/03/26 16:39:10 $

[a,method,thresh,sigma,H,kx,ky] = parse_inputs(varargin{:});

% Transform to a double precision intensity image if necessary
if ~isa(a, 'double')
  a = im2double(a);
end

m = size(a,1);
n = size(a,2);
rr = 2:m-1; cc=2:n-1;

% The output edge map:
e = repmat(false, m, n);

if strcmp(method,'canny')
  % Magic numbers
  GaussianDieOff = .0001;
  PercentOfPixelsNotEdges = .7; % Used for selecting thresholds
  ThresholdRatio = .4;        % Low thresh is this fraction of the high.
```

```
% Design the filters - a gaussian and its derivative

pw = 1:30; % possible widths
ssq = sigma*sigma;
width = max(find(exp(-(pw.*pw)/(2*sigma*sigma))>GaussianDieOff));
if isempty(width)
  width = 1;  % the user entered a really small sigma
end

t = (-width:width);
gau = exp(-(t.*t)/(2*ssq))/(2*pi*ssq);     % the gaussian 1D filter

% Find the directional derivative of 2D Gaussian (along X-axis)
% Since the result is symmetric along X, we can get the derivative along
% Y-axis simply by transposing the result for X direction.
[x,y]=meshgrid(-width:width,-width:width);
dgau2D=-x.*exp(-(x.*x+y.*y)/(2*ssq))/(pi*ssq);

% Convolve the filters with the image in each direction
% The canny edge detector first requires convolution with
% 2D gaussian, and then with the derivitave of a gaussian.
% Since gaussian filter is separable, for smoothing, we can use
% two 1D convolutions in order to achieve the effect of convolving
% with 2D Gaussian.  We convolve along rows and then columns.

%smooth the image out
aSmooth=imfilter(a,gau,'conv','replicate');       % run the filter accross rows
aSmooth=imfilter(aSmooth,gau','conv','replicate'); % and then accross columns

%apply directional derivatives
ax = imfilter(aSmooth, dgau2D, 'conv','replicate');
ay = imfilter(aSmooth, dgau2D', 'conv','replicate');

mag = sqrt((ax.*ax) + (ay.*ay));
magmax = max(mag(:));
if magmax>0
  mag = mag / magmax;   % normalize
end

% Select the thresholds
if isempty(thresh)
  [counts,x]=imhist(mag, 64);
  highThresh = min(find(cumsum(counts) > PercentOfPixelsNotEdges*m*n)) / 64;
  lowThresh = ThresholdRatio*highThresh;
  thresh = [lowThresh highThresh];
elseif length(thresh)==1
```

```
    highThresh = thresh;
    if thresh>=1
      error('The threshold must be less than 1.');
    end
    lowThresh = ThresholdRatio*thresh;
    thresh = [lowThresh highThresh];
  elseif length(thresh)==2
    lowThresh = thresh(1);
    highThresh = thresh(2);
    if (lowThresh >= highThresh) | (highThresh >= 1)
      error('Thresh must be [low high], where low < high < 1.');
    end
  end

  % The next step is to do the non-maximum supression.
  % We will accrue indices which specify ON pixels in strong edgemap
  % The array e will become the weak edge map.
  idxStrong = [];
  for dir = 1:4
    idxLocalMax = cannyFindLocalMaxima(dir,ax,ay,mag);
    idxWeak = idxLocalMax(mag(idxLocalMax) > lowThresh);
    e(idxWeak)=1;
    idxStrong = [idxStrong; idxWeak(mag(idxWeak) > highThresh)];
  end

  rstrong = rem(idxStrong-1, m)+1;
  cstrong = floor((idxStrong-1)/m)+1;
  e = bwselect(e, cstrong, rstrong, 8);
  e = bwmorph(e, 'thin', 1);  % Thin double (or triple) pixel wide contours

elseif any(strcmp(method, {'log','marr-hildreth','zerocross'}))
  % We don't use image blocks here
  if isempty(H),
    fsize = ceil(sigma*3) * 2 + 1;  % choose an odd fsize > 6*sigma;
    op = fspecial('log',fsize,sigma);
  else
    op = H;
  end

  op = op - sum(op(:))/prod(size(op)); % make the op to sum to zero
  b = filter2(op,a);

  if isempty(thresh)
    thresh = .75*mean2(abs(b(rr,cc)));
  end
```

```
% Look for the zero crossings:  +-, -+ and their transposes
% We arbitrarily choose the edge to be the negative point
[rx,cx] = find( b(rr,cc) < 0 & b(rr,cc+1) > 0 ...
    & abs( b(rr,cc)-b(rr,cc+1) ) > thresh );   % [- +]
e((rx+1) + cx*m) = 1;
[rx,cx] = find( b(rr,cc-1) > 0 & b(rr,cc) < 0 ...
    & abs( b(rr,cc-1)-b(rr,cc) ) > thresh );   % [+ -]
e((rx+1) + cx*m) = 1;
[rx,cx] = find( b(rr,cc) < 0 & b(rr+1,cc) > 0 ...
    & abs( b(rr,cc)-b(rr+1,cc) ) > thresh);   % [- +]'
e((rx+1) + cx*m) = 1;
[rx,cx] = find( b(rr-1,cc) > 0 & b(rr,cc) < 0 ...
    & abs( b(rr-1,cc)-b(rr,cc) ) > thresh);   % [+ -]'
e((rx+1) + cx*m) = 1;

% Most likely this covers all of the cases.   Just check to see if there
% are any points where the LoG was precisely zero:
[rz,cz] = find( b(rr,cc)==0 );
if ~isempty(rz)
  % Look for the zero crossings: +0-, -0+ and their transposes
  % The edge lies on the Zero point
  zero = (rz+1) + cz*m;   % Linear index for zero points
  zz = find(b(zero-1) < 0 & b(zero+1) > 0 ...
    & abs( b(zero-1)-b(zero+1) ) > 2*thresh);     % [- 0 +]'
  e(zero(zz)) = 1;
  zz = find(b(zero-1) > 0 & b(zero+1) < 0 ...
    & abs( b(zero-1)-b(zero+1) ) > 2*thresh);     % [+ 0 -]'
  e(zero(zz)) = 1;
  zz = find(b(zero-m) < 0 & b(zero+m) > 0 ...
    & abs( b(zero-m)-b(zero+m) ) > 2*thresh);     % [- 0 +]
  e(zero(zz)) = 1;
  zz = find(b(zero-m) > 0 & b(zero+m) < 0 ...
    & abs( b(zero-m)-b(zero+m) ) > 2*thresh);     % [+ 0 -]
  e(zero(zz)) = 1;
end

else  % one of the easy methods (roberts,sobel,prewitt)

  % Determine edges in blocks for easy methods
  nr = length(rr); nc = length(cc);

  blk = bestblk([nr nc]);
  nblks = floor([nr nc]./blk); nrem = [nr nc] - nblks.*blk;
  mblocks = nblks(1); nblocks = nblks(2);
  mb = blk(1); nb = blk(2);
```

124

```
if strcmp(method,'sobel')
   op = [-1 -2 -1;0 0 0;1 2 1]/8; % Sobel approximation to derivative
   bx = abs(filter2(op',a)); by = abs(filter2(op,a));
   b = kx*bx.*bx + ky*by.*by;
   if isempty(thresh), % Determine cutoff based on RMS estimate of noise
      cutoff = 4*sum(sum(b(rr,cc)))/prod(size(b(rr,cc))); thresh = sqrt(cutoff);
   else            % Use relative tolerance specified by the user
      cutoff = (thresh).^2;
   end
   rows = 1:blk(1);
   for i=0:mblocks,
      if i==mblocks, rows = (1:nrem(1)); end
      for j=0:nblocks,
         if j==0, cols = 1:blk(2); elseif j==nblocks, cols=(1:nrem(2)); end
         if ~isempty(rows) & ~isempty(cols)
            r = rr(i*mb+rows); c = cc(j*nb+cols);
            e(r,c) = (b(r,c)>cutoff) & ...
            ( ( (bx(r,c) >= (kx*by(r,c)-eps*100)) & ...
            (b(r,c-1) <= b(r,c)) & (b(r,c) > b(r,c+1)) ) | ...
            ( (by(r,c) >= (ky*bx(r,c)-eps*100 )) & ...
            (b(r-1,c) <= b(r,c)) & (b(r,c) > b(r+1,c))));
         end
      end
   end

elseif strcmp(method,'prewitt')
   op = [-1 -1 -1;0 0 0;1 1 1]/6; % Prewitt approximation to derivative
   bx = abs(filter2(op',a)); by = abs(filter2(op,a));
   b = kx*bx.*bx + ky*by.*by;
   if isempty(thresh), % Determine cutoff based on RMS estimate of noise
      cutoff = 4*sum(sum(b(rr,cc)))/prod(size(b(rr,cc))); thresh = sqrt(cutoff);
   else            % Use relative tolerance specified by the user
      cutoff = (thresh).^2;
   end
   rows = 1:blk(1);
   for i=0:mblocks,
      if i==mblocks, rows = (1:nrem(1)); end
      for j=0:nblocks,
         if j==0, cols = 1:blk(2); elseif j==nblocks, cols=(1:nrem(2)); end
         if ~isempty(rows) & ~isempty(cols)
            r = rr(i*mb+rows); c = cc(j*nb+cols);
            e(r,c) = (b(r,c)>cutoff) & ...
            ( ( (bx(r,c) >= (kx*by(r,c)-eps*100) ) & ...
            (b(r,c-1) <= b(r,c)) & (b(r,c) > b(r,c+1)) ) | ...
            ((by(r,c) >= (ky*bx(r,c)-eps*100) )  & ...
            (b(r-1,c) <= b(r,c)) & (b(r,c) > b(r+1,c)) ) );
```

```
              end
            end
          end

      elseif strcmp(method, 'roberts')
          op = [1 0;0 -1]/sqrt(2); % Roberts approximation to diagonal derivative
          bx = abs(filter2(op,a)); by = abs(filter2(rot90(op),a));
          b = kx*bx.*bx + ky*by.*by;
          if isempty(thresh), % Determine cutoff based on RMS estimate of noise
              cutoff = 6*sum(sum(b(rr,cc)))/prod(size(b(rr,cc))); thresh = sqrt(cutoff);
          else               % Use relative tolerance specified by the user
              cutoff = (thresh).^2;
          end
          rows = 1:blk(1);
          for i=0:mblocks,
              if i==mblocks, rows = (1:nrem(1)); end
              for j=0:nblocks,
                  if j==0, cols = 1:blk(2); elseif j==nblocks, cols=(1:nrem(2)); end
                  if ~isempty(rows) & ~isempty(cols)
                      r = rr(i*mb+rows); c = cc(j*nb+cols);
                      e(r,c) = (b(r,c)>cutoff) & ...
                      ( ( (bx(r,c) >= (kx*by(r,c)-eps*100)) & ...
                      (b(r-1,c-1) <= b(r,c)) & (b(r,c) > b(r+1,c+1)) ) | ...
                      ( (by(r,c) >= (ky*bx(r,c)-eps*100)) & ...
                      (b(r-1,c+1) <= b(r,c)) & (b(r,c) > b(r+1,c-1)) ) );
                  end
              end
          end
      else
          error([method,' is not a valid method.']);
      end
end

if nargout==0,
    imshow(e);
else
    eout = e;
end


%%%%%%%%%%%%%%%%%%%%%%%%%%%%%%%%%%%%%%%%%%%%%%
%%%%%%%%%%%%%%%%%%%%%
%
%   Local Function : cannyFindLocalMaxima
%
function idxLocalMax = cannyFindLocalMaxima(direction,ix,iy,mag);
```

```
%
% This sub-function helps with the non-maximum supression in the Canny
% edge detector.  The input parameters are:
%
%   direction - the index of which direction the gradient is pointing,
%           read from the diagram below. direction is 1, 2, 3, or 4.
%   ix      - input image filtered by derivative of gaussian along x
%   iy      - input image filtered by derivative of gaussian along y
%   mag     - the gradient magnitude image
%
%    there are 4 cases:
%
%                    The X marks the pixel in question, and each
%        3    2        of the quadrants for the gradient vector
%      O----0----0      fall into two cases, divided by the 45
%      4 |       | 1    degree line.  In one case the gradient
%        |       |      vector is more horizontal, and in the other
%      O    X    O      it is more vertical.  There are eight
%        |       |      divisions, but for the non-maximum supression
%      (1)|      |(4)   we are only worried about 4 of them since we
%      O----O----O       use symmetric points about the center pixel.
%       (2)  (3)


[m,n,o] = size(mag);

% Find the indices of all points whose gradient (specified by the
% vector (ix,iy)) is going in the direction we're looking at.

switch direction
case 1
  idx = find((iy<=0 & ix>-iy)  | (iy>=0 & ix<-iy));
case 2
  idx = find((ix>0 & -iy>=ix)  | (ix<0 & -iy<=ix));
case 3
  idx = find((ix<=0 & ix>iy) | (ix>=0 & ix<iy));
case 4
  idx = find((iy<0 & ix<=iy) | (iy>0 & ix>=iy));
end

% Exclude the exterior pixels
if ~isempty(idx)
  v = mod(idx,m);
  extIdx = find(v==1 | v==0 | idx<=m | (idx>(n-1)*m));
  idx(extIdx) = [];
end
```

```matlab
ixv = ix(idx);
iyv = iy(idx);
gradmag = mag(idx);

% Do the linear interpolations for the interior pixels
switch direction
case 1
  d = abs(iyv./ixv);
  gradmag1 = mag(idx+m).*(1-d) + mag(idx+m-1).*d;
  gradmag2 = mag(idx-m).*(1-d) + mag(idx-m+1).*d;
case 2
  d = abs(ixv./iyv);
  gradmag1 = mag(idx-1).*(1-d) + mag(idx+m-1).*d;
  gradmag2 = mag(idx+1).*(1-d) + mag(idx-m+1).*d;
case 3
  d = abs(ixv./iyv);
  gradmag1 = mag(idx-1).*(1-d) + mag(idx-m-1).*d;
  gradmag2 = mag(idx+1).*(1-d) + mag(idx+m+1).*d;
case 4
  d = abs(iyv./ixv);
  gradmag1 = mag(idx-m).*(1-d) + mag(idx-m-1).*d;
  gradmag2 = mag(idx+m).*(1-d) + mag(idx+m+1).*d;
end
idxLocalMax = idx(gradmag>=gradmag1 & gradmag>=gradmag2);




%%%%%%%%%%%%%%%%%%%%%%%%%%%%%%%%%%%%%%%%
%%%%%%%%%%%%%%%%%%%%%
%
%   Local Function : parse_inputs
%
function [I,Method,Thresh,Sigma,H,kx,ky] = parse_inputs(varargin)
% OUTPUTS:
%  I     Image Data
%  Method Edge detection method
%  Thresh Threshold value
%  Sigma  standard deviation of Gaussian
%  H     Filter for Zero-crossing detection
%  kx,ky  From Directionality vector

error(nargchk(1,5,nargin));

I = varargin{1};
```

```
checkinput(I,{'double','logical','uint8','uint16'},...
        {'nonsparse'},mfilename,'I',1);

% Defaults
Method='sobel';
Thresh=[];
Direction='both';
Sigma=2;
H=[];
K=[1 1];

methods = {'canny','prewitt','sobel','marr-hildreth','log','roberts','zerocross'};
directions = {'both','horizontal','vertical'};

% Now parse the nargin-1 remaining input arguments

% First get the strings - we do this because the intepretation of the
% rest of the arguments will depend on the method.
nonstr = [];   % ordered indices of non-string arguments
for i = 2:nargin
  if ischar(varargin{i})
    str = lower(varargin{i});
    j = strmatch(str,methods);
    k = strmatch(str,directions);
    if ~isempty(j)
      Method = methods{j(1)};
      if strcmp(Method,'marr-hildreth')
        warning('"Marr-Hildreth" is an obsolete syntax, use "LoG" instead.');
      end
    elseif ~isempty(k)
      Direction = directions{k(1)};
    else
      error(['Invalid input string: ''' varargin{i} '''.']);
    end
  else
    nonstr = [nonstr i];
  end
end

% Now get the rest of the arguments

switch Method

case {'prewitt','sobel','roberts'}
  threshSpecified = 0;  % Threshold is not yet specified
  for i = nonstr
```

```
    if prod(size(varargin{i}))<=1 & ~threshSpecified % Scalar or empty
      Thresh = varargin{i};
      threshSpecified = 1;
    elseif prod(size(varargin{i}))==2  % The dreaded K vector
      warning(['BW = EDGE(... , K) is an obsolete syntax. '...
        'Use BW = EDGE(... , DIRECTION), where DIRECTION is a string.']);
      K=varargin{i};
    else
      error('Invalid input arguments');
    end
  end

case 'canny'
  Sigma = 1.0;        % Default Std dev of gaussian for canny
  threshSpecified = 0;  % Threshold is not yet specified
  for i = nonstr
    if prod(size(varargin{i}))==2 & ~threshSpecified
      Thresh = varargin{i};
      threshSpecified = 1;
    elseif prod(size(varargin{i}))==1
      if ~threshSpecified
        Thresh = varargin{i};
        threshSpecified = 1;
      else
        Sigma = varargin{i};
      end
    elseif isempty(varargin{i}) & ~threshSpecified
      % Thresh = [];
      threshSpecified = 1;
    else
      error('Invalid input arguments');
    end
  end

case 'log'
  threshSpecified = 0;  % Threshold is not yet specified
  for i = nonstr
    if prod(size(varargin{i}))<=1  % Scalar or empty
      if ~threshSpecified
        Thresh = varargin{i};
        threshSpecified = 1;
      else
        Sigma = varargin{i};
      end
    else
      error('Invalid input arguments');
```

```matlab
      end
    end

case 'zerocross'
    threshSpecified = 0;  % Threshold is not yet specified
    for i = nonstr
      if prod(size(varargin{i}))<=1 & ~threshSpecified % Scalar or empty
        Thresh = varargin{i};
        threshSpecified = 1;
      elseif prod(size(varargin{i})) > 1 % The filter for zerocross
        H = varargin{i};
      else
        error('Invalid input arguments');
      end
    end

case 'marr-hildreth'
    for i = nonstr
      if prod(size(varargin{i}))<=1  % Scalar or empty
        Thresh = varargin{i};
      elseif prod(size(varargin{i}))==2  % The dreaded K vector
        warning('The [kx ky] direction factor has no effect for "Marr-Hildreth".');
      elseif prod(size(varargin{i})) > 2 % The filter for zerocross
        H = varargin{i};
      else
        error('Invalid input arguments');
      end
    end

otherwise
    error('Invalid input arguments');
end

if Sigma<=0
    error('Sigma must be positive');
end

switch Direction
case 'both',
    kx = K(1); ky = K(2);
case 'horizontal',
    kx = 0; ky = 1; % Directionality factor
case 'vertical',
    kx = 1; ky = 0; % Directionality factor
otherwise
    error('Unrecognized direction string');
```

```
end


if isrgb(I)
   error('RGB images are not supported. Call RGB2GRAY first.');
end
```

A.2. Averaged Centerline Intensity

```
clear all
sum1 = 0;
num = 150;
for i = 1:9
i1 = num2str(i);
filename = ['C:\Documents and Settings\Administrator\My
Documents\Rocket_combustor\schlieren_data\08_26_06\Images\LN2_He_300\LN2_
He_300_a_00000',i1];
A = imread(filename,'jpeg');
A = double(A);
sum1 = A + sum1;
end
sum2 = sum1;
for i = 10:99
i1 = num2str(i);
filename = ['C:\Documents and Settings\Administrator\My
Documents\Rocket_combustor\schlieren_data\08_26_06\Images\LN2_He_300\LN2_
He_300_a_0000',i1];
A = imread(filename,'jpeg');
A = double(A);
sum2 = A + sum2;
end
sum3 = sum2;
for i = 100:num
i1 = num2str(i);
filename = ['C:\Documents and Settings\Administrator\My
Documents\Rocket_combustor\schlieren_data\08_26_06\Images\LN2_He_300\LN2_
He_300_a_000',i1];
A = imread(filename,'jpeg');
A = double(A);
sum3 = A + sum3;
end
sum = sum3;
avg = sum/(num);
figure
imagesc(avg)
image size = avg(92:922,81:920), center will be 496, 0.5 inch = 69 pixels,
```

```
cen_a = flipud(avg(92:903,496));
%****************************************************************
**********************************
sum1 = 0;
num = 150;
for i = 1:9
i1 = num2str(i);
filename = ['C:\Documents and Settings\Administrator\My
Documents\Rocket_combustor\schlieren_data\08_26_06\Images\LN2_He_300\LN2_
He_300_b_00000',i1];
A = imread(filename,'jpeg');
A = double(A);
sum1 = A + sum1;
end
sum2 = sum1;
for i = 10:99
i1 = num2str(i);
filename = ['C:\Documents and Settings\Administrator\My
Documents\Rocket_combustor\schlieren_data\08_26_06\Images\LN2_He_300\LN2_
He_300_b_0000',i1];
A = imread(filename,'jpeg');
A = double(A);
sum2 = A + sum2;
end
sum3 = sum2;
for i = 100:num
i1 = num2str(i);
filename = ['C:\Documents and Settings\Administrator\My
Documents\Rocket_combustor\schlieren_data\08_26_06\Images\LN2_He_300\LN2_
He_300_b_000',i1];
A = imread(filename,'jpeg');
A = double(A);
sum3 = A + sum3;
end
sum = sum3;
avg = sum/(num);
figure
imagesc(avg)
cen_b = flipud(avg(466:853,496));
%****************************************************************
**********************************
cen_flow = [cen_a
   cen_b]
filter = 10;
for i = 1:1200/filter
cen_flow_mean(i) = mean(cen_flow((i-1)*filter+1:filter*i));
```

```
end
figure
x = 6*1200/(60*830*0.33):6*1200/(60*830*0.33):6*1200/(830*0.33);
plot(x,cen_flow_mean,'r');
xlabel('Axial Distance (x/D)')
ylabel('Centerline Intensity')
hold on
colormap gray
```

A.3. Averaged Radial Intensity and Shear Angle

```
clear all
sum1 = 0;
num = 150;
for i = 1:9
i1 = num2str(i);
filename = ['C:\Documents and Settings\Administrator\My
Documents\Rocket_combustor\schlieren_data\09_12_06\Images\LN2_He_40\LN2_H
e_40_a_00000',i1];
A = imread(filename,'jpeg');
A = double(A);
sum1 = A + sum1;
end
sum2 = sum1;
for i = 10:99
i1 = num2str(i);
filename = ['C:\Documents and Settings\Administrator\My
Documents\Rocket_combustor\schlieren_data\09_12_06\Images\LN2_He_40\LN2_H
e_40_a_0000',i1];
A = imread(filename,'jpeg');
A = double(A);
sum2 = A + sum2;
end
sum3 = sum2;
for i = 100:num
i1 = num2str(i);
filename = ['C:\Documents and Settings\Administrator\My
Documents\Rocket_combustor\schlieren_data\09_12_06\Images\LN2_He_40\LN2_H
e_40_a_000',i1];
A = imread(filename,'jpeg');
A = double(A);
sum3 = A + sum3;
end
sum = sum3;
avg = sum/(num);
```

```
nrows = [avg(200,300:700)' avg(300,300:700)' avg(400,300:700)' avg(500,300:700)'
avg(600,300:700)' avg(700,300:700)' avg(800,300:700)'];
figure
imagesc(avg)
for j = 700:-100:300
        for i = 350:500
                if avg(j,i) <= 120
                rstart = i;
                break
        end
end
for i = 650:-1:500
        if avg(j,i)  <= 120
        rend = i;
        break
        end
end
spray_width = (rend-rstart)*6.0/839;
spray_length = (920-j)*6.0/830;
r0 = 0.33/2;
rs = spray_width/2;
ls = spray_length + r0*spray_length/(rs-r0);
spray_angle = 2*(180/pi)*atan(rs/ls)
end
sum1 = 0;
num = 150;
for i = 1:9
i1 = num2str(i);
filename = ['C:\Documents and Settings\Administrator\My
Documents\Rocket_combustor\schlieren_data\09_12_06\Images\LN2_He_40\LN2_H
e_40_b_00000',i1];
A = imread(filename,'jpeg');
A = double(A);
sum1 = A + sum1;
end
sum2 = sum1;
for i = 10:99
i1 = num2str(i);
filename = ['C:\Documents and Settings\Administrator\My
Documents\Rocket_combustor\schlieren_data\09_12_06\Images\LN2_He_40\LN2_H
e_40_b_0000',i1];
A = imread(filename,'jpeg');
A = double(A);
sum2 = A + sum2;
end
sum3 = sum2;
```

```
for i = 100:num
i1 = num2str(i);
filename = ['C:\Documents and Settings\Administrator\My
Documents\Rocket_combustor\schlieren_data\09_12_06\Images\LN2_He_40\LN2_H
e_40_b_000',i1];
A = imread(filename,'jpeg');
A = double(A);
sum3 = A + sum3;
end
sum = sum3;
avg = sum/(num);
nrows = [nrows avg(600,300:700)' avg(700,300:700)' avg(800,300:700)'];
xlswrite(nrows,'LN2_He_40',{'200','300','400','500','600','700','800','600b','700b','800
b'},'LN2_He_40.xls')
figure
imagesc(avg)
for j = 700:-100:600
        for i = 350:500
                if avg(j,i) <= 120
                rstart = i;
                break
                end
        end
for i = 650:-1:500
        if avg(j,i)  <= 150
        rend = i;
        break
        end
end
spray_width = (rend-rstart)*6.0/839;
spray_length = 5.5 + (920-j)*6.0/830;
r0 = 0.33/2;
rs = spray_width/2;
ls = spray_length + r0*spray_length/(rs-r0);
spray_angle = 2*(180/pi)*atan(rs/ls)
end
```

Appendix B: List of Publications

B.1 Journal Publications

• Gautam, V. and Gupta, A. K., "Simulation of Flow and Mixing from a Cryogenic Rocket Injector", Journal of Propulsion and Power, Jan-Feb 2007, pp 123-130.

• Gautam, V. and Gupta, A. K., "Cryogenic Flow and Atomization from a Coaxial Injector", Accepted for Publication in Journal of Propulsion and Power, 2007.

• Gautam, V. and Gupta, A. K., "Observation of Unsteady Cryogenic Flows from a Coaxial Rocket Injector", Accepted for Publication in Journal of Propulsion and Power, 2007.

B.2 Publications in Conference Proceedings

• Gautam, V. and Gupta, A. K.: Spectroscopic Analysis of Fuel Lean Flames for Propulsion Applications, ASME Power Conference 2004, Baltimore, Maryland, PWR 2004-52074.

• Gautam, V. and Gupta, A. K., "Thermal Field Analysis of Hydrocarbon Flames for Propulsion Applications", 43rd Aerospace Sciences Meeting and Exhibits, Reno, Nevada, Jan. 10 - 13, 2005, Paper No. AIAA 2005-1445.

• Gautam, V. and Gupta A. K., "Simulation of Mixing in Rocket Engine Injectors under In-Space Conditions", 41st AIAA/ASME/SAE/ASEE Joint Propulsion Conference, Tucson, Arizona, July 10 - 13, 2005, AIAA-2005-3571.

• Gautam, V. and Gupta A. K., "Simulation of Flow, Mixing and Ignition of a Rocket Injector", 44th Aerospace Sciences Meeting and Exhibits, Reno, Nevada, Jan. 09 - 12, 2006, Paper No. AIAA 2006-1160.

• Gautam, V. and Gupta A. K., "Propellant Mixing in a Cryogenic Rocket Engine Under Transient Conditions", 42nd AIAA/ASME/SAE/ASEE Joint Propulsion Conference, Sacramento, California, July 09 - 12, 2006, Paper No. AIAA-2006-4529.

• Gautam, V. and Gupta A. K., "Cryogenic Flow Instability and Mixing from a Coaxial Rocket Injector", 45th Aerospace Sciences Meeting and Exhibits, Reno, Nevada, Jan. 08 - 11, 2007, Paper No. AIAA-2007-0573.

• Gautam, V. and Gupta A. K., "Characterization of Cryogenic Flow and Atomization from a Coaxial Rocket Injector", 43rd AIAA/ASME/SAE/ASEE Joint Propulsion Conference, Cincinnati, Ohio, July 08 - 11, 2007, Paper No. AIAA-2008-5567.

• Gautam, V. and Gupta A. K., "Cryogenic Liquid Jet Atomization from a Shear Coaxial Injector", Accepted in 46th Aerospace Sciences Meeting and Exhibits, Reno, Nevada, Jan. 07 - 10, 2008, Paper No. AIAA-2008-1044.

• Gautam, V. and Gupta A. K., "Cryogenic Flow from a Coaxial Rocket Injector under Low Pressure In-Space Propulsion Conditions", Accepted in 46th Aerospace Sciences Meeting and Exhibits, Reno, Nevada, Jan. 07 - 10, 2008, Paper No. AIAA-2008-1047.

Appendix C: Some of the Relevant Papers

Simulation of Flow and Mixing from a Cryogenic Rocket Injector

V. Gautam[1] and A. K. Gupta[2]

Mechanical Engineering Department, University of Maryland, College Park, MD 20742

The effects of confinement, momentum ratio and recess on the global flow and mixing characteristics of a cryogenic LN_2 stream surrounded by a coaxial gaseous jet from a simulated rocket injector are presented. High speed cinematography was used to examine the dynamic behavior of the LN_2 jet, while IR thermal imaging was used to demonstrate the cooling effect from the LN_2 jet on the surrounding gases and entrained air moisture. Furthermore, high speed Schlieren imaging was used to examine the effect of momentum ratio on the destabilization of LN_2 jet prior to its breakup and eventual mixing with the surrounding gases.

The experimental results showed that the LN_2 jet disperses into ligaments and droplets prior to its vaporization. For the confined conditions, the LN_2 core persists over longer distances downstream of the injector exit before full vaporization. Confinement also reduces the entrainment of the surrounding air as well as the transfer of heat from the surroundings. The LN_2 jet was found to expand earlier and reduced destabilization and mixedness with the surrounding gases with increase in momentum ratios of the coaxial jets. Changing the recess length in the injector had a negligible effect on the LN_2 jet close to the injector exit. However, at downstream

---

[1] Graduate Student, Student Member AIAA
[2] Professor, Fellow AIAA

139

locations the recess length provided significant affect on the jet expansion and entrainment of surrounding air.

The effect of momentum ratio was also examined quantitatively using the particle image velocimetry (PIV) diagnostics but using gas/gas (i.e., single phase) conditions. The results showed the effect of the momentum ratio of the two coaxial gas flows on the subsequent flow field development and mixing.

I. Introduction

HIGH thrust-to-weight ratio and consistent performance over a range of operating conditions make cryogenic rocket engines one of the best options for space propulsion. However, the scope of space missions is becoming more demanding, and so are the requirements of rocket engine performance. In order to help improve the performance of current rocket engine combustors, several key issues need to be considered. The objective of this paper is to analyze some of the key issues related to the fuel-oxidizer flow field and mixing in cryogenic rocket engine injectors at atmospheric pressures, so that the results can be used to simulate the conditions prior to ignition and combustion.

Injector performance is one of the most important issues related to the development of a new generation of rocket engines because of its strong impact on the rocket engine performance and reliability. The development of an optimum injector for a rocket engine requires multiple considerations, such as, efficient fuel-oxidizer mixing, quick ignition, combustion stability, thermal compatibility, size, weight, losses, and ease of manufacturing. Among these factors, one of the most critical is efficient fuel-oxidizer mixing, because it directly impacts the other important factors. In case of cryogenic propellants, efficient mixing becomes even more critical due to the simultaneous presence of liquid and gaseous phases inside the chamber. The liquid jet is required to destabilize, disintegrate and evaporate quickly in order to achieve good mixing prior to ignition and combustion. The destabilization of liquid jet in a two phase coaxial flow takes place because of several complex physical processes, such as, development of shear layer from the velocity gradient, turbulent interactions and vorticity produced by boundary layer, and interaction between inertial, surface tension and viscous forces. Since it is still very difficult to accurately study the combined effects of all parameters analytically or numerically, due to their complex interdependencies and the large

140

uncertainties associated with each parameter, experimental techniques are considered more reliable and accurate to determine the mixing behavior and injector performance.[1,2,3,4,5]

Cryogenic rocket injectors can be classified into several categories based on their configuration. The most common classification is impinging vs. non-impinging. In case of an impinging injector, mixing takes place by direct impingement of the fuel and oxidizer streams, which are aligned at an acute angle to each other. A non-impinging injector, on the other hand, takes the form of a coaxial element where the fuel and oxidizer streams flow in parallel. In this case, mixing takes place through the development of a shear layer. Coaxial injectors are often preferred to other injector designs because of their simpler design, lower pressure losses, and better combustion stability. The inner flow in a coaxial injector is generally liquid (LOX), while the outer one is gaseous (GH_2). Table 1 shows some typical operating conditions for a characteristic coaxial liquid rocket injector.[3,4,5]

Table 1. Some typical operating conditions for characteristic coaxial rocket engine injectors

Propellant	Typical Velocities (m/s)	Velocity Ratio	Momentum Ratio	Mixture Ratio
LOX/GH_2	(20 – 40) / (200 – 400)	0.1 – 0.05	5 – 10	5 – 10

Although much research has been conducted lately on cryogenic propellant injection to improve the understanding of the fuel-oxidizer mixing and combustion processes inside rocket engines, our understanding of the mixing and ignition is still primitive. Pal et al.[6] studied the size and distribution of the LOX droplets under reacting conditions and investigated the droplet behavior under non-reacting conditions, as well, with water as a stimulant. Vingert et al.[7] studied the high pressure injection and mixing processes of cryogenic propellants under non-reacting conditions using LN_2 as stimulant for LOX. Meyer et al.[8-11] studied the mixing and combustion processes of cryogenic propellants experimentally under sub- and super-critical conditions using optical diagnostic techniques. They observed the vaporization, mixing and combustion phenomena of the propellants at high chamber pressures of up to 10 MPa. They also analyzed the high-pressure injection and mixing processes of cryogenic propellants under non-reacting conditions using LN_2 and gaseous helium (He) as simulants. Candel et al.[12-13] studied the sub- and trans-critical combustion of cryogenic propellants using laser

diagnostic techniques. In a more recent study, Oschwald et al.[14] investigated the effect of chamber pressure, initial jet temperature and acoustic waves on the atomization, mixing and combustion phenomena of LOX/H_2 coaxial rocket injectors. They also compared their work with some of the previous research conducted on this topic. However, in spite of these numerous research efforts, the atomization, evaporation, mixing, and ignition behavior of cryogenic propellants under all operating conditions, i.e. from below atmospheric to super atmospheric conditions, is still relatively unpredictable.

In general, the flowfield from a typical coaxial injector can be divided into three different zones. The first zone, located close to the injector exit, is known as the initial merged zone. In this zone both the inner liquid core and the outer gaseous one are present with very little or almost no interaction between one another. The expansion of the jets is also very little in this zone. The second or intermediate merged zone is the zone where the inner liquid core starts breaking into large ligament-like structures that vaporize quickly. Shear layer development and primary mixing between the inner and outer flows take place in this zone; thus it is considered a very important zone from the ignition point of view. The third and final zone, also known as the fully merged zone, is characterized by complete breakup of the inner liquid core into smaller ligaments and droplets that vaporize and expand very rapidly. In this zone the flow is fully developed, and secondary mixing between the two fluids takes place. Thus, this zone is considered important to achieve high combustion efficiency and intensity, which results in compact combustor size.[14, 15]

The shapes and sizes of the above discussed mixing zones depend on several parameters, such as, the physical and chemical characteristics of the propellants, the velocity ratio between the inner and outer jets, the inlet temperature of the propellants, the geometry of the injector exit, the ambient temperature and pressure inside the mixing chamber, and the momentum flux ratio between the jets. Gautam and Gupta,[15] Strakey et al.,[16] Villermaux et al.,[17,18] and Lasheras et al.[19] showed that the momentum flux ratio (defined as $MR = \sqrt{\rho_1 v_1^2 / \rho_2 v_2^2}$) is one of the key parameters for single-phase or two-phase coaxial-jet mixing. They also showed that the length of the inner potential core, as well as the shapes and sizes of the various zones, is significantly affected by the momentum flux ratio.

Since cryogenic rocket propellants have extremely distinct flow characteristics compared to gaseous propellants, it is necessary to implement new experimental designs and techniques to quantify the flow behavior and mixing performance. High speed cinematography, Schlieren imaging, infrared thermal imaging, and particle image velocimetry (PIV) have been used in this work to examine the flow and mixing characteristics of a single coaxial injector and simulate the characteristic rocket injector performance prior to ignition. The experimental results obtained here assist in better understanding of the flow behavior and mixing from rocket engine injectors. Besides, the results obtained can also be used to validate numerical models under non-reacting flow conditions.

II. Experimental setup and conditions

The test rig consists of a coaxial injector and a downstream mixing chamber of square cross-section, as shown in Fig. 1. The injector has an adjustable recess length, The inner tube diameter of the injector is $D = 0.33$ inches with a wall thickness of 0.02 inches. The inner diameter of the outer tube is 0.5 inches. The mixing chamber has a side length of 1 inch and a height of 13 inches. Gaseous N_2, helium (He) or CO_2 are supplied through the outer annulus of the injector while LN_2 flows through the inner tube. In this study, LN_2 was used to simulate LOX because LN_2 is chemically inert, easy and safe to install for laboratory testing, and environmentally benign. Table 2 shows some of the physical properties of LN_2 and LOX. It can be seen that the values of the boiling temperature, viscosity and surface tension are close; thus the liquid breakup into ligaments and droplets will be similar for both fluids. The experimental test matrix of the flow conditions examined here is given in Table 3.

Table 2 Some physical properties of LOX and LN$_2$

Fluid	Density	Boiling Point	Surface Tension	Viscosity
LOX	1141 kg/m^3	-183 °C [90K]	0.0132 N/m	0.000197 Pa*s
LN$_2$	808 kg/m^3	-196 °C [77K]	0.0089 N/m	0.000163 Pa*s

143

Table 3 Test matrix of the examined flow conditions

Case #	Inner flow (liquid)	Outer flow (gaseous)	Recess Length [inches]	Inlet Velocity [m/s] (Inner/Outer)	Momentum Ratio (Inner/Outer)
1	LN_2	He (7°C)	0	11 / 19.5	40
2	LN_2	N_2 (7°C)	0	11 / 19.5	15
3	LN_2	N_2 (7°C)	0.1	11 / 19.5	15
4	LN_2	N_2 (7°C)	0.2	11 / 19.5	15
5	LN_2	CO_2 (7°C)	0	11 / 19.5	12
6	LN_2	He (7°C)	0	5 / 42	8
7	LN_2	N_2 (7°C)	0	5 / 42	3
8	LN_2	CO_2 (7°C)	0	5 / 42	2.5

High speed cinematography, Schlieren imaging and IR thermal imaging were used to examine the global flow features of the LN_2 jet in a surrounding gaseous stream. The entrainment of the ambient air into the jet was also investigated by confining the flow, wherein two cases of confined and semi-confined were considered. For the latter, the jet was confined from two opposite sides thus leaving the other two sides of the chamber unconfined. This configuration can thus simulate injector-wall interaction.

Time resolved images of the LN_2 jet flow were acquired at 512 frames/sec with a resolution of 1024×1024 pixels. Thermal images of the flow were captured using a long range (8 – 9 µm) infrared camera equipped with a quantum wall infrared photon (QWIP) detector to analyze the infrared light emitted from the cold flow and its warmer surroundings. The radiance captured by the infrared camera depends mainly on the object temperature, background temperature and the emissivity of the source object. For an opaque source object at temperature T and emissivity ε, and for a background temperature T_b, the total radiance L captured is given by:

$$L = \varepsilon L_o (T) + (1-\varepsilon)L_b (T_b)$$

(1)

where, L is in Watt/m^{2}sr, $\{\varepsilon L_o (T)\}$ is the radiance emitted by the source, and $\{(1 -\varepsilon) L_b (T_b)\}$ the radiance reflected off the source due to background emissions. The infrared camera detector measures

the captured radiation in Watts, whereas the surface area and solid angles are calculated from the source size, optics aperture, detector size, and the distance between the source and the camera. Several other factors can also affect the radiance captured. These include the ambient temperature, relative humidity, and the transmission of the external optics. The ThermaCAM software of the camera has inbuilt correction functions for these factors. The net radiance emitted by the source can be calculated from:

$$L_o\left(T\right) = \frac{1}{\varepsilon}\left[L - \left(1 - \varepsilon\right)L_b\left(T_b\right)\right]$$

(2)

Once this net radiance is known, the camera software calculates the corresponding temperature from a digitally stored calibration look-up table. The images presented here were captured at a frequency of 60 Hz, and they represent the average of 300 instantaneous images.

The effect of momentum ratio on mixing was examined using the PIV technique under single-phase gaseous flow conditions. A different coaxial injector was used for this purpose with a central tube of a 0.8-mm inner diameter surrounded by a 12.89-mm ID outer tube. This geometry allowed examination of large range of momentum flux ratios between the inner and outer jets. The results demonstrated here are only for the momentum ratios of 0.69 and 0.81. At higher momentum ratios the effect was even more significant. Detailed flow dynamics and strain rates have been obtained for the shown momentum ratios.

A 2-D PIV system was used to examine the features of the flow field. The test section was illuminated by means of a solo PIV Nd:YAG laser. Submicron glass balloon particles were introduced into the annular flow using a fluidized bed. A charged coupled device (CCD) camera with an active pixel array of 1280 × 1024 was used to record the images. The camera, placed normal to the laser sheet, was operated by a control module for image acquisition. The camera was equipped with mechanical shutters and a narrow band-pass filter (0.87 nm) at a center wavelength of 532 nm to allow for maximum transmission of the signal, thus enhancing the recorded images of the particles present in the gas flow. The frequencies of the laser and the camera were synchronized at 5 Hz. The measured area in the test section was 30 × 45 mm in the radial and axial directions (x and y), respectively. Five-

hundred image pairs were acquired for each case to determine the mean and turbulence properties associated with the flow field.

III. Results and Discussion

A. Global flow field data with liquid nitrogen

The goal of this study is to examine the flow and mixing characteristics of LN_2 flow surrounded by a coaxial gaseous jet, in order to simulate the flows from rocket engine injectors. Therefore, the effects of jet confinement, momentum flux ratio and the recess length of the LOX post on the flow expansion, heat transfer and the entrainment of the surrounding air have been investigated.

Figure 2a shows an image of an unconfined LN_2 jet in a coaxial GN_2 stream. This image has been extracted from a high speed clip taken at 500 frames/sec. The close-up view of the flow, shown in figure 2b, is an image from a clip taken at 1000 frames/sec. The evolutionary behavior of the LN_2 jet in a coaxial gaseous stream can be seen. The expansion of the jets and its effect on the surrounding entrained air can also be visualized. The dense white fog, visible downstream of the injector exit, is due to the rapid condensation and freezing of the moisture present in the surrounding air that gets entrained into the gaseous jet. Although the presence of this white fog around the LN_2 stream deteriorates the visibility of the jet, one can still observe that it disperses into ligaments and droplets prior to its vaporization further downstream, where it eventually mixes with the surrounding gas.

Since mixing and combustion takes place in a confined environment in all practical systems, the effect of confinement on the global flow characteristics has also been examined. Figure 3 shows the effect of confinement on the LN_2/GN_2 flow for three different cases of: a) unconfined, b) semi-confined (two sides confined), and c) fully confined. The visibility in figure 3c is poor because two sides of the confinement had metallic bars, which allowed for very little light to illuminate the flow. The dark stripes between y/D = 10 and y/D = 15 are the shadow of clamps used to hold together the confinement walls of the chamber. Nevertheless, the impact of confinement on the evolution of the LN_2 flow can still be observed. An examination of these images shows the significant effect of confinement on the flow expansion, mixing and heat exchange with the surrounding gases. The LN_2 jet persists over longer distances for the semi-confined and fully confined cases as compared to the

146

unconfined case. This suggests that the vaporization and expansion of the LN_2 jet are reduced with confinement. Significantly less white fog is also observed around the LN_2 jet downstream of the injector exit in the fully confined case, which means less entrainment of the surrounding air into the gaseous flow. For the confined case the LN_2 jet does not even fully disperse within the shown section of the mixing chamber. Droplets of LN_2 could be recognized near the injector exit, which suggests reduced heat transfer from the surroundings to the LN_2 jet.

In order to further assess the flow behavior and mixing, infrared (IR) thermal images of the flow were taken to analyze the cooling effect of the LN_2 jet (leaving the injector exit at 77 K) on the surrounding gases and the entrained air moisture. The minimum temperature that can be measured accurately by the IR camera is -20^oC, and the surrounding atmospheric temperature was set to 25° C. Although LN_2 has an emissivity close to 1.0 whereas the emissivity of the surrounding gases is about 0.05, the calculation of temperature was done inside the ThermaCAM camera software using a single value of the emissivity of 0.05 for all the data presented here. As can be seen from equation (2), the value of the emissivity affects the absolute values of the detected temperatures only and not the temperature gradients inside the flow. The reason behind choosing the value of 0.05 for the overall emissivity is that the gas-phase mixing is considered more important since this contributes directly to mixture ignition.

Figures 4a and b show IR thermal images of a LN_2/GN_2 flow for the unconfined and semi-confined cases, respectively. The LN_2 jet leaving the injector appears warm when its temperature is, in fact, cryogenic, because of the large reflection of light from the liquid surface, which suggests little or no interaction of the LN_2 jet with the surrounding gases in this region. This region is designated as the initial merged zone as discussed earlier. As the flow progresses, it starts vaporizing and mixing with the surrounding gas. The cooling effect from the LN_2 jet on its surroundings is recognizable from the increasing darkness of the flow grey shade. Further downstream the flow appears much darker due to the cold gaseous flow and the condensed moisture of the surrounding air. The effect of confinement on the LN_2 jet can be seen in figure 4b. The length of the warm appearing LN_2 jet is increased significantly for the semi-confined case which suggests that it persists over a longer distance as compared to the unconfined case. The sidebars are warmer near the injector exit than they are further

downstream, which shows the low cooling effect from the LN_2 jet in that region. The sidebars and the surrounding gases become colder as the flow progresses downstream due to the vaporization and mixing of the LN_2 jet with the surrounding gases. The colder regions of the flow are reduced significantly as compared to the unconfined case which confirms the reduction in the cooling effect from the LN_2 jet and reduced entrainment of the surrounding air into the annular gaseous jet. An IR thermal image of the fully confined case was not taken because the quartz glass of the mixing chamber inhibits IR radiation from passing through.

Recess is used in most coaxial injectors to enhance the combustion stability. A qualitative assessment of the effect of recess on evaporation and mixing of the LN_2 jet in a coaxial gaseous jet has been conducted in this work. Figure 5 shows high-speed images of a LN_2/GN_2 flow for three different recess cases of: a) no recess, b) 0.1-inch recess length, and c) 0.2-inch recess length. Slight increases in jet expansion can be observed at locations closer to the injector exit. Moreover, the density of the white fog (frozen moisture) increases with increase in distance downstream of the injector exit which suggests higher entrainment of the surrounding air into the jet as well as stronger cooling effect from the LN_2 jet with increased recess length.

Figure 6 shows IR thermal images of the LN_2/GN_2 flow for the three different recess length cases described above. The images look very similar at the locations close to the injector exit. This suggests that changing the recess length does not affect the evaporation of the LN_2 jet much at early stages of the flow evolution. However, further downstream the recess length shows a significant effect on the expansion of the jets as well as entrainment of the surrounding air. The colder (darker) region of the flow widens significantly with increase in recess length at downstream locations from the injector exit. This shows higher expansion of the jets as well as higher entrainment of the surrounding air into the jet. These results provide further support and confirmation to the data obtained using high-speed cinematography.

Experimental data were obtained to examine the effect of momentum ratio on the global features of the LN_2 jet flowing inside different coaxial gaseous jets (i.e., different momenta of the LN_2 jet to outer jet). The momentum flux ratio is defined here as $MR = \sqrt{\rho_1 v_1^2 / \rho_2 v_2^2}$, where ρ_1 and v_1 are the density and velocity of inner jet (LN_2), respectively, while ρ_2 and v_2 are those of the annular gaseous jet,

respectively. For the present injector geometry, the momentum flux ratio and the momentum ratio are the same, because the cross-sectional areas of the two jets are equal. Figure 7 shows the effect of three different momentum ratios on the subsequent high-speed images, namely, a) MR = 12 (LN_2/CO_2), b) MR = 15 (LN_2/GN_2), and c) MR = 40 (LN_2/He). The volumetric flow rates of the gaseous flows were kept equal, so that different momentum ratios are associated with different densities of the coaxial gases. As can be seen from figure 7, the central LN_2 jet persists over longer distances at higher momentum flux ratios, which suggests reduced mixing with the surrounding gas, and subsequently lower heat transfer. The entrainment of the surrounding air into the annular gaseous jet starts closer to the injector exit for higher momentum flux ratio, which is revealed by the evolution of the dense white fog. This behavior is attributed to the change in density of the annular gaseous jet.

The last set of thermal images presented in figure 8 is for the same momentum ratios depicted in figure 7. It can be observed that the cooling effect from the LN_2 jet on the surrounding gases starts earlier for lower momentum ratio case because the length of the warm appearing section of the LN_2 jet (where there is almost no interaction with the surrounding gases) is reduced for smaller momentum ratio case. This implies faster evaporation of the LN_2 jet and more mixing with the surrounding gases for lower momentum ratio case.

In order to further examine the effect of recess and momentum ratio, axial and radial temperature distributions were plotted. Figure 9a shows the centerline temperature distributions for the five investigated recess length and momentum ratio cases. It can be seen that recess length has very little effect on the centerline temperature distribution close to injector exit. However, it does affect the LN_2 flow at downstream locations; this can be seen from the differences in temperature distribution after around 15 diameters downstream of the injector exit. In contrast, the results show significant effect of momentum ratio on the centerline temperature distribution. The colder temperature region moves closer to the injector exit with decrease in momentum ratio. This suggests faster evaporation of LN_2 jet and more mixing with the surrounding gases with decrease in momentum ratio. Figure 9b provides a plot of the radial temperature distribution at an axial location of y/D = 30. At this location no significant effect of the momentum ratio on the temperature distribution can be observed. The colder region reduces slightly in size for MR = 40 case, which suggests less cooling of the surrounding gases

149

and reduced mixing. On the other hand, recess length has a significant effect on the radial temperature distribution. The colder region broadens for larger recess lengths, which suggests higher jet expansion and more entrainment of the surrounding gases, as concluded previously.

High speed Schlieren imaging technique was used to examine the development of shear layer between the two fluids and its impact on the destabilization of cryogenic jet. Figure 10 shows the effect of changing momentum ratio on the evolutionary behavior of shear layer development between the two flows and destabilization of cryogenic jet. The three examined cases are: a) MR = 8 (LN_2/He), b) MR = 3 (LN_2/GN_2), and c) MR = 2.5 (LN_2/CO_2). The flow conditions examined in this experiment are slightly different than the previous cases because it was difficult to accurately quantify the jet destabilization frequencies for previous cases. One can clearly see a stable liquid jet emerging from the injector exit surrounded by a gaseous jet. As the flow progresses further downstream, the formation of vortical structures from shear layer development causes the inner liquid core to break-up and mix with the surrounding gases. For the GN_2 and CO_2 cases, the presence of two different flows close to the injector exit could not be seen because of smaller density gradients between the injected gas and atmospheric air immediately near to the injector exit. The results shown in Fig. 10 clearly show an increase in formation of vortical structures with decrease in momentum ratio between the jets. This suggests faster breakup of liquid jet and increased mixedness with the surrounding gases at decreased momentum ratios.

The focus in the present experiments was to capture the large size vortical structures inside the flow since they are responsible for the LN_2 jet dispersion. Thus the intent of the experiments were to capture the smaller frequency structures that appear on the interface between the LN_2 jet and the surrounding gas flow due to coalescence of high frequency structures. Table 4 shows calculated experimental jet destabilization frequencies for the cases discussed above and lie in the range of about 200 to 300 Hz. The corresponding Strouhal numbers based on inner jet diameter (jet preferred mode) and vorticity thickness of the gas flow were calculated to be about 0.4 and 2×10^{-3}, which are in the range reported in the literature. Note that the sample experimental frequencies are offered here to provide an order of magnitude estimates on the vortical frequencies and Strouhl number associated with the flow. In contrast the finer scale theoretical frequencies provide the formation of smallest vortical structures that

coalesce together to form larger vortical structures and lead to the eventual breakup of liquid jet. An estimate of these frequencies is made from the convective velocity of the flow. The convective velocity u_c of the interface is calculated as, $u_c = (\sqrt{\rho_l} v_l + \sqrt{\rho_g} v_g)/(\sqrt{\rho_l} + \sqrt{\rho_g})$. The theoretical instability frequencies f_{th} is calculated as, $f_{th} = (u_c/\delta_w)(\rho_g/\rho_l)^{0.5}$ where, δ_w is vorticity thickness of gaseous stream.[18] The calculated frequencies were found to be 1266, 6231 and 8710 corresponding to the convective velocity of 5.5, 6.4, and 6.7 m/s, respectively. These theoretical frequencies are much higher than the calculated experimental frequencies, as expected, since the experimentally measured frequencies are from larger vortical structures present in the flow.

A visual observation of the flow revealed that indeed a range of frequencies are present in the flow. Thus, depending on the specific region examined in the flow, different frequency may be evaluated. Therefore, the calculated experimental frequency from the flow must be taken as a guideline on the low frequency associated with the flow while the theoretical frequency is the primary instability frequency of the liquid jet. These results suggest that the vortical frequencies responsible for liquid jet destabilization and break up decreased with decrease in gaseous jet density and momentum ratio. The results also suggest that the jet preferred mode is the dominant destabilization mode for the liquid jet instability for the cases analyzed. These results compare favorably well with the experimental results reported by Villermaux[18] and Lasheras et al[19]. However, further experiments and analysis may be supported to further enrich this conclusion.

Table 4 Destabilization frequencies for some of the examined cases

Case	u_c [m/s]	Re_{gas}	f_{ex} (Experimental, low frequency)	Strouhal No. ($f_{ex}D/u_c$)	Strouhal No. ($f_{ex}\delta_w/u_c$)
6	5.5	2931	245	0.38	0.0028
7	6.4	25104	294	0.39	0.0019
8	6.7	43136	327	0.42	0.0018

B. Shear Layer Mixing

In order to provide a further quantification on the effect of momentum ratio on flow dynamics and shear layer mixing, 2-D particle image velocimetry diagnostics was carried out. The LN_2 jet was

replaced with a gaseous helium stream due to the complexity associated with flow seeding of the cryogenic LN_2 jet required for PIV measurements. The momentum ratio was controlled by using different outer gases (O_2 and CO_2) having different densities, similar to the approach used for the inner LN_2 jet. Even with the use of a gaseous helium jet, similar effects of the momentum ratio were observed. Figures 11a and b compare the distributions of the axial velocity associated with the two configurations of He/O_2 and He/CO_2 from the injector, respectively. Significant differences in the velocity decay and the magnitude of maximum velocity can be recognized. The He/O_2 flow case has higher axial velocity than that for the He/CO_2 case but a slightly narrower shear layer region at the downstream locations. This is attributed primarily to the change in momentum ratio between the inner and outer jets. The lower axial velocity associated with the He/CO_2 allow for lower velocity gradients to provide higher shear layer mixing with decrease in the momentum ratio.

Closer examination of the effect of momentum ratio on the shear layer mixing was conducted by plotting the distributions of axial velocity and shear strain at different axial locations. Figures 12a and b show the distributions of axial velocity and shear strain for both flow configurations at $y/D = 0.16$. The profiles of axial velocities are similar to each other, which was expected at this location close to the injector exit. The dips recognizable in the velocity profiles near to the centerline are attributed to the fact that only the outer flow of the injector was seeded and that no significant mixing had occurred at this very early stage of the flow evolution. The shear strain profile shows four distinct peaks because of the existence of two distinct flows in that region. The negative magnitudes of some of the peaks are due to the change in direction of the shear strain. It should be noted that all four peaks are at the same radial location for both flow configurations, as expected. Also the magnitude of shear strain is higher for the He/O_2 configuration (having higher momentum ratio). As the flow progresses further downstream the distinction between the profiles of the two flow configurations fades away gradually, which can be seen in Figs. 13a and b (e.g., at $y/D = 1.16$). The peaks of axial velocity start to merge, and so do the shear strain, which suggests an increase in mixing between the coaxial jets. Similarly, as one moves further away from the injector exit, the distinct peaks almost completely merge into one another to evolve with the existence of only one flow, as depicted in figures 14a and b (at $y/D = 2.32$). This suggests that the two flows are completely mixed at this far axial location. The higher magnitudes

of axial velocity and shear strain rate associated with the He/O_2 flow at the three axial locations of figures 11 – 13 confirm that mixing and jet expansion are slower at higher momentum ratio.

IV. Conclusions

The experimental results presented here show the effect of confinement, momentum ratio, and recess length on the vaporization and mixing in a coaxial rocket engine injector. Some of the experimental jet destabilization frequencies as well as the characteristic primary instability frequencies present in the coaxial jets have been examined using cryogenic fluid and surrounding gas of different densities. A combination of various non-intrusive diagnostic techniques has provided insightful features of the injector performance characteristics under simulated rocket injector operating conditions prior to ignition.

The LN_2 jet disperses into ligaments and droplets prior to vaporization. The confinement reduces the vaporization of the LN_2 jet by increasing the axial distance over which the jet persists before full vaporization. Confinement significantly reduces the entrainment of surrounding gases and heat transfer from the surroundings to the injector fluids.

Increase in momentum ratio results in early expansion of the outer gas flow and higher entrainment of the surrounding gases. However, the LN_2 jet persists over longer distances for higher momentum ratios, leading to its reduced mixing with the surrounding gases. The recess length has little effect on the evaporation of the LN_2 jet but affects the expansion of the flow and entrainment of the surrounding gases significantly at downstream locations. The results also revealed an increase in liquid jet instability with decrease in momentum ratio between the inner and outer flows of the injector. The flowfield results obtained from the 2-D PIV diagnostics using gas/gas flows assist in understanding the role of momentum ratio on mixing in LN_2/gas flows. Mixing has been shown to enhance with decrease in momentum ratio between the inner and outer jets.

153

Meyer as the Project Manager. Support provided by Jakub Gmurczyk and Pierre Rousseau is much appreciated.

References

[1]Sutton, G. P. and Biblarz, O.: Rocket Propulsion Elements, 7th Edition, John Willey and Sons, 2001.

[2]Beer, J. M. and Chigier, N. A.: Combustion Aerodynamics, Applied Science Publishers, Ltd., London, 1972.

[3]Huzel, D., Huang, D.: Modern Engineering for Design of Liquid Propellant Rocket Engines, Chapter 4, Progress in Aeronautics and Astronautics, Vol. 147, AIAA, 1992.

[4]Vingert, L., Gicquel, P., Lourme, D., and Menoret, L.: Coaxial Injector Atomization, Progress in Aeronautics and Astronautics, Vol. 169, AIAA, 1994.

[5]Yang, V., Habiballah, M., Popp, M. and Hulka, J.: Liquid Rocket Thrust Chambers: Aspects of Modeling, Analysis and Design, Chapters 9-10, Progress in Aeronautics and Astronautics, Vol. 200, AIAA, 2004.

[6]Pal, S., Moser, M. D., Ryan, H. M., Foust, M. J., Santoro, R. J.: Shear Coaxial Inyector Atomization Phenomena for Combusting and Non-Combusting Conditions, Atomization and Sprays, Vol. 6, 1996, pp. 227-244.

[7]Vingert, L., Gicquel, P., Ledoux, M., Care, I., Micci, M., and Glogowski, M.: Atomization in Coaxial Jet Injectors, Chapters 3, Progress in Aeronautics and Astronautics, Vol. 200, AIAA, 2004, pp. 105-140.

[8]Mayer, W. and Tamura, H.: Propellant Injection in a Liquid Oxygen/Gaseous Hydrogen Rocket Engine, Journal of Propulsion and Power, Vol. 12, No. 6, Nov-Dec 1996, pp. 1137-1147.

[9]Mayer, W., Schik, A., Vielle, B., Chauveau, C., Gokalp, I., Talley, D., Woodward, R.: Atomization and Breakup of Cryogenic Propellants Under High Pressure Subcritical and Supercritical Conditions, Journal of Propulsion and Power, Vol. 14, No. 5, September-October 1998, pp. 835-842.

[10]Mayer, W., Schik, A., Schaffler, M., and Tamura, H.,: Injection and Mixing Processes in High Pressure Liquid Oxygen/Gaseous Hydrogen Rocket Combustors, Journal of Propulsion and Power, Vol. 16, No. 5, Sep.-Oct. 2000, pp. 823-828.

[11]Mayer, W., Ivancic, B., Schik, A., and Hornung, U.,: Propellant Atomization and Ignition Phenomena in Liquid Oxygen/ Gaseous Hydrogen Rocket Combustors, Journal of Propulsion and Power, Vol. 17, No. 4, July-Aug. 2001, pp. 794-799.

[12]Candel, S., Herding, G., Synder, R., Scouflaire, P., Rolon, C., Vingert, L., Habiballah, M., Grisch, F., Pealat, M., Bouchardy, P., Stepowski, D., Cessou, A. and Colin, P.: Experimental Investigation of Shear Coaxial Cryogenic Jet Flames, Journal of Propulsion and Power, Vol. 14, No. 5, September-October 1998, pp. 826-834.

[13]Candel, S., Juniper, M., Singla, G., Scouflaire, P., Rolon, C.,: Structure and Dynamics of Cryogenic Flames at Supercritical Pressure, Combustion Science and Technology, 178, 2006, pp. 161-192.

[14]Oschwald, M., Smith, J. J., Branam, R., Hussong, J., Schik, A., Chehroudi, B. and Talley, D.: Injection of Fluids into Supercritical Environments, Combustion Science and Technology, 178, 2006, pp. 49-100.

[15]Gautam, V., and Gupta, A. K.: Simulation of Mixing in Rocket Engine Injector under In-Space Conditions, 41st AIAA/ASME/ASME/SAE/ASEE Joint Propulsion Conference, Tucson, AZ, July 10-13, 2005, AIAA 2005-1445.

[16]Strakey, P. A., Talley, D. G. and Hutt, J. J.: Mixing Characteristics of Coaxial Injectors at High Gas/Liquid Momentum Ratios, Journal of Propulsion and Power, Vol. 17, No. 2, March-April 2001, pp. 402-410.

[17]Villermaux, E. and Rehab, H.: Mixing in Coaxial Jets, Journal of Fluid Mechanics, Vol. 425, 2000, pp. 161-185.

[18]Villermaux, E.: Mixing and Spray Formation in Coaxial Jets, Journal of Propulsion and Power, Vol. 14, No. 5, Sep-Oct 1998, pp. 807-817.

[19]Lasheras, J.C. and Hoppfinger, E. J.: Liquid Jet Instability and Atomization in a Coaxial Gas Stream, Annual Review Fluid Mechanics, Vol. 32, 2000, pp. 275-308.
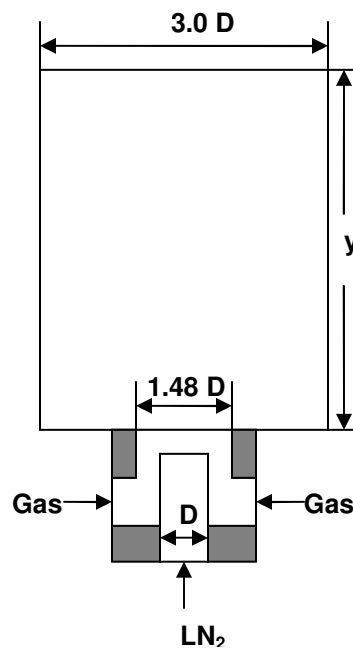
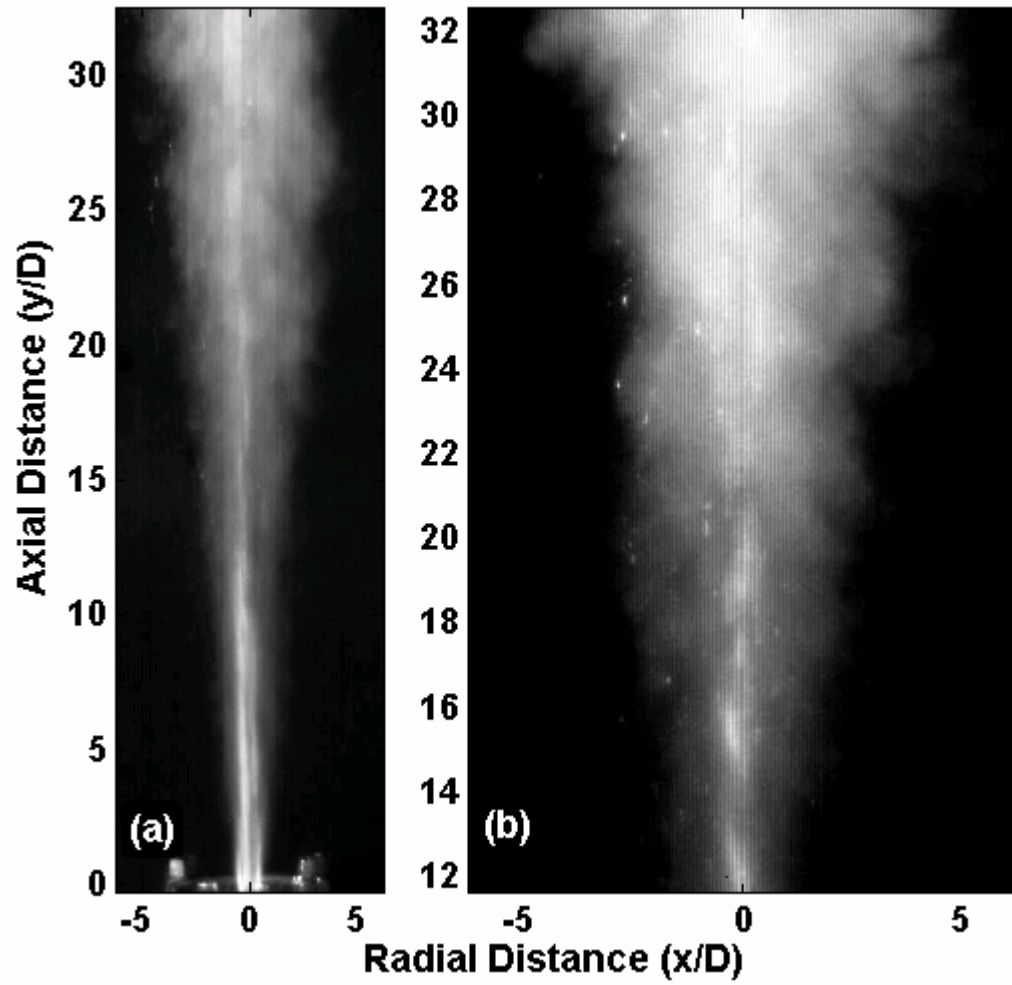**Fig. 1.   Schematic diagram of the test coaxial injector**

Fig. 2. High speed images of unconfined LN$_2$/GN$_2$ flow with no recess;

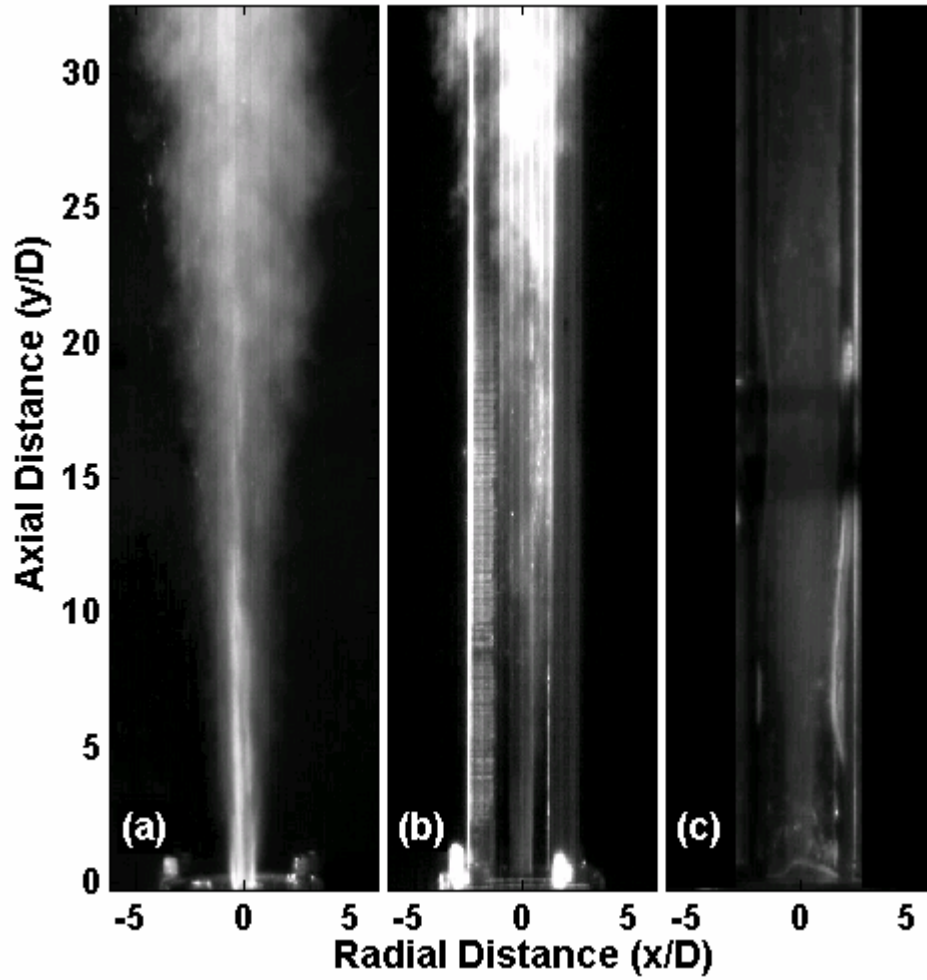**a) 500 frames/sec, b) 1000 frames/sec**

Fig. 3. High speed images of LN$_2$/GN$_2$ flow with no recess for

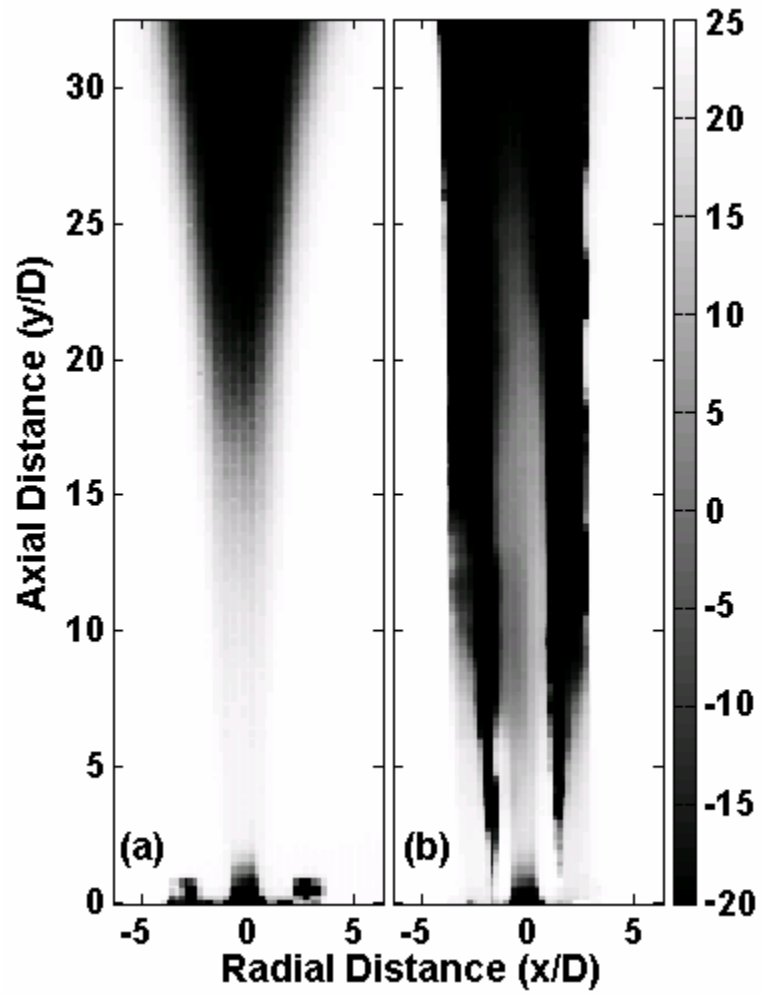**a) unconfined, b) two sides confined, and c) fully confined cases**

Fig. 4. Temperature distribution (°C) of LN$_2$/GN$_2$ flow with no recess for
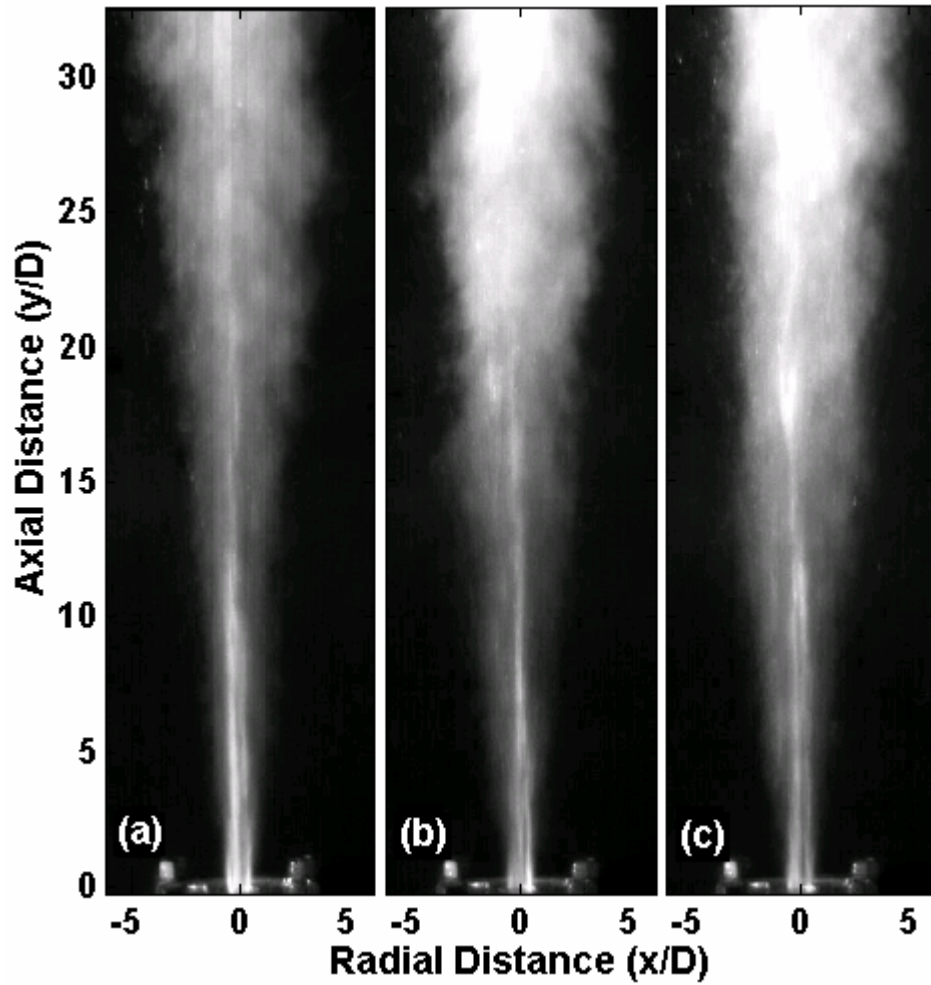
a) unconfined, and b) two sides confined cases

Fig. 5. High speed images of LN$_2$/GN$_2$ flow for

a) no recess, b) 0.1-inch recess, and c) 0.2-inch recess cases
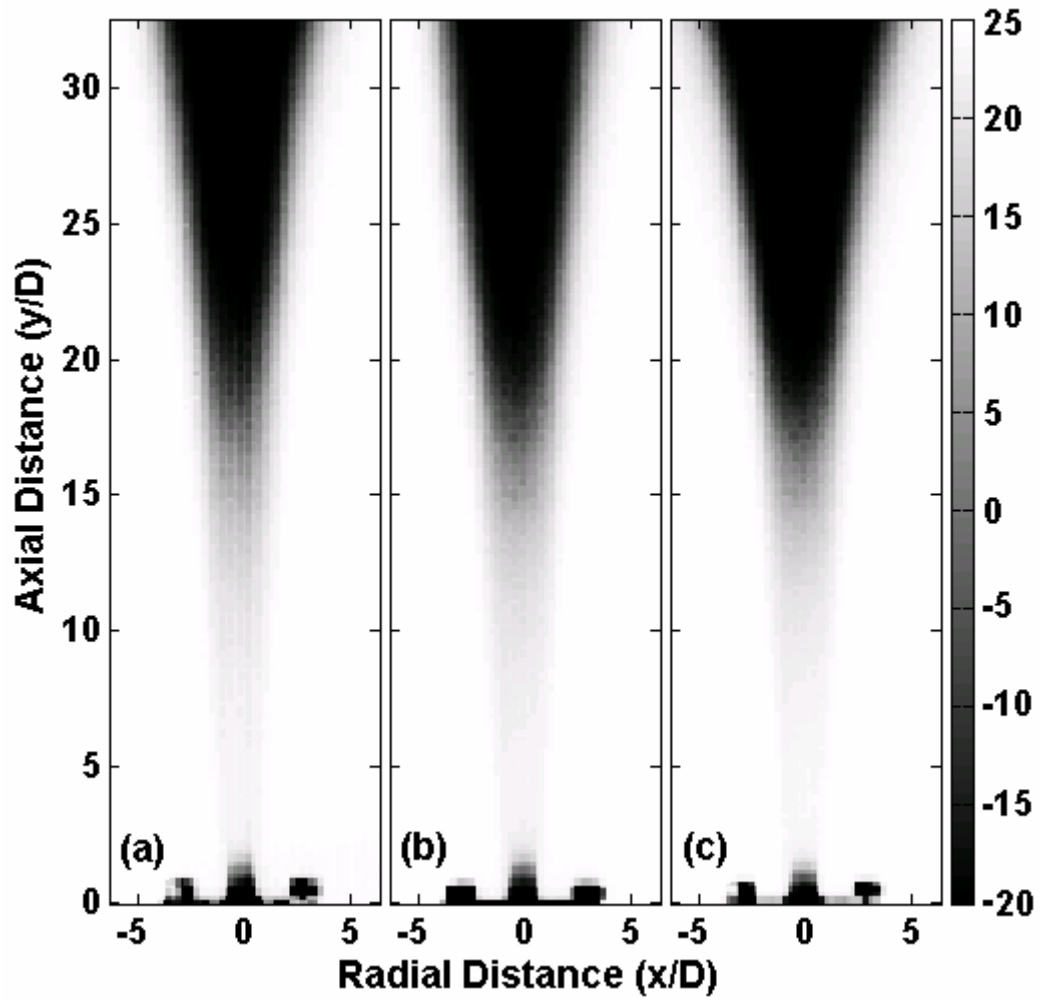
Fig. 6. Temperature distribution (°C) of LN$_2$/GN$_2$ flow for a) no recess, b) 0.1-inch recess, and c) 0.2-inch recess cases
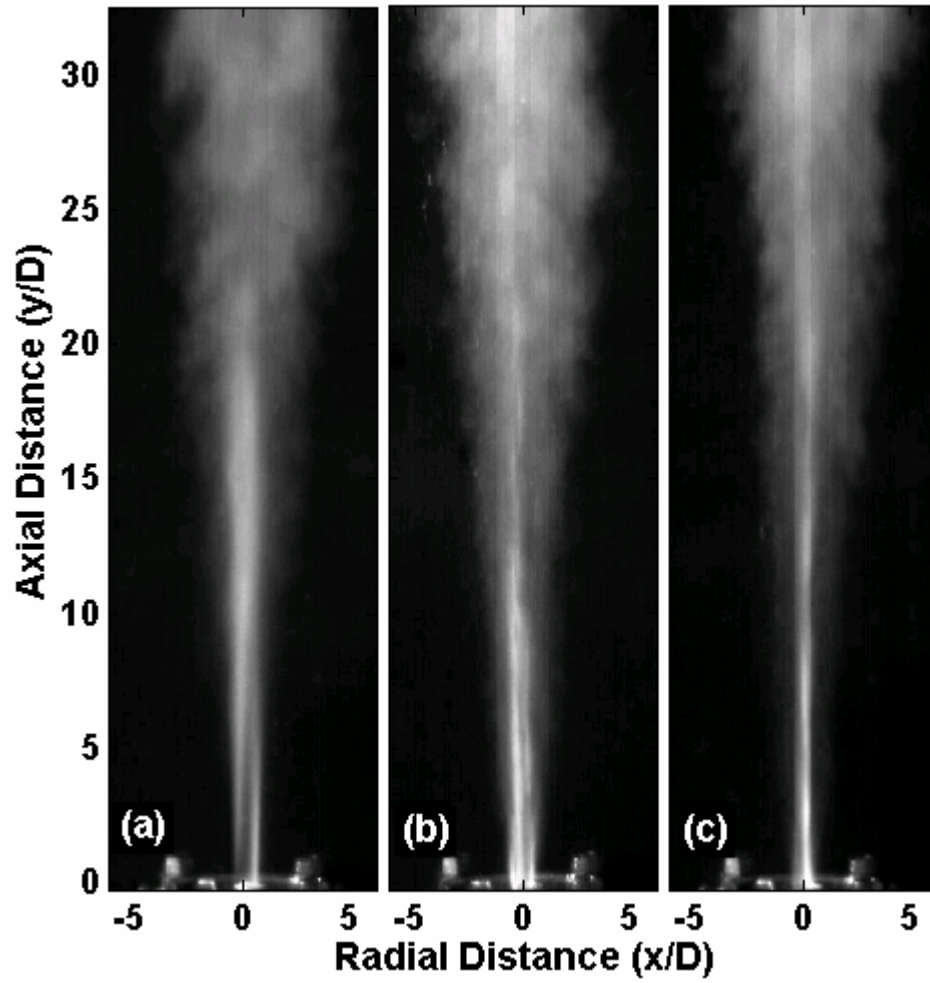
Fig. 7. High speed images of LN$_2$/Gas flow with no recess for
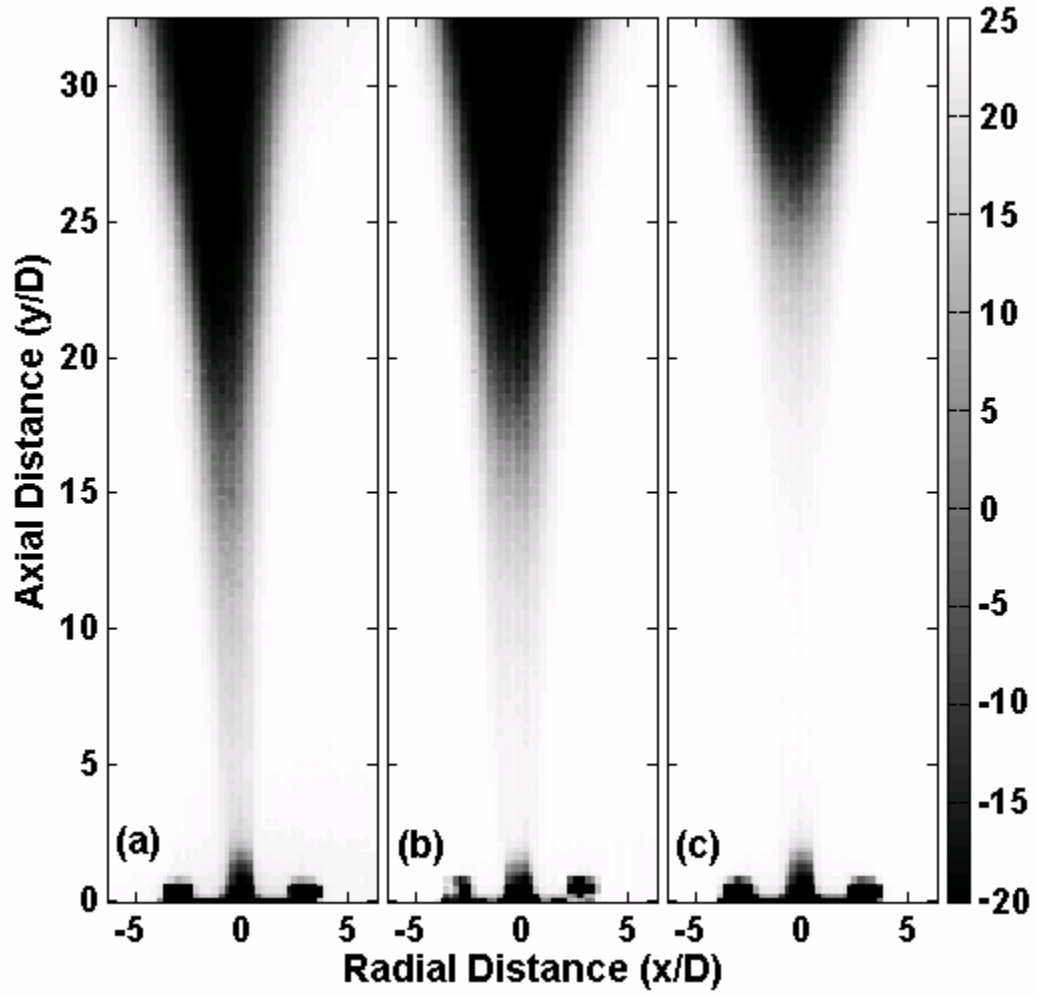
a) MR = 12, b) MR = 15, and c) MR = 40

Fig. 8. Temperature distribution (°C) of LN₂/Gas flow with no recess for

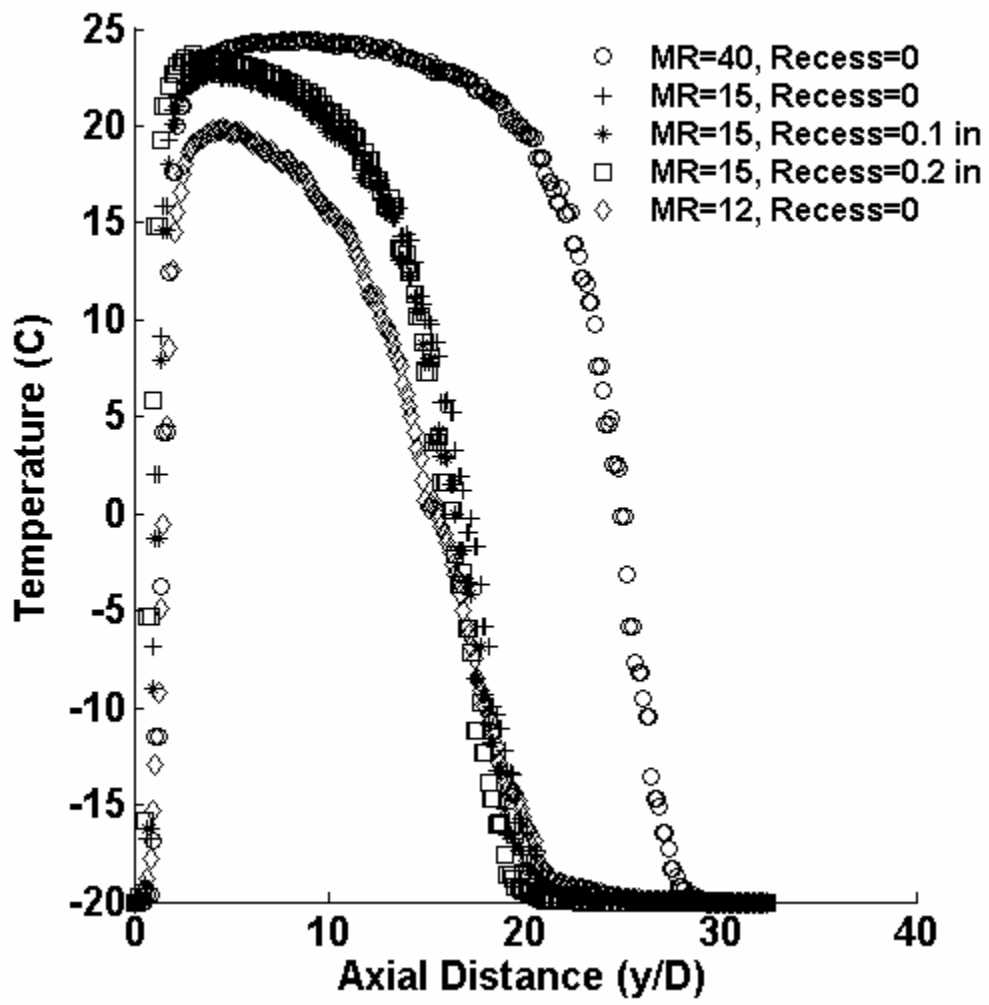**a) MR = 12, b) MR = 15, and c) MR = 40**

Fig. 9a. Distribution of centerline temperature (extracted from the IR thermal images)
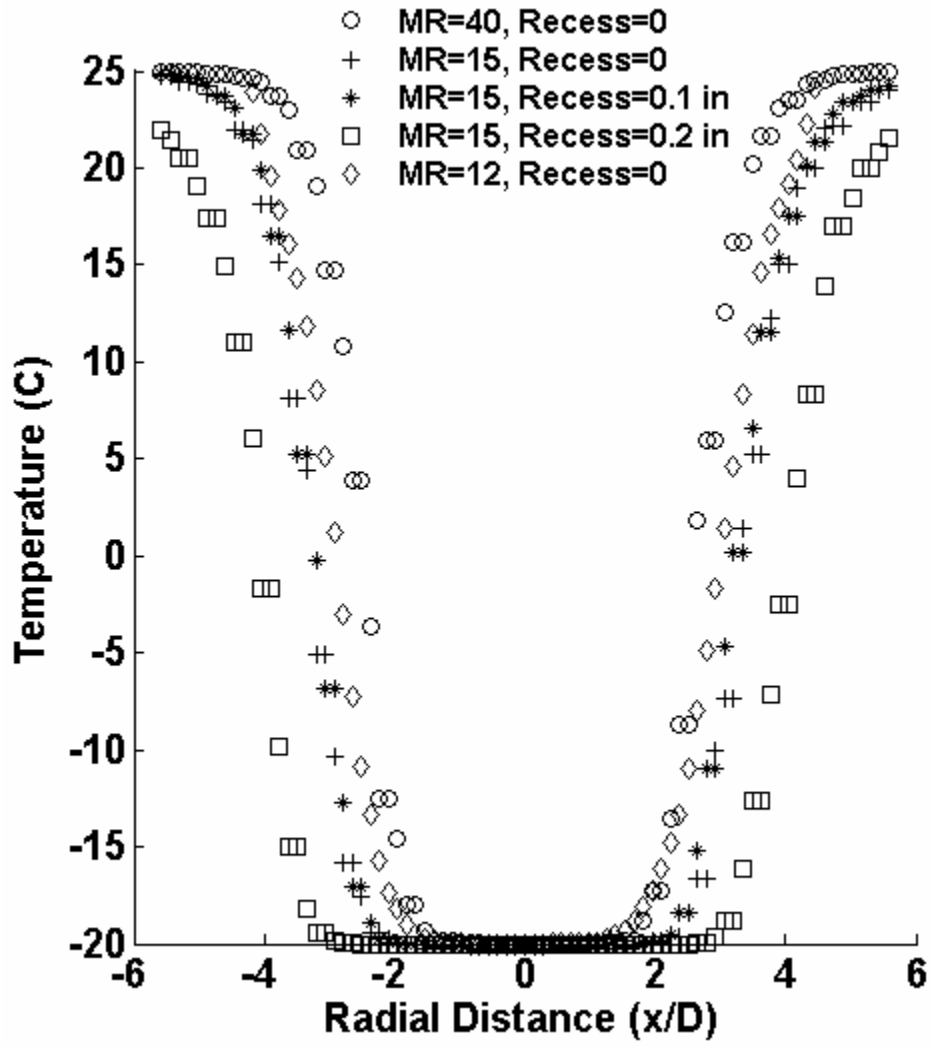
Fig. 9b. Distribution of radial temperature at y/D = 30 (extracted from the IR thermal images)
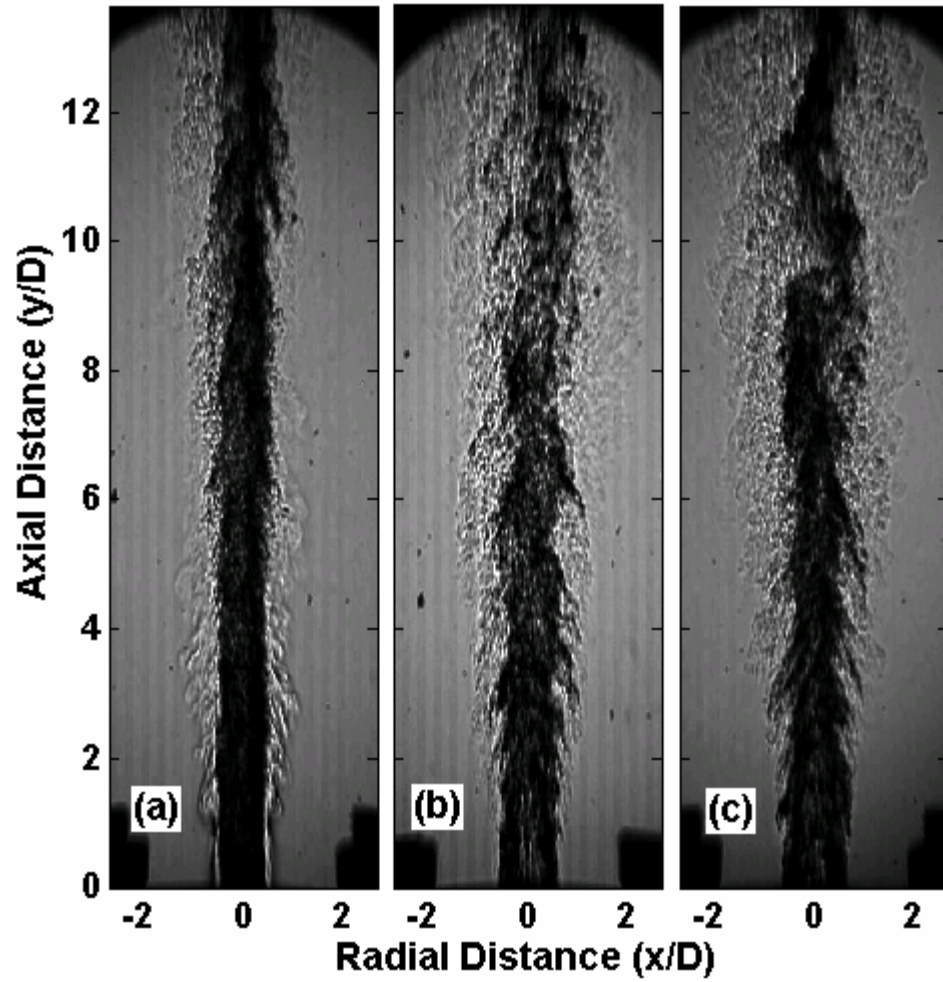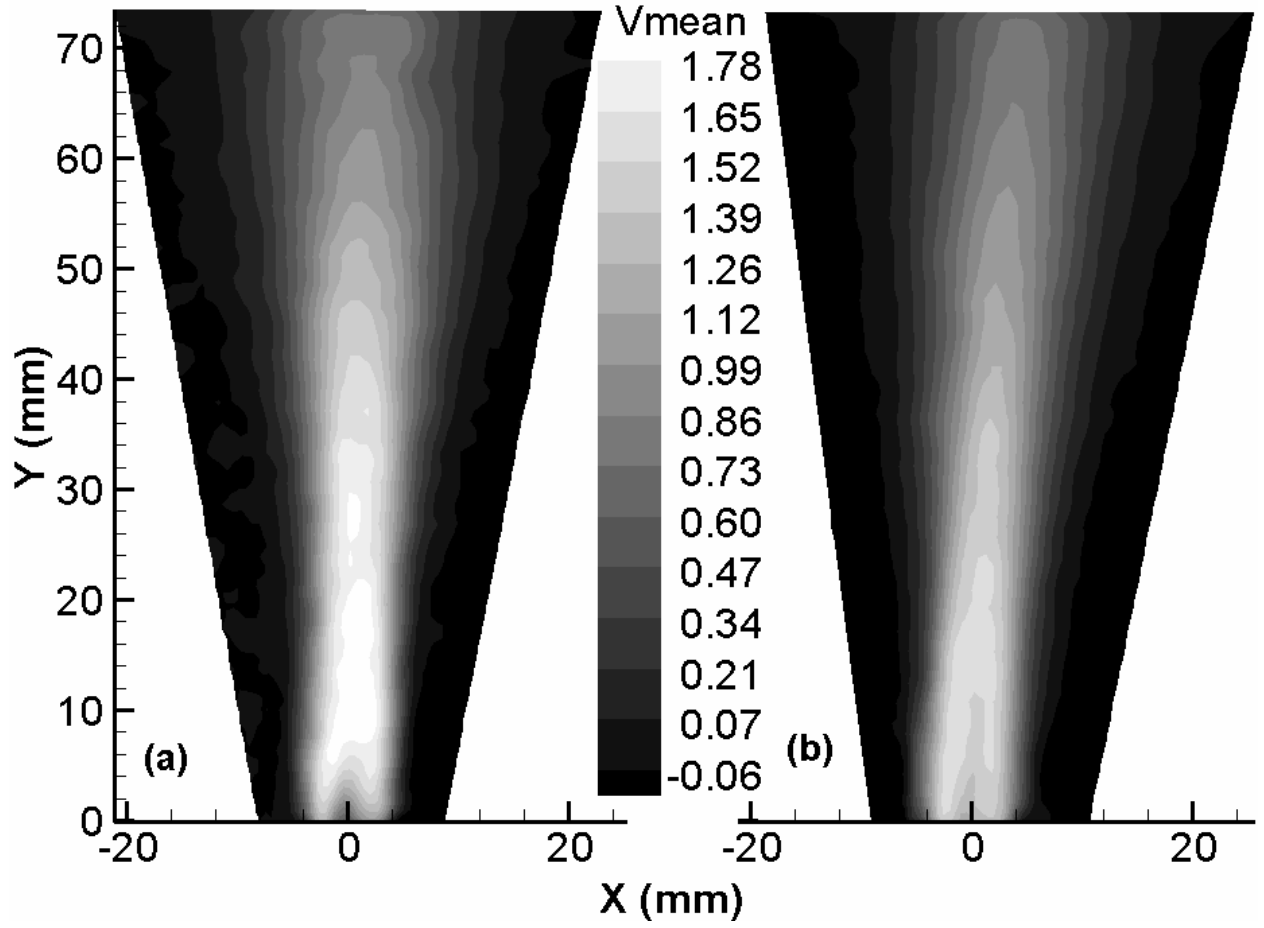
Fig. 10. Schlieren Images of LN$_2$/Gas flow with no recess for

a) MR = 8, b) MR = 3, and c) MR = 2.5

Fig. 11. Distribution of mean axial velocity [m/s] for gas/gas flow for

a) He/O₂ (MR = 0.81), and b) He/CO₂ (MR = 0.69)
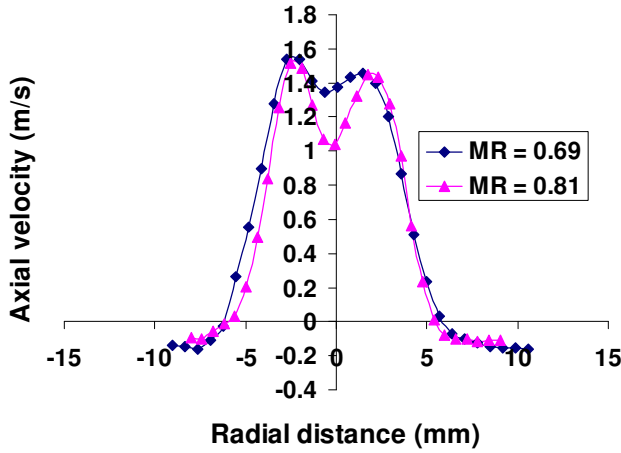
Fig. 12a. Axial velocity distribution at y/D = 0.16
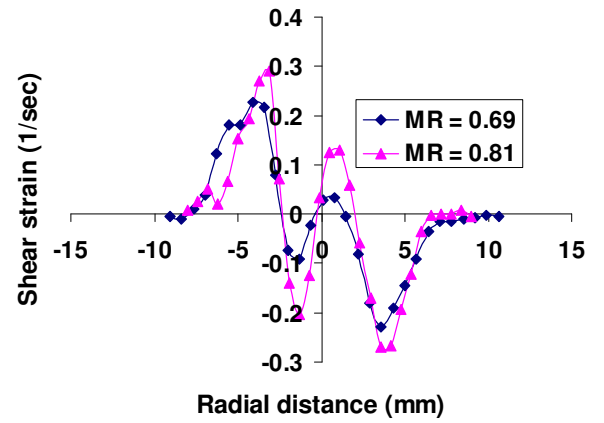

Fig. 12b. Shear strain distribution at y/D = 0.16
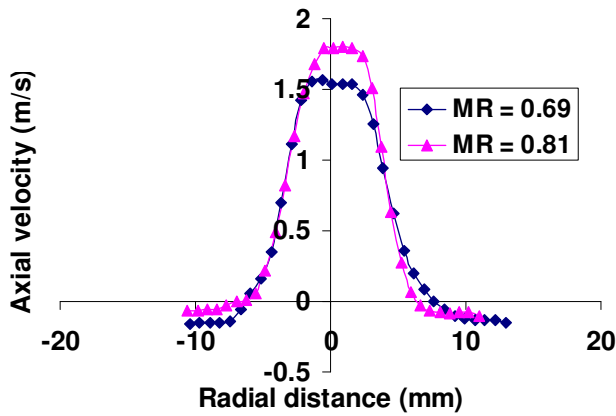

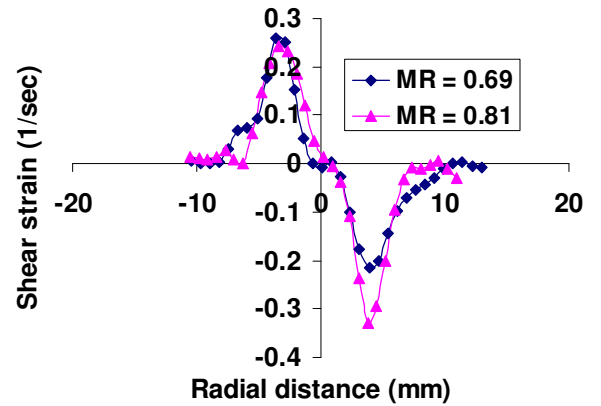**Fig. 13a. Axial velocity distribution at y/D = 1.16**

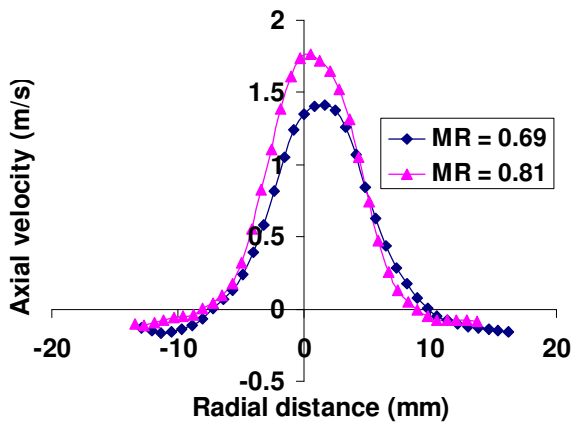**Fig. 13b. Shear strain distribution at y/D = 1.16**

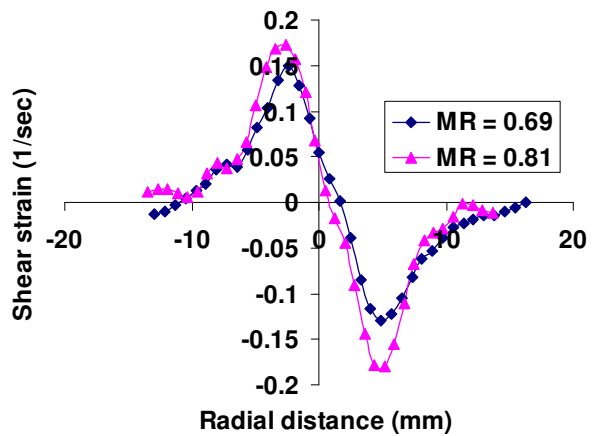**Fig. 14a. Axial velocity distribution at y/D = 2.32**

Fig. 14b. Shear strain distribution at y/D = 2.32

Transient Cryogenic Flow and Mixing from a Coaxial Rocket Injector

V. Gautam* and A.K.Gupta**
Mechanical Engineering Department
University of Maryland
College Park, MD 20742
***email: akgupta@eng.umd.edu*

An experimental facility has been assembled to simulate the transient flow and mixing behavior from a single element co-axial injector that is characteristic of those used in cryogenic rocket engines. In most cases the coaxial jet flow from a cryogenic rocket injector consists of a central liquid oxygen core surrounded by an annular gaseous hydrogen flow. For the present experiments we have simulated the cryogenic propellant behavior with liquid nitrogen flowing through the inner tube and gaseous Helium through the outer annulus. Specifically we have examined the liquid nitrogen flow instability, breakup and mixing with the coaxial gaseous jet under realistic transient and steady-state conditions prior to ignition. The initial, dynamic interaction of the cryogenic fluid with the surrounding quiescent air and coaxial gas has been imaged for the first time. The observations showed significant effect of transient behavior of cryogenic flow during initial startup on the onset of instabilities in cryogenic rocket engines. The results also provided the role of shear layer development on cryogenic flow instability, breakup and mixing with coaxial gaseous jet.

The experimental diagnostic technique used here is Schlieren imaging using a high speed camera to analyze the flow and mixing behavior of LN_2 jet. The Schlieren images were processed using image processing techniques to obtain quantitative information of the flow.

1. Introduction

Coaxial injectors have always been one of the most crucial technological challenges associated with cryogenic rocket engines because their performance directly affects the reliability and performance of the engine. The ignition and combustion characteristics of the engine depend strongly on the flow and mixing of cryogenic propellants (usually liquid oxygen and gaseous hydrogen) from the injector. However, in spite of several attempts in the past, the conditions affecting cryogenic propellants in liquid-fuelled-rocket engines have not been widely studied. Flow and mixing between coaxial jets of cryogenic liquids and gases have been examined under steady-state conditions in limited studies[1,2,3,4,5,6]. Although the cryogenic propellants are injected into the rocket engine under steady state conditions, the initial introduction of propellants into the combustor are far from steady state. Thus, the objective of this research is to analyze the transient flow behavior of cryogenic fluid and gaseous jet from a coaxial rocket injector.

In liquid propellant rocket engine combustors, ignition of propellants takes place through several steps. At the start the combustion chamber is filled with unreacted propellants to mix and generate combustible mixture in some local regions of the combustor. Then a sufficient amount of energy is supplied through an igniter to elevate the temperature of that mixture above the ignition temperature. Once the mixture is ignited combustion propagate throughout the combustor and stabilize. However to

achieve the ignition inside an extremely cold two phase system is a huge challenge. The cold liquid jet is required to destabilize, disintegrate and evaporate quickly in order to achieve good mixing prior to ignition. A combination of various destabilization processes accompanied with complex thermo-physical processes related to phase change makes it very complicated to understand and analyze mixing behavior of two phase cryogenic flow. Therefore, it is very critical to analyze the transient mixing behavior of the propellants for high reliability and performance of cryogenic rocket engines.

Previous research and testing of cryogenic rockets engines have suggested that the liquid oxygen flow rate through the injector prior to ignition is substantial enough to chill the injector surfaces sufficiently so that the oxygen entering the combustion chamber is probably two-phase. Hydrogen fuel is in gaseous form under conditions occurring in the injector immediately prior to ignition. Emdee et al.[7] and McNelis et al.[8] have shown the effect of transient flow and mixing phenomena on ignition and combustion behavior of cryogenic rocket engine. They have also shown the effect of transient processes on engine reliability. Thus, close examination of the initial mixing between two-phase oxygen and gaseous hydrogen flows is necessary to develop a better understanding of the fate of propellant pre-ignition conditions. This initial mixing of propellants under unsteady two-phase conditions also triggers the onset of combustion instabilities.

Some experimental and numerical simulation work on the 2-D transient mixing of gaseous propellants has been carried out at NASA in conjunction with some other collaborative researchers[9]. Although the operational conditions were not as realistic, the results still showed the important effect of unsteady initial conditions on mixing of propellants and combustion instability.

Cryogenic oxygen presents substantial experimental and modeling complexities since its state is unknown under realistic engine operating conditions. Although some limited data are available using cryogenic fluids, none are under realistic engine operating conditions. A true understanding of the fate of cryogenic fluid under realistic operating conditions of the injector is critical for providing pivotal information on the performance of the engine. In this research, the behavior of liquid nitrogen stream (to simulate the cryogenic liquid oxygen), surrounded by a coannular stream of gaseous helium (to simulate gaseous hydrogen), have been examined starting from the initial cryogenic fluid injector exit under realistic engine operating conditions. The initial dynamic interaction of the cryogenic liquid with the surrounding gas has been imaged for the first time. These observations are significant, because instabilities observed at the two-phase boundary during initial startup clearly reveal the onset of phase behavior and flow instability which then may affect ignition and the onset of unstable combustion in most cryogenic rocket engines.

2. Experimental Setup

The facility consisted of a supply system for cryogenic liquid nitrogen and gaseous helium, a single injector, an enclosure surrounding the injector, an exhaust system and an elevation mechanism for traversing the facility in axial direction. A schematic diagram of the experimental facility and a photograph of the facility are shown in Figures 1a and 1b, respectively. The enclosure surrounding the flow was removed during tests presented here in order to gain full optical access thus aiding high quality of data on flow visualization. Fig. 2a shows a schematic diagram of the injector and injector face plate with dimensions as well as a photograph of the face plate through which the flows emerge. The co-axial injector and faceplate geometry is representative of those used in many practical engines. The control board of the facility along with the gas supply lines is shown in Fig. 2b. It contains two supply lines and large number of orifices for gaseous flow to obtain gases of different but known densities and large range of gas velocities. The flows were controlled with fast response solenoid-actuated valves. The mass flowrate of helium was measured using a choked orifice and a pressure transducer. The average temperature of the gaseous flow at the injector exit was measured using a thermocouple and found to be 263 K. The gas velocity was calculated under the assumption of ideal gas density. Since the pressure inside the chamber of a rocket engine is not high prior to the engine startup, tests were carried out at normal atmospheric pressure.

Cryogenic Fluid flow Measurement

The precise measurement of cryogenic fluids is a challenge and is not reported much in the literature. For the present experiments the flow rate of liquid nitrogen was measured using a high-precision turbine flowmeter, designed to handle cryogenic liquids. The challenge here was to ensure that the fluid entering and exiting the turbine flow meter still remain in liquid form since any transformation would result in erroneous results on the metered cryogenic flow rate. Therefore, to assure that the measurements are accurate, the flowmeter had to be cooled down to LN_2 temperatures

before getting steady-state readings to confirm liquid flow through the flowmeter with no vapor or two phase flow formation. The procedure of acquiring LN_2 flowrate measurements starts by bleeding LN_2 out through the turbine flowmeter at very low flowrates, until the temperature of flowmeter reaches the LN_2 cryogenic temperature. Once this has been achieved, the bleed valve is closed and the fast response control valve to the injector is opened completely before starting the measurements. This approach assured that the variations in flowrate reduce to less than 5%. The flowrate through the injector was also calculated using Bernoulli's equation by measuring pressures upstream and downstream of the coaxial injector. The difference in measured and calculated flow velocities was less than ±5% for several different test runs which is actually quite reasonable for a cryogenic fluid that posses complex flow and heat transfer characteristics. This procedure allowed one to alleviate the onset of artificial very high cryogenic flow rate at the start of the experiment (due to art effect), and determine the true flow rates using two different approaches.

A high-speed camera, capable of recording up to 10,000 monochrome images per second, was used to record Schlieren images of the flow. The resolution of the camera was 1024×1024 pixels. The liquid and gaseous streams, as well as the two phase regions in the flow, could be examined directly using this technique. The experimental test matrix of the flow conditions examined in this paper is given in Table 1.

Case No.	Inner Fluid	Outer Fluid	Velocity [m/s] (liquid/gas)	Density Ratio (gas/liquid)	Momentum Ratio (gas/liquid)	Mass Ratio (gas/liquid)
1	LN_2	He	5 / 0	—	0	—
2	LN_2	He	5 / 300	2.3E-04	0.83	1.4E-02

Table 1. Test matrix for the flow inlet conditions examined

3. Results and Discussion

Results obtained at two specific experimental conditions are reported here. In the first case, the flow of liquid nitrogen fed through the inner tube of the injector was controlled in order to produce an average, steady-state cryogenic fluid velocity of 5 m/s. No gas was fed through the outer tube of the injector. The flow was initiated when a solenoid-operated control valve was opened. Schlieren images, showing the evolutionary behavior of the LN_2 jet after its exit from the injector during the initial 500 milliseconds of the experiment, are shown in Fig. 3a and 3b. Time zero in this image corresponds to the very first trace of the cryogenic jet exiting the injector. Note that D in the figure represents the inner diameter of inner tube in the injector.

The Schileren images reveal that initially, the nitrogen emerged as vapor, and is visible in the image due to the gradient in density between the cold nitrogen gas and the surrounding ambient air. This is attributed to the rapid evaporation of the liquid nitrogen jet after it comes in contact with the initially warmer injector tubes downstream of the cryogenic valve. During the first few milliseconds, the jet formed a mushroom-shaped structure, indicating that the interface between the flow and the quiescent surroundings was shaped by a starting vortex. After 7 milliseconds, liquid nitrogen began to emerge, and a dynamically-evolving two-phase flow was established. The interface between the cryogenic liquid and the surrounding gas was highly unstable, with the observation of numerous ligaments and smaller droplets and this is attributed to Kelvin-Helmholtz instability mechanisms. An order of magnitude estimate of the frequencies of vortical structures at the interface showed them to be in the range of 300-3000 Hz. The higher frequencies were very close to the Kelvin-Helmholtz frequencies of the interface predicted by previous researchers[10] and the lower frequencies were of the larger vortical structure that were formed due to the coalescence of smaller vortical structures generated by Kelvin-Helmholtz instability.

The time period over which this initial vapor flow extends is not constant and depends on the complex heat transfer phenomena. One can simply think of this as how warm the injector tubes were, compared to the cryogenic temperature of liquid nitrogen (77 K), when the valve is opened. In the results presented here, this period is approximately 50 ms long. During these 50 ms, the injector walls get just cold enough only to allow a "puff" of non-evaporated liquid to be injected, yet still not cold enough to sustain a continuous jet of liquid flow. This puff is recognizable by the darker regions at the injector exit at 50 ms. Because the injector walls are still significantly warm at this moment, local

vapor formation continues to exist in their vicinity with less vapor formation at the centerline away form the walls, which explains the global Schlieren images presented here characterizing the flow in the 50 – 300 ms time frame. The darker regions, associated with the initial liquid puff at 50 ms, disappear at 100 ms, once the puff is over, and lighter regions dominate especially close to the injector walls turning slightly darker at the centerline where the local vapor formation is less and begin to possess abundance of cryogenic fluid. Once the walls gradually approach the cryogenic temperature of liquid nitrogen (at some time duration between 300 and 400 ms), the local vapor formation near the walls diminishes, and the flow is dominated by the dark regions of central liquid flow, until no significant changes are observed anymore (i.e., the steady state conditions are almost been achieved) at about 500 ms. It is worth mentioning again here that the development of the flow from the moment the fluid leaves the injector exit to the achievement of steady state involves the same qualitative analysis described above but is not limited to the same instants presented here. In other words, the appearance of the initial liquid puff and the achievement of steady state can be roughly at about 30 and 350 ms, respectively, if the experiment is restarted with colder injector walls.

The flow features are also presented with flows of both cryogenic fluid and coaxial surrounding gas. In the second experiment, a steady stream of liquid nitrogen was allowed to emerge from the central tube of the injector. The injector system was allowed to cool down to 77 K at which point the steady mean velocity of liquid nitrogen was 5 m/s. A solenoid valve on the helium line was then opened to allow a flow of helium with a mean axial velocity of 300 m/s to emerge from the outer annulus of the injector. This condition produced a gas/liquid momentum ratio of 0.83. The Schlieren images obtained for the first 100 milliseconds under these experimental conditions are shown in Fig. 4a and Fig. 4b.

The sheath of helium emerging from the outer annulus was, again, found to form a toroidal vortex during the initial few milliseconds of its emergence. This vortex formation is due to the Rayleigh-Taylor instability mechanism which occurs when a lighter fluid is injected into a denser medium. It's also worth noting that initially the time taken by the gaseous jet to reach the top of the image is much longer than the liquid nitrogen jet even though the gaseous jet is injected at a much higher speed (300 m/s) than the liquid nitrogen jet (5 m/s). This is due to the higher momentum of liquid nitrogen jet than gaseous helium jet and the dispersion of gaseous helium due to its very high diffusivity. A more complex interaction between the helium and nitrogen streams was observed after first few milliseconds. Momentum was exchanged between the helium and nitrogen streams, in ways that produced distortions of the interface at a variety of length scales. The frequencies of these length scales were found to be in the range of 300-3000 Hz as predicted by previous researchers[5,6,11]. The scales involved affect mixing, and are significant in understanding mechanisms driving unstable phenomena in reacting systems. The evolutionary behavior of the flow reveals that the flow upon exit from the injector is unsteady at the initial injection of the cryogenic fluid in to the rocket engine. Once this instability is formed this sustains or grows itself in the engine to affect the mixture ratio, ignition and combustion behavior. These instabilities once formed persisted for the entire duration of the experiments, much beyond the initial few milliseconds of the data presented here. This data exemplifies the presence of instabilities in rocket engines right from the beginning of engine start-up.

Fig. 5a shows an instantaneous high-speed Schlieren image of steady-state LN_2 jet in a coaxial He flow. This image shows the development of the shear layer between the two flows. Initially a stable liquid jet can be seen emerging from the injector exit along with the coaxial He jet. As the flow progresses further downstream, the formation of vortical structures, as a result of shear layer development, destabilized the inner liquid core to break-up and mix with the surrounding gases. The liquid cryogenic jet expansion, potential core length, and the characteristic frequency associated with the unstable LN_2 jet can also be observed from Fig. 5a. In contrast, Fig. 5b shows an average of 150 high-speed Schlieren images for the same case. It can be seen that the vortical structures are not visible for the averaged case anymore, because of the cancellation and smoothening of the flow structures during the averaging process. In both parts of Fig. 5, however, the LN_2 jet is opaque to the light and thus appears dark (because of the very low light intensity, close to zero, in this region), whereas the surroundings gases are brighter and have a higher light intensity.

Figure 6 shows axial distribution of the averaged centerline intensity obtained from the averaged image. This plot shows the behavior of the LN_2 jet quantitatively, as it progresses further downstream of the injector exit. The increase in centerline intensity indicates the process of jet breakup and mixing with the surrounding gases. One can see that the increase in centerline intensity remains gradual, until

171

the breakup length of the potential core is reached. Beyond this point, the liquid jet breaks up much more rapidly, and the centerline intensity started to increase exponentially, which suggests enhanced mixing with the surrounding gases.

4. Conclusions

An experimental facility capable of obtaining accurate and repeatable transient measurements with LN$_2$ has been assembled. The behavior of liquid nitrogen stream (to simulate the cryogenic liquid oxygen), surrounded by a coannular stream of gaseous helium (to simulate gaseous hydrogen), have been examined starting from the initial cryogenic fluid injector exit under realistic engine operating conditions. The initial, dynamic interaction of the cryogenic fluid with the surrounding quiescent air and coaxial gas has been analyzed for the first time. These observations are significant, because instabilities observed at the two-phase boundary during initial startup does have a direct effect on ignition and the onset of unstable combustion in most cryogenic rocket engines.

The results showed significant effect of initial conditions on transient behavior of cryogenic flow. The liquid nitrogen jet initially emerged as vapor due to warm injector tubes. During the first few milliseconds, the jet formed a mushroom-shaped structure, indicating that the interface between the flow and the quiescent surroundings was shaped by a starting vortex. The results also showed the formation of vortical structures on the interface between the cryogenic liquid and the surrounding quiescent air with the observation of numerous ligaments and smaller droplets.

The effect of coaxial gaseous jet on the onset of cryogenic fluid instabilities and jet breakup has also been analyzed. The formation of a toroidal vortex due to Rayleigh-Taylor instability mechanism during the initial few milliseconds of gaseous flow has been observed. The complex interaction between the cryogenic stream and gaseous helium jet due to heat and momentum transfer was also observed. The results provided the role of shear layer development on the evolutionary behavior of gaseous jet and its effect on cryogenic flow instability and mixing behavior.

A combination of the non-intrusive Schlieren diagnostic technique and digital image processing has allowed us to examine the detailed features of the transient cryogenic jet under realistic rocket engine operating conditions. The results of this work provide insightful information on the flow and mixing behaviors of cryogenic jet inside a coaxial gaseous stream. Moreover, these results also exemplify the presence of instabilities in rocket engines right from the beginning of engine start-up.

Acknowledgments

References

[1]Vingert, L., Gicquel, P., Ledoux, M., Care, I., Micci, M. and Glogowski, M., "Atomization in Coaxial Jet Injectors," Chapters 3, Progress in Aeronautics and Astronautics, Vol. 200, AIAA, 2004, pp. 105-140.

[2]Mayer, W., Smith, J., "Fundamentals of Supercritical Mixing and Combustion of Cryogenic Propellants," Chapter 9, Progress in Aeronautics and Astronautics, Vol. 200, AIAA, 2004, pp. 339-367.

[3]Oschwald, M., Smith, J. J., Branam, R., Hussong, J., Schik, A., Chehroudi, B. and Talley, D., "Injection of Fluids into Supercritical Environments," Combustion Science and Technology, 178, 2006, pp. 49-100.

[4]Gautam, V. and Gupta A. K., "Simulation of Flow and Mixing from a Coaxial Rocket Injector", 44th Aerospace Sciences Meeting and Exhibits, Reno, Nevada, Jan. 09 - 12, 2006, Paper No. AIAA 2006-1160.

[5]Gautam, V. and Gupta A. K., "Cryogenic Flow and Mixing from a Single Element Coaxial Rocket Injector", 42nd AIAA/ASME/SAE/ASEE Joint Propulsion Conference, Sacramento, California, July 09 - 12, 2006, Paper No. AIAA-2006-4529.

[6]Gautam, V. and Gupta, A. K.: Simulation of Flow and Mixing from a Cryogenic Rocket Injector, Accepted for Publication in Journal of Propulsion and Power, 2006 (in press).

[7]Emdee, J.L., Fentress, C.S. and Malinowski, M.R., "Development Testing for the RL10E-1 Engine," AIAA Paper No. 97-3094, July 1997.

[8]McNelis, N.B. and Haberbusch, M.S., "Hot Fire Ignition Test with Densified Liquid Hydrogen Using a RL10B-2 Cryogenic H2/O2 Rocket Engine," AIAA Paper No. 97-2688, July 1997.

[9]Personal communication with researchers at NASA and Purdue University.

[10]Lin, S.P. and Reitz, R. D., "Drop and Spray Formation from a Liquid Jet," Annual Review Fluid Mechanics, Vol. 30, 1998, pp. 85-105.

[11]Lasheras, J.C. and Hoppfinger, E. J., "Liquid Jet Instability and Atomization in a Coaxial Gas Stream," Annual Review Fluid Mechanics, Vol. 32, 2000, pp. 275-308.
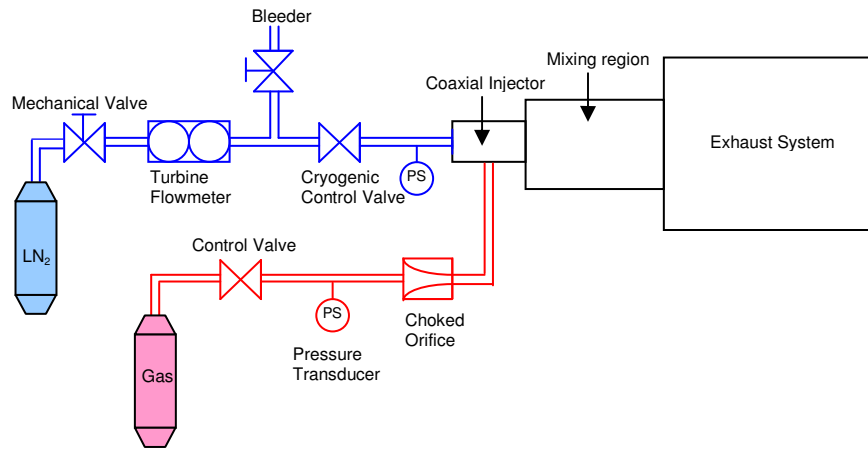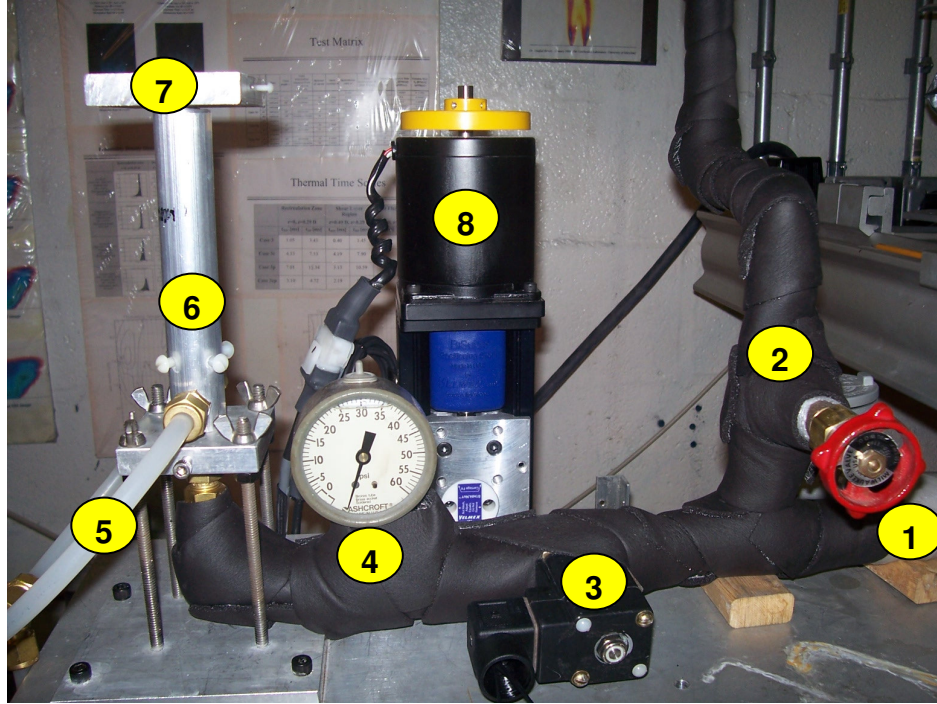
Fig. 1a. Schematic diagram of the experimental facility

1) Turbine flow meter, 2) Bleed connection, 3) LN₂ solenoid valve, 4) Pressure gauge, 5) Gas supply, 6) Injector, 7) Face plate, 8) Elevation mechanism

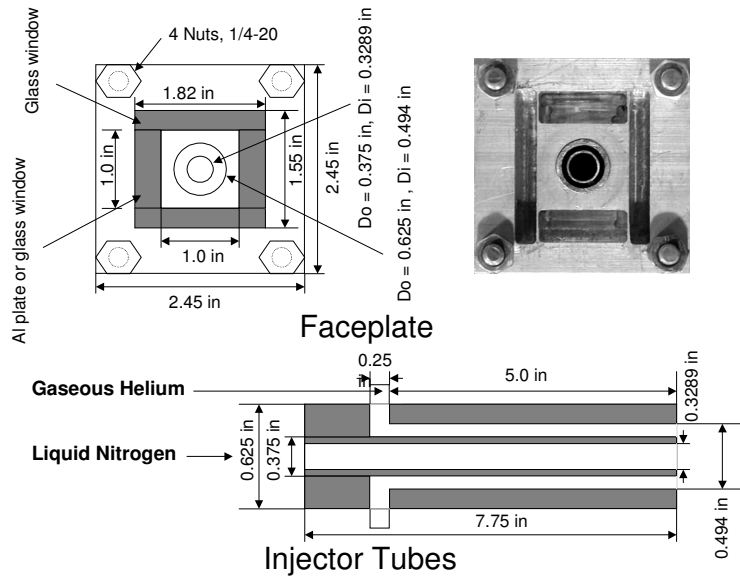**Fig. 1b. Photograph of the single rocket injector experimental facility**

Fig. 2a. The injector faceplate and injector dimensions
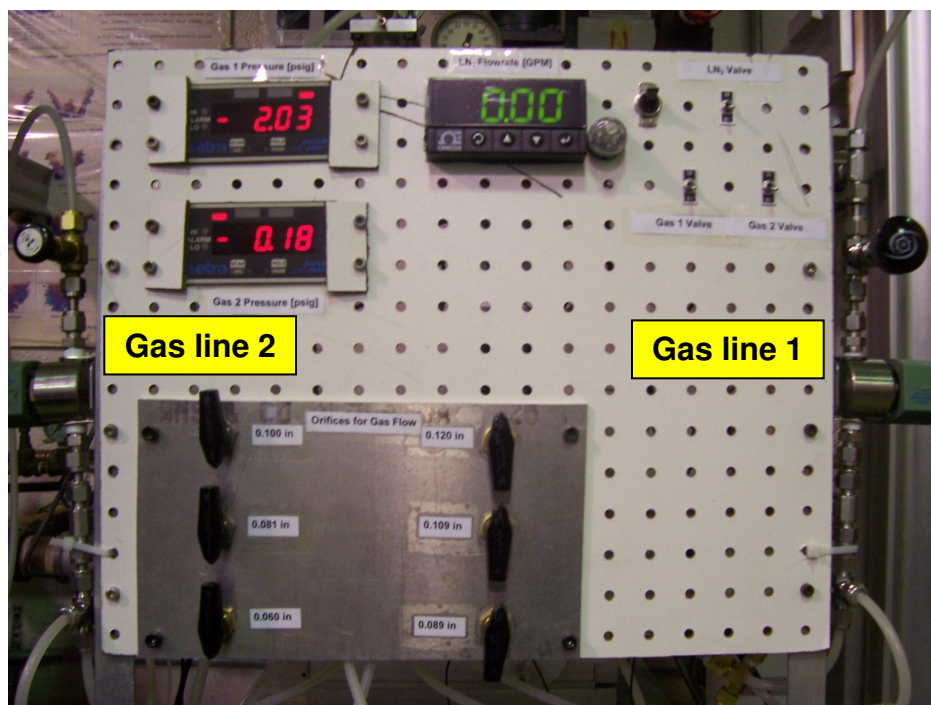
Fig. 2b. Photograph of facility control board along with gaseous flow lines
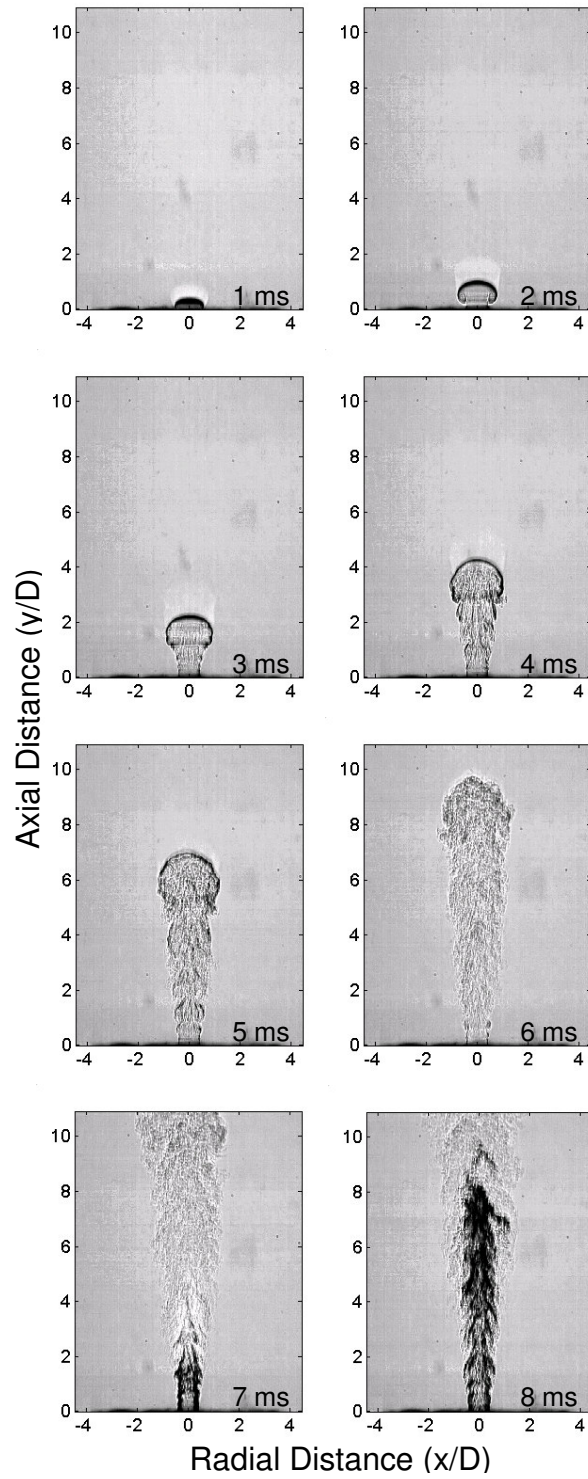
Fig. 3a. Initial emergence of liquid nitrogen jet into quiescent air without a surrounding flow of helium during the first 8ms; D = 0.33 inches
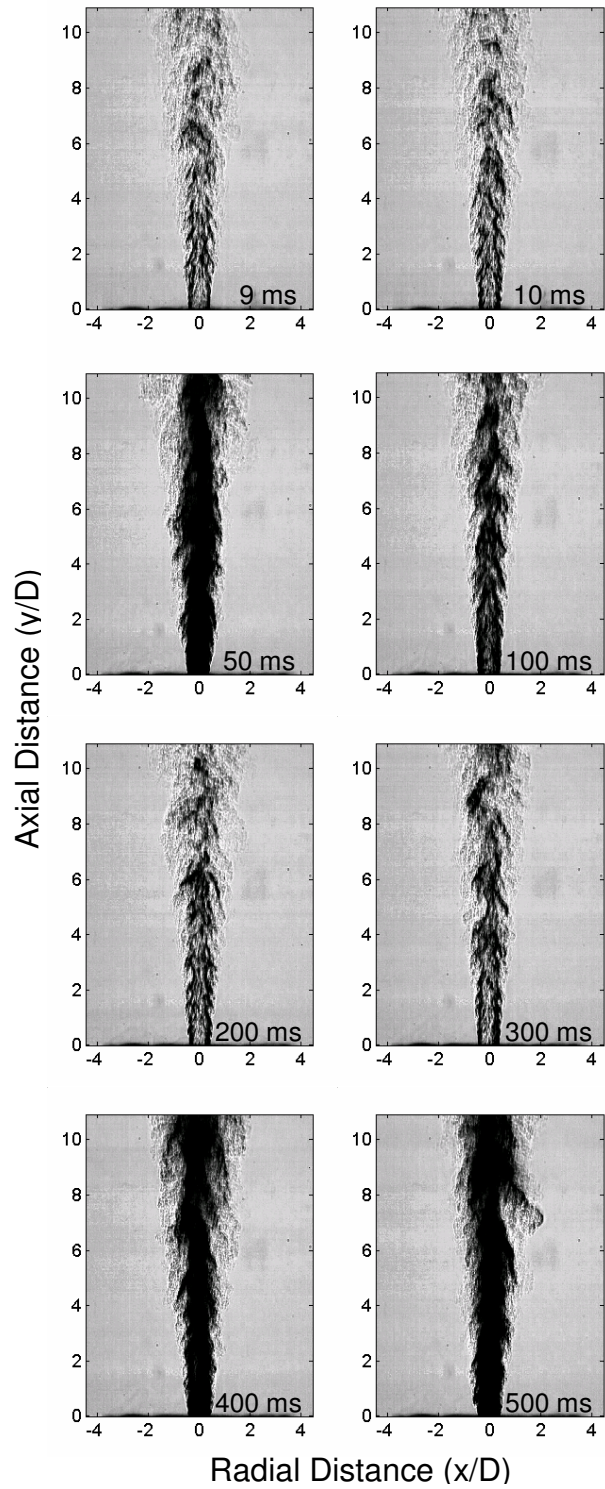
Fig. 3b. Fate of liquid nitrogen jet from 10 to 500 ms after intial exit emerging into quiescent air without a surrounding flow of helium; D = 0.33 inches

177
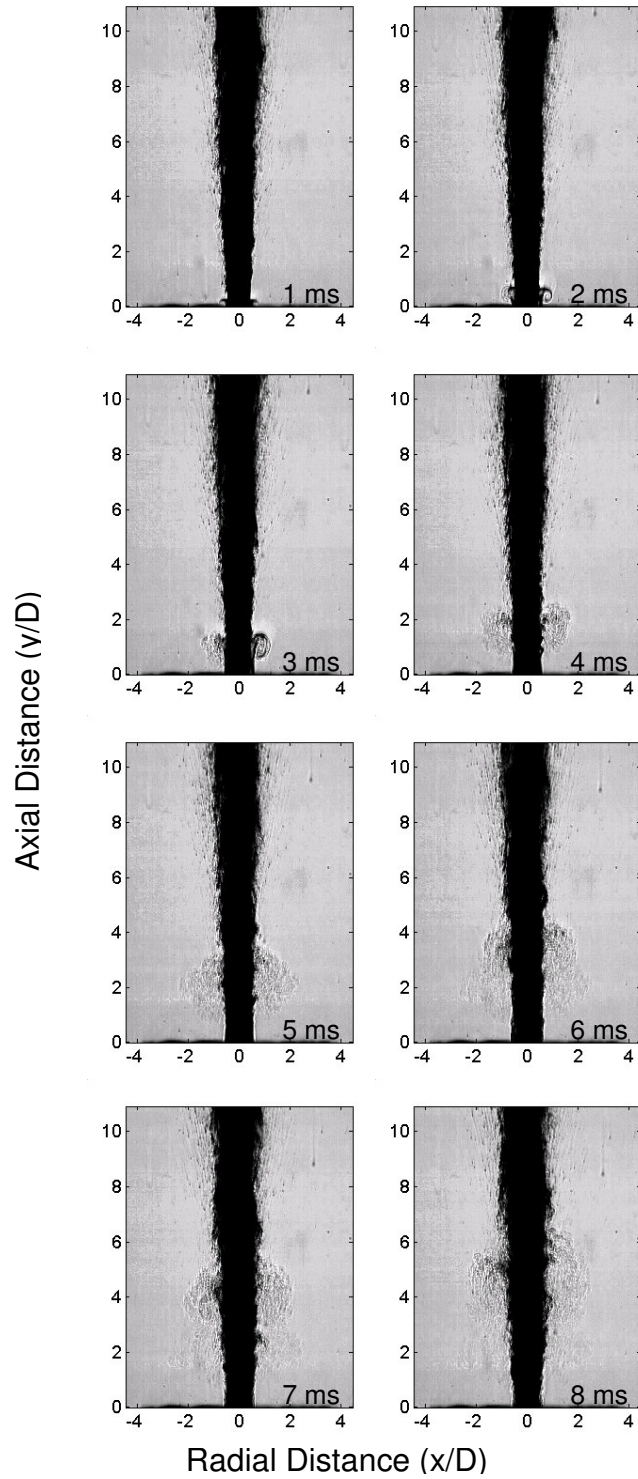
Fig. 4a. The fate of liquid nitrogen during the first 8 ms from the injector exit with steady stream of annular helium flow around the LN2 jet; D = 0.33 inches
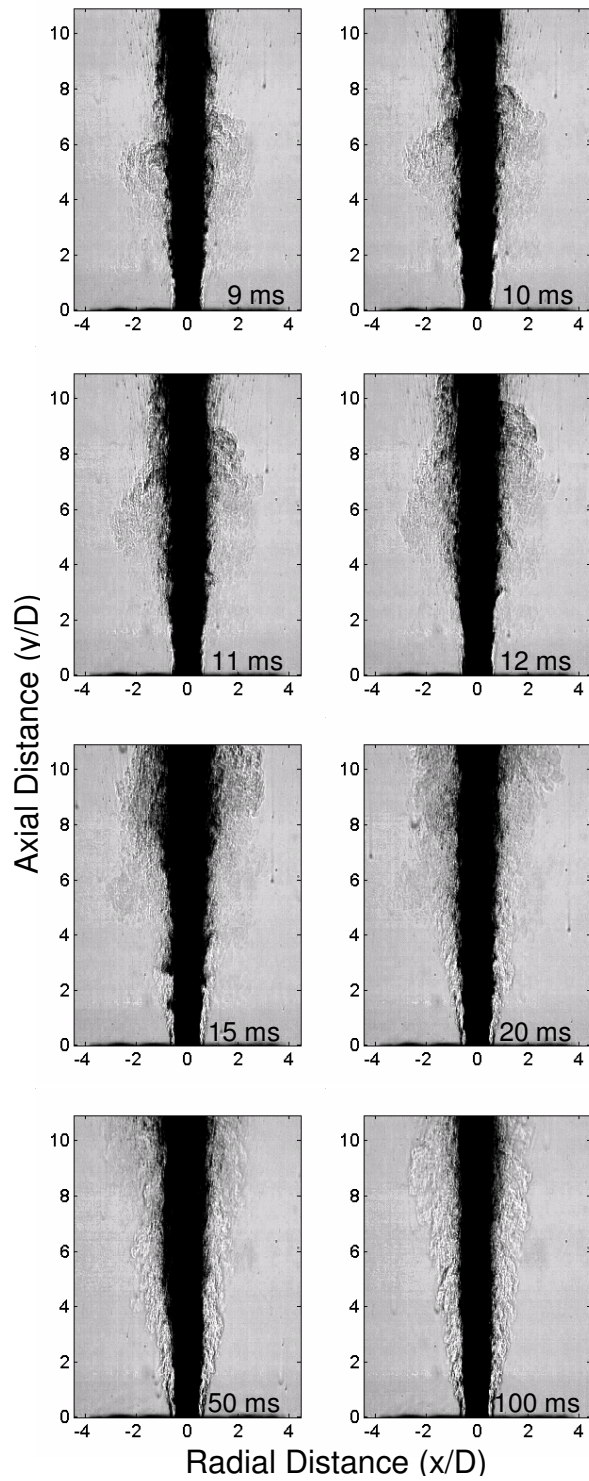
Fig. 4b. The fate of liquid nitrogen during the first 9 to 100 ms from the injector exit with steady stream of annular helium flow around the LN2 jet; D = 0.33 inches

179

**Figure 5. High-speed Schlieren image of steady-state LN$_2$/He flow;
a) Instantaneous image, b) Average of 150 images**

Figure 6. Averaged centerline intensity distribution of steady-state LN$_2$/He flow

Characterization of Cryogenic Flow and Atomization from a Coaxial Rocket Injector
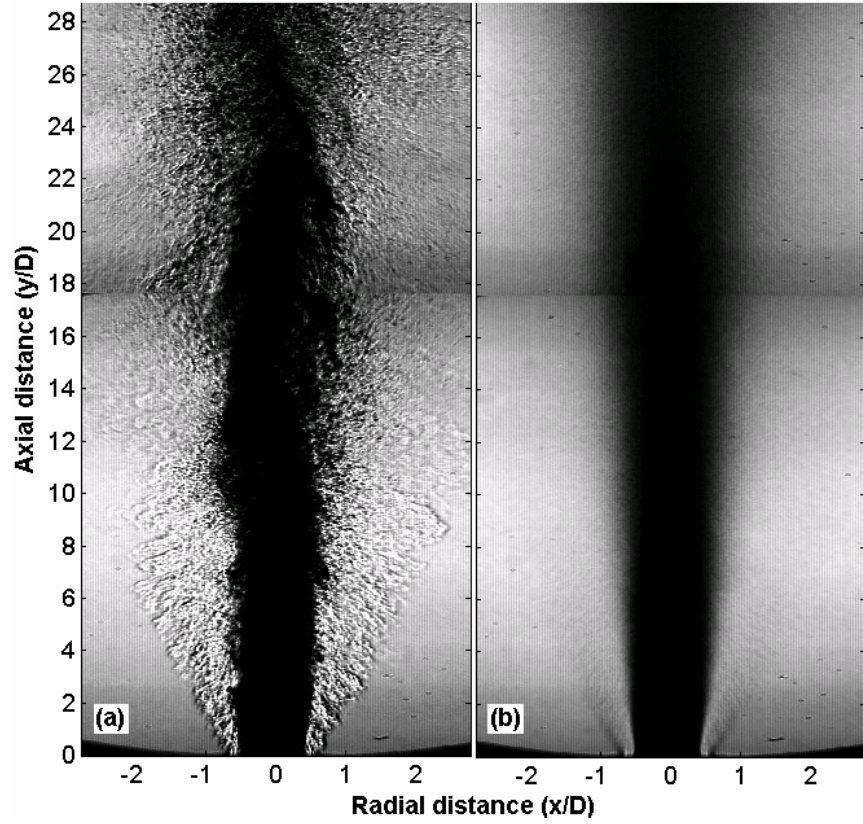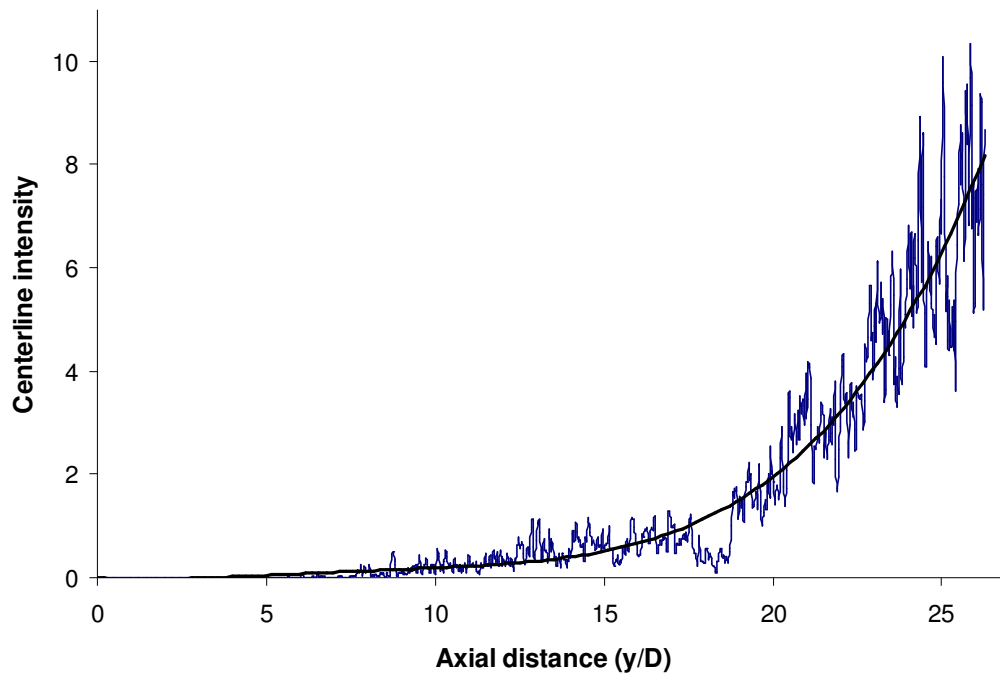
V. Gautam* and A.K.Gupta**
Mechanical Engineering Department
University of Maryland, College Park, MD
*email: akgupta@eng.umd.edu

The effect of some of the important flow parameters, such as, velocity ratio, density ratio and momentum ratio have been examined experimentally on potential core length of the cryogenic fluid injected from a single-element coaxial injector. The injector simulated one element of the cryogenic rocket engine injectors under realistic operating conditions. This work focuses specifically on the evolution of liquid nitrogen jet instability and breakup under steady state atmospheric conditions. The results showed significant role of velocity ratio, density ratio, momentum ratio along with the strong heat transfer effect of the surrounding atmosphere on the cryogenic liquid nitrogen jet behavior. The potential core length of the cryogenic liquid nitrogen showed a local peak as a function of velocity of the gaseous jet. However, the core length showed insensitivity to changes in density of the gaseous jet. The results also provided a strong evidence of the heat-shielding effect of the coaxial gaseous jet. The heat transfer from the surroundings to the cold LN_2 jet is reduced significantly by the presence of the gaseous jet, which strongly affects the potential core length of liquid nitrogen jet.

The experimental diagnostic technique used here is Schlieren imaging using a high speed camera to analyze the global flow behavior of liquid nitrogen jet. The Schlieren images were processed using image processing techniques to obtain quantitative information of the flow.

1. Introduction

Cryogenic flow from a shear coaxial injector is one of the most crucial research areas associated with the rocket engine technology for future space propulsion. Although there have been several attempts to analyze and predict the behavior of cryogenic jet in the presence of a high speed coaxial gaseous jet, the current knowledge is still not adequate. The objective of this research is to analyze the destabilization and disintegration of cryogenic flow from a shear coaxial injector under typical rocket engine operating conditions prior to ignition.[1]

Non-isothermal flow conditions and huge variations in physical properties of the fluids make it difficult to accurately analyze the flow behavior of a cryogenic jet. The destabilization and disintegration of a liquid jet in a two-phase coaxial flow takes place due to several complex physical processes, such as, the development of a shear layer due to velocity gradients, the turbulent interactions and vorticity produced by the boundary layer, and the interaction between inertial, surface tension and viscous forces. A combination of all these destabilization processes along with the complex thermo-

physical processes related to phase change makes it very challenging to understand and analyze the flow and atomization behaviors of two-phase cryogenic flows.[2,3,4]

Apart from other operational conditions such as, fluid properties, surrounding conditions and injector inlet characteristics, two most important parameters that affect the physical processes associated with liquid jet destabilization and break up in coaxial flows are velocity and density ratios between the jets. Gautam and Gupta[5], Strakey et al.[6] and Villermaux[7] have shown that the momentum flux ratio ($MR = \rho_g v_g^2 / \rho_l v_l^2$) is one of the key parameters for single-phase or two-phase coaxial jet mixing. The subscripts g and l in the above equation refers to gas and liquid phases, respectively.

They demonstrated that the liquid-jet breakup and mixing with the surrounding gases are significantly affected by the momentum flux ratio between the jets. Villermaux and Rehab[8], Farago and Chigier[9], Rehab et al.[10], and Lasheras et al.[11] in their earlier investigations provided some characterization of coaxial jets using non-cryogenic fluids. Although the work performed on non-cryogenic fluids is not directly relevant to real rocket injector conditions, the results obtained from these investigations provided important insightful information on the physical processes associated with coaxial jet injection and mixing. Some other more relevant work has been reported on the behavior of cryogenic fluids under super-atmospheric sub-critical and super-critical conditions. Pal et al.[12], Vingert et al.[13] and Mayer et al.[14-18] studied the high-pressure injection and mixing processes of cryogenic propellants under reacting and non-reacting conditions. In another more recent study, Oschwald et al.[19] investigated the effect of chamber pressure, initial jet temperature and acoustic waves on the atomization, mixing, and combustion phenomena of LOX/H_2 coaxial rocket injectors. Gautam and Gupta[20-23] studied the flow and evaporation characteristics of cryogenic fluids under normal atmospheric conditions to gain insight on the initial mixing that affects the ignition. However, despite all these research efforts, the complete understanding of cryogenic fluid injection and mixing behavior prior to ignition under all relevant rocket engine conditions is still a major challenge.

This study analyzes breakup length of a cryogenic LN$_2$ jet surrounded by a coaxial gaseous stream at normal atmospheric pressure conditions using high-speed Schlieren diagnostic technique. Specifically the characteristic inner potential core lengths have been examined for different velocities and densities of the surrounding gaseous jet. The experimental matrix allowed for detailed examination of some of the important flow parameters, such as the velocity, density, and momentum ratio of the jets.

2. Experimental Setup and Condition

The single element experimental facility, described in detail in ref. 23, is used to simulate the cryogenic flow behavior from a coaxial injector. For this research, the cryogenic propellant behavior of liquid oxygen (LOX) was simulated with liquid nitrogen (LN$_2$) flowing through the inner tube of the coaxial injector. Gaseous Helium (He) was used to simulate the behavior of gaseous hydrogen flowing through the outer annulus. A schematic diagram of the injector tubes along with the injector face plate with dimensions through which the flows emerge is shown in Fig. 1. The inner injector tube has inner diameter of D = 0.33 inches with a wall thickness of 0.02 inches. The flows of the gaseous and cryogenic fluids into the experimental facility were controlled using fast response (< 50 ms) solenoid valves.

The flowrate of the gaseous jet was measured using precision orifices preceded with a digital pressure sensor. The average temperature of the gaseous flow at the injector exit was measured using a thermocouple, and the velocity was calculated under the assumption of ideal gas density. The flowrate of LN$_2$ was measured using a liquid turbine flowmeter as described in ref 23. The volumetric flowrate of steady LN$_2$ jet was fixed at 4.5 GPM for all experiments conducted in this study with average temperature and density of the LN$_2$ jet at the injector exit taken as 77 K and 808 kg/m^3, respectively. The measured temperature of the LN$_2$ at the injector exit was found to be very close to this temperature.

The experimental test matrix of the flow conditions examined in this paper is given in Table 3. Two different set of experiments were performed to analyze the effect of gas velocity and density on the flow characteristics of the cryogenic jet. In the first experimental set (cases 1-13), the density of co-flowing gas was kept constant (helium at 0.185 kg/m^3) while varying its velocity. On the other hand, for the second experimental set (cases 14-17), the velocity of co-flowing gas was kept constant and its

182

density varied by mixing two gases of different density but similar calorific properties (helium and argon).

Schlieren clips of the full flowfield have been obtained using a high-speed camera at a framing rate of 512 frames/second having resolution of 1024 × 512 pixels. The camera responds to visible wavelengths of the spectrum. The images, extracted from the video clips, were processed using the image-processing toolbox of the Matlab software to provide the potential core lengths under the various cases.

3. Results and Discussion

Results analyzing the effects of change in velocity and density of the gaseous stream on the evolutionary behavior of the LN_2 jet are discussed here. Figure 2a shows an instantaneous Schlieren image of a steady liquid nitrogen jet (dark high density jet) surrounded by a coaxial helium stream (light low density jet). The image also shows the development of the shear layer between the two coaxial jets. A steady liquid jet surrounded by a coaxial helium jet can be seen close to the injector exit until around 2 diameters downstream. The formation of vortical structures due to the development of shear layer starts taking place as the flow progresses further downstream. These vertical structures destabilize the inner

Case No.	Inner Fluid	Outer Fluid	Velocity [m/s] (liquid/gas)	Density Ratio (gas/liquid)	Momentum Ratio (gas/liquid)	Mass Ratio (gas/liquid)
1	LN_2	He	5 / 0	—	0	—
2	LN_2	He	5 / 5	2.3E-04	2.3E-04	2.4E-04
3	LN_2	He	5 / 10	2.3E-04	9.2E-04	4.8E-04
4	LN_2	He	5 / 20	2.3E-04	3.7E-03	9.7E.04
5	LN_2	He	5 / 30	2.3E-04	8.3E-03	1.5E-03
6	LN_2	He	5 / 40	2.3E-04	14.7E-03	1.9E-03
7	LN_2	He	5 / 50	2.3E-04	23.0E-03	2.4E-03
8	LN_2	He	5 / 100	2.3E-04	91.9E-03	4.9E-03
9	LN_2	He	5 / 150	2.3E-04	0.21	7.2E-03
10	LN_2	He	5 / 200	2.3E-04	0.37	9.7E-03
11	LN_2	He	5 / 250	2.3E-04	0.57	1.2E-02
12	LN_2	He	5 / 300	2.3E-04	0.83	1.4E-02
13	LN_2	He	5 / 325	2.3E-04	0.98	1.6E-02
14	LN_2	(Gas mix)	5 / 100	5.2E-04	0.21	1.1E-02
15	LN_2	(Gas mix)	5 / 100	9.2E-04	0.37	1.9E-02
16	LN_2	(Gas mix)	5 / 100	1.4E-03	0.57	3.0E-02
17	LN_2	(Gas mix)	5 / 100	2.3E-03	0.92	4.8E-02

Table 1. Test matrix for the flow inlet conditions examined

liquid core to break-up into droplets and ligaments[22] and mix with the surrounding gases. This image also shows the spray expansion, potential core length, and the characteristic frequency associated with the unstable LN_2 jet. Figure 2b, on the other hand, shows an average of 150 high-speed Schlieren images for the same case. This image was obtained to calculate the average potential core length of the

liquid nitrogen jet. It can be seen that the vortical structures are not visible for the averaged case because of the cancellation and smoothening of the unsteady flow structures during the averaging process.

The axial distribution of the centerline intensity obtained from the averaged image is shown in figure 3. The centerline intensity was plotted to show the behavior of the LN_2 jet quantitatively, as it progresses downstream of the injector exit. The increase in centerline intensity indicates the decrease in density of the fluid at the centerline to reveal the process of LN_2 jet breakup and mixing with the surrounding gases. The increase in centerline intensity (decrease in fluid density) remains low and insignificant, until the breakup length of the liquid potential core is reached. Beyond this point, the liquid jet breaks into droplets and ligaments and start rapid vaporization. This rapid evaporation of liquid droplets and ligaments and its mixing with the surrounding gases further reduces the density of centerline fluid to cause in an exponential increase in the centerline intensity. For the present experiments, the potential core length is defined as the point where the centerline intensity has the largest axial gradient. The axial gradients were analyzed using the image processing capabilities of Matlab. This point was found to be close to an intensity of 1.0 for all the cases. A comparison of the centerline intensities for some of the selected cases are shown in Figure 3b. The gas velocity significantly affects the centerline intensity distribution and subsequently the potential core length of the cryogenic fluid jet, as discussed below.

The potential core lengths obtained from the centerline intensity distribution are presented in Figure 4. The theoretical potential core lengths, proposed by previous researchers in a semi-empirical form, have also been plotted for the purpose of comparison. A close look at this plot reveals some interesting features. The experimentally determined potential core length of the LN_2 jet increases with increase in velocity of the gaseous jet, until this velocity reaches a value of approximately 100 m/s, beyond which the potential core length of the cryogenic (liquid) jet decreases. Whereas according to previous research, the potential core length of the liquid jet should decrease with increase in velocity of the gaseous jet, because this increases the momentum ratio between the jets. These predictions are undoubtedly accurate for sub-critical non-cryogenic fluid (water or ethanol for example). The unique behavior of LN_2 jet is, however, due to the heat transfer effects of the warmer surroundings on the supercritical LN_2 jet. All of the previous archival research, conducted on the characterization of the potential core length of a liquid jet inside a coaxial gaseous one, has been carried out on non-cryogenic fluids, where the flows were mostly isothermal. However, the non-cryogenic fluid cases are substantially different than that for a cryogenic LN_2 jet injected in warm surroundings. The vaporization of LN_2 due to the heat transfer from the surroundings has an effect as significant as that of the shearing of the surrounding gaseous jet on the breakup of the LN_2 jet. In light of this vitally important fact, the discrepancy observed in Figure 4 between the results from this work with the previous research can be explained as follows.

Initially, when the cryogenic LN_2 is injected solely with no coaxial gaseous jet, the LN_2 jet is in direct contact with the warm surrounding air that acts as a heat source for the cryogenic jet. The heat transfer from the surrounding atmosphere allows fast vaporization of the central LN_2 core to assist in rapid dispersion of the cryogenic jet, resulting in a short potential core length. However, when the coaxial gaseous jet is introduced, it creates a gaseous sheath around the cold LN_2 jet, preventing it from gaining heat from the surroundings because of its really low thermal conductivity. At low helium velocities (up to about 100 m/s), the destabilization of LN_2 due to the shearing effects of helium is still low and not as effective. However, the destabilization due to heat transfer, which is the dominant mode of destabilization at these conditions, gets affected by the introduction of helium. This results in longer potential cores with slight increase in helium velocity. Close to a helium velocity of 100 m/s, the shear-layer destabilizing effect of the helium jet becomes comparable to its heat-shielding effect. Thus both effects balance each other out and the potential core length achieves a local maximum. At higher velocities, the shear-layer destabilization effect of the helium jet overcomes its heat-shielding one, and the potential core length decreases. At a helium velocity of about 325 m/s, the potential core length becomes even shorter than the corresponding one in the absence of the helium jet, which suggests that at and above this velocity, the effect of shear-layer destabilization of helium on the LN_2 jet completely prevails over the helium heat-shielding effect. A schematic of the individual effects of heat shielding and shear-layer destabilization is plotted in Figure 5, together with their combined effect on the potential core length of the cryogenic LN_2 jet.

Another important feature of figure 4 is longer potential core length of cryogenic LN_2 jet than non-cryogenic ones at momentum ratios closer to 1. This is due to another effect of heat transfer from coaxial gaseous jet to cold LN_2 jet. The moment coaxial gaseous jet comes in contact with cold LN_2 jet, an infinitesimally small layer of gaseous nitrogen forms at the interface of the two fluids. This gaseous nitrogen layer expands radially outwards and pushes the coaxial gas away from the LN_2 jet, which in turns reduces the shearing effect of coaxial gaseous jet on central cryogenic jet. This reduction in shearing effect causes the larger liquid core lengths at higher momentum ratios.

The second set of experiments conducted in this study on the characterization of the LN_2 potential core length were aimed at investigating the effect of density of the gaseous jet while keeping its injection velocity constant (cases 14 – 17 in Table 1). Figure 6 shows a comparison of the flow centerline intensity with the LN_2 jet surrounded by a gas mixture of a different density for several of the cases examined. The velocity of the gaseous jet has been kept constant at 100 m/s, which is the point of largest potential core length, as observed from the previous analysis. Figure 6 reveals an interesting observation when compared to Figure 3b. All the centerline intensity curves of the different densities coincide, which suggests that there is little or no effect of changing the gas density on the behavior of the cryogenic liquid nitrogen jet. Another fact to notice from Figure 6 is that the centerline intensity curve changes considerably, once a surrounding gaseous jet is introduced. This again suggests the heat shielding effect of the coaxial gaseous jet.

In order to further strengthen the observations made from Figure 4, figure 7 show the variation of potential core length with variation in density of the surrounding gas. It can be seen from Figures 7 that the potential core length remains almost unaffected with the change in density of the surrounding gas jet, although changing the gas density changes the momentum ratio of the jets. Figure 8 follows the same discussion and shows the variation of the potential core lengths with the momentum ratio of the jets for both velocity based and density based cases. Since the density of the gaseous jet was kept constant throughout for cases 1 – 13 where only the velocity was changed, it can be easily seen that the potential core length follows a similar trend as velocity when plotted against the momentum ratio. However, for cases 14-17, where the velocity was kept constant and gas density changed, momentum ratio shows almost negligible effect on the potential core length.

To further understand this relatively unique behavior we have examined some of the heat transfer characteristics of the gases used to create these gas mixture jets of different densities. For the present experiments, helium and argon have been used in different proportions to create a gas mixture of the desired target density. Since helium and argon are both monoatomic gases, their heat capacities are the same, but their individual thermal conductivities possess a striking difference. While the thermal conductivity of helium is approximately 151 mW/m.K, that of argon is only 18 mW/m.K. This suggests that as the density of the gas mixture is increased by mixing more argon and less helium, the momentum ratio of the gas mixture jet increases but at the expense of decreased thermal conductivity at the same time. Figure 9 shows the variation of thermal conductivity (mW/m.K) of the mixture gaseous jet with momentum ratio between the liquid and gas jet for the fixed liquid and gas jet velocities, wherein thermal conductivities for the mixtures are calculated by the correlation given in ref 24. Hence, it can be seen that increasing the density of the coaxial gas leads to two different physical phenomena to balance each other out, namely a longer LN_2 potential core resulting from a heat-shielding argon-rich gaseous jet and a shorter core resulting from this higher-momentum-ratio jet. Hence, no significant change occurs in the potential core length of the LN_2 jet as the density of the surrounding gas mixture is changed. These results strengthen our belief further on the importance of the effect of heat transfer on cryogenic fluid flow, which has not been emphasized or examined in prior research.

4. Conclusions

The effects of some of the most important flow parameters such as, velocity, density, and momentum ratios of a flow emerging from a characteristic single-element coaxial rocket engine injector have been examined experimentally over a range of experimental conditions. The flow conditions examined are characteristic of the rocket engine conditions at lift-off prior to ignition to provide a simple analogy and simulation of the flow and mixing behaviors from single-element injectors under relevant rocket engine operating conditions. The potential core length of the cryogenic liquid jet has been examined experimentally for different coaxial gas velocities and densities.

The results revealed a key effect of heat transfer from the surroundings on the flow behavior of such an injector flow that involves a central cryogenic fluid jet surrounded by an outer gaseous flow. The effect of momentum ratio was found to be pronounced as well but more deeply manifested in the variations of the velocity of the surrounding gaseous jet than that from the variations of gaseous jet density. The potential core length of the cryogenic LN_2 shows a local peak when plotted against the velocity of the gaseous jet. However, the core length showed insensitivity to changes in density of the gaseous jet. Present results provide new insights as the previous results had suggested that the potential core length of the liquid jet should decrease absolutely with the increase in velocity of the gaseous jet, because of the increased the momentum ratio between the jets. These suggestions are undoubtedly accurate, if the liquid jet is a sub-critical non-cryogenic fluid (e.g., water or alcohol). The unique behavior of LN_2 jet is, however, due to the heat transfer effects of the surroundings on the supercritical LN_2 jet. The results provide a strong evidence of the heat-shielding effect of the coaxial gaseous jet. The heat transfer from the surroundings to the cold LN_2 jet is reduced significantly by the presence of the gaseous jet, which strongly affects the potential core length of the LN_2 jet.

A combination of the non-intrusive Schlieren diagnostic technique and digital image processing has allowed us to examine the detailed features of the cryogenic injector jet under simulated rocket engine operating conditions. The results from this research provide insightful information on the flow and mixing behavior of cryogenic jet flowing concentrically in a surrounding coaxial gaseous stream. Moreover, these results can also be used to validate computational models under non-reacting flow conditions.

Acknowledgments

References

[1]Huzel, D., Huang, D., *Modern Engineering for Design of Liquid Propellant Rocket Engines*, Progress in Aeronautics and Astronautics, Vol. 147, AIAA, Washington, DC, 1992, pp. 104-110.

[2]Lasheras, J.C. and Hoppfinger, E. J., "Liquid Jet Instability and Atomization in a Coaxial Gas Stream," *Annual Review Fluid Mechanics*, Vol. 32, 2000, pp. 275-308.

[3]Vingert, L., Gicquel, P., Lourme, D., and Menoret, L*.,* "Coaxial Injector Atomization," *Liquid Rocket Engine Combustion Instability*, edited by Yang, V. and Anderson W. E., Progress in Aeronautics and Astronautics, Vol. 169, AIAA, Washington, DC, 1994, pp. 145-189.

[4]Mayer, W., and Smith, J. J., "Fundamentals of Supercritical Mixing and Combustion of Cryogenic Propellants", *Liquid Rocket Thrust Chambers: Aspects of Modeling, Analysis and Design*, edited by Yang, V., Habiballah, M., Popp, M. and Hulka, J., Progress in Aeronautics and Astronautics, Vol. 200, AIAA, Washington, DC, 2004, pp. 339-367.

[5]Gautam, V., and Gupta, A. K., "Simulation of Mixing in Rocket Engine Injector under In-Space Conditions," *41st AIAA/ASME/ASME/SAE/ASEE Joint Propulsion Conference*, Tucson, AZ, July 10-13, 2005, AIAA 2005-1445.

[6]Strakey, P. A., Talley, D. G. and Hutt, J. J., "Mixing Characteristics of Coaxial Injectors at High Gas/Liquid Momentum Ratios," *Journal of Propulsion and Power*, Vol. 17, No. 2, March-April 2001, pp. 402-410.

[7]Villermaux, E., "Mixing and Spray Formation in Coaxial Jets," *Journal of Propulsion and Power*, Vol. 14, No. 5, Sep-Oct 1998, pp. 807-817.

[8]Villermaux, E. and Rehab, H., "Mixing in Coaxial Jets," *Journal of Fluid Mechanics*, Vol. 425, 2000, pp. 161-185.

[9]Farago, Z., and Chigier, N., "Morphological Classification of Disintegration of Round Liquid Jets," *Atomization and Sprays*, Vol. 2, No. 2, 1992, pp. 137-153.

[10]Rehab H, Villermaux E, Hopfinger, E. J., "Flow regimes of large velocity ratio coaxial jets," *Journal of Fluid Mechanics*, Vol. 345, 1997, pp. 357-381.

[11]Lasheras, J.C., Villermaux, E. and Hopfinger, E. J., "Breakup and Atomization of a Round Jet by a High Speed Annular Air Jet," *Journal of Fluid Mechanics*, Vol. 357, 1998, pp. 351-379.

[12]Pal, S., Moser, M. D., Ryan, H. M., Foust, M. J., Santero, R. J., "Shear Coaxial Injector Atomization Phenomena for Combusting and Non-Combusting Conditions," *Atomization and Sprays*, Vol. 6, 1996, pp. 227-244.

[13]Vingert, L., Gicquel, P., Ledoux, M., Care, I., Micci, M., and Glogowski, M., "Atomization in Coaxial Jet Injectors," *Liquid Rocket Thrust Chambers: Aspects of Modeling, Analysis and Design*, edited by Yang, V., Habiballah, M., Popp, M. and Hulka, J., Progress in Aeronautics and Astronautics, Vol. 200, AIAA, Washington, DC, 2004, pp. 105-140.

[14]Mayer, W. and Tamura, H., "Propellant Injection in a Liquid Oxygen/Gaseous Hydrogen Rocket Engine," *Journal of Propulsion and Power*, Vol. 12, No. 6, Nov-Dec 1996, pp. 1137-1147.

[15]Mayer, W., Schik, A., Vielle, B., Chauveau, C., Gokalp, I., Talley, D. and Woodward, R., "Atomization and Breakup of Cryogenic Propellants Under High Pressure Subcritical and Supercritical Conditions," *Journal of Propulsion and Power*, Vol. 14, No. 5, September-October 1998, pp. 835-842.

[16]Mayer, W., Schik, A., Schaffler, M., and Tamura, H., "Injection and Mixing Processes in High Pressure Liquid Oxygen/Gaseous Hydrogen Rocket Combustors," *Journal of Propulsion and Power*, Vol. 16, No. 5, Sep.-Oct. 2000, pp. 823-828.

[17]Mayer, W., Ivancic, B., Schik, A. and Hornung, U., "Propellant Atomization and Ignition Phenomena in Liquid Oxygen/ Gaseous Hydrogen Rocket Combustors," *Journal of Propulsion and Power*, Vol. 17, No. 4, July-Aug. 2001, pp. 794-799.

[18]Branam, R. and Mayer, W., Schik, "Characterization of Cryogenic Injection at Supercritical Pressures," *Journal of Propulsion and Power*, Vol. 19, No. 3, May-June 2003, pp. 342-355.

[19]Oschwald, M., Smith, J. J., Branam, R., Hussong, J., Schik, A., Chehroudi, B. and Talley, D., "Injection of Fluids into Supercritical Environments," *Combustion Science and Technology*, 178, 2006, pp. 49-100.

[20]Gautam, V. and Gupta, A. K., "Simulation of Flow and Mixing from a Coaxial Rocket Injector," *44th AIAA Aerospace Sciences Meeting*, Reno, NV, January 9-12, 2006, AIAA 2006-1160.

[21]Gautam, V. and Gupta A. K., "Cryogenic Flow and Mixing from a Single Element Coaxial Rocket Injector," *42nd AIAA/ASME/SAE/ASEE Joint Propulsion Conference*, Sacramento, California, July 09 - 12, 2006, Paper No. AIAA-2006-4529.

[22]Gautam, V. and Gupta, A. K., "Simulation of Flow and Mixing from a Cryogenic Rocket Injector," *Journal of Propulsion and Power*, Vol. 23, No. 1, Jan-Feb 2007, pp 123-130.

[23]Gautam, V. and Gupta, A. K., "Cryogenic Flow Instability and Mixing from a Coaxial Rocket Injector," *45th Aerospace Sciences Meeting and Exhibits*, Reno, Nevada, Jan. 08 - 11, 2007, Paper No. AIAA-2007-0573.

[24]Mason, E. A., and Saxena, S. C., "Approximate Formula for the Thermal Conductivity of Gas Mixtures," *The Physics of Fluids*, Vol. 1, No. 5, Sep.-Oct. 1958, pp. 361-369.
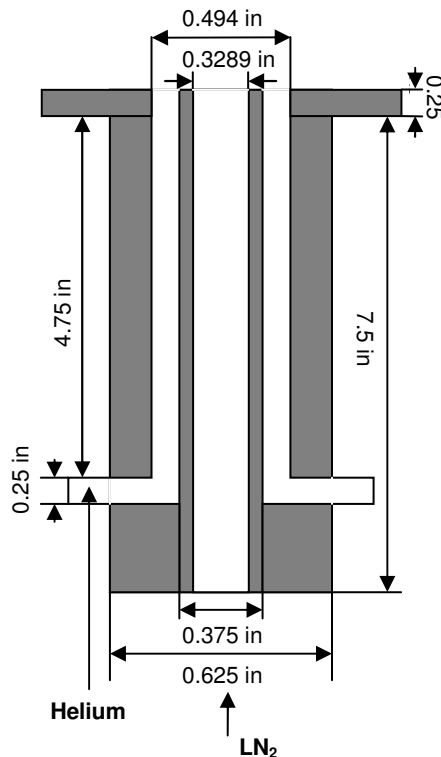
Figure 1. A schematic diagram of the coaxial injector setup along with the dimensions
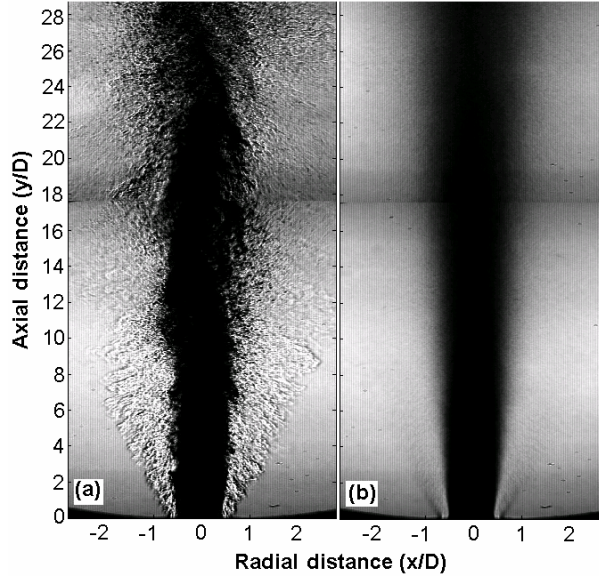
Figure 2. Sample high-speed Schlieren image of LN$_2$/He flow (MR ≈ 1.0); (a) Instantaneous image,(b) Average of 150 images
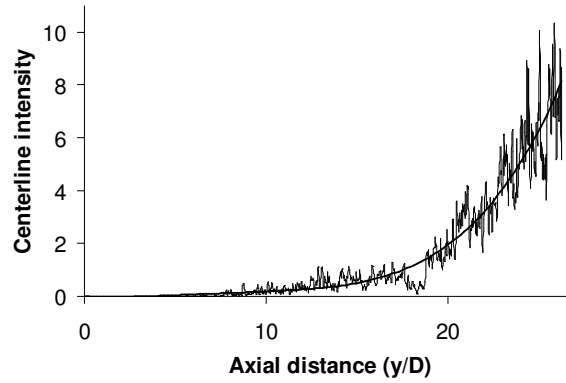

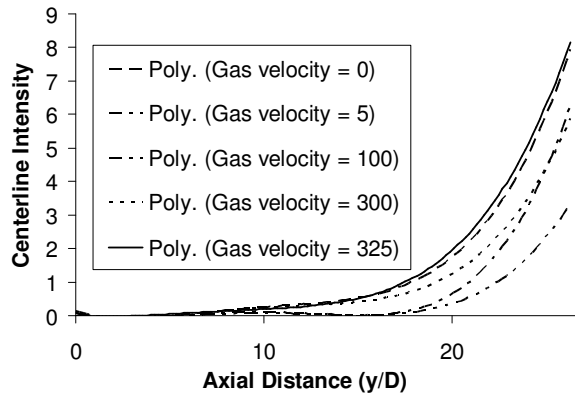**Figure 3a. Averaged centerline intensity distribution of LN$_2$/He flow (MR ≈ 1.0)**

Figure 3b. Averaged centerline intensity distribution of LN$_2$/He flow for different velocities of the coaxial gaseous jet
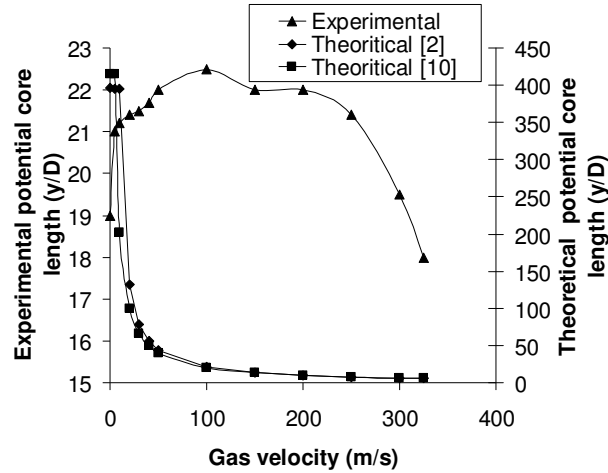
188

Figure 4. Potential core length of LN$_2$ jet for different velocities of the coaxial gaseous jet
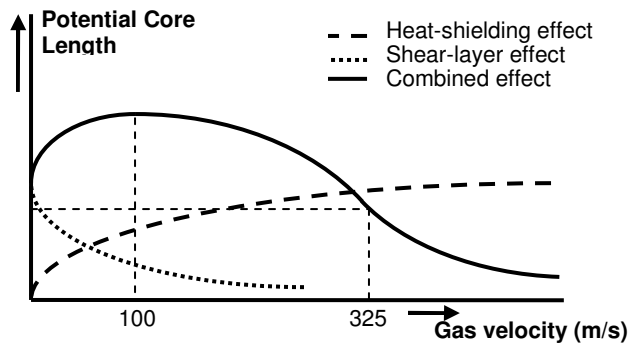

Figure 5. A schematic diagram of the effects of different parameters affecting the potential core length

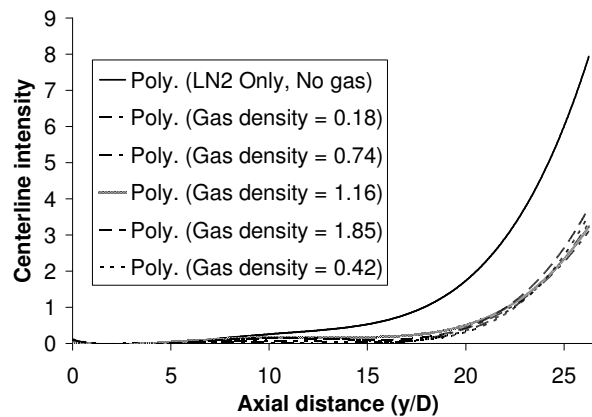**Figure 6. Averaged centerline intensity distribution of the flowfield for different densities of the coaxial gaseous jet**
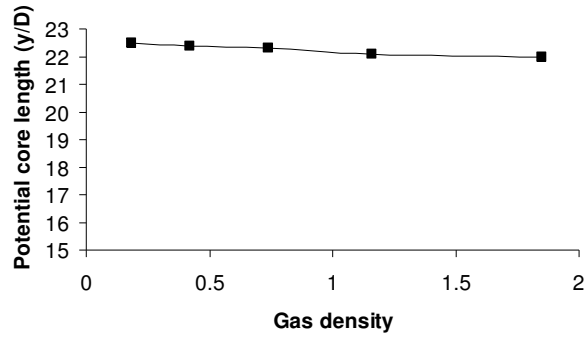
189

Figure 7. Potential core length of the LN₂ jet for different coaxial gas densities
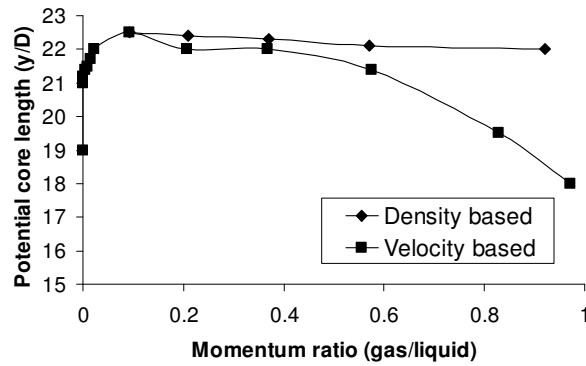

Figure 8. Variation of the potential core length of the LN₂ jet with the momentum ratio of the jets
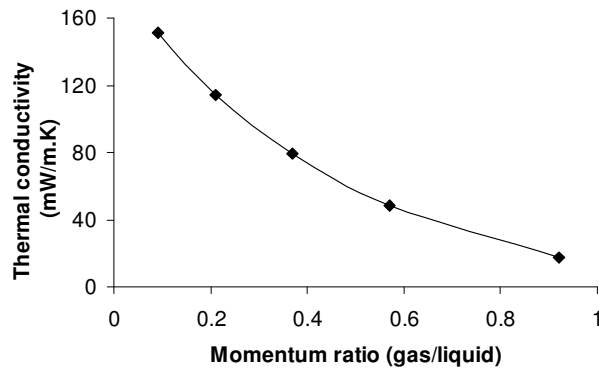

Figure 9. Variation of thermal conductivity with the momentum ratio (density based) of the jets

Thesis Bibliography

1. Arai, M., Shimizu, M. and Hiroyasu, H.: Breakup length and Spray Angle of High Speed Jet, ICLASS-85, pp. 1B/4/1-10

2. Arai, M., Shimizu, M. and Hiroyasu, H.: Similarity between the Breakup length of a High Speed Liquid Jet in Atmospheric and Pressurized Conditions, and Spray Angle of Jet, ICLASS-91, paper 61.

3. Arai, T. and Hashimoto, H.: Disintegration of a Thin Liquid Sheet in a Concurrent Gas Stream, Proceedings of the 3rd International Conference on Liquid Atomization and Spray Systems, 1985, pp 6B/1/11-7.

4. Bazarov, V. G. and Yang, V.: Liquid Propellant Rocket Engine Injector Dynamics, Journal of Propulsion and Power, Vol. 14, No. 5, September-October 1998, pp. 797-806.

5. Beer, J. M. and Chigier, N. A.: Combustion Aerodynamics, Applied Science Publishers, Ltd., London, 1972.

6. Bellan, J.: Supercritical (and subcritical) Fluid Behavior and Modeling: Drops, Streams, Shear and Mixing Layers, Jets and Sprays, Progress in Energy and Combustion Science, Vol. 26, 2000, pp. 329-366.

7. Branam, R. and Mayer, W.: Length Scales in Cryogenic Injection at Supercritical Pressure, Experiments in Fluids Vol. 33, 2002, pp. 422-428.

8. Branam, R. and Mayer, W.: Characterization of Cryogenic Injection at Supercritical Pressure, Journal of Propulsion and Power Vol. 19, No. 3, 2003, pp. 342-355.

9. Branam, R. and Mayer, W.: Atomization Characteristics on the Surface of Round Liquid Jet, Experiments in Fluids Vol. 36, 2004, pp. 528-539.

10. Bruno, T. J.: Experimental Approached for the Study and Application of Supercritical Jets, Combustion Science and Technology, 178, 2006, pp. 3-46.

11. Byoung-Do Kim and Stephen D. Heister: Two-Phase Modeling of Hydrodynamic Instabilities in Coaxial Injectors, Journal of Propulsion and Power, Vol. 20, No. 3, May–June 2004.

12. Candel, S., Herding, G., Synder, R., Scouflaire, P., Rolon, C., Vingert, L., Habiballah, M., Grisch, F., Pealat, M., Bouchardy, P., Stepowski, D., Cessou, A. and Colin, P.: Experimental Investigation of Shear Coaxial Cryogenic Jet Flames, Journal of Propulsion and Power, Vol. 14, No. 5, September-October 1998, pp. 826-834.

13. Candel, S., Juniper, M., Singla, G., Scouflaire, P. and Rolon, C.: Structure and Dynamics of Cryogenic Flames at Supercritical Pressure, Combustion Science and Technology, 178, 2006, pp. 161-192.

14. Carreau, J. L., Porcheron, E., Visage, D. Le and Roger, F.: Liquid Core Characterization of Coaxial Liquid Oxygen / Inert Gas Jets, International Journal of Fluid Mechanics Research, No. 4-6, 1997, pp. 498-507.

15. Carreau, J. L., Porcheron, E., Visage, D. Le and Roger, F.: Liquid Core Characterization of Coaxial Liquid Oxygen / Inert Gas Jet, 7th International Conference on Liquid Atomization and Spray Systems, Seoul, Korea, 1997.

16. Carreau, J. L., Porcheron, Prevost, L., E., Visage, D. Le and Roger, F., Gicquel, P. and Vingert, L.: Atomization of a Liquid Oxygen Jet by a Coaxial Inert Gas Jet, 14th Conference on Liquid Atomization and Spray Systems, Florence, 1997.

17. Chandrasekhar S.: Hydrodynamic and Hydromagnetic Stability, 1961, New York, Dover.

18. Chehroudi, B., Chen, S. H., Bracco, F. V. and Onuma, Y.: On the Intact Core of Full Cone Sprays, SAE paper 850126, 1985.

19. Chehroudi, B., Cohn, R., and Talley, D. G.: Cryogenic Shear Layers: Experiments and Initial Growth Rates of Round Cryogenic Jets at Subcritical and Supercritical Pressures, International Journal of Heat and Fluid Flow, Vol. 23, No. 5, 2002, pp. 554–563.

20. Chehroudi, B., Talley, D. G., and Coy, E. B.: Visual Characteristics and Initial Growth Rates of Round Cryogenic Jets at Subcritical and Supercritical Pressures, Physics of Fluids, Vol. 14, No. 2, Feb. 2002, pp. 850–861.

21. Chigier, N., and Reitz, R.D: Regimes of Jet Breakup and Breakup Mechanisms (Physical Aspects), Recent Advances in Spray Combustion: Spray Atomization and Drop Burning Phenomena – Volume I, Edited by K. Kuo, Progress in Astronautics and Aeronautics, AIAA, Washington, DC, 1996, Chap. 4, pp. 109-135.

22. Davis, D. W., and Chehroudi, B.: Measurements in an Acoustically Driven Coaxial Jet Under Sub-, Near- and Super-Critical Conditions, Journal of Propulsion and Power, Vol. 23, No. 2, March-April 2007, 364-374.

23. Emdee, J.L., Fentress, C.S. and Malinowski, M.R.: Development Testing for the RL10E-1 Engine, July 1997, AIAA-97-3094.

24. Engelbert, C., Hardalupas, Y., Whitelaw, J. H., Breakup Phenomena in Coaxial Airblast Atomizers, Proceedings: Mathematical and Physical Sciences, Vol. 451, No. 1941, Osborne Reynolds Centenary Volume. (Oct. 9, 1995), pp. 189-229.

25. Eroglu, H., Chigier, N. and Farago, Z.: Coaxial Atomizaer Liquid Intact Lengths, Physics of Fluids, Vol 3, No. 2, Feb 1991, pp. 303-308

26. Farago, Z., and Chigier, N.: Morphological Classification of Disintegration of Round Liquid Jets in a Coaxial Air Stream, Atomization and Sprays, Vol. 2, 1992, pp. 137-153.

27. Ferraro, M., Kujala, R. J., Thomas, J. L., Glogowski, M. and Micci, M.: Effects of GH_2/LOX Velocity and Momentum Ratios on Shear Coaxial Injector Atomization, Journal of Propulsion and Power, Vol. 18, No.1, 2002 Technical Notes.

28. Gautam, V. and Gupta, A. K.: Simulation of Flow and Mixing from a Coaxial Rocket Injector, 44th AIAA Aerospace Sciences Meeting, Reno, NV, January 9-12, 2006, AIAA 2006-1160.

29. Gautam, V. and Gupta A. K.: Cryogenic Flow and Mixing from a Single Element Coaxial Rocket Injector, 42nd AIAA/ASME/SAE/ASEE Joint Propulsion Conference, Sacramento, California, July 09 - 12, 2006, AIAA-2006-4529.

30. Gautam, V. and Gupta, A. K.: Simulation of Flow and Mixing from a Cryogenic Rocket Injector, Journal of Propulsion and Power, Vol. 23, No. 1, Jan-Feb 2007, pp. 123-130.

31. Gautam, V. and Gupta, A. K.: Transient Cryogenic Flow and Mixing from a Coaxial Rocket Injector, 45th Aerospace Sciences Meeting and Exhibits, Reno, Nevada, Jan. 08 - 11, 2007, AIAA-2007-0573.

32. Gautam, V. and Gupta A. K.: Characterization of Cryogenic Flow and Atomization from a Coaxial Rocket Injector, 43rd AIAA/ASME/SAE/ASEE Joint Propulsion Conference, Cincinnati, OH, July 08 - 11, 2007, AIAA-2007-5567.

33. Glogowski, M., Bar-Gill, M., Puissant, C., Kaltz, T., Milicic, M., and Micci, M., "Shear Coaxial Injector Instability Mechanisms," 30th AIAA/ASME/SAE/ASEE Joint Propulsion Conference and Exhibit, Indianapolis, IN, June 27-29, 1994, AIAA-94-2774.

34. Habiballah, M., Orain, M., Grisch, F., Vingert, L., Gicquel, P.: Experimental Studies of High-pressure Cryogenic Flames on the Mascotte Facility, Combustion Science and Technology, 178, 2006, pp. 101-128.

35. Hutt, J. J. and Cramer, J. M.: Advanced Rocket Injector Development at the Marshall Space Flight Center, Space Program and Technologies Conference, Huntsville, AL, Sep. 1996, AIAA-96-4266.

36. Huzel, D., Huang, D.: Modern Engineering for Design of Liquid Propellant Rocket Engines, Progress in Aeronautics and Astronautics, Vol. 147, AIAA, Washington, DC, 1992, pp. 104-110.

37. Immich, H. and Mayer, W.: Cryogenic Liquid Rocket Engine Technology Developments within the German National Technology Programme, 33rd AIAA/ASME/SAE/ASEE Joint Propulsion Conference and Exhibit, Seattle, WA, July 6-9, 1997, AIAA-1997-2822

38. Ivancic, B. and Mayer, W.: Time and Length Scales of Combustion in Liquid Rocket Thrust Chambers, Journal of Propulsion and Power, Vol. 18, No. 2, March-April. 2002, pp. 247-253.

39. Lasheras, J. C., Villermaux, E. and Hopfinger, E. J.: Break-up and atomization of a round water jet by a high-speed annular air jet, Journal of Fluid Mechanics, Vol. 357, 1998, pp. 351-379.

40. Lasheras, J.C. and Hoppfinger, E. J.: Liquid Jet Instability and Atomization in a Coaxial Gas Stream, Annual Review Fluid Mechanics, Vol. 32, 2000, pp. 275-308.

41. Lin, S. P. and Reitz, R. D.: Drop and Spray Formation from a liquid Jet, Annual Review of Fluid Mechanics 1998, Vol. 30, pp. 85–105.

42. Lefebvre, A.H.., Atomization and Sprays, 1st ed., Routledge, Oxford, UK,1989.

43. Marmottant, P. and Villermaux, E. On spray formation, Journal of Fluid Mechanics, Vol. 498, 2004, pp. 73–111.

44. Mason, E. A., and Saxena, S. C.: Approximate Formula for the Thermal Conductivity of Gas Mixtures, The Physics of Fluids, Vol. 1, No. 5, Sep.-Oct. 1958, pp. 361-369.

45. Mayer, W.: Coaxial Atomization of a Round Liquid Jet in a High Speed Gas Stream: A Phenomenological Study, Characteristics on the Surface of Round Liquid Jet, Experiments in Fluids Vol. 16, 1994, pp. 401-410.

46. Mayer, W. and Tamura, H.: Propellant Injection in a Liquid Oxygen/Gaseous Hydrogen Rocket Engine, Journal of Propulsion and Power, Vol. 12, No. 6, Nov-Dec 1996, pp. 1137-1147.

47. Mayer, W., Schik, A., Vielle, B., Chauveau, C., Gokalp, I., Talley, D., Woodward, R.: Atomization and Breakup of Cryogenic Propellants Under High Pressure Subcritical and Supercritical Conditions, Journal of Propulsion and Power, Vol. 14, No. 5, September-October 1998, pp. 835-842.

48. Mayer, W., Schik, A., Schaffler, M., and Tamura, H.,: Injection and Mixing Processes in High Pressure Liquid Oxygen/Gaseous Hydrogen Rocket Combustors, Journal of Propulsion and Power, Vol. 16, No. 5, Sep.-Oct. 2000, pp. 823-828.

49. Mayer, W., Ivancic, B., Schik, A., and Hornung, U.,: Propellant Atomization and Ignition Phenomena in Liquid Oxygen/ Gaseous Hydrogen Rocket Combustors, Journal of Propulsion and Power, Vol. 17, No. 4, July-Aug. 2001, pp. 794-799.

50. McNelis, N.B. and Haberbusch, M. S.: Hot Fire Ignition Test with Densified Liquid Hydrogen Using a RL10B-2 Cryogenic H2/O2 Rocket Engine, AIAA-97-2688, July 1997.

51. Oefelein, J. C. and Yang, V.: Modeling High Pressure Mixing and Combustion Processes in Liquid Rocket Engines, Journal of Propulsion and Power, Vol. 14, No. 5, September-October 1998, pp. 843-857.

52. Oschwald, M. and Micci, M.: Spreading Angle and Centerline Variation of Density of Supercritical Nitrogen Jets, Atomization and Spray, Vol. 11, 2002, pp. 91-106.

53. Oschwald, M., Smith, J. J., Branam, R., Hussong, J., Schik, A., Chehroudi, B. and Talley, D.: Injection of Fluids into Supercritical Environments, Combustion Science and Technology, Vol. 178, 2006, pp. 49-100.

54. Paster, R. D. and Stohler, S. L.: SSME Evolution for Next Generation Launch Systems, 25th AIAA/ASME/SAE/ASEE Joint Propulsion Conference, Monterey, California, July 10 - 12, 1989, AIAA-89-2502.

55. Porcheron, E., Carreau, J. L., Prevost, L., Visage, D. Le, Roger, F.,: Effect of Injection Gas Density on Coaxial Liquid Jet Atomization, Atomization and Sprays, Vol. 12, Issue 1, 2002, pp. 209-227.

56. Porcheron, E., Prevost, L., Carreau, J.L and Roger, F.: Coaxial Atomization: Influence of the Gas Jet density on the Liquid Core Characteristics, 16th Annual Conference on Liquid Atomization and Spray Systems, 11-13 September 2000, Darmstadt (Deutchland).

57. Pal, S., Moser, M. D., Ryan, H. M., Foust, M. J., Santoro, R. J.: Shear Coaxial Injector Atomization Phenomena for Combusting and Non-Combusting Conditions, Atomization and Sprays, Vol. 6, 1996, pp. 227-244.

58. Raynal L. : Instabilite et entrainement à l'interface d'une couche de melange liquide-gaz, Thèse de Doctorat, Université Joseph Fourier, Grenoble, France, 1997.

59. Rehab H, Villermaux E, Hopfinger, E. J.: Flow Regimes of Large Velocity Ratio Coaxial Jets," Journal of Fluid Mechanics, Vol. 345, 1997, pp. 357-381.

60. Reitz, R. D. and Bracco, F. V.: Mechanisms of atomization of a liquid jet, Physics of Fluids, Vol 25, No. 10, October 1982, pp. 1730-1742.

61. Sankar, S. V., Rosa, A. Brena de la, Isakovic, A., Bachalo, W. D.: Liquid Atomization by Coaxial Rocket Injectors, 29th Aerospace Sciences Meeting, Reno, NV, Jan. 7-10, 1991, AIAA-91-0691.

62. Smith, J., Klimenko, D., Clauss, W. and Mayer, W.: Supercritical LOX/Hydrogen Rocket Combustion Investigations Using Optical Diagnostics, 38th AIAA/ASME/SAE/ASEE Joint Propulsion Conference and Exhibit, Indianapolis, IN, July 7-10, 2002, AIAA-2002-4033.

63. Spaulding, D. B.: The Art of Partial Modeling, 9th International Symposium on Combustion, The Combustion Institute, 1963, pp. 833-843.

64. Strakey, P. A., Talley, D. G. and Hutt, J. J.: Mixing Characteristics of Coaxial Injectors at High Gas/Liquid Momentum Ratios, Journal of Propulsion and Power, Vol. 17, No. 2, March-April 2001, pp. 402-410.

65. Sutton, G.P., and Biblarz, O.: Rocket Propulsion Elements, 7th ed., John Wiley & Sons, Inc., New York, 2001, Chaps. 6 - 9.

66. Varga, C. M., Lasheras, J. C. AND Hopfinger, E. J.: Initial breakup of a small-diameter liquid jet by a high-speed gas stream, J. Fluid Mech., Vol. 497, 2003, pp. 405–434.

67. Villermaux, E.: Mixing and Spray Formation in Coaxial Jets, Journal of Propulsion and Power, Vol. 14, No. 5, Sep-Oct 1998, pp. 807-817.

68. Villermaux, E., Marmottant, Ph., and Duplat, J.: Ligament Mediated Spray Formation, Physics Review Letters, Vol 92, No 7, Feb 2004, pp. 74501-1,4.

69. Vingert, L., Gicquel, P., Lourme, D., and Menoret, L.: Coaxial Injector Atomization, Progress in Aeronautics and Astronautics, Vol. 169, AIAA, 1994.

70. Vingert, L., Gicquel, P., Ledoux, M., Care, I., Micci, M., and Glogowski, M.: Atomization in Coaxial Jet Injectors, Chapters 3, Progress in Aeronautics and Astronautics, Vol. 200, AIAA, 2004, pp. 105-140.

71. Wilke, C. R.: A Viscosity Equation for Gas Mixtures, The Journal of Chemical Physics, Vol. 18, No. 4, April 1950, pp. 517-519.

72. Woodward, R.: Doctoral Dissertation, Submitted to Department of Mechanical Engineering, Penn State University, 1994.

73. Woodward, R., Pal, S., Santoro, R. J. and Kuo, K.: Recent Advances in Spray Combustion: Spray Atomization and Drop Burning Phenomena – Volume I, Edited by K. Kuo, Progress in Astronautics and Aeronautics, AIAA, Washington, DC, 1996, Chap 8, pp. 185-209.

74. Worlund, A. L. and Stohler, S. L.: Space Shuttle Main Engine Evolutions, 37th AIAA/ASME/SAE/ASEE Joint Propulsion Conference, Salt Lake City, Utah, July 08 – 11, 2001, AIAA-2001-3417.

75. Wu P-K; Tseng L-K; Faeth G. M.: Primary breakup in gas/liquid mixing layers for turbulent liquids, Atomization and Sprays, Vol. 2, pp. 295-317

76. Yeralan, S., Pal, S. and Santoro, R. J.: Experimental Studies on Major Species and Temperature Profiles of Liquid Oxygen/Gaseous Hydrogen Rocket Combustion, Journal of Propulsion and Power, Vol. 17, No. 4, July-August 2001, pp. 788-793.

77. Yang, V., Habiballah, M., Popp, M. and Hulka, J.: Liquid Rocket Thrust Chambers: Aspects of Modeling, Analysis and Design, Chapters 9-10, Progress in Aeronautics and Astronautics, Vol. 200, AIAA, 2004.